



The University of
Nottingham

UNITED KINGDOM • CHINA • MALAYSIA

**Synthesis of Nanomaterials for Biomedical
Applications**

Selina Vi Yu Tang, BSc.

**Thesis submitted to the University of Nottingham
for the degree of Doctor of Philosophy**

January 2014

Abstract

This Thesis describes an investigation into the use of a continuous hydrothermal reactor for the synthesis of nanomaterials with potential use in three different biomedical applications – bone scaffolds, fluorescent biomarkers and MRI contrast agents.

In Chapter 1, an introduction to nanotechnology is given, followed by a brief account of the most prominent routes of nanomaterial synthesis. This includes a literature review of the key publications to date, which use different reactor designs for the continuous hydrothermal synthesis of nanoparticles. This Chapter also describes some problems associated with nanomaterial synthesis, along with the aims and motivations of this PhD.

Chapter 2 details the principles behind the main characterisation techniques which are used in the work throughout this Thesis. Some advantages and limitations of each technique are given.

Chapter 3 reports the synthesis of three different morphologies of hydroxyapatite. Attempts to introduce a drug and cations into the structure of hydroxyapatite are also detailed. Finally, cell proliferation and bone nodules assays showed that hydroxyapatite synthesised via this route exhibits no cytotoxic effect on mouse embryonic stem cells.

The synthesis of ZnS is the focus of Chapter 4, with the production of uncoated particles along with the implementation of three different stabilisers. The addition of 3-Mercaptopropionic acid was shown to decrease cluster size, shift the isoelectric point of particles, and alter their photoluminescent properties.

In Chapter 5, the synthesis of Fe_2O_3 , Fe_3O_4 , $\text{Gd}(\text{OH})_3$ and Co_3O_4 are described. The structural properties of these materials are analysed, as well as their capacity as contrast agents for magnetic resonance imaging. While relaxivity data for Co_3O_4 proved poor, Fe_3O_4 based materials showed relaxivity values comparable to some commercial contrast agents.

To conclude, a summary of the work detailed in this Thesis is delivered in Chapter 6. The most pertinent findings from this work are put forward, followed by a discussion of future work which could lead on from this Thesis.

Acknowledgments

There have been many people who have helped me through the course of my PhD research, and I am grateful to every one of them.

First and foremost, I'd like to thank my supervisors Prof. Ed Lester and Dr Andrei Khlobystov for their support and advice over the last 4 years.

I'd like to thank Dave Clift for his help with SEM; Dr Stephen Briddon for his help and advice with fluorometry analysis; Dr Michael Fay for obtaining the TEM images used in this Thesis; Dr Nigel Neate for his help in using the D8 XRD diffractometer, Vanessa Loczenski Rose for her help with the cell assays described in Chapter 3; and Don Yee for his help obtaining the SEM data in Chapter 4. I'd also like to thank Dr Peter Dunne for his help and advice with XRD analysis.

Huge thanks to my colleagues who have helped or advised me during my PhD studies: Dr Graham Rance, Dr Sherif Elbasuney, Dr Tom Huddle, Miquel Gimeno-Fabra, and Haiping Shen.

The funding for this work came from the EPSRC, with additional funding from Promethean Particles through a CASE award – thanks go to them.

I am grateful to Drs Pete Gooden, Sandy Reid and Helen Hobbs of Promethean Particles for giving me the opportunity to work on an Industrial Placement with them during my PhD – the knowledge I gained was invaluable. Additional thanks to Pete and Sandy, along with Dr Sam Tang and Ste Ambrose for taking the time to proofread my Chapters.

I'd like to extend an additional thank you to Ste Ambrose for his patience, for helping me navigate computer software (Figure 3.8 appears courtesy of his awesome rendering skills), and for his culinary skills which ensured I never ran on empty while working (MFEO).

Finally, I'd like to thank Sam, Tim, Rotion, Violet-Rosabelle, Xavier and my parents, Helen and David, for their unconditional love and support.

Affirmation

The work reported in this Thesis has not been published elsewhere, with the exception of the following publications:

Journal Publications

Q. Wang, **S. V. Y. Tang**, E. Lester & D. O'Hare, Synthesis of ultrafine layered double hydroxide (LDHs) nanoplates using a continuous-flow hydrothermal reactor. *Nanoscale*, **2013**, 5, 114-117, DOI: **10.1039/c2nr32568c**

E. Lester, **S. V. Y. Tang**, A. Khlobystov, V. L. Rose, L. BATTERY & C. J. Roberts, Producing nanotubes of biocompatible hydroxyapatite by continuous hydrothermal synthesis. *CrystEngComm*, **2013**, 15, 3256-3260, DOI: **10.1039/c3ce26798a**

F. Moro, **S. V. Y. Tang**, F. Tuna & E. Lester, Magnetic properties of cobalt oxide nanoparticles synthesised by a continuous hydrothermal method. *Journal of Magnetism and Magnetic Materials*, **2013**, 348, 1-7. DOI: **http://dx.doi.org/10.1016/j.jmmm.2013.07.064**

Conference Proceedings

Selina Tang, Edward Lester, Andrei Khlobystov, Producing Multifunctional Nanocomposites from Different Morphologies of Hydroxyapatite, *2nd International Solvothermal and Hydrothermal Association (ISHA) Conference*, Beijing, China, July **2010**

Selina Tang, Edward Lester, Andrei Khlobystov, Producing Hydroxyapatite Nanocomposites for Multifunctional Bone Scaffolds, *Technology World NanoForum*, London (Excel), UK, December **2010**

Selina Tang, Andrei Khlobystov, Stephen Briddon, Edward Lester, Continuous Hydrothermal Synthesis of Stabilized Zinc Sulphide Nanoparticles with Fluorescent Properties, *10th International Symposium of Supercritical Fluids (ISSF)*, San Francisco CA, USA, May **2012**

Selina Tang, Alexandra Martín-Cortes, Andrei Khlobystov, David Grant, Edward Lester, The Impact of Blending Novel Forms of Hydroxyapatite from Continuous Hydrothermal Synthesis into Bone Scaffolds, *10th International Symposium of Supercritical Fluids (ISSF)*, San Francisco CA, USA, May **2012**

Selina Tang, Andrei Khlobystov, Stephen Briddon, Edward Lester, Continuous Hydrothermal Synthesis of Stabilized Zinc Sulphide Nanoparticles with Fluorescent Properties, *2nd International Solvothermal and Hydrothermal Association (ISHA) Conference*, Austin TX, USA, January **2013**

Edward Lester, **Selina Tang**, Andrei Khlobystov, Steve Briddon, Christopher Starkey, Peter Dunne, The Continuous Production of Nanoparticles for Biomedical Applications, *7th International Conference on Materials for Advanced Technologies (ICMAT)*, Singapore, July **2013**

Table of Contents

| | | |
|-------|---|----|
| 1 | Background | 1 |
| 1.1 | Introduction to Nanotechnology | 1 |
| 1.2 | Advantages of Nanoscale..... | 2 |
| 1.2.1 | Melting Point..... | 3 |
| 1.2.2 | Magnetic Properties | 4 |
| 1.2.3 | Catalytic Properties..... | 5 |
| 1.2.4 | Advantages in Biomedicine | 5 |
| 1.3 | Safety of Nanomaterials | 6 |
| 1.4 | Synthesis of Nanomaterials..... | 7 |
| 1.4.1 | Top-Down Approaches | 7 |
| 1.4.2 | Bottom-Up Approaches | 8 |
| 1.5 | Hydrothermal Synthesis of Nanomaterials | 12 |
| 1.5.1 | Supercritical Water (ScW) and Sub-critical Water | 13 |
| 1.6 | Solvothermal Synthesis of Nanomaterials | 17 |
| 1.7 | Batch and Continuous-flow systems | 18 |
| 1.7.1 | Continuous-flow Hydrothermal Reactors..... | 19 |
| 1.7.2 | The University of Nottingham Counter-Current Reactor | 41 |
| 1.8 | Commercialisation of Hydrothermal Synthesis..... | 51 |
| 1.8.1 | Hanwha Chemical..... | 51 |
| 1.8.2 | Promethean Particles Ltd..... | 51 |
| 1.9 | Challenges of Nanomaterial Synthesis | 54 |
| 1.9.1 | Particle Stability | 54 |
| 1.9.2 | Methods of avoiding Particle Coagulation | 55 |
| 1.9.3 | Methods of Determining Particle Stability..... | 56 |
| 1.10 | Aims of this PhD..... | 58 |
| 2 | Structural Characterisation Techniques | 60 |
| 2.1 | Scanning Electron Microscopy (SEM) | 60 |
| 2.2 | Transmission Electron Microscopy (TEM) | 63 |
| 2.3 | Energy Dispersive X-Ray Spectroscopy (EDX/EDS) | 65 |
| 2.4 | X-Ray Diffraction (XRD) | 65 |
| 2.5 | Time-of-Flight Secondary Ion Mass Spectrometry (ToF-SIMS) | 69 |
| 2.6 | Dynamic Light Scattering (DLS) | 70 |
| 2.7 | Zeta (ζ) Potential..... | 73 |

| | | |
|-------|---|-----|
| 3 | Hydroxyapatite | 76 |
| 3.1 | Introduction..... | 76 |
| 3.1.1 | Hydroxyapatite (HA), $\text{Ca}_{10}(\text{PO}_4)_6(\text{OH})_2$ | 76 |
| 3.1.2 | Current applications using HA | 77 |
| 3.1.3 | Potential Applications for HA | 79 |
| 3.1.4 | Current Methods of Producing HA | 80 |
| 3.1.5 | Chapter Aims | 84 |
| 3.2 | Methodology | 86 |
| 3.2.1 | Synthesis of HA..... | 86 |
| 3.2.2 | Characterisation Methods | 98 |
| 3.2.3 | Material Application Methods..... | 98 |
| 3.3 | Results and Discussion | 100 |
| 3.3.1 | HA Platelets (HA-1) and Rods (HA-2) | 100 |
| 3.3.2 | The Effect of Precursor pH | 102 |
| 3.3.3 | The Effect of Precursor Concentration | 110 |
| 3.3.4 | Addition of Simvastatin | 113 |
| 3.3.5 | Addition of Zinc..... | 115 |
| 3.3.6 | <i>In Vitro</i> Cell Assays..... | 117 |
| 3.4 | Conclusions | 120 |
| 4 | Fluorescent Nanomaterials | 122 |
| 4.1 | Introduction..... | 122 |
| 4.1.1 | Fundamentals of Fluorescence | 122 |
| 4.1.2 | Quantum Dots | 123 |
| 4.1.3 | Applications using Quantum Dots | 125 |
| 4.1.4 | Synthesis of Quantum Dots | 127 |
| 4.1.5 | Disadvantages of Cadmium-Based Materials | 129 |
| 4.1.6 | Zinc Sulphide, ZnS | 130 |
| 4.1.7 | Capping Agents and Stabilisers | 130 |
| 4.1.8 | Chapter Aims | 131 |
| 4.2 | Methodology | 132 |
| 4.2.1 | Synthesis of CdS using the Nozzle Reactor | 132 |
| 4.2.2 | Initial Synthesis of ZnS using the Nozzle Reactor | 133 |
| 4.2.3 | Refined Method for ZnS Synthesis | 134 |
| 4.2.4 | Synthesis of ZnS using Thiourea | 135 |
| 4.2.5 | Synthesis of ZnS with Surfactants/Stabilisers..... | 135 |
| 4.2.6 | Structural Characterisation | 140 |
| 4.2.7 | Fluorometry Analysis | 141 |

| | | |
|-------|--|-----|
| 4.3 | Results and Discussion | 142 |
| 4.3.1 | Cadmium Sulphide, CdS | 142 |
| 4.3.2 | Initial synthesis of ZnS..... | 144 |
| 4.3.3 | Synthesis with Thiourea as the Sulphur Source | 147 |
| 4.3.4 | Synthesis of ZnS with Surfactants | 148 |
| 4.4 | Conclusions | 167 |
| 5 | Magnetic Resonance Imaging (MRI) Contrast Agents | 171 |
| 5.1 | Introduction..... | 171 |
| 5.1.1 | Principles of MRI | 171 |
| 5.1.2 | MRI Scans | 174 |
| 5.1.3 | Relaxation Time, Rate and Relaxivity | 175 |
| 5.1.4 | Role of Contrast Agents..... | 176 |
| 5.1.5 | Commercial Contrast Agents..... | 180 |
| 5.1.6 | Current Methods of Synthesising Contrast Agents..... | 183 |
| 5.1.7 | Project Aims | 184 |
| 5.2 | Methodology | 186 |
| 5.2.1 | Hydrothermal Synthesis of Nanoparticles..... | 186 |
| 5.2.2 | MRI Characterisation of Samples | 196 |
| 5.3 | Results and Discussion | 199 |
| 5.3.1 | Hematite, Fe ₂ O ₃ | 199 |
| 5.3.2 | Magnetite, Fe ₃ O ₄ | 207 |
| 5.3.3 | Gadolinium Hydroxide, Gd(OH) ₃ | 214 |
| 5.3.4 | Cobalt Oxide, Co ₃ O ₄ | 218 |
| 5.4 | Conclusions | 224 |
| 6 | Conclusions and Future Work..... | 227 |
| 6.1 | Conclusions | 227 |
| 6.2 | Future Work | 231 |
| 7 | Bibliography | 233 |
| 8 | Appendix..... | 248 |

List of Figures

| | |
|---|----|
| Figure 1.1. A summary of the different fields in which nanoparticles have been applied (Tsuzuki, 2009). | 3 |
| Figure 1.2. Illustration showing the increase in specific surface area with smaller particle size (Nano.gov, 2013). | 4 |
| Figure 1.3. A graph illustrating changes to ionic product, density and dielectric constant of water with increasing temperature, at a constant pressure of 24 MPa (Kritzer <i>et al.</i> , 1999). | 14 |
| Figure 1.4. Schematic diagram of the apparatus typically used by Adschiri <i>et al.</i> for continuous hydrothermal synthesis of nanoparticles (Adschiri <i>et al.</i> , 2000). | 20 |
| Figure 1.5. Image showing the internal structure and water flow in the T-piece reactor used by Adschiri <i>et al.</i> , collected using neutron radiography (Takami <i>et al.</i> , 2012). | 21 |
| Figure 1.6. Schematic of the reactor system used by Arai <i>et al.</i> (Kawasaki <i>et al.</i> , 2010). | 24 |
| Figure 1.7. Cross sectional photographs and drawings of the T-piece reactors used by Arai <i>et al.</i> (Kawasaki <i>et al.</i> , 2010). | 25 |
| Figure 1.8. (a) Reactor system design used by AIST, incorporating (b) the Central Collision Mixer (CCM) (Sue <i>et al.</i> , 2011). | 26 |
| Figure 1.9. (a) Diagram of the equipment used by Darr <i>et al.</i> (b) A diagram of the counter-current reactor geometry (Tighe <i>et al.</i> , 2012). | 27 |
| Figure 1.10. Diagram showing the geometry of the Confined Jet Reactor (CJR) used by Darr <i>et al.</i> (Gruar <i>et al.</i> , 2013). | 30 |
| Figure 1.11. A schematic diagram of the continuous flow reactor system used by Kim <i>et al.</i> for the synthesis of metal oxide nanoparticles in supercritical water or methanol. B: balance; C: condenser; F: 0.2 μm metal filter; L: liquid container; P: pressure gauge; R: supercritical reactor; T: thermocouple; V1: | |

| | |
|---|----|
| needle valve; V2: relief valve; V3: three-way valve; V4: safety valve; FT1: DI water/methanol feed tank; FT2: precursor solution feed tank; HP1: high pressure pump for DI water/methanol; HP2: high pressure pump for precursor solution; PH: preheater; PR: back pressure regulator; RH: reactor heater; WP: water preheater line (Kim <i>et al.</i> , 2008)..... | 32 |
| Figure 1.12. CFD simulations of the three tee reactors investigated at the Korea Institute of Science and Technology for the synthesis of LiFePO ₄ nanoparticles (Hong <i>et al.</i> , 2013). | 34 |
| Figure 1.13. A schematic diagram of continuous hydrothermal reactor system built by Aymes <i>et al.</i> in 2001 (Aimable <i>et al.</i> , 2009b)..... | 37 |
| Figure 1.14. Diagram showing the X configuration of the mixing point, drilled into a block of Inconel 625, used in the systems by Aymes <i>et al.</i> | 38 |
| Figure 1.15. Revised system design by Aymes <i>et al.</i> , built in 2006..... | 39 |
| Figure 1.16. Model depicting the geometry of the reactor patented by Aymes <i>et al.</i> (Aymes <i>et al.</i> , 2011)..... | 40 |
| Figure 1.17. Schematic diagram of the continuous hydrothermal reactor system used by Demoisson <i>et al.</i> (Demoisson <i>et al.</i> , 2011)..... | 41 |
| Figure 1.18. Diagram showing the configuration of the counter-current Nozzle reactor, invented at The University of Nottingham (Lester and Azzopardi, 2005, Lester <i>et al.</i> , 2006). | 43 |
| Figure 1.19. Orientation of parts used to construct the counter current Nozzle Reactor (Lester <i>et al.</i> , 2006). | 44 |
| Figure 1.20. Schematic diagram of the counter current reactor system at the University of Nottingham. | 45 |
| Figure 1.21. A photo of the counter-current reactor system. | 47 |
| Figure 1.22. Photograph of the Pilot Scale reactor system which incorporates the counter-current Nozzle reactor technology, courtesy of Promethean Particles Ltd (see Section 1.8.2). | 50 |

Figure 1.23. Ratios of surfactant to nanoparticle where (a) shows insufficient surfactant concentration resulting in partial coverage, (b) displays optimum surfactant coverage and maximum stability, and (c) shows too much surfactant leading to layer collapse and unstable particles (Lubrizol, 2013). .56

Figure 2.1. An illustration showing the components in a typical scanning electron microscope (Flegler et al., 1995).61

Figure 2.2. (a) A simplified depiction of how a typical TEM operates; (b) a schematic showing a 3-dimensional tube is viewed as a 2-dimensional image under a TEM.....63

Figure 2.3. A diagram showing the basis of XRD analysis.66

Figure 2.4. A diagram of the hydrodynamic diameter of a particle which is reported by DLS analysis (Malvern, 2013).....71

Figure 2.5. A schematic representation of what is measured by zeta potential (Malvern, 2013).74

Figure 3.1 Images illustrating the continuous hydrothermal reactor system. The reactor section is highlighted in (b), showing the superheated aqueous $(\text{NH}_4)_2\text{HPO}_4$ (red) solution mixing with the ambient $\text{Ca}(\text{NO}_3)_2 \cdot 4\text{H}_2\text{O}$ (yellow) to form particles at the interface (c).87

Figure 3.2. Chemical structure of (a) Simvastatin in its inactive lactone form, and (b) Simvastatin in its active hydroxyl acid form.94

Figure 3.3. (a) SEM and (b) TEM images of particles in sample HA-1..... 100

Figure 3.4. (a) SEM image and (b) TEM image of particles in HA-2..... 102

Figure 3.5. SEM image of HA-3..... 103

Figure 3.6. HRTEM images of (a) HA-4a; (b) HA-4b; (c) HA-4c; (d) HA-4d; (e) HA-4e; and (f) HA-4f..... 105

Figure 3.7. (a) SEM image of 'open-ended rods', (b) darkfield imaging in TEM and (c) TEM image show tube structures while (d) is an SEM image showing a tube in the middle of the rolling process (highlighted with a red arrow). 106

| | |
|---|-----|
| Figure 3.8. Images illustrating the scrolling of a sheet, so that the corners meet. | 107 |
| Figure 3.9. SEM images of (a) HA-6, and (b) HA-7..... | 109 |
| Figure 3.10. XRD patterns for samples HA-1 to HA-7. The expected peak pattern for hexagonal hydroxyapatite (ICCD PDF 74-566) is shown at the bottom.. | 109 |
| Figure 3.11. SEM images of (a) HA-8, (b) HA-9, (c) HA-10, (d) HA-11. | 111 |
| Figure 3.12. SEM image of HA-12. | 112 |
| Figure 3.13. XRD patterns for HA-8 to HA-Zn. Patterns for HA-1 and HA-2 are also shown for comparison. The expected peak pattern for hexagonal hydroxyapatite (ICCD PDF 74-566) is shown at the bottom. For HA-9, peaks indicated with a black square match monoclinic brushite (ICCD PDF 9-77) while other peaks match monetite; for HA-Zn, peaks labelled with black triangles correspond to monoclinic parascholzite (ICCD PDF 35-495)..... | 113 |
| Figure 3.14. (a) SEM Image and (b) TEM image of HA-SIM. | 114 |
| Figure 3.15. ToF-SIMS Data for HA-1, HA-2 and HA-SIM. | 115 |
| Figure 3.16. (a) TEM image of sample HA-Zn, and an elemental distribution map for (b) Ca, (c) O, (d) P, and (e) Zn. | 116 |
| Figure 3.17. XRD pattern of HA-Zn; the predominant phases are hexagonal hydroxyapatite (ICCD PDF 74-566, shown at the bottom) and monoclinic parascholzite (ICCD PDF 35-495, peaks shown with blue triangles). Additional smaller peaks match calcium hydrogen phosphate (ICCD PDF 77-128)..... | 117 |
| Figure 3.18. Results from the cell proliferation assay performed using three different concentrations of nanoparticles from sample HA-1 and sample HA- Zn, after 1, 3 and 6 days of incubation. | 118 |
| Figure 3.19. Images from the bone nodule assay - Cells cultured in osteogenic media with hydroxyapatite from Sample HA-1 at various concentrations, (a) 100 µg/ml; (b) 10 µg/ml; (c) 1 µg/ml; (d) control | 119 |

| | |
|---|-----|
| Figure 4.1. Illustration of a typical QD structure; a CdSe core is surrounded by a ZnS shell and functionalised with siloxane and methacrylate (MMA) (Park et al., 2010). | 124 |
| Figure 4.2. A schematic diagram showing the reactor setup for the refined synthesis method of ZnS. | 134 |
| Figure 4.3. A schematic diagram displaying the reactor setup for the synthesis reaction of ZnS with capping agents..... | 136 |
| Figure 4.4. Photos of (a) CdS 240, (b) CdS 300, and (c) CdS 400. | 142 |
| Figure 4.5. (a) and (b) show TEM images of sample CdS 400. | 144 |
| Figure 4.6. XRD pattern for sample ZnS 400, with expected peak positions of cubic ZnS (ICCD PDF 80-20) shown in black, and hexagonal ZnS (ICCD PDF 80-7) shown in red. | 145 |
| Figure 4.7. a) and b) TEM images and c) HRTEM images of sample ZnS 400. . | 146 |
| Figure 4.8. EDX Spectrum collected for sample ZnS 400..... | 147 |
| Figure 4.9. XRD pattern for Sample ZnS-TU-400. Peaks match zinc sulphate hydrate and zinc hydrogen phosphate. | 148 |
| Figure 4.10. XRD Patterns of the four ZnS samples with the matched peak positions of different ZnS phases shown below. Numbered labels indicate the ICCD PDF file number..... | 150 |
| Figure 4.11. SEM images of (a) Uncapped ZnS; (b) ZnS:PVP 5/5; (c) ZnS:NaOH 5/5; and (d) ZnS:3-MPA 5/5. | 154 |
| Figure 4.12. Zeta potential profiles for the four samples, as a function of pH.. | 157 |
| Figure 4.13. A schematic diagram depicting ZnS particles surface modified with 3-MPA. | 158 |
| Figure 4.14. (a) The excitation spectra ($\lambda_{em} = 540$ nm) and (b) emission spectra ($\lambda_{ex} = 360$ nm) for Uncapped ZnS and ZnS produced with three different surfactants using 5:5 flow ratios. The spectra of the precursors and water blank were obtained as a control. | 161 |

| | |
|---|-----|
| Figure 4.15. (a) The excitation spectra ($\lambda_{em} = 540 \text{ nm}$) and (b) emission spectra ($\lambda_{ex} = 360 \text{ nm}$) for ZnS:3-MPA samples produced using different precursor flow ratios. The spectra of the precursors and water blank were obtained as a control. | 164 |
| Figure 5.1. An image of an MRI scanner depicting the different components (Action, 2013)..... | 173 |
| Figure 5.2. A diagram showing the z (longitudinal) and xy (transverse) planes of magnetisation. The relationship between T_2 relaxation time and spin recovery is also summarised (Oldendorf, 1988). | 175 |
| Figure 5.3. (a) Native MR Image (no contrast agent present) of liver in a patient with cholangiocellular carcinoma (cancer), and (b) MR image after T_2 weighted contrast agent has been administered. Differentiation of the lesion is vastly improved after contrast agent is introduced (AG, 2013). | 179 |
| Figure 5.4. A schematic diagram showing the reaction setup for synthesis of Fe_2O_3 | 187 |
| Figure 5.5. A schematic diagram showing the reaction setup for Fe_3O_4 synthesis. | 190 |
| Figure 5.6. A schematic diagram showing the reaction setup for Co_3O_4 synthesis. | 193 |
| Figure 5.7. A schematic diagram showing the reaction setup for $\text{Gd}(\text{OH})_3$ synthesis. | 195 |
| Figure 5.8. Photo of the Halbach 0.5 T Table-Top MRI Scanner at Nottingham Trent University..... | 197 |
| Figure 5.9. Photos of the Bruker 2.35 T MRI scanner at Nottingham Trent University. | 198 |
| Figure 5.10. Photograph of Fe_2O_3 Samples in First Temperature Set. | 199 |
| Figure 5.11. Photograph of Fe_2O_3 Samples in Second Temperature Set..... | 200 |
| Figure 5.12. Photograph of Fe_2O_3 Samples in Third Temperature Set..... | 200 |

| | |
|--|-----|
| Figure 5.13. A bar chart summarising the r_2 relaxivities of the 12 samples of synthesised Fe_2O_3 , calculated using the T_2 times acquired using the 0.5 T Halbach scanner, and Equation 2. | 202 |
| Figure 5.14. Images collected from the 2.35 T MRI scanner showing T_2 relaxation times (in ms) and R_2 relaxation for a) $\text{Fe}(\text{NO}_3)_3 \cdot 9\text{H}_2\text{O}$, b) HEM A1, c) HEM A2, d) HEM A3, e) HEM A4. | 203 |
| Figure 5.15. A chart summarising the particle size data obtained from DLS analysis, for the 12 synthesised Fe_2O_3 samples. | 204 |
| Figure 5.16. XRD patterns obtained for samples HEM A1, HEM B1, and HEM C1. At the bottom are the expected peak positions for Fe_2O_3 (ICCD PDF 86-550). | 206 |
| Figure 5.17. Photo of Fe_3O_4 Samples in Second Temperature Set. | 207 |
| Figure 5.18. Images collected from the 2.35 T MRI scanner showing T_2 relaxation times (in ms) and R_2 relaxation for (a) water blank, (b) 0.025 M Ammonium Iron Citrate (precursor), (c) MAG G1, (d) MAG G2, (e) MAG G3, and (f) MAG G4. | 209 |
| Figure 5.19. XRD patterns obtained for samples MAG G1 and MAG G3. At the bottom are the expected peak positions for cubic Fe_3O_4 (ICCD PDF 88-315). | 212 |
| Figure 5.20. (a) and (b) are TEM images of MAG G1, uncoated Fe_3O_4 | 213 |
| Figure 5.21. TEM image of MAG G3, Fe_3O_4 nanoparticles coated in dextran. ... | 214 |
| Figure 5.22. Photo of the Second Set of $\text{Gd}(\text{OH})_3$ Samples. | 215 |
| Figure 5.23. XRD Pattern obtained for GAD E1, with the expected peak positions of hexagonal $\text{Gd}(\text{OH})_3$ (ICCD PDF 83-2037) shown below. | 218 |
| Figure 5.24. Darkfield TEM image of sample Co_3O_4 showing particles with cubic morphology. | 220 |
| Figure 5.25. Graph showing the particle size distribution of Co_3O_4 particles. | 220 |

| | |
|--|-----|
| Figure 5.26. The XRD pattern obtained for sample Co_3O_4 . Peaks correspond with the expected pattern of cubic Co_3O_4 (ICCD PDF 009-0418), which are shown below. | 222 |
| Figure 5.27. High magnification HRTEM image of Co_3O_4 nanoparticles illustrating the interplanar spacing. | 223 |
| Figure A1. SEM images of (a) ZnS:NaOH 9/1, (b) ZnS:NaOH 8/2, (c) ZnS:NaOH 7/3, (d) ZnS:NaOH 6/4. | 248 |
| Figure A2. SEM images of (a) ZnS:3MPA 9/1, (b) ZnS:3MPA 8/2, (c) ZnS:3MPA 7/3, (d) ZnS:3MPA 6/4. | 249 |
| Figure A3. SEM images of (a) ZnS:PVP 9/1, (b) ZnS:PVP 8/2, (c) ZnS:PVP 7/3, (d) ZnS:PVP 6/4. | 250 |
| Figure A4. (a) The excitation spectra ($\lambda_{\text{em}} = 540 \text{ nm}$) and (b) emission spectra ($\lambda_{\text{ex}} = 360 \text{ nm}$) for ZnS:PVP samples produced using different precursor flow ratios. The spectra of the precursors and water blank were obtained as a control. | 253 |
| Figure A5. (a) The excitation spectra ($\lambda_{\text{em}} = 540 \text{ nm}$) and (b) emission spectra ($\lambda_{\text{ex}} = 360 \text{ nm}$) for ZnS:NaOH samples produced using different precursor flow ratios. The spectra of the precursors and water blank were obtained as a control. | 254 |

List of Tables

| | |
|---|-----|
| Table 1.1. The critical temperatures and pressures of three solvents. (Fang, 2010)..... | 17 |
| Table 3.1. Reactor system temperatures for synthesis of HA-1 | 87 |
| Table 3.2. System temperatures during synthesis of HA-4 sample | 90 |
| Table 3.3. A summary of experimental details for synthesis of various HA samples..... | 96 |
| Table 4.1. Reaction temperatures for each ZnS Sample. | 133 |
| Table 4.2. Reactor System temperatures for samples synthesised using thiourea. | 135 |
| Table 4.3. System temperatures for synthesis of ZnS with surfactants. | 137 |
| Table 4.4. Flow ratios for the different ZnS:3-MPA Samples. | 138 |
| Table 4.5. Flow ratios for the different ZnS:PVP Samples. | 139 |
| Table 4.6. Flow ratios for the different ZnS:NaOH Samples. | 140 |
| Table 4.7. Summary of crystal phase and crystalline size for each sample, as derived from XRD analysis. | 152 |
| Table 4.8. A table showing the average cluster size for each sample, as measured from SEM images. | 155 |
| Table 4.9. A summary of the average crystallite size, average cluster size, and wavelength of peak emission for each ZnS sample. | 165 |
| Table 5.1. Summary of Temperatures and Flows for first set of Fe ₂ O ₃ Samples. | 188 |
| Table 5.2. Summary of Temperatures and Flows for second set of Fe ₂ O ₃ Samples. | 188 |
| Table 5.3. Summary of Temperatures and Flows for third set of Fe ₂ O ₃ Samples. | 189 |
| Table 5.4. Summary of Temperatures and Flows for First Set of Fe ₃ O ₄ Samples. | 191 |

| | |
|--|-----|
| Table 5.5. Summary of Temperatures and Flows for Second Set of Fe ₃ O ₄ Samples. | 191 |
| Table 5.6. A Summary of Temperatures for the Synthesis of Co ₃ O ₄ Sample.... | 193 |
| Table 5.7. A Summary of Temperatures and Flows for the Synthesis of the First Set of Gd(OH) ₃ Samples. | 195 |
| Table 5.8 . A Summary of Temperatures and Flows for the Synthesis of the Second Set of Gd(OH) ₃ Samples. | 196 |
| Table 5.9. Summary of the measured T ₂ relaxation times for the Fe ₂ O ₃ samples, precursor and water blank. The r2 values, calculated using Equation 2, are also given. | 201 |
| Table 5.10. Summary of the T ₂ relaxation times for the Fe ₃ O ₄ samples, precursor and water blank, measured using the Halbach 0.5 T MRI Scanner. The r2 values, calculated using Equation 2, are also given. | 208 |
| Table 5.11. Summary of the measured T ₂ relaxation times for the Gd(OH) ₃ samples, precursor and water blank. The r2 values, calculated using Equation 2, are also given. | 216 |
| Table 5.12. Summary of the measured T ₂ relaxation times for the sample of Co ₃ O ₄ , its precursor, and water blank. The r2 values, calculated using Equation 2, are also given. | 219 |
| Table 5.13. The d-spacing for each plane in the Co ₃ O ₄ crystal, and the respective peak position, as calculated from the XRD pattern. | 222 |
| Table A1. Zeta Potential data for Uncapped ZnS. | 251 |
| Table A2. Zeta Potential data for ZnS:3MPA 5/5. | 251 |
| Table A3. Zeta Potential data for ZnS:PVP 5/5. | 252 |
| Table A4. Zeta Potential data for ZnS:NaOH 5/5. | 252 |

List of Abbreviations

| | |
|----------|--|
| 3-MPA | 3-mercaptopropionic acid |
| AIST | (National Institute of) Advanced Industrial Science and Technology |
| BPR | back pressure regulator |
| BSE | backscattered electrons |
| CaP | calcium phosphate |
| CCM | central collision mixer |
| CFD | computational fluid dynamics |
| CFHS | continuous flow hydrothermal synthesis |
| CJR | Confined Jet Reactor |
| cm | centimetre |
| DI | deionised |
| DLS | dynamic light scattering |
| DNA | deoxyribonucleic acid |
| EDX | energy dispersive X-ray spectroscopy |
| EU | European Union |
| FP7 | Seventh Framework Programme |
| FTIR | fourier-transform infra-red |
| FWHM | the full-width of the peak at half maximum |
| g | gram |
| h | hour |
| HA | hydroxyapatite |
| HitCH | High-throughput Continuous Hydrothermal |
| HPLC | high-performance liquid chromatography |
| HRTEM | high resolution transmission electron microscopy |
| ICCD PDF | International Centre for Diffraction Data powder diffraction file |
| IEP | isoelectric point |
| kg | kilogram |
| KIST | Korea Institute of Science and Technology |
| kV | kilovolt |
| LAI | light adsorption imaging |
| LCA | life cycle analysis |
| M | molar |
| mESC | mouse embryonic stem cells |
| min | minute |

| | |
|------------|--|
| ml | millilitre |
| mm | millimetre |
| mol | moles |
| MPa | mega pascal |
| MRI | magnetic resonance imaging |
| ms | millisecond |
| MS1 | metal salt pump 1 |
| MS2 | metal salt pump 2 |
| NADP/NADPH | nicotinamide adenine dinucleotide phosphate |
| nm | nanometre |
| NP | nanoparticle |
| PL | photoluminescent |
| PVP | polyvinylpyrrolidone |
| PZC | point of zero charge |
| QD | quantum dots |
| QELS | quasi-elastic light scattering |
| RAMSI | Rapid Automated Materials Synthesis Instrument |
| RF | radio frequency |
| RFU | relative fluorescence units |
| SChEME | School of Chemical, Environmental and Mining Engineering |
| ScW | supercritical water |
| SE | secondary electrons |
| SEM | scanning electron microscopy |
| SHYMAN | Sustainable Hydrothermal Manufacture of Nanomaterials |
| SMEs | small and medium enterprises |
| SNU | Seoul National University |
| SPION | superparamagnetic iron oxide nanoparticle |
| STEM | scanning transmission electron microscopy |
| TCH | thiocarbohydrazide |
| TEM | transmission electron microscopy |
| TGA | thermal gravimetric analysis |
| ToF-SIMS | time-of-flight secondary ion mass spectrometry |
| TTCP | tetracalcium phosphate |
| UCL | University College London |
| USPION | ultrasmall superparamagnetic iron oxide nanoparticle |
| UV | ultraviolet |
| XRD | X-ray diffraction |
| YAG | yttrium aluminium garnet |

List of Symbols

| | |
|----------------|---|
| % | percent |
| ° | degrees |
| " | inch |
| < | less than |
| > | more than |
| μL | micro litre |
| μM | micro molar |
| μm | micro metre |
| μmol | micro moles |
| Å | angstroms |
| C | centigrade |
| <i>D</i> | crystallite size |
| H _c | magnetic coercivity |
| K _w | dissociation constant of water |
| mM | milli molar |
| P _c | critical pressure |
| r ₂ | relaxivity |
| s | second |
| T | tesla |
| T ₁ | relaxation time for the longitudinal component of MRI |
| T ₂ | relaxation time for the transverse component of MRI |
| T _c | critical temperature |
| w/w% | mass fraction |
| β | full-width of the peak at half maximum |
| ζ | zeta |
| θ | incident angle |
| λ | wavelength |

Chapter 1

Background

This Chapter will introduce the concept of nanotechnology and define some key terms. The relevance of this research field will be discussed, thereby providing the fundamental motivations for this PhD project. The history of nanotechnology will only be described briefly; instead this Chapter will focus more on the current technologies employed in the synthesis of nanomaterials, and how these can be, or currently are, applied at a commercial level.

1.1 Introduction to Nanotechnology

It can be argued that whilst nanoparticles (NPs) have existed naturally for millions of years, the 'notion' of nanotechnology was first introduced in 1959 by Richard Feynman in his talk "There's Plenty of Room at the Bottom", where he described the potential to develop a system of manipulating individual atoms and molecules. Since then, the field of nanotechnology has acquired great interest, particularly in the last thirty years or so, as techniques to study and analyse particles have advanced. The field of nanotechnology encompasses the synthesis, study and manipulation of particles which are between one and one hundred nanometres in at least one dimension; where a nanometre is defined as one billionth (or 10^{-9}) of a metre.

1.2 Advantages of Nanoscale

What makes nanomaterials such an interesting area of research is that it is not simply the miniaturisation of particles. At the nanoscale, some material properties are affected by the laws of atomic physics, and so behave in a different way or exhibit properties unlike those of the traditional bulk material. This is not the case for a macro to micro size transition and is described as the quantum size effect phenomenon (Bhushan, 2010). Depending on the material in question, a range of properties can be enhanced at the nanoscale – a few examples are highlighted in the subsequent Sections. As a result of these enhanced properties, nanomaterials have been utilised in a plethora of applications, as summarised in Figure 1.1.

Furthermore, the enhanced properties are often seen for significantly lower weight loadings of nanoscale material compared to the bulk scale equivalent. In an applied sense, this translates to less nanomaterial additive required in a product, compared to the same micron - or larger - scale compound, to give the same effect. This means, for most applications, lower production and processing costs for the manufacturers which can be passed on to consumers; for some niche fields, such as electronics, devices can be made smaller without compromising on performance.

turn, means costs are lowered and any detrimental effect on the environment (through mass extraction and unsustainable consumption) is reduced.

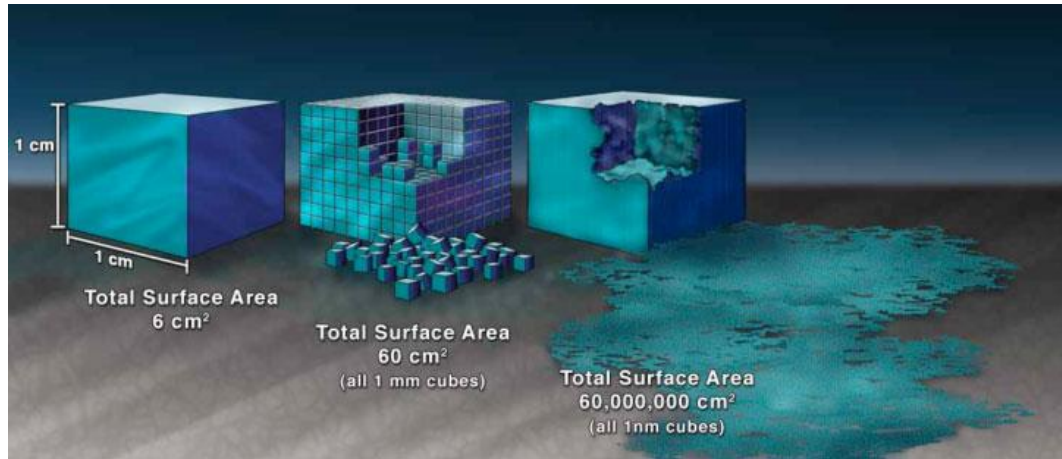


Figure 1.2. Illustration showing the increase in specific surface area with smaller particle size (Nano.gov, 2013).

1.2.2 Magnetic Properties

It was first speculated in 1930 that ferromagnetic particles (those which form permanent magnets or are permanently attracted to magnets) could display super-paramagnetic behaviour (this is where the magnetisation is at an average of zero, but particles can become magnetised by an external magnetic field), if the particles were small enough (Frenkel and Dorfman, 1930). Since then, this theory was proved and ferrite particles of particle size 10 nm were shown to exhibit super-paramagnetic behaviour with low magnetic coercivity, H_c , that is the intensity of field required to demagnetise the particles (Sato *et al.*, 1987). It is believed that such phenomena seen in magnetic nanoparticles is due to the large proportion of atoms at the particle surface, a magnetic dead layer, where atoms cannot maintain ferromagnetism over a distance (Willard *et al.*, 2004).

1.2.3 Catalytic Properties

Due to the increased surface area to volume ratio of nanoparticles, compared to bulk or even micron-scale particles, nano-catalysts have demonstrated higher efficiencies or rates of conversion with a smaller mass of material. For example, TiO₂ nanoparticles were shown to be more effective than larger particles in the photocatalytic degradation of pollutants (Loryuenyong *et al.*, 2013).

1.2.4 Advantages in Biomedicine

Many of the building blocks of biological systems, namely DNA and proteins, are sized in the nanometre range; for example, haemoglobin has a 5.5 nm diameter while insulin measures 3 nm in width and a DNA double helix has intra-strand spacing of 2 nm (Alberts *et al.*, 2002). As pharmaceutical research begins to focus on developing drugs at a nanoscale level, the ability to directly target erroneous proteins, usually the cause of many biochemical disorders, becomes feasible (Liu and Webster, 2007). Furthermore, nanoparticles – due to their small size – have the potential to penetrate cell membranes and bind to DNA (Geinguenaud *et al.*, 2012) or penetrate the blood brain barrier (Krol *et al.*, 2013). While much research exploits this possibility as an opportunity to treat genetic mutations or abnormalities, this also gives rise to the thought that nanomaterials could pose a massive health and safety risk, an issue which is discussed in Section 1.3.

1.3 Safety of Nanomaterials

While the advantages of nanomaterials in biomedicine have been reported in the literature, and highlighted in Section 1.2.4, there has been much speculation in the scientific community, and in the wider public, over the hazards involved with nanotechnology. As this field of research receives more attention, particularly in the public eye, more studies are being conducted globally to ascertain a definitive answer on whether 'nano' should be considered synonymous with 'toxic', and what it means to have nanoparticles present in our everyday products. One such study was initiated by BMBF, the German Federal Ministry of Education and Research, and led by BASF - one of the biggest chemicals companies in the world. The three year project concluded that chemical composition remains the most important factor contributing to toxicity and health risks, and the particle size is of secondary importance. The study also found that functionalization of particles could reduce toxicity as the surfaces became shielded (BASF, 2013). It is generally agreed that a degree of caution should be exercised when handling nanomaterials, as it is a relatively new area of research, and handling dry powders should be avoided to minimise the risks of particle inhalation. Nevertheless, more emerging nanotoxicology studies are finding that nanoparticles should not be feared in the way that mass media tend to portray them.

1.4 Synthesis of Nanomaterials

The size, morphology and surface area of the nanomaterial are crucial to its function and application. Generally speaking, these characteristics are determined by the method employed to prepare the material. As such, the synthesis method is a highly significant step in determining the characteristics and properties of the nanomaterial product. Typically, the methods of nanoparticle synthesis are categorised as one of two approaches: top-down or bottom-up. These terms will be elaborated upon in Sections 1.4.1 and 1.4.2.

1.4.1 Top-Down Approaches

The most common example of top-down production of nanoparticles is mechanochemical milling of micron-scale or bulk scale materials, where larger particles are broken down to smaller ones. There are several reports in the literature describing the use of different types of milling to produce magnetic materials (Manh *et al.*, 2009, Sampathkumaran *et al.*, 2011); materials for electronic applications (Chen *et al.*, 2010, Hallmann *et al.*, 2011, Zaghbi *et al.*, 2011); and for the synthesis of nanoscale drugs in the pharmaceutical industry (Laaksonen *et al.*, 2011, Basa *et al.*, 2008). In these papers, the length of time of milling and the milling speed is described as affecting the structure of the final product. As well as milling, laser ablation has also been used for NP synthesis (Amendola *et al.*, 2011).

However, compared to bottom-up approaches, the volume of reports using top-down methods to synthesise nanoparticles is severely lacking; this is likely to be due to the inherent drawbacks of top-down methods relative to bottom-up procedures. Examples of such disadvantages include limited control over particle

size and morphology, wide particle size distributions and, in some cases, can be time intensive where processes can take up to 20 hours (Manh *et al.*, 2009). These shortcomings mean most researchers tend to prefer bottom-up approaches instead.

1.4.2 Bottom-Up Approaches

Converse to top-down methods, the bottom-up approach generally builds larger structures from the smaller building blocks, namely atoms (Rotello, 2004). The main examples of bottom-up synthesis are chemical, and can be further classified depending on phase; these will be subsequently elaborated upon.

1.4.2.1 Solid State Reactions

In these reactions, solid reactants tend to be mixed then heated at high temperatures either in air, or another gas flow of choice (Sohrabnezhad and Valipour, 2013). Reports have described the use of solid-state reactions to produce CuO (Sohrabnezhad and Valipour, 2013) and Si₃N₄ (Dasog and Veinot, 2012) amongst other materials. These types of reactions have the disadvantages of being inherently energy intensive and producing dry powders which can pose health risks if inhaled.

1.4.2.2 Vapour-Phase Methods

Vapour-phase approaches, such as spray pyrolysis, involve a salt solution which is mixed with a carrier gas (e.g. nitrogen) and nebulised or atomised to produce droplets, into a furnace at high temperatures – typically >800 °C. The high temperature leads to solvent evaporation and chemical reaction. This method has reportedly been used to synthesise GaN (Ogi *et al.*, 2009) and TiO₂

(Figgemeier *et al.*, 2007) nanoparticles, amongst other materials. Although this method is continuous and produces particles with a narrow size distribution, its energy intensive nature is a drawback. In addition, like solid state reactions, products are typically nanopowders, which must be handled with care.

1.4.2.3 Liquid-Phase Methods

This classification of synthesis technique for the manufacture of nanomaterials is perhaps the most relevant and important because the method used in this PhD (and which will be described in subsequent Sections) falls under this category. As a result, liquid phase processes will be described in a little more detail than for previous techniques.

Co-Precipitation

Co-precipitation techniques are widely utilised due to the facile nature of the process. Typically, aqueous metal salts are mixed, at ambient or raised temperatures, with a base which acts as a precipitating agent. Co-precipitation is a widely used technique for the synthesis of ferrite nanomaterials (Rahman *et al.*, 2013, Amiri and Shokrollahi, 2013) and in some cases, the process is performed in an inert atmosphere (Lu *et al.*, 2007). While the method benefits from its simplicity, it has been seen that particle size, morphology and composition of the product is heavily reliant on the type of precursor used, pH, and the reaction temperature. Furthermore, particles produced by co-precipitation have been hindered by a wide particle size distribution. Usually, a short nucleation phase followed by a slow growth period leads to a narrow size distribution – which is not the case with this method (Lu *et al.*, 2007).

Microemulsion

Microemulsions are systems which contain two immiscible liquids - usually water and oil - and a surfactant (Fanun, 2010). The water generally contains dissolved metal salts, and small droplets of the water in oil are stabilised by the surfactant. Likewise, droplets of oil can be stabilised in the water, depending on the ratio of the two. The droplet size can be manipulated by altering different parameters, and can fall within the nanometer range. These tiny droplets then act as 'nanoreactors' inside which particle synthesis can occur. The size of the droplet subsequently dictates, and limits the size of the final particle (López-Quintela *et al.*, 2004). The microemulsion method has been utilised to synthesise BaTiO₃, CaCO₃, CeO₂, ZrO₂, and SnO₂, amongst other materials (Ganguli *et al.*, 2008). The reaction mechanisms to control particle size and size distribution are still not fully understood, limiting the wider use of this method.

Sol-Gel

Sol-Gel methods are a commonly reported route for nanoparticle synthesis, particularly for metal oxides (Bezzi *et al.*, 2003, Senthilkumar and Selvi, 2008, Isasi-Marín *et al.*, 2009). Typically, precursors are converted to a colloidal solution, or 'sol', which gradually develops into a 'gel' network - a matrix of solid nanoparticles dispersed in a liquid phase - over time (or gelling agents may be used to speed the process up). Through centrifugation, filtration or evaporation, the nanoparticles can then be isolated to yield the product. As a low cost, facile method which does not require any specialist equipment, sol-gel remains one of the most popular methods of nanoparticle synthesis.

However there are some disadvantages to these techniques, such as the need for templates, which can be costly and need to be removed after synthesis (Chon Chen *et al.*, 2013, Tang *et al.*, 2013); low purity; or require additional steps to process the material (such as calcination and milling steps) (Dawson, 1988,

Hakuta *et al.*, 1998). Moreover, the high cost of some processes (these can either be high cost of equipment, precursors, or running costs) coupled with low yield and long reaction times can mean that, even if the method produces extremely high quality nanoparticles, there is little to no potential of scaling-up the technology to a commercially-viable level (Tighe *et al.*, 2013).

Conversely, hydrothermal synthesis has been demonstrated to allow greater control over the composition and morphology of products. Furthermore, additional processing steps are minimal, and products are dispersed in water rather than as a nanopowder, making this a preferential method for nanomaterial synthesis.

1.5 Hydrothermal Synthesis of Nanomaterials

Hydrothermal synthesis has been described as the use of aqueous solvents in conditions of high temperature and pressure to dissolve and recrystallise materials which, under standard conditions, are relatively insoluble (Ballman and Laudise, 1963). In addition, 'high temperature' has been defined as a temperature exceeding the boiling point of the solvent being used as the reaction medium, and as a result, elevated pressure must be involved (Demazeau, 2010).

Within the field of hydrothermal synthesis, processes can be further classified depending on the temperature and pressure of the water reaction media. Where the water has a temperature and pressure above its critical point ($T_c=374\text{ }^\circ\text{C}$ and $P_c=22.1\text{ MPa}$), it is termed supercritical. The properties of supercritical water (ScW) are described in Section 1.5.1.

In the last three decades, there has been an increasing interest in using hydrothermal processes to synthesise nanomaterials (Ioku *et al.*, 1988, Somiya and Roy, 2000, Adschiri *et al.*, 1992, Adschiri *et al.*, 2000). Because the main reaction media is water, rather than noxious solvents, the technology attracts a lot of interest as a sustainable or "green" technology. Furthermore, the diverse research devoted to hydrothermal synthesis has shown a wide range of nanomaterials can be produced via this route – including, but not limited to: metals (Aksomaityte *et al.*, 2013), metal oxides (Adschiri *et al.*, 2001, Cabanas *et al.*, 2000, Cabañas *et al.*, 2007, Leybros *et al.*, 2012, Lester *et al.*, 2012), metal organic frameworks (Gimeno-Fabra *et al.*, 2012), hydroxides (Wang *et al.*, 2013), carbonates (Nassar, 2013, Ni *et al.*, 2011), phosphates (Chaudhry *et al.*, 2006, Lester *et al.*, 2013), and sulfides (Liu *et al.*, 2001). This demonstrates the

versatility of hydrothermal synthesis, and that it is relevant to a wide range of applications.

1.5.1 Supercritical Water (ScW) and Sub-critical Water

Under ambient conditions, water is polar - making it a good solvent for dissolving ionic salts, but not for non-polar compounds. Yet, when water is heated in a pressurised environment towards its critical point ($T_c=374\text{ }^\circ\text{C}$ and $P_c=22.1\text{ MPa}$), the hydrogen bonds between water molecules break down. This leads to a decrease in dielectric constant and an increase in dissociation constant, K_w , meaning the breakdown of water molecules to H^+ and OH^- ions (Lester *et al.*, 2006). At and above the critical point, water becomes a supercritical fluid and exhibits unique behaviour. It has greatly reduced surface tension and acts as a solvent but diffuses as a gas (Wandeler and Baiker, 2000). Figure 1.3 summarises the changes in density, dielectric constant and ionic product of water with changes to temperature, at a constant pressure of 24 MPa.

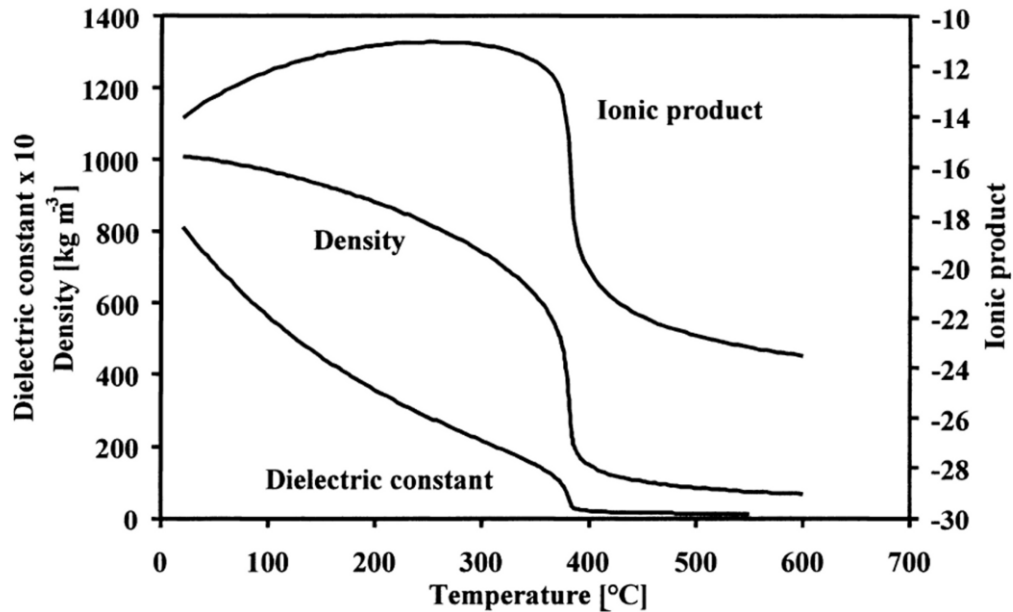


Figure 1.3. A graph illustrating changes to ionic product, density and dielectric constant of water with increasing temperature, at a constant pressure of 24 MPa (Kritzer *et al.*, 1999).

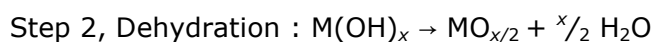
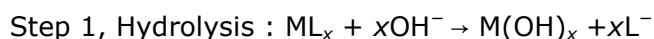
Unlike water at ambient conditions, ScW is weakly-polar; it can dissolve non-polar molecules while having low solubility for inorganic ionic salts. Consequently, the latter precipitates out of ScW; this principle forms the basis for the synthesis of fine inorganic particles in ScW. Due to this principle, and the interesting properties of ScW, it has been increasingly used in recent years as a reaction medium for the production of nanoscale metals and metal oxides. The reaction mechanism for particle formation in ScW is given in Section 1.5.1.1.

Still, it is important to note that not all hydrothermal processes require or use water above its critical point; many described methods use temperatures as low as 150 °C and pressures below 24 MPa (Wang *et al.*, 2013). Thus, pressurised water at temperatures between 100 °C and 374 °C is termed sub-critical or near-critical.

It has been shown that for some materials, particle size, particle morphology, and product yield are affected by the reaction temperature. In the case of ZrO_2 , particle size and the precursor conversion rate increase with elevated reaction temperatures (Hobbs *et al.*, 2009). For hydroxyapatite, $\text{Ca}_{10}(\text{PO}_4)_6(\text{OH})_2$, different particle shapes are produced with varying reaction temperature (Lester *et al.*, 2013). Therefore, depending on the requirements of the particle properties, or in the interest of balancing yield with energy consumption, lower reaction temperatures may be utilised.

1.5.1.1 Reaction Mechanisms and Metal Oxide Formation in ScW

As described by Adschiri *et al.* (Adschiri *et al.*, 1992) and subsequently Lester *et al.* (Lester *et al.*, 2006), the proposed formation of metal oxides begins with a metal salt in ScW readily undergoing hydrolysis without addition of any base, due to the high K_w , and high OH^- concentration in the solvent. The metal hydroxide consequently experiences a dehydration step which results in the formation of metal oxide nanoparticles as described by the following, where ML is a metal salt:



1.5.1.2 Other Applications of Supercritical Water

The properties of ScW described in Section 1.4.1 make it a solvent of interest for applications other than for the synthesis of nanoparticles.

One of the major applications of ScW is the oxidation and breakdown of hydrocarbons (for example, to treat waste water). Due to the non-polar nature of ScW, it becomes completely miscible with organic compounds meaning it can transport molecules more effectively. Compared to other methods of hydrocarbon breakdown – such as incineration – ScW oxidation is less energy intensive and is proving to be a sustainable “green” technology (Al-Duri *et al.*, 2008).

ScW has also reportedly been used to chemically recycle carbon fibre by dissolving epoxy resins which were bound to the fibres (Piñero-Hernanz *et al.*, 2008). This method of chemical recycling showed the recovered fibres to have up to 98% of the tensile strength, compared to virgin fibres. Again this shows that ScW is fast becoming a media for many sustainable applications.

1.6 Solvothermal Synthesis of Nanomaterials

Where organic solvents, such as alcohols, are used in the place of aqueous solvents, the synthesis is termed solvothermal instead (Xu and Wang, 2012). In the same way as water, the solvent is termed supercritical when it is at its critical point. This point varies for different solvents; the critical temperatures and pressures for methanol, ethanol, and acetone are given in Table 1.1.

Table 1.1. The critical temperatures and pressures of three solvents. (Fang, 2010).

| Solvent | Critical Temperature (T_c , °C) | Critical Pressure (P_c , MPa) |
|----------|------------------------------------|----------------------------------|
| Methanol | 239 | 8.1 |
| Ethanol | 241 | 6.1 |
| Acetone | 235 | 4.7 |

As with hydrothermal methods, the solvent can also be used as a reaction media below its critical point, while increases in reaction temperature beyond T_c may lead to increased yield. Although not as sustainable or cost-effective as using water, the use of organic solvents the synthesis of materials which are not favoured in water – in particular, metal nanoparticles without the need for toxic reducing agents (Choi *et al.*, 2010, Shin *et al.*, 2010), or provides better compatibility for phase transfer or formulation into other media (Veriansyah *et al.*, 2009).

1.7 Batch and Continuous-flow systems

Chemical processes can generally be categorised as being conducted using either batch or continuous flow systems – this is not exclusive to hydrothermal synthesis of nanomaterials, or indeed to the synthesis of nanomaterials overall. Like many researchers in their respective chemical fields, the nanotechnology community is divided over which type of system is superior for the production of nanomaterials.

For hydrothermal synthesis of nanoparticles, batch systems typically employ an autoclave-type reactor into which the reactants are placed; this is then heated by an oven, or a sand or oil bath. Conversely, continuous systems use pumps to drive reactants through a heated, pressurised pipework reactor system. While batch systems are arguably simpler and easier to design, operate and maintain, continuous systems are known for high reaction rates within a very short residence time (< 1 minute) (Fang, 2010). While short reaction times carry several benefits, there are some reactions which appear to require long reaction times and, to date, have only been produced by batch methods (Kasuga *et al.*, 1998, Sekino *et al.*, 2006, Bavykin *et al.*, 2004). In addition, batch reactors allow the use of reagents which are water or solvent insoluble, but continuous reactors require salts to be dissolved to prevent blockages at the pumps or other points of the system. Nevertheless, batch systems are more difficult to reproduce at larger scale compared to continuous-flow systems. Thus, if batch synthesis reactions can be tailored for a continuous-flow system, the products could be manufactured at a volume more meaningful for commercial use. Continuous-flow hydrothermal systems which are currently used at a commercial scale are described in Section 1.8.

In general, during the synthesis of nanomaterials, particle size, size distribution, morphology and crystallinity of the product can be controlled by altering individual process parameters; these being temperature, pressure, concentration and pH of precursors, and flow rates (Lester *et al.*, 2012, Adschiri *et al.*, 2000, Sue *et al.*, 2006). Continuous systems allow more control over these experimental parameters, and carry more potential to be scaled up (Tighe *et al.*, 2013, Fang, 2010). With these benefits over batch processes, continuous-flow systems which have been described in literature for the synthesis of nanomaterials will be discussed in more detail in Section 1.7.1.

1.7.1 Continuous-flow Hydrothermal Reactors

Many researchers see the benefits of continuous flow reactors, which were discussed in Section 1.7. It is generally understood that the method of mixing reactant streams in continuous flow systems plays a vital role in determining the size and size distribution of the synthesised particles. As such, several groups have built and experimented with different mixer/reactor designs for the hydrothermal synthesis of nanomaterials. Each research group has produced different materials, and for varying applications. A brief history of how research into continuous hydrothermal synthesis began, and a selection of the most prominent work will be discussed in the subsequent Sections. The reactor design used for the work described here will then be discussed in Section 1.7.2.

1.7.1.1 Adschiri *et al.* (Tohoku University)

The process of hydrothermal fine particle synthesis was first transferred from batch to continuous-flow reactors by Professor Tadafumi Adschiri and his research group at Tohoku University in Sendai, Japan (Adschiri *et al.*, 1992). This pioneering work described the use of ten different water-soluble metal salts

for the synthesis of seven different metal oxides, with residence times below 2 minutes. Later publications also focussed on the use of their continuous flow reactor for the production of CeO_2 (Hakuta *et al.*, 1998), ZrO_2 and TiO_2 (Adschiri *et al.*, 2000), and AlOOH (Adschiri *et al.*, 2001). The equipment set up used for synthesis is given in Figure 1.4, where the mixing point was a T-piece fitting. As well as being a readily available, off-the-shelf part, this configuration allowed the rapid heating of precursor streams, especially compared to batch processed. The published works typically used metal salts of concentrations up to 0.1 M, total flow rates up to 10 ml/min and thus produced dry weight equivalents of metal oxide nanoparticles up to 10 g/h (Adschiri *et al.*, 2000). Since these publications, other researchers have discussed the drawbacks of using T-piece mixers – these will be elaborated upon in Section 1.7.2.

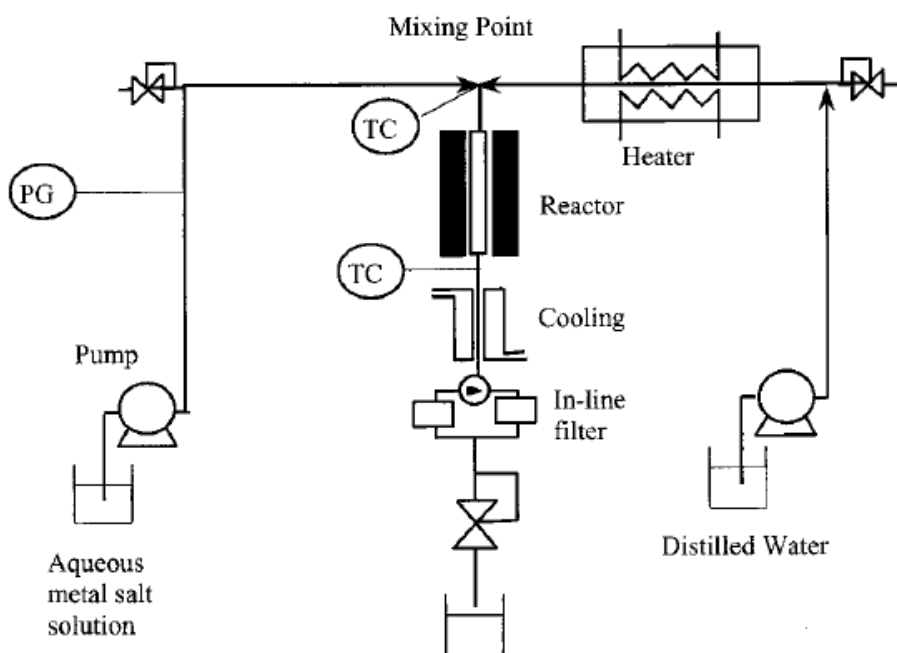


Figure 1.4. Schematic diagram of the apparatus typically used by Adschiri *et al.* for continuous hydrothermal synthesis of nanoparticles (Adschiri *et al.*, 2000).

Adschiri *et al.* recently published some very interesting research, where they used neutron radiography to visualise the flows of water inside their mixing point (Takami *et al.*, 2012). The mixing patterns inside continuous flow reactors have long plagued researchers in the field; due to the high temperatures and pressures required for synthesis, reactors are typically constructed from stainless steel tubing and fittings thus the internal flows cannot be seen. As such, researchers have had to rely on computational fluid dynamics (CFD) and other forms of modelling to visualise flow arrangements. However, the use of a neutron beam is a breakthrough in the field and Adschiri *et al.* have shown that it is possible to use this form of radiography to observe flow arrangements within the reactor, as seen by the image shown in Figure 1.5.

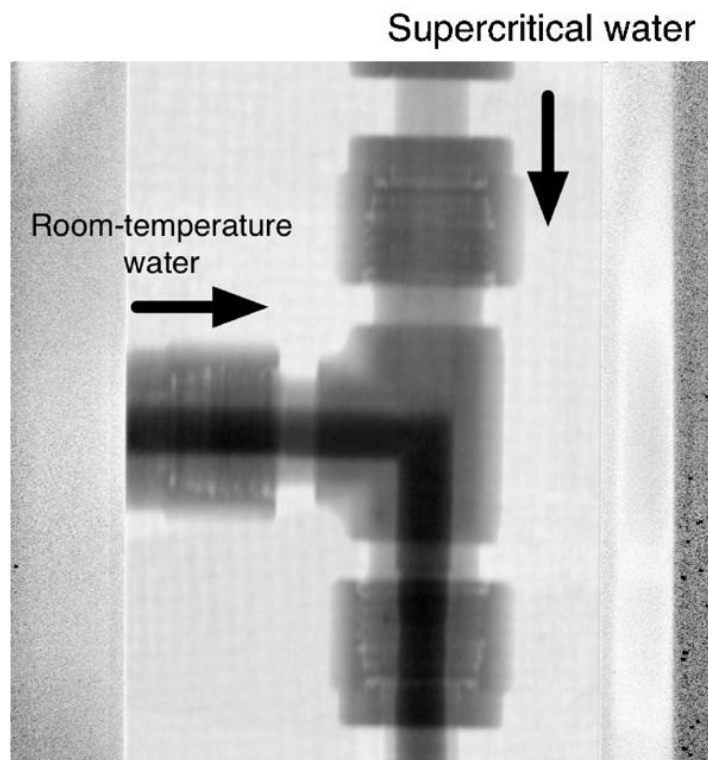


Figure 1.5. Image showing the internal structure and water flow in the T-piece reactor used by Adschiri *et al.*, collected using neutron radiography (Takami *et al.*, 2012).

Still, despite the development of this continuous flow reactor, the research group of Prof. Adschiri has recently published work using batch type reactors to synthesise nanoparticles of HfO_2 (Sahraneshin *et al.*, 2012a), yttrium aluminium garnet (YAG) (Sahraneshin *et al.*, 2012b), and zirconium dioxide (ZrO_2) (Taguchi *et al.*, 2012). Unlike many reported batch methods of hydrothermal synthesis, the described protocols required a relatively short reaction time of 10 minutes. Conversely, the disadvantage of this method is the small reactor volume; with only 5 ml of product yielded per reaction, there is little scope for scale up. This small reactor volume appears to be by design but may be a requirement for successful synthesis. In addition, reverting to a batch process despite the availability of a hydrothermal flow system suggests these nanomaterials may not be producible on their flow reactor.

Other work published by Adschiri *et al.* in recent years, described the use of both their 5 ml batch reactor and flow reactor to synthesise cobalt aluminate nanoparticles (Lu *et al.*, 2013). Their results showed that they were able to synthesise their intended material, CoAl_2O_4 , using their flow reactor while their batch system produced $\text{Co}_{1-x}\text{Al}_x$ layered double hydroxide (Co-Al-LDH) as the principle phase. This was due to the discrepancies between heating in the two systems; the reactants in the autoclave reach their reaction temperature after 5 minutes while in the flow reactor, heating takes <1 second. The slower heating in the batch reactor produced the LDH as an intermediate and lead to a growth phase for the remainder of the reaction. The authors speculate that a much longer reaction time (>10 hours) is required to dehydrate the LDH to CoAl_2O_4 . Meanwhile the rapid heating in the flow reactor lead to total dehydration of the precursors, and therefore highlights the further benefits of continuous flow reactors with rapid heating systems.

1.7.1.2 Hakuta *et al.* (AIST)

Yukiya Hakuta, Hiromichi Hayashi and Kunio Arai are researchers in the field of hydrothermal synthesis of nanoparticles, using both batch and continuous-flow reactors to produce materials. They are associated with the National Institute of Advanced Industrial Science and Technology (AIST) in Japan and Tohoku University, and have often collaborated with Prof. Adschiri. As such, they conduct much of their research using flow reactors with a similar T-piece mixer geometry as Prof. Adschiri. A diagram of the reactor system typically used for their work is shown in Figure 1.6. After the T-piece, the flow passes into a heated 'reactor' which allows particle development. After the reactor, the product stream is quenched by mixing with a flow of deionised water at ambient temperature.

Between the three researchers, they have published works using continuous flow hydrothermal synthesis to generate AlOOH (Hakuta *et al.*, 2005), CuO, Fe₂O₃, NiO, ZrO₂ (Sue *et al.*, 2006), BaTiO₃ (Matsui *et al.*, 2008), ferrites (Sato *et al.*, 2008), perovskite oxide (Lu *et al.*, 2008) and Al₂O₃ (Noguchi *et al.*, 2008).

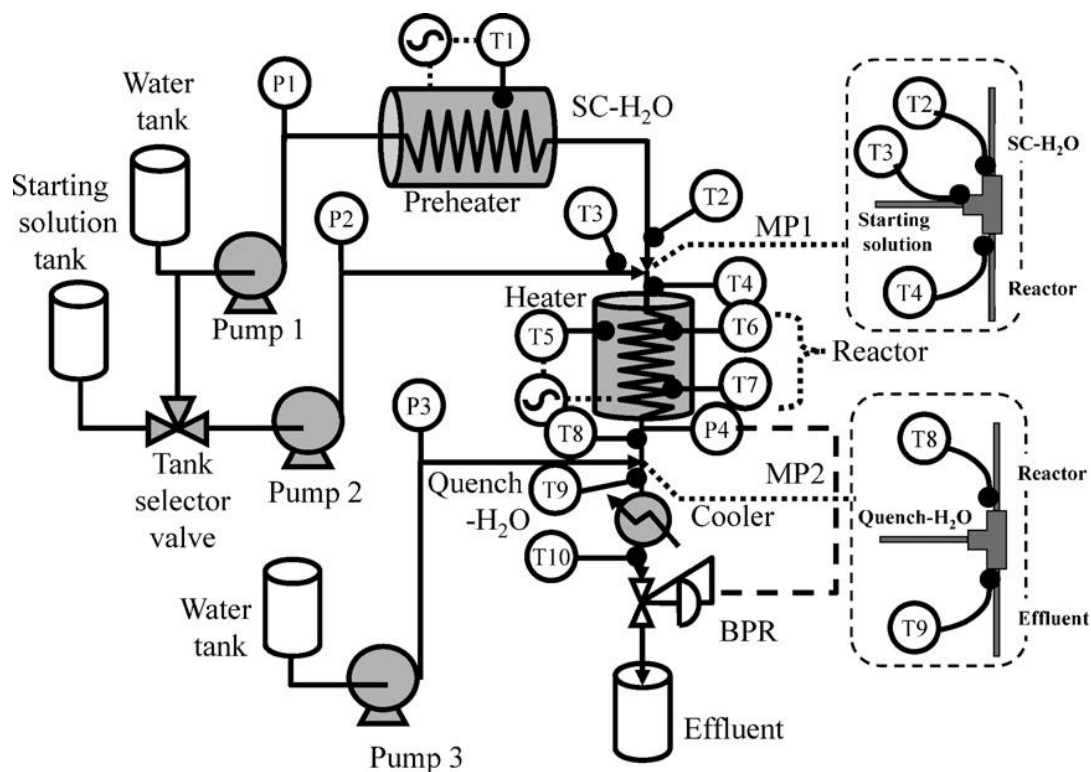


Figure 1.6. Schematic of the reactor system used by Arai et al. (Kawasaki et al., 2010).

Although this work is similar to that previously described by Adschiri, Arai *et al.* have also developed microreactor T-pieces for the synthesis of NiO (Kawasaki *et al.*, 2010). Cross sectional images of the three microreactors used can be seen in Figure 1.7. This study found that quicker heating rates resulted from smaller internal volumes of the T-pieces, which in turn, lead to small particles being produced. The microreactor T-piece has also been employed for the synthesis of Ni nanoparticles (Sue *et al.*, 2009).

While the production of smaller particles may be advantageous, the microreactors used have internal diameters as small as 0.3 mm, which may lead to problems with blockages if the particles begin to aggregate (see Section 1.9 for more details on particle aggregation). With such small reactor volumes being vital to determine particle size, there is also a limitation on the quantity of material that can be manufactured.

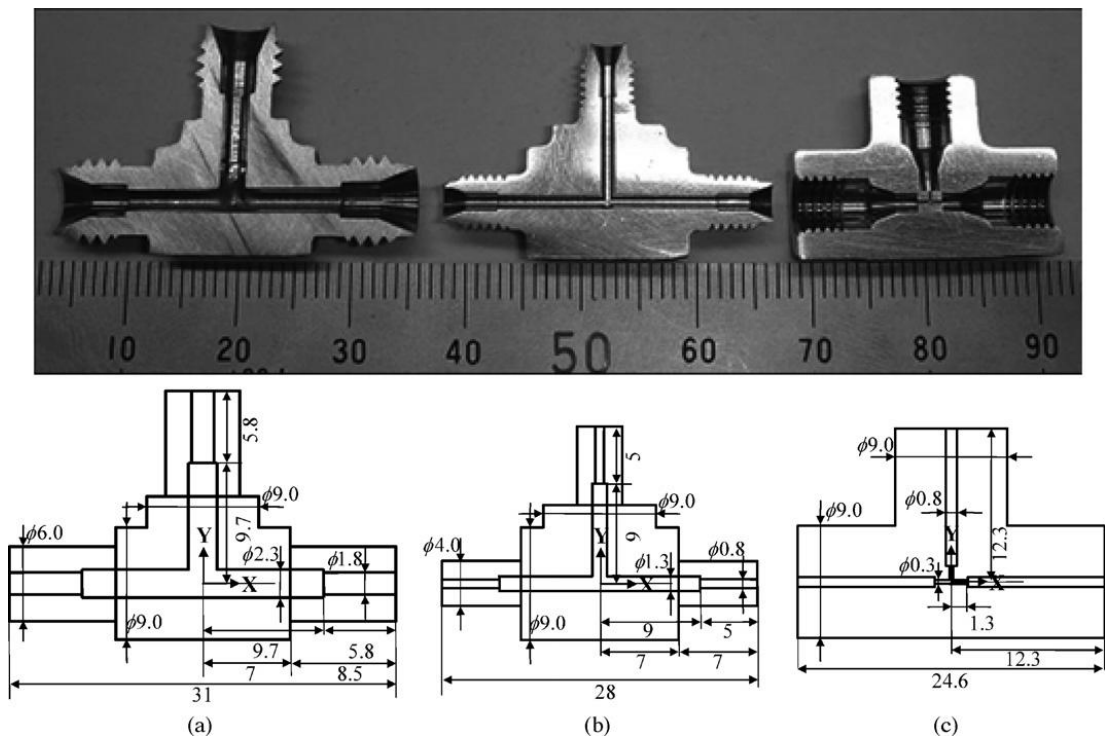


Figure 1.7. Cross sectional photographs and drawings of the T-piece reactors used by Arai *et al.* (Kawasaki *et al.*, 2010).

In 2011, a publication from Hakuta and others (including some from AIST) recognised some problems associated with T-piece mixers – particularly the creation of nanoparticles with a wide size distribution. As a result, a new mixing configuration was described, named the Central Collision Mixer (CCM), and is depicted in Figure 1.8 (b). The metal salt solution is pumped in a downflow and is met by four streams of heated water flowing in horizontally. This reactor configuration was used to synthesis nickel ferrite nanoparticles and the authors found that the CCM yielded smaller particles which had a narrower size distribution compared to using a conventional T-piece mixer (Sue *et al.*, 2011).

This mixer design is a recent development, with only a few publications describing its use, and so the details of its reliability and reproducibility are currently unclear. Still, the CCM geometry appears to show it as a custom made

part which could provide problems if reproducing this reactor, and increase costs.

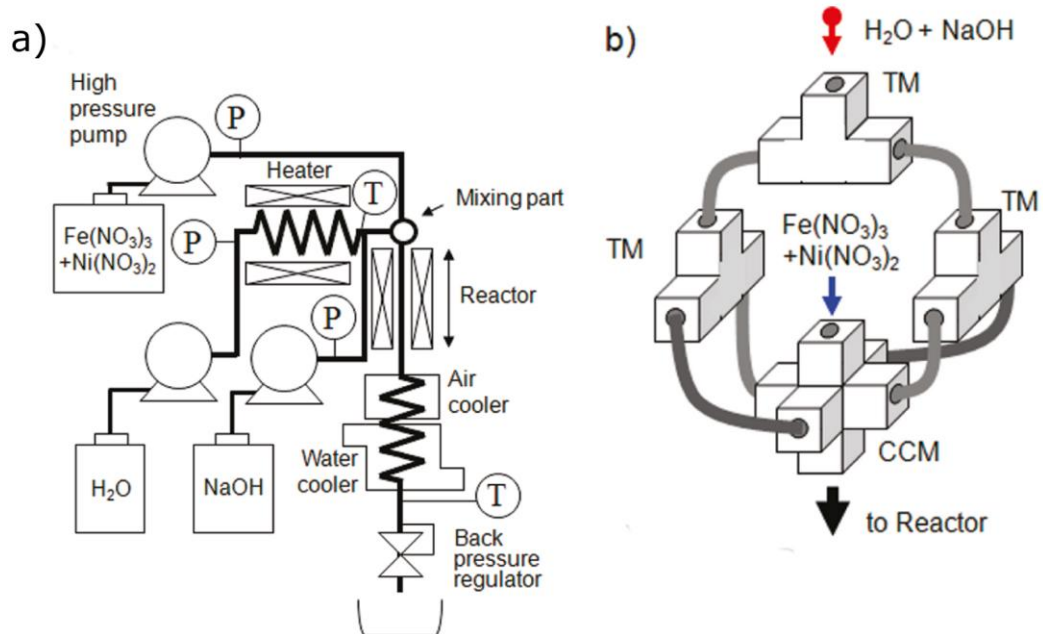


Figure 1.8. (a) Reactor system design used by AIST, incorporating (b) the Central Collision Mixer (CCM) (Sue *et al.*, 2011).

In addition to the reactor designs described previously, Hakuta *et al.* introduced a swirling micro mixer reactor in 2007, which created a vortex to mix the metal salt flow with the superheated water flow (Wakashima *et al.*, 2007). However, future publications by the authors revert to the use of T-piece mixers and discussions using this swirling mixer are limited.

1.7.1.3 Darr *et al.* (University College London)

Prof. Jawwad Darr and his research group are based at University College London (UCL) and have been conducting work in the field of continuous hydrothermal synthesis since 2007. Until recently, Darr *et al.* have been using the counter current reactor design (Lester *et al.*, 2006) which was used for the course of the work described in this Thesis, and which will also be discussed in Section 1.7.2. Schematic diagrams of the reactor configuration are given in Figure 1.9. Darr *et al.* also draw reference to the original research article in several of their papers (Boldrin *et al.*, 2007, Tighe *et al.*, 2012).

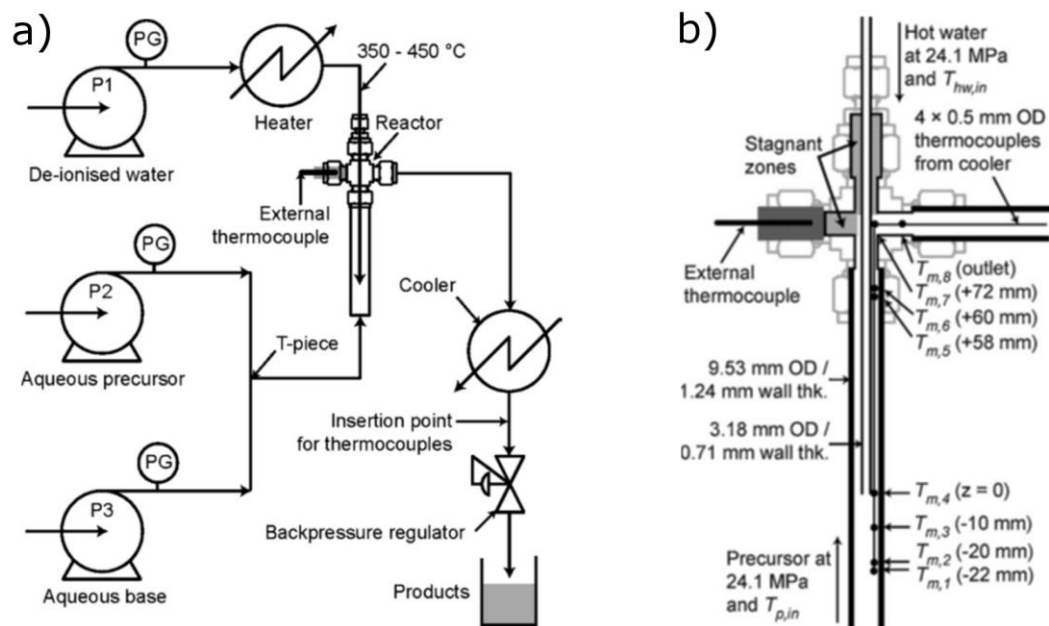


Figure 1.9. (a) Diagram of the equipment used by Darr *et al.* (b) A diagram of the counter-current reactor geometry (Tighe *et al.*, 2012).

Darr *et al.* have published a series of papers describing the use of this counter current reactor in the continuous flow hydrothermal synthesis (CFHS) of an array of nanomaterials. These include hydroxyapatite (Chaudhry *et al.*, 2006), spinel

structures (Boldrin *et al.*, 2007), titanium dioxide (Zhang *et al.*, 2009b), sodium titanate (Zhang *et al.*, 2010), indium oxide (Elouali *et al.*, 2012) and nanophosphors (Gruar *et al.*, 2012).

Additionally, Darr *et al.* have also developed a high throughput system for producing Zn-Ce oxides based on the counter current reactor, named the High-throughput Continuous Hydrothermal (HitCH) synthesis. Using the HitCH system at lab scale (total flow rates up to 40 ml/min), the research group showed that they were able to produce a large array of samples in a short time frame, which they were able to rapidly obtain X-ray diffraction patterns for, using the beamline at Diamond Light Source (Weng *et al.*, 2009, Parker *et al.*, 2011). Furthermore, the group have converted the process to be automated; using a robot, the system produced, cleaned and printed lab scale samples of nanoparticles. Named RAMSI (Rapid Automated Materials Synthesis Instrument), the equipment was used to produce europium-doped yttrium oxide, $Y_2O_3:Eu^{3+}$ phosphors. In some cases, the authors found that the produced nanoparticles had to be heat treated in air at up to 1200 °C for them to display fluorescent properties (Lin *et al.*, 2010). As well as being time consuming, and energy intensive, heat treatment at such high temperatures is known to cause densification, grain growth (Ostwald ripening) and in turn, eliminate the nanoscale aspect to the particles (German, 2010). Currently, only this material has been reportedly synthesised using RAMSI.

In 2012, Darr *et al.* published a paper detailing observations (from in situ temperature measurements) of jetting effects in the counter current reactor; this is where the superheated flow of water infiltrates the flow of metal salt and may lead to non-homogenous mixing and in turn, a wide particle size distribution. This jetting effect was only noted for certain flow ratios and may be affected by the types of pumps used in the system. More recently Darr *et al.* developed a

new reactor configuration, which they named the Confined Jet Reactor (CJR) – shown in Figure 1.10 (Tighe *et al.*, 2012).

Contrary to the previous counter current reactor used by the group, the CJR uses a co-current mixing regime. Here, the heated water stream is pumped through an inner tube, as an upflow, into the bottom of the reactor. The precursors (at ambient temperature) are pumped into the sides of the reactor cross piece, entering below the outlet of the water stream. The formed nanoparticles then flow upwards to the heat exchanger. Whilst Darr *et al.* explained that particle accumulation and blockages in pipes “often occurs due to substantial preheating of the incoming metal salt precursor stream prior to being brought into contact with the much hotter water stream” (Gruar *et al.*, 2013) the CJR does exactly this, i.e. the cool precursor feeds come in to contact with the hot inner pipe carrying the water stream, before they actually meet and mix with the heated water. This suggests that precipitation and particle accumulation, to some degree, could occur on the surface of the heated inner tube.

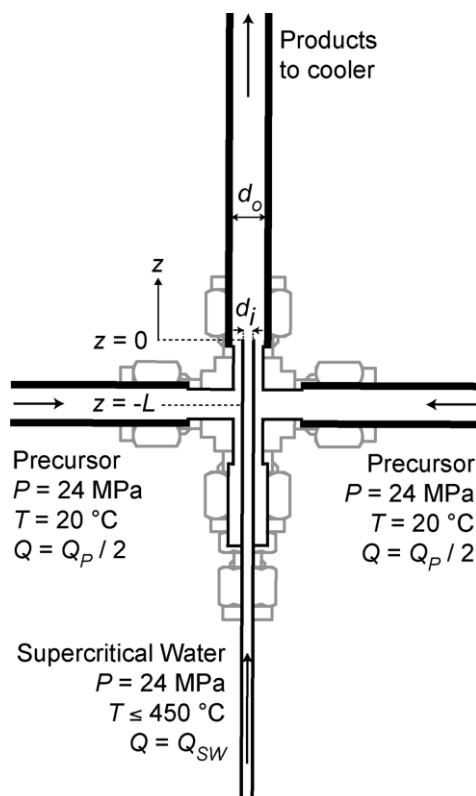


Figure 1.10. Diagram showing the geometry of the Confined Jet Reactor (CJR) used by Darr *et al* (Gruar *et al.*, 2013).

The CJR has apparently been scaled up from lab (total flow rates up to 40 ml/min to produce 1-10 g/h) to pilot scale (total flow rates up to 800 ml/min >1 kg/h) by Darr *et al.* to produce cerium and zinc oxides (Gruar *et al.*, 2013, Tighe *et al.*, 2013). The researchers showed high reproducibility of particles at the two different scales.

1.7.1.4 Kim and Lee *et al.* (KIST and SNU)

Between the Korea Institute of Science and Technology (KIST) and Seoul National University (SNU), Jaehoon Kim and Youn-Woo Lee have published a selection of papers describing continuous hydrothermal and solvothermal methods to produce a wide range of nanomaterials.

In the published collaborative works of Kim and Lee, they recognise that clogging or blocking in reactors is a common problem associated with continuous hydrothermal synthesis of nanoparticles. However, rather than addressing the issue by changing their reactor or mixer geometry, they opted for a change in reaction media from water to methanol instead (Kim *et al.*, 2008, Veriansyah *et al.*, 2010b). They found that using methanol led to a greater availability of soluble surface modifiers which could be used to bind to particles, while methanol itself acted as a surface modifier as well. However, the biggest drawbacks of using methanol instead of water are the implication of increased running costs and health and safety risks.

The continuous flow reactor used in these works is shown in Figure 1.11. Like the reactor setups used by the Japanese research groups described in Sections 1.7.1.1 and 1.7.1.2, their reactor system consists of a T-piece mixing point where the heated water or methanol stream flows from the top of the T-piece as a downflow, and meets the cooler metal salt stream which flows in from the side arm of the T-piece. The mixed feeds then flow down into a heated cylinder with a volume of 14.58 cm³, which is the reactor. This vessel extends the residence time of the reaction, which can aid particle growth or increase reaction conversion.

This reactor has been used by KIST and SNU to synthesise CeO₂ (Kim *et al.*, 2008), ZnO (Veriansyah *et al.*, 2010b) and Fe₃O₄ (Veriansyah *et al.*, 2010a) in supercritical methanol. For the study of ZnO synthesis, the products from the solvothermal process were compared to those from hydrothermal; the researchers found that using methanol as a solvent affected the surface groups of particles, as well as size, morphology and dispersability into ethylene glycol.

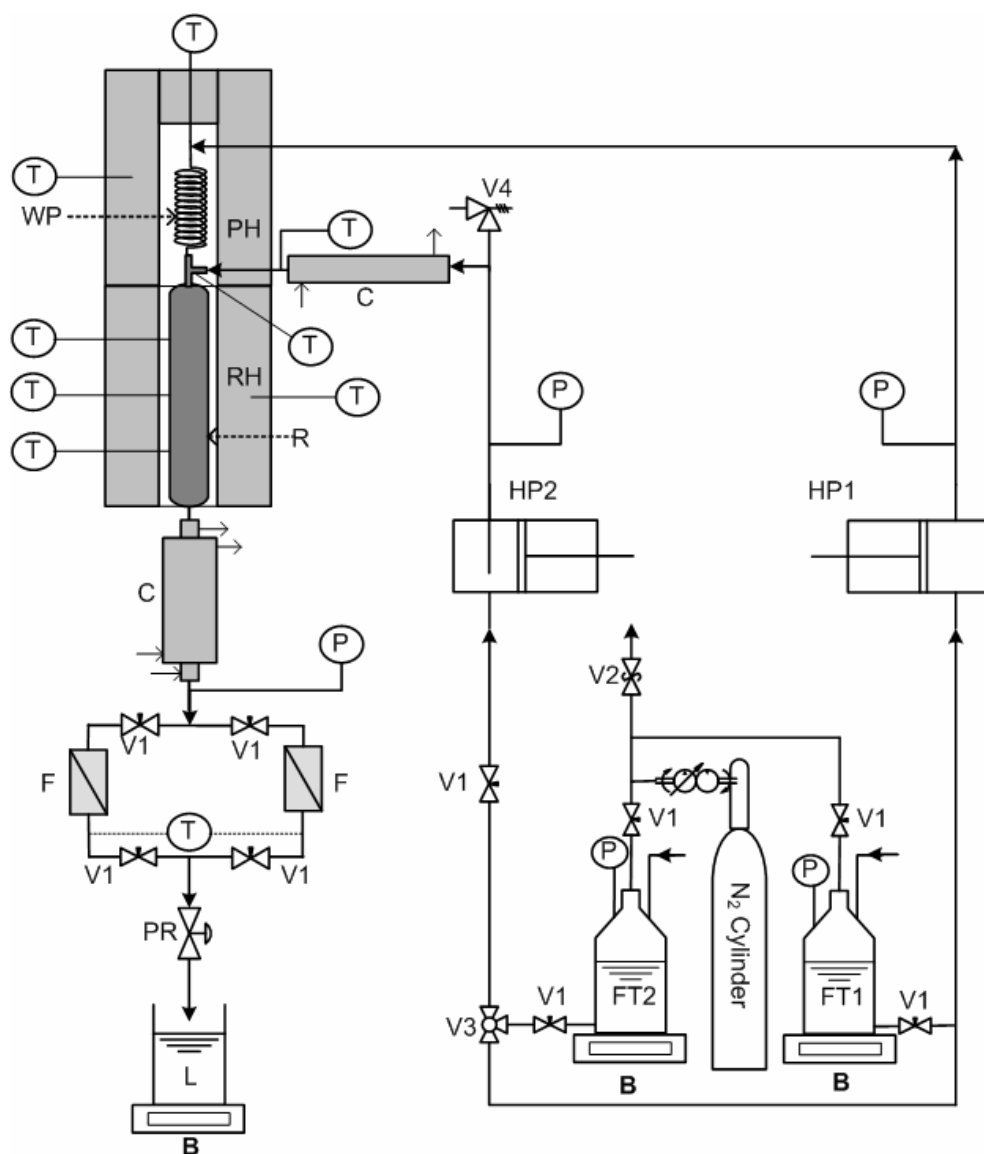


Figure 1.11. A schematic diagram of the continuous flow reactor system used by Kim *et al.* for the synthesis of metal oxide nanoparticles in supercritical water or methanol. B: balance; C: condenser; F: 0.2 μm metal filter; L: liquid container; P: pressure gauge; R: supercritical reactor; T: thermocouple; V1: needle valve; V2: relief valve; V3: three-way valve; V4: safety valve; FT1: DI water/methanol feed tank; FT2: precursor solution feed tank; HP1: high pressure pump for DI water/methanol; HP2: high pressure pump for precursor solution; PH: preheater; PR: back pressure regulator; RH: reactor heater; WP: water preheater line (Kim *et al.*, 2008).

Kim *et al.* have recently published work which investigated the mixing patterns inside T-piece reactors with three different geometries, and how these affected the properties of synthesised LiFePO_4 particles for use in battery materials (Hong *et al.*, 2013); the three different T-piece geometries are shown from the CFD images in Figure 1.12. While the 90° Tee is an off-the-shelf part from Swagelok, The 50° and Swirling Tees are both custom made by the research group. The study also examined the effect of different temperatures, flow rates and concentrations on the structure and properties of the product.

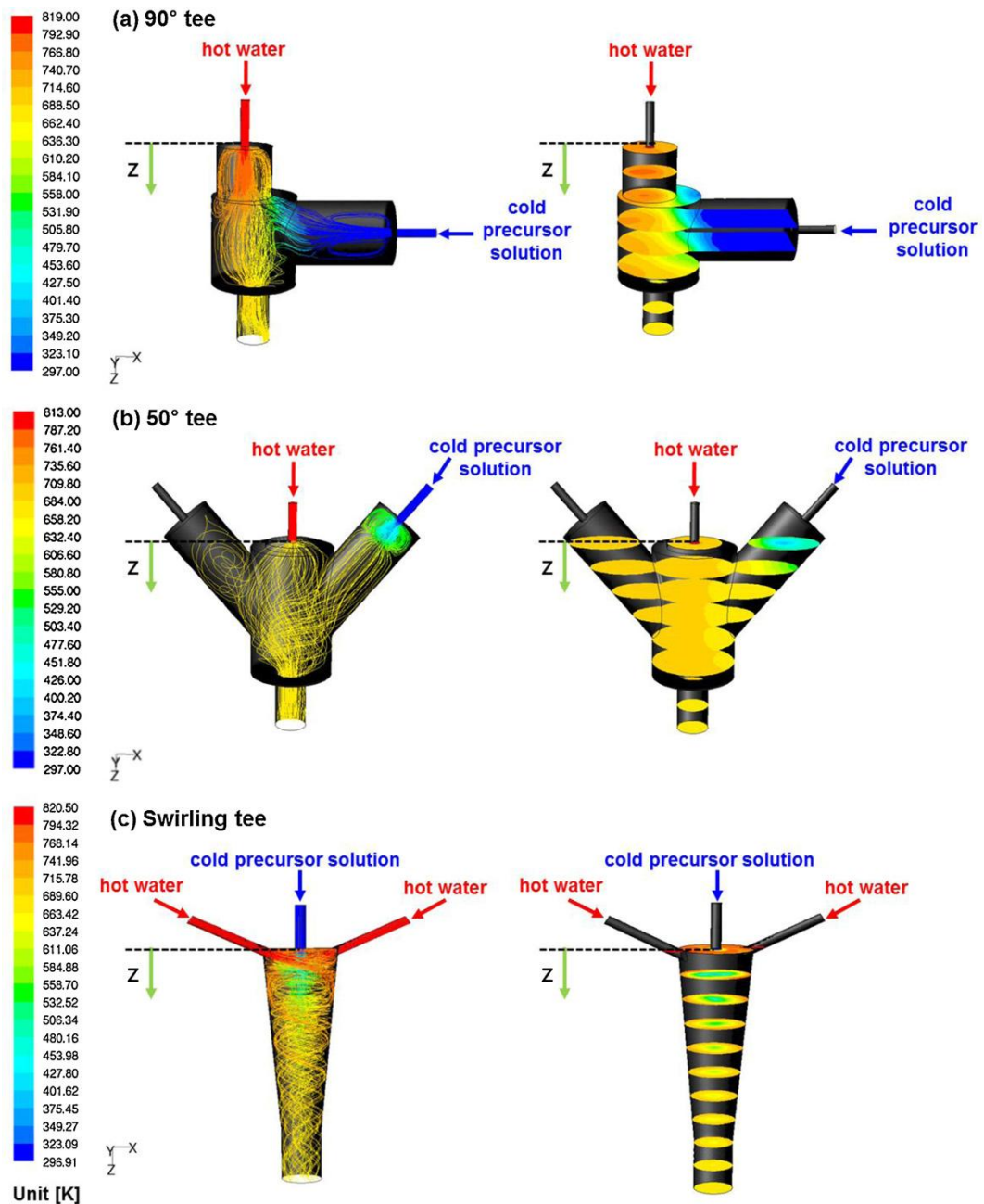


Figure 1.12. CFD simulations of the three tee reactors investigated at the Korea Institute of Science and Technology for the synthesis of LiFePO_4 nanoparticles (Hong *et al.*, 2013).

Data from X-ray diffraction (XRD) obtained during the study found that the Swirling Tee mixer produced LiFePO_4 particles with a higher degree of crystallinity than the other two mixers, as well decreasing the ratio of Fe_3O_4

impurity detected. The authors put this down to a more efficient mixing regime in the Swirling Tee, which in turn provides more rapid nucleation of LiFePO_4 particles while inhibiting the formation of impurities. This effect was accentuated with higher flow rates, hence likely to cause more turbulent mixing.

Images collected using Scanning Electron Microscopy (SEM) found that, at various flow rates tested, the Swirling Tee produced much smaller particles (100-400 nm diameter spheres) compared to the 90° Tee (platelets with lengths of 200-600 nm) and the 50° Tee (platelets with lengths between 300-700 nm). Moreover, using higher flow rates for each mixer type saw a decrease in particle size – again, likely due to more rapid fluid mixing and faster heat transfer between fluids.

As a result of the smaller particle size, higher crystallinity, and lower degree of impurities, the LiFePO_4 particles synthesised using the Swirling Tee showed much more promise as a battery material than those made using the other Tee geometries. As such, this reactor design could be promising for production of other nanomaterials. On the contrary, a disadvantage of the Swirling Tee is the custom-made design, which will inherently be more expensive than off-the-shelf parts. Furthermore, the products described in this paper exhibit wide particle size distributions, which may be due to a large range of residence times in the reactor, rather than rapid heating of the precursor stream followed by quick cooling. One possible reason for this could be that the product stream is hotter, and therefore less dense, than the cold precursor stream entering the top of the Swirling Tee. Therefore, the less dense product stream will naturally rise to the top of the mixer, rather than being drawn to the reactor outlet at the bottom. In between pulses of incoming precursor (pulsing caused by the pumps), a degree of flow (and particle) recirculation will occur - leading to more growth of these particles compared to those which are quickly pushed out of the reactor due to

the positive pulse from the precursor being pumped in. Of course, this theory depends on the ratio of buoyancy and inertia forces acting on the product stream, but provides speculative reasoning for particle size distribution.

1.7.1.5 Aymes *et al.* (University of Burgundy)

Based in Dijon, France, research into continuous hydrothermal synthesis of nanoparticles by the research group of Daniel Aymes began when a reactor was built in 2001, as shown in Figure 1.13 (Aimable *et al.*, 2009b). This reactor setup used an “X geometry” to mix the superheated water flow with two precursor solutions. To create this geometry, the flows were created by drilling into a solid block of Inconel 625, shown in Figure 1.14. After the mixing point, the fluids then flowed into a 2 metre long Inconel reactor tube in a “zigzag” configuration. The paper states that this geometry maintains a constant temperature throughout the reactor length, while minimising particle agglomeration. Using this reactor design, Aymes *et al.* were able to synthesise BaZrO₃ (Aimable *et al.*, 2008); LiFePO₄ (Aimable *et al.*, 2009a); ZrO₂; anatase TiO₂ and a range of spinel ferrites (Aimable *et al.*, 2009b).

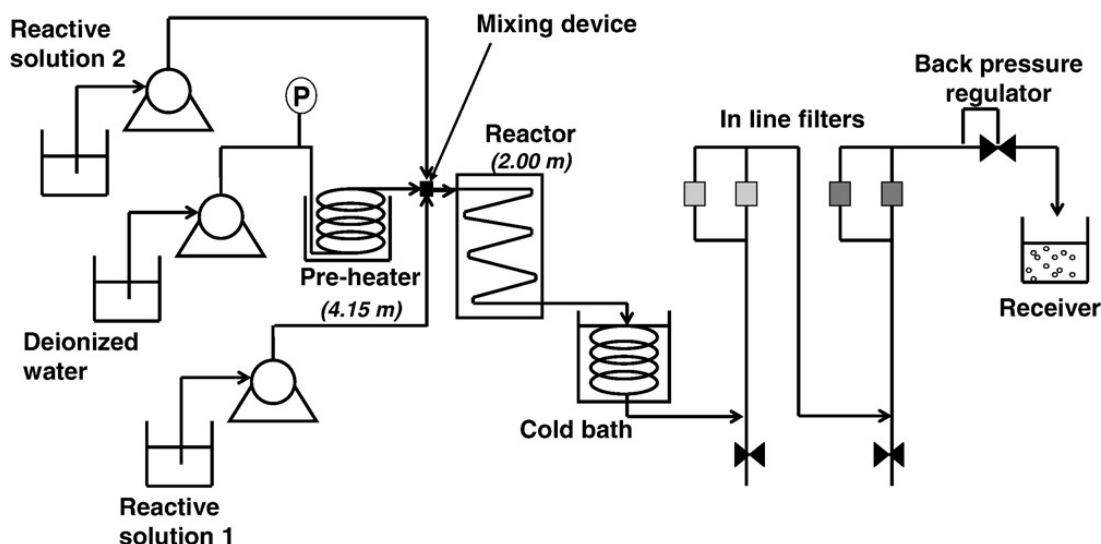


Figure 1.13. A schematic diagram of continuous hydrothermal reactor system built by Aymes *et al.* in 2001 (Aimable *et al.*, 2009b).

Inconel 625 is a strong alloy, allowing high temperatures and pressures to be used and, unlike stainless steel 316, is not corroded through exposure to halides. This advantage of Inconel also means it is significantly more expensive than stainless steel, and drives setup costs up; this means the overall cost of nanoparticle production is greater than using stainless steel equipment. While using Inconel parts provides more corrosion resistance if using halide precursors (which are generally cheap, and so the cost of Inconel can be justified), the published works of Aymes *et al.* describe the use of non-halide based precursors, therefore negating the need for this expensive alloy. Furthermore, the Inconel block used by Aymes *et al.* is a specialised design, as opposed to using off-the-shelf parts, which can require additional pressure safety steps (prior to commissioning) and drive costs up further.

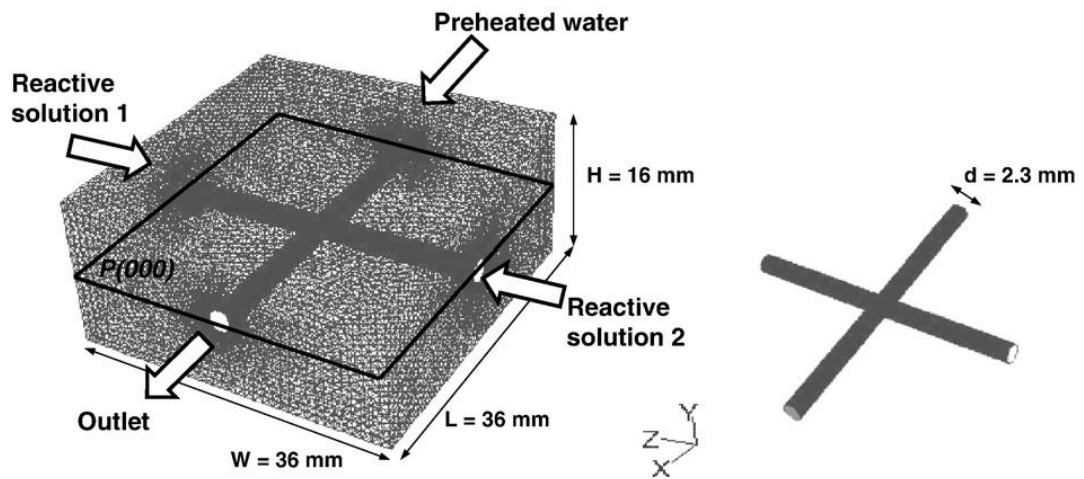


Figure 1.14. Diagram showing the X configuration of the mixing point, drilled into a block of Inconel 625, used in the systems by Aymes *et al.*

After conducting heat transfer studies, the research group found that they could reach the necessary temperatures for supercritical water by using shorter lengths of pre-heater and reactor tubing, thereby reducing residence times as well. A diagram of their revised reactor system is given in Figure 1.15. However, the Inconel block used as the mixing device (Figure 1.14) remained the same.

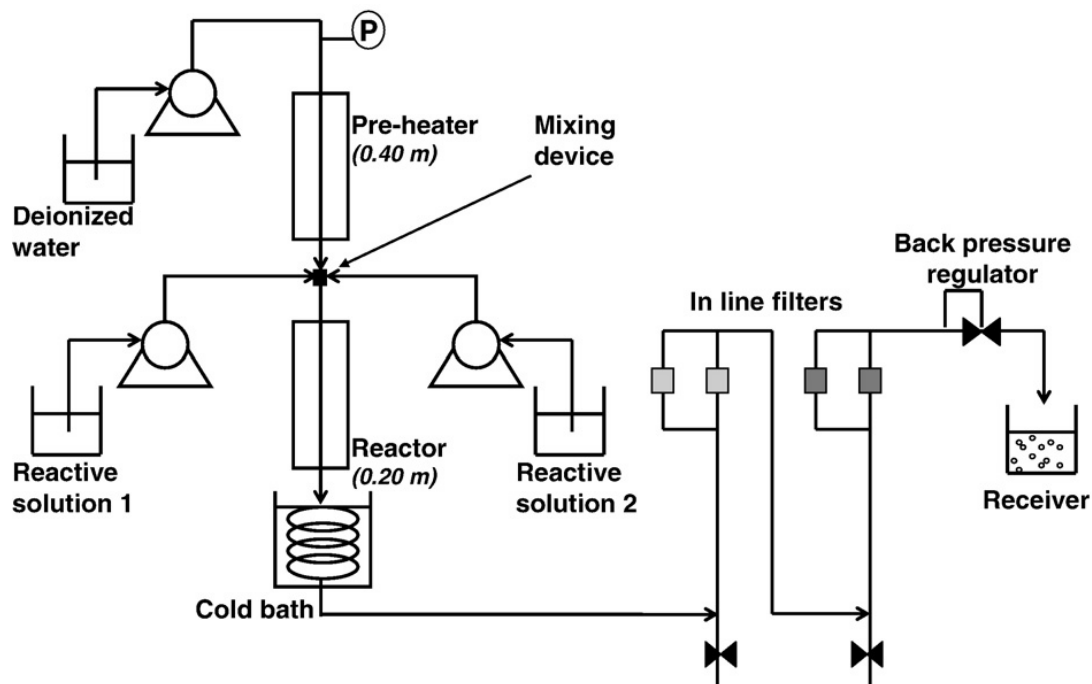


Figure 1.15. Revised system design by Aymes *et al.*, built in 2006.

Despite the published papers describing the reactor designs shown in Figure 1.13, Figure 1.14 and Figure 1.15, a paper was later published by Demoisson *et al.* (contemporaries of Aymes at the same institution) describing a very different reactor design, which they patented with Aymes (Aymes *et al.*, 2011, Demoisson *et al.*, 2011); this suggests that the previous X reactor geometry had operation issues which were not discussed in the patent. Interestingly, the authors draw reference to the benefits of the Nottingham counter-current reactor design which will be discussed in Section 1.7.2.

Their new reactor design, shown in Figure 1.16, was patented in 2011 and like their earlier designs, uses a block of Inconel 625 into which holes are drilled and bored. Therefore the reactor has the inherent advantages and drawbacks described previously for their earlier designs. However, the main difference from their previous "X" reactor geometry is the adoption of a counter-current system.

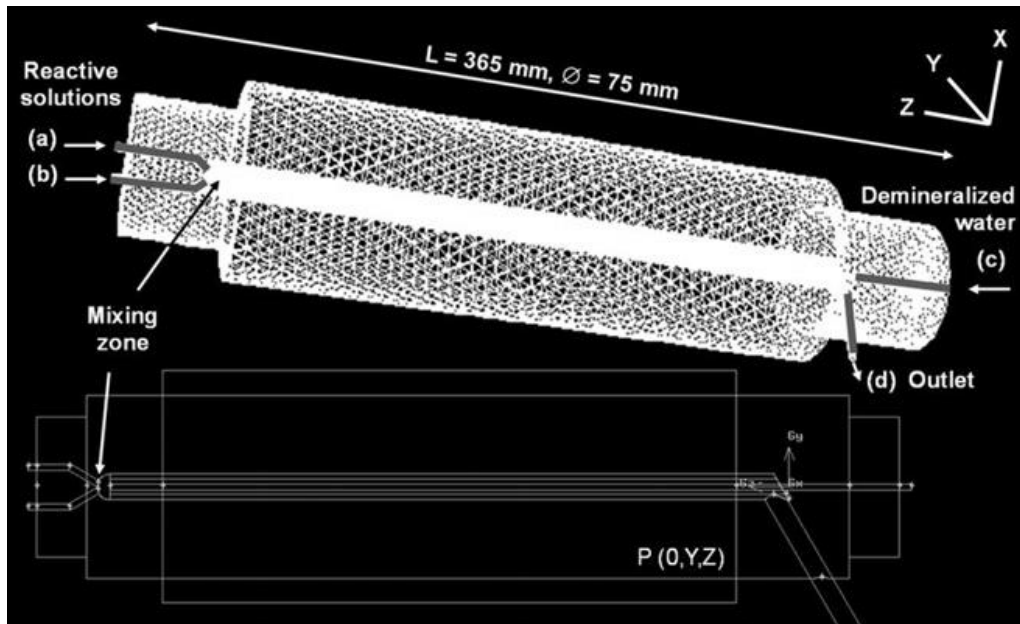


Figure 1.16. Model depicting the geometry of the reactor patented by Aymes *et al.* (Aymes *et al.*, 2011).

A schematic diagram of the whole continuous reactor system used by Aymes *et al.* is given in Figure 1.17. The principle differences between this and earlier designs are the reactor, and the elimination of a separate mixing point and reactor; instead, these two entities are combined into one chamber.

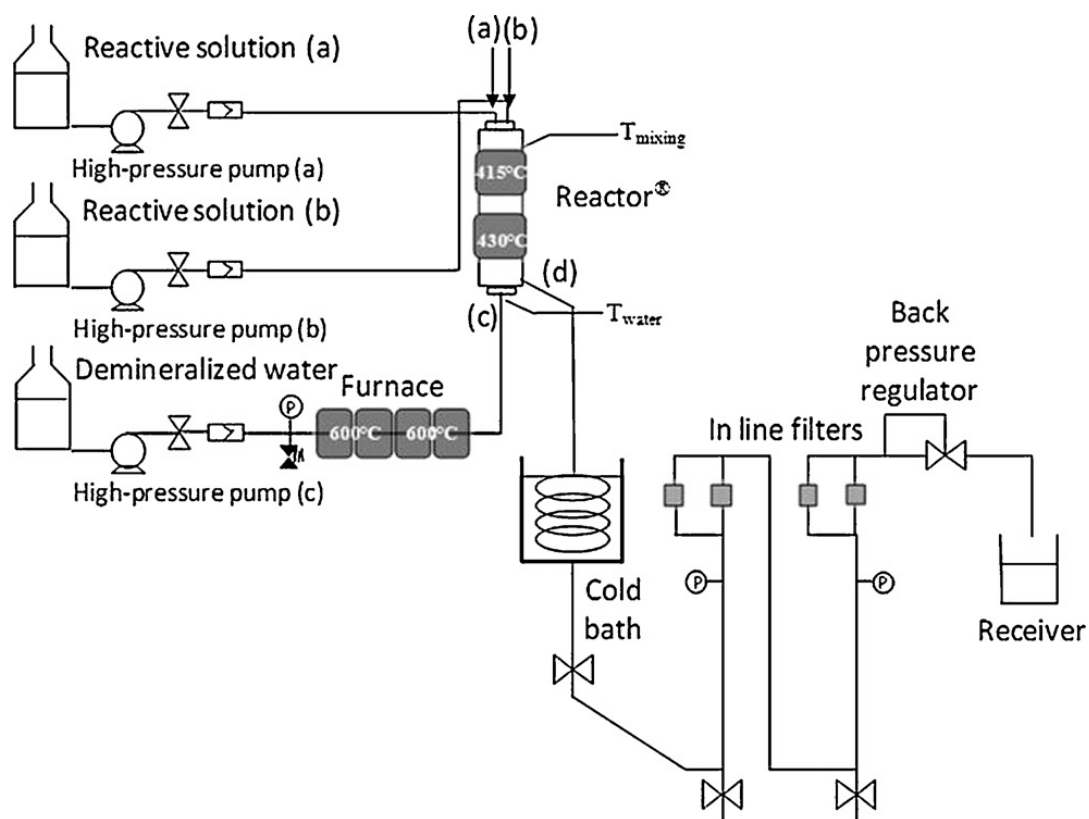


Figure 1.17. Schematic diagram of the continuous hydrothermal reactor system used by Demoisson *et al.* (Demoisson *et al.*, 2011).

1.7.2 The University of Nottingham Counter-Current Reactor

Since the transition from batch to continuous-flow hydrothermal synthesis by Prof. Adschiri *et al.* in the 1990s, the process has been hindered by blockages in the reactor, as highlighted in previous Sections. In the late 1990s and early 2000s, research into continuous hydrothermal synthesis of nanoparticles was started at The University of Nottingham by the Clean Technology Group. They employed a T-piece reactor for the synthesis of cerium-doped, zirconium oxides (Cabañas *et al.*, 2000) and ferrites (Cabañas and Poliakoff, 2001). However, the use of this reactor type led to problems with inconsistent products, and blockages which meant experiments had to be aborted before completion. In

response to this, work was conducted by SChEME (School of Chemical, Environmental and Mining Engineering) at The University of Nottingham to investigate the fluid dynamics and mixing mechanism within the T-piece reactor (Blood *et al.*, 2004). Where previous studies used CFD to model mixing regimes, Blood *et al.* developed light adsorption imaging (LAI) - a method which used fluids of similar density and viscosity to supercritical water and the metal salt precursor feed, to visualise their interaction when mixed. By adding a dye to the stream representing the metal salt feed, the researchers were able to use image analysis techniques to quantitatively conclude the positions of 'stagnant zones', where localised mixing or recirculation occurred, or 'flow partitioning', where the two streams would flow separately with improper mixing. The study concluded that, regardless of the orientation of the flows in the T-piece, the reactor geometry would lead to poor mixing conditions and, in turn, particle build-up and blockages. This was consistent with experimental observations.

Continuing on from this work, the researchers within SChEME used LAI and CFD analysis, alongside experimental data to model alternative reactor designs (Lester *et al.*, 2006). This paper presented a novel reactor design which exploited the natural convection forces in the system to drive turbulent mixing, and prevented the previously seen problems of flow partitioning, or development of stagnant zones. The new reactor design, termed the counter-current Nozzle Reactor, was then patented (Lester and Azzopardi, 2005) and is shown in Figure 1.18. This reactor was used for the work described in this Thesis, the details of which will be described in Sections 1.7.2.1.

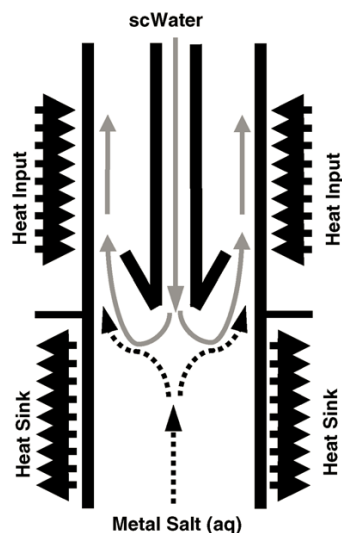


Figure 1.18. Diagram showing the configuration of the counter-current Nozzle reactor, invented at The University of Nottingham (Lester and Azzopardi, 2005, Lester *et al.*, 2006).

1.7.2.1 Reactor Geometry

During the research conducted for this work, the equipment setup displayed in Figure 1.20 was used. A photo of the system is also provided in Figure 1.21. There are some slight differences from the setup previously described in literature (Lester *et al.*, 2006). Firstly, the in-line filter before the back pressure regulator (BPR) was removed. A filter was originally incorporated to remove large aggregates from the sample, and to preserve the BPR. However, it was found that, compared to previous reactor geometries, fewer large aggregates were produced. Moreover, without the filter, the collected particles are more representative of the reaction product. While the filter prevented blockages at the BPR (which would cause loss of pressure), the filter itself served as a potential point of blockage if large aggregates were present. As such, it was better to conduct experiments without it.

In addition, two extra pumps have been introduced for a second metal salt feed, and a “capping point” feed to introduce surfactants (typically organic compounds) after the reactor, but before the BPR. Depending on the reaction, these pumps are not necessarily required so are not used, without affecting the rest of the experimental setup.

In the initial publication describing the counter current Nozzle reactor, some experiments described the addition of a cone (a Swagelok ferrule) to the end of the inner pipe, while others omitted it. The function of the cone was to mimic a spinning disc reactor and dissipate flow of the heated water, therefore maximising mixing. However, for the reactor used here, the cone was not used in order to maximise the flow area available.

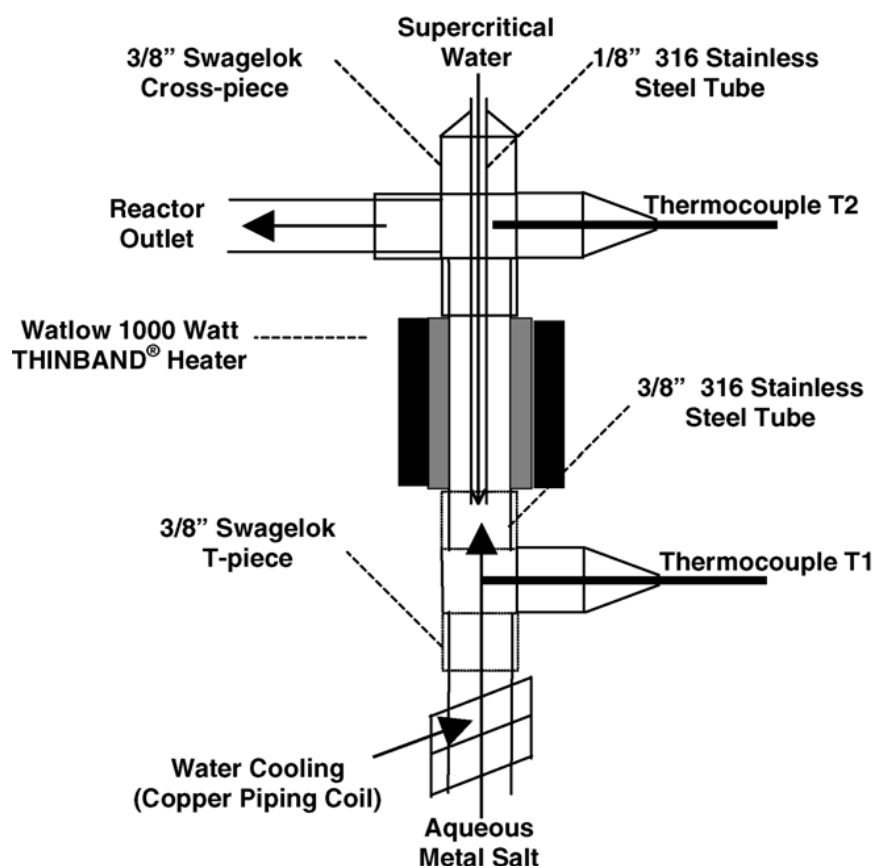


Figure 1.19. Orientation of parts used to construct the counter current Nozzle Reactor (Lester *et al.*, 2006).

A diagram of the reactor geometry is given in Figure 1.19. It is a pipe-in-pipe configuration where the heated water feed enters through the thinner inner tube ($1/8''$ outer diameter), and the cool metal salt feed is flowed up into the outer pipe ($3/8''$ outer diameter). Mixing and particle formation occurs at the interface, then the product is carried up and out of the side arm of the cross piece to the cooling loop.

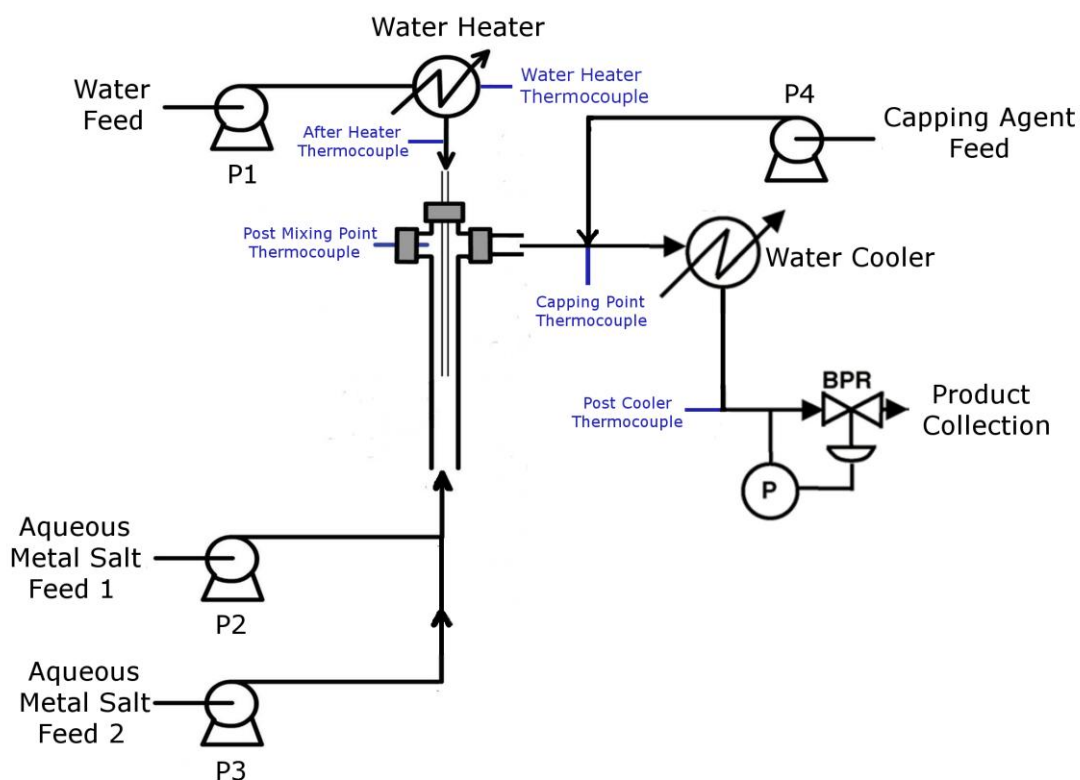


Figure 1.20. Schematic diagram of the counter current reactor system at the University of Nottingham.

For nanoparticle synthesis experiments, a vessel of water (or if required, a thermally-stable precursor) was pumped at a pre-set flow rate up to 25 ml/min, using a Gilson HPLC pump (Model 305 equipped with a 25 SC pump head). This then flowed through a check valve and into a coiled tube around an electrical heater block, where the heater set point could be controlled up to 500 °C. A thermocouple within the water heater block provided an electronic reading

(referred to as the "Water Heater Temperature") as well as acting as a feedback control. After the heater, the feed flowed past a thermocouple to give the "After Heater Temperature", then into the inner pipe of the reactor.

Meanwhile, the metal salt feed(s) were pumped, each with a maximum flow rate of 10 ml/min, using Gilson HPLC (high-performance liquid chromatography) pumps (Model 305, equipped with a 10 SC pump head) through check valves and into the bottom of the counter current reactor as an upflow. As the product rose and exited the reactor through one side arm of the cross piece, a thermocouple attached at the other cross piece side arm monitored the temperature. This gave the "Post Mixing Point Temperature".

Upon leaving the reactor, the product stream was partially cooled by one cooling loop. Here, a flow of mains tap water moved over the pipe carrying the product stream without directly coming into contact with it. After this first cooling loop, there was a cross piece at which another feed (e.g. a surfactant or capping agent), could be pumped in. A check valve on this feed meant the process was unaffected if this pump was not operating. A thermocouple was present on the other arm of the cross piece, allowing the "Capping Point Temperature" to be monitored.

The product stream subsequently flowed through a second cooling loop which brought the temperature to around ambient. The two cooling loops could be operated independently, permitting the temperature of the capping point to be 'tuned'. The product stream passed through the back pressure regulator, BPR, (manufactured by Tescom, USA) and the product suspension flowed out at ambient pressure into a collect vessel.

The BPR constricted the flow to an adjusted level or set point and maintained it, hence controlling the system pressure. Being a continuous system, the pressure throughout the entire equipment was consistent. BPRs can be pneumatic or manual, where the former is air-actuated and the latter is spring loaded. The air or the spring pushes a needle down onto a seal causing restriction in the flow.

To measure the system pressure, a piezoelectric pressure transducer and bourdon gauge were attached in the water feed. The piezoelectric transducer was attached to a control box to give an electronic reading.



Figure 1.21. A photo of the counter-current reactor system.

1.7.2.2 Advantages of the Counter Current Design

Much of the early work into continuous hydrothermal synthesis used a T-piece fitting as a mixing device, as described in previous Sections of this Chapter. In many cases, the T-piece was upright with the heated water feed

entering through the side arm and the cold metal salt flowing down; the bottom arm of the Tee then formed the product outlet. When Blood *et al.* performed LAI analysis on their T-piece pseudo reactor, as described in Section 1.7.2, they found that the water would rise into the top arm of the Tee. This was due to the lower density and consequent higher buoyancy of the superheated water. By flowing upwards, the metal salt feed became heated, causing the nucleation of particulates. Without a strong flow to transport the particles away, this led to accumulation and blockage at the top arm of the Tee. This observation caused researchers to see the importance of differences in density between the two flows.

The counter-current Nozzle reactor has the superheated water feed flowing down the inner pipe before meeting the cold metal salt feed. The counter current geometry ensures the metal salt stream is not heated prior to mixing, as this could cause precipitation of the salt and in turn, blockage. Furthermore, as the two streams meet, mixing and heating of the metal salt feed is rapid and immediate - leading to the nucleation of particulates. After particle formation, the product stream is hotter, less dense and thus more buoyant than the metal salt upflow; therefore particles inherently flow upwards toward the reactor outlet. The flow from both the water and metal salt also drives particle movement, thereby preventing particle build-up, as well as creating a short residence time which can prevent particle growth. Subsequent to leaving the reactor, particles are quickly cooled in the cooling loop to inhibit particle growth.

Unlike the reactor designs from Adschiri, Arai and others (Adschiri *et al.*, 2000, Hakuta *et al.*, 1998, Kawasaki *et al.*, 2010, Aimable *et al.*, 2009b), the Nozzle reactor combines the mixing device and reactor into one entity which also promotes instant and rapid heating of the precursor stream, and short residence times.

1.7.2.3 Continuous Hydrothermal Scale Up

While developing the counter current Nozzle reactor, Lester *et al.* had the aim of designing a reactor system which was capable of making the process of synthesising nanoparticles industrially viable. This meant it needed to be capable of being scaled up without having a detrimental effect on product quality. Moreover, the scale up process needed to be economically feasible, as any nanomaterial synthesis (or any emerging technology) that presents high manufacturing costs will have difficulty in gaining widespread industrial interest.

In 2007, Lester *et al.* succeeded in building a pilot scale reactor system based on the technology of the counter current Nozzle reactor, a photo of which is shown in Figure 1.22, and is owned by Promethean Particles Ltd. (see Section 1.8.2). The water and precursor flows are driven by two dosing pumps from Milton Roy (Milroyal B) – each with a maximum flow rate of 400 ml/min. The water stream is heated using a custom-built electrical heater (Watlow, output of 9 x 4.3 kW). All pipes and fittings within the system are from Swagelok; where the lab scale reactor uses a Swagelok cross-piece with an outer diameter of $\frac{3}{8}$ " (0.9525 cm), the pilot scale reactor contains a cross-piece with an outer diameter of $1\frac{1}{2}$ " (3.81 cm) and a wall thickness of $\frac{1}{4}$ " (0.635 cm). Likewise, at the lab scale, the inner pipe which carries the heated water stream has an outer diameter of $\frac{1}{8}$ " (0.3175 cm). The equivalent pipe on the pilot reactor measures $\frac{1}{2}$ " as its outer diameter with a wall thickness of 0.083" (0.211 cm). The system pressure is maintained by a pneumatic back pressure regulator (Tescom) and the product stream is cooled to ambient by a mains water fed heat exchanger built using Swagelok parts. Typical synthesis experiments on the lab scale equipment employ a total flow rate ca. 30 ml/min to generate g/h of equivalent dry material, while the pilot reactor system is capable of flow rates up to 800 ml/min, to produce kg/day.



Figure 1.22. Photograph of the Pilot Scale reactor system which incorporates the counter-current Nozzle reactor technology, courtesy of Promethean Particles Ltd (see Section 1.8.2).

Currently, The University of Nottingham are involved in an EU-funded, Seventh Framework Programme (FP7) project entitled SHYMAN (Sustainable Hydrothermal Manufacture of Nanomaterials). One of the main objectives within this project is the design and build of a commercial scale plant (production at 1000 tonnes per annum) based on the counter-current Nozzle reactor - making it the largest scale production plant, using continuous hydrothermal technology, in the world. The SHYMAN project will be discussed further in Section 1.8.2.1.

1.8 Commercialisation of Hydrothermal Synthesis

1.8.1 Hanwha Chemical

Hanwha Chemical is a Korean company established in 1965. Traditionally, they have produced plastics, such as polyethylene (PE) and polyvinyl chloride (PVC), and battery materials, as well as having biopharmaceutical departments dedicated to drug development and production (Hanwha, 2013). In recent years they have turned their attention to nanotechnology and built a pilot plant for the hydrothermal synthesis of a range of metal oxide nanoparticles, via a continuous process. Their pilot scale facility has the capacity to produce the equivalent of 4 kg of dry powder per hour, and was built to gather scale-up data in order to develop an even larger plant.

At the end of 2010, Hanwha Chemical built a commercial plant for the manufacture of lithium iron phosphate, LiFePO_4 – a material gaining much global interest for battery applications. This plant employs the process of continuous supercritical hydrothermal synthesis, and has a capacity of >200 tons per annum – the current largest plant of this type in the world (Adschiri *et al.*, 2011).

1.8.2 Promethean Particles Ltd.

A spin-out company was formed in 2008 called Promethean Particles to take advantage of the patented Nozzle reactor. The company conducts gram/hour scale feasibility studies to develop bespoke nanoparticle dispersions for industrial customers in a diverse range of applications. In addition, a Pilot scale reactor (as described in Section 1.7.2.3) is capable of producing nanomaterials at a scale of 1 ton per annum, to meet larger demands.

As well as commercial projects, Promethean Particles participate in EU-funded FP7 Projects, providing nanomaterials to Consortium Partners. At the time of writing, there are 3 FP7 projects running in parallel – POINTS (Printable Organic-Inorganic Transparent Semiconductor Devices) started in May 2011 and runs until May 2014; NanoMILE (Engineered nanomaterial mechanisms of interactions with living systems and the environment: a universal framework for safe nanotechnology) began in March 2013 and runs until March 2017; and SHYMAN (Sustainable Hydrothermal Manufacture of Nanomaterials), which started in May 2012 and will conclude at the end of April 2016. The SHYMAN Project revolves around the 'Nozzle' reactor.

1.8.2.1 The SHYMAN Project

The SHYMAN Project is an EU funded Seventh Framework Programme (FP7) study which started in May 2012 and will run over the course of 4 years (SHYMAN, 2013). With 16 Consortium partners from academia, industry and SMEs (small and medium enterprises), the aims of the project fall into three main categories:

- The design, commission and build of a commercial scale plant, with the ability to produce nanomaterials at a capacity of up to 1000 tons per annum. As such, it will become the largest continuous hydrothermal production plant in the world. Modelling (e.g. computational fluid dynamics, CFD, and pseudo-fluids modelling) will be employed to determine the deviations in fluid mixing with increasing scale while engineers from academia and industry will consider and design solutions for minimising the energy consumption of the plant, and maximising product yield.

- The development and characterisation of existing and novel nanomaterials (produced by the University of Nottingham and Promethean Particles) which can be formulated by industrial partners into their current products, in order to replace less sustainable additives, or enhance their existing properties. Industrial partners include multi-national companies Solvay, Repsol, PPG, and Fiat.
- The analysis of waste products generated during the manufacturing process, and development of waste water recycling schemes, in order to reduce waste emissions and other detrimental effects on the environment. Moreover, Life Cycle Analysis (LCA) will be performed to assess if nanomaterials produced using this technology are more sustainable compared to from other existing technologies. As with many chemical and engineering methods, particularly at pilot or commercial scale, a lot of focus falls on environmental impact, and whether the process adheres to the Principles of Green Engineering (Tang *et al.*, 2008).

By reaching these aims, the SHYMAN Project will develop commercial products containing nanomaterials, as well as a plant capable of manufacturing these nanomaterials to meet global demand. A highly interesting and exciting project, SHYMAN demonstrates the real potential of the technology described in this Thesis.

1.9 Challenges of Nanomaterial Synthesis

In previous Sections of this Chapter, the wide variety of benefits from nanoparticles has been described. However, the synthesis of nanoparticles is not without its challenges. This is true for most methods of synthesis, not just continuous hydrothermal routes. A major challenge facing the synthesis of nanomaterials, is achieving particles which are stable and do not agglomerate. This issue will be discussed in Section 1.9.1.

1.9.1 Particle Stability

Due to the small size of nanoparticles, a high proportion of the component atoms within each particle are present on the surface. Coupled with the high surface area-to-volume ratio, nanoparticles have a much higher surface energy compared to bulk material (Nanda *et al.*, 2003). This results in nanoparticles inherently being drawn to each other to minimise their surface energy. The net result, if no opposing forces prevent them from doing so, is that nanoparticles will coagulate into larger clusters. There are two forms of coagulation: flocculation, which is reversible; and agglomeration, which is irreversible. While flocculation can usually be solved by agitation of particles and dispersing them in high viscosity media, agglomeration is not as simple. It poses a huge disadvantage as, in many cases, the particles no longer move as individual particles, but as larger micron-scale aggregates. The properties of the particle can also be affected, no longer exhibiting the advantageous properties seen at the nanoscale; in these cases, measures should be taken to prevent it from occurring, otherwise the principle of having nanoparticles becomes void. Preventing particle aggregation is particularly pertinent in continuous systems,

as large clusters are more likely to cause blockages – especially at bench scale where pipes are narrow.

1.9.2 Methods of avoiding Particle Coagulation

Depending on the degree of coagulation between nanoparticles, a few different methods can be used to break particles up or keep them apart. These can be classified into mechanical or chemical methods. For flocculated particles, mechanical methods can be employed; here, equipment is used to physically break up flocculates, such as sonicators, homogenisers or dispersers. These use physical force, such as sound energy or shear forces, to disrupt clusters and disperse them into a carrier media. If the media has a high viscosity, the particles disperse more slowly through the fluid, reducing the chance of re-flocculation.

However, without altering the surface charge or chemistry of the particles, they are able to re-coagulate. Hence, chemical methods are often more effective at preventing particle coagulation. Capping agents or surfactants (surface active agents) can be added to bind to the particle surface which, in turn, provides either steric stabilisation (generally the case when polymeric surfactants are used) or charge stabilisation (such as the use of acids or bases). Choosing a suitable surfactant for each nanoparticle species can be difficult, as it should be compatible with the solvent media, as well as able to chemically bind to the particle surface. In addition, the concentration ratio between nanoparticles and surfactant needs to be balanced; insufficient surfactant means incomplete coverage and exposed particle surfaces are still able to bind and coagulate, while too much surfactant can lead to 'overcrowding' on the particle surface, a compression of surfactant layer, and a similarly detrimental effect. This is depicted in Figure 1.23. Of course, this ratio is also dependent on particle size -

smaller particles have a larger surface area and therefore require more surfactant molecules to bind to it (Lubrizol, 2013).

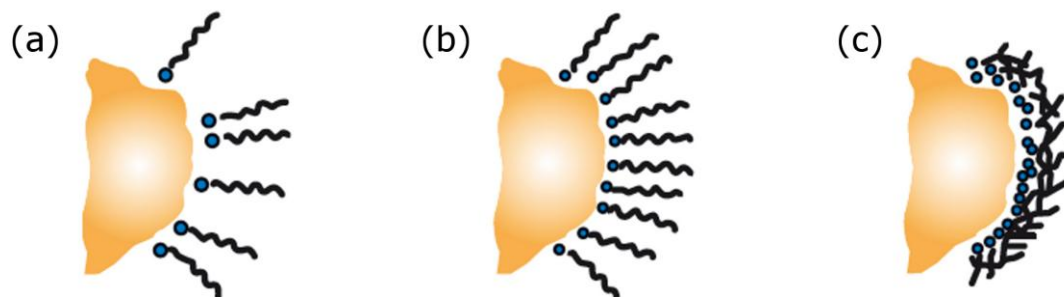


Figure 1.23. Ratios of surfactant to nanoparticle where (a) shows insufficient surfactant concentration resulting in partial coverage, (b) displays optimum surfactant coverage and maximum stability, and (c) shows too much surfactant leading to layer collapse and unstable particles (Lubrizol, 2013).

It has also been shown that surface modification can be used to transfer nanoparticles into different solvent phases (Ohara et al., 2008); improve particle dispersability into fluids (Kim et al., 2008); limit crystal growth in a particular direction which then affects particle morphology (Mousavand et al., 2006, Mousavand et al., 2007); or alters particle size (Taguchi et al., 2012).

1.9.3 Methods of Determining Particle Stability

If particle coagulation occurs, the clusters typically become denser than the carrier solvent (in most studies, this solvent is water or basic alcohols) and fall to the bottom of the vessel resulting in phase separation. Therefore, it is very easy to observe by eye if coagulation is evident. Consequently, many assessments of particle stability are empirical.

Still, the particles in a suspension may have sufficient surface charge to remain stable in the short term, but will coagulate over time. Therefore the degree of surface charge (attractive or repulsive forces acting on a particle) should be measured to ascertain if the particles are truly stable. Zeta potential is a widely used method to quantify particle charge. Although the technique does not conclusively give information about whether particles have a positive or negative charge, it is a reliable method for measuring long term particle stability. Zeta Potential, and other structural characterisation techniques, will be discussed in more detail in Chapter 2.

1.10 Aims of this PhD

Through the course of this Chapter, the benefits of using nanoparticles have been described for a vast range of applications. While nanotechnology as a field of research has existed for decades, its emergence into industrial application remains in its infancy. With increasing numbers of studies highlighting nanoparticles as safe to use, coupled with the exceptional data obtained from research, more and more industries want to test and apply nanoparticles into their products. This developing demand calls for synthesis procedures which stretch far beyond the lab-scale, while keeping costs and negative environmental impacts down.

The merits of continuous hydrothermal synthesis have been described in this Chapter, with the importance of optimised reactor design being highlighted. In response to this need, the counter-current Nozzle reactor was designed and constructed at the University of Nottingham at both lab and pilot scale. While studies have been conducted using the Nozzle reactor for the synthesis of a few different nanomaterials (Hobbs *et al.*, 2009, Lester *et al.*, 2012, Aksomaityte *et al.*, 2013), the immense range of nanomaterials which could potentially be produced by this method, largely remains uncharted territory. Because reactor geometry plays such a vital role in the structural properties (size, shape, crystallinity) of the synthesised particles, the products from the Nozzle reactor may be vastly different to those made using a different continuous hydrothermal reactor, even though synthesis is based on the same principle method. Since particle structure ultimately dictates functional performance, products from two different reactors could exhibit very different properties.

Therefore the invention of the Nozzle reactor opens up a vast field of research - comprising the synthesis of a material, optimisation of the process, structural characterisation of the products, and application testing. The latter provides assessment of how materials can be applied to give real-world meaning. All the while, this technology has been proven to be scalable, with high product reproducibility. This principle forms the motivation of this PhD work.

The aims of this work are to use a novel continuous hydrothermal reactor (the counter current Nozzle reactor) in the synthesis of a range of nanomaterials for three different biomedical applications, to characterise the structure of those nanomaterials, and finally to test the particles for properties which are specific to that application. Testing performance properties and characteristics is key to assessing the viability of applying the nanoparticles in a specific end application.

Chapter 2

Structural Characterisation Techniques

This chapter will discuss the analysis techniques used in Chapters 3, 4 and 5 to characterise the structural properties of nanomaterials. For each procedure, the principles of each technique will be discussed, along with the data which can be obtained from it. The methods of sample characterisation which are more specific to each individual Chapter, such as testing of application properties, will be discussed in the relevant Chapter.

2.1 Scanning Electron Microscopy (SEM)

SEM is a surface imaging technique which allows the user to study the particle size, topography, and morphology of samples using magnifications between 100 and 100,000 times. With standard optical microscopes, light is used to form an image. With SEM, images are formed with an electron beam generated from an electron gun. Electrons are a type of ionizing radiation; using them not only means that higher magnifications are possible due to their shorter wavelength compared to visible light, but there is also a larger field of depth compared to light microscopy. This means a large area of the sample is in focus at one time, giving an image which is a good 3-dimensional representation of the sample.

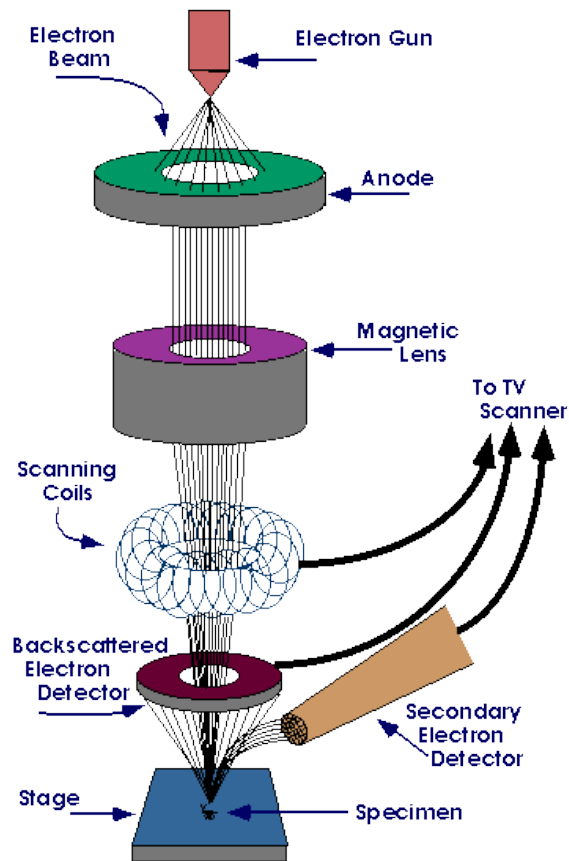


Figure 2.1. An illustration showing the components in a typical scanning electron microscope (Flegler et al., 1995).

Samples of powders or particles are held on an aluminium stub using adhesive carbon tape. If required, the surface of the sample and stub can be coated with a very thin layer of metal such as gold, to enhance conductivity and in turn, improve the flow of electrons across the sample surface. The stub is then loaded into the sample chamber. The electron beam travels down the microscope under vacuum from the gun, through a series of apertures and electromagnetic lenses to control and modify the beam, as well as prevent electron spray, before reaching the sample (the beam can be controlled to scan across a specific area of the sample). The orientation of these components is shown in Figure 2.1. When the beam of electrons hits the sample, they interact and different signals are generated, including secondary electrons (SE), backscattered electrons

(BSE), and X-rays. Detectors are in place to pick up each of these signals. The detected electron intensity is converted to light intensity which gives a visual image that can be digitally viewed. SE are electrons expelled from the sample atoms as a result of interactions with the (primary) electrons of the beam. SE generally have low energy and are used to give the best imaging resolution, where contrast in the image is principally due to sample topography. On the other hand, BSE are electrons from the beam that have been scattered back after collisions with the nuclei of sample atoms, where nuclei with a higher atomic number cause more electrons to be scattered back. As a result, these atoms appear brighter in BSE images and in turn, contrast in these images can give information about sample composition (Griffith and Danilatos, 1993).

Simple sample preparation, rapid data acquisition, high magnification imaging, and being a non-destructive technique (meaning samples can be analysed repeatedly) make SEM a very useful technique. However, disadvantages are that only solid material can be analysed, which has to fit in the sample chamber (usually a maximum of 10 cm). Samples usually have to be stable under high vacuum, although microscopes with low vacuum or environmental modes are available. In addition, some samples (particularly organic samples) are beam sensitive and can become damaged (Flegler et al., 1995).

The SEM kit used in this study is a FEI Quanta 600 with a lanthanum hexaboride (LaB_6) filament to generate an electron beam. In most cases, an accelerating voltage of 25 or 30 kV is used.

2.2 Transmission Electron Microscopy (TEM)

TEM operates using a similar principle to SEM, where electrons are used as a "light" source. However, unlike SEM, the electron beam travels through the sample (Figure 2.2 (a)). Some electrons may become scattered depending on the density of the material, but those that are not, hit a screen at the bottom of the microscope to form a "projection" of the sample where parts may appear darker than others depending on density. Thus, TEM can be useful for visualising hollow structures (Figure 2.2 (b)) (Williams and Carter, 2009).

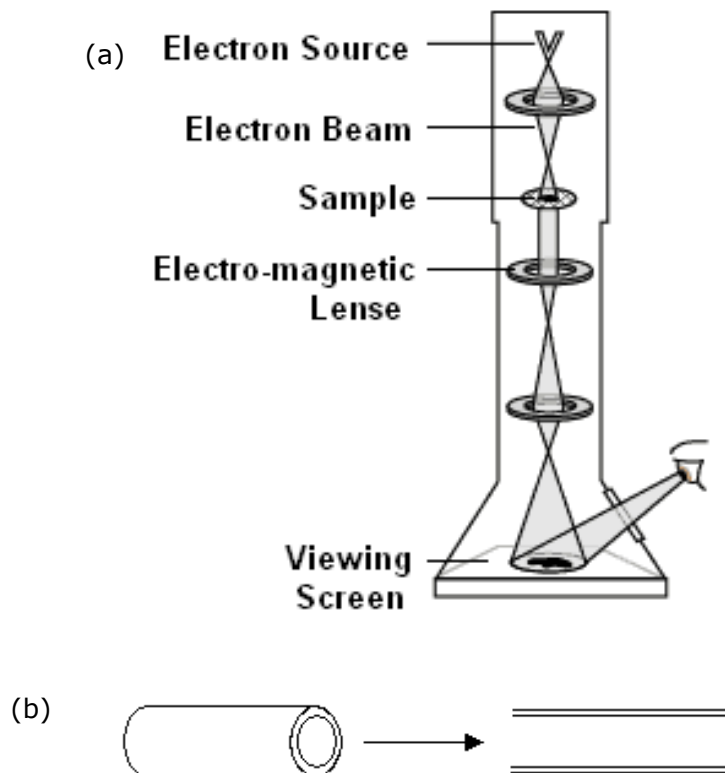


Figure 2.2. (a) A simplified depiction of how a typical TEM operates; (b) a schematic showing a 3-dimensional tube is viewed as a 2-dimensional image under a TEM.

There are different types of TEM, for example Scanning TEM (STEM), high resolution TEM (HRTEM) and analytical electron microscopy (AEM), providing a choice over image analysis. TEM also allows higher magnifications than SEM and can determine, to an extent, the internal structure of particles. In addition, the crystal lattice of particles can even be observed with HRTEM. Nevertheless, the trade-off of higher magnifications is the decreased sample area, which questions if an image obtained using TEM is truly representative of the full sample. Furthermore, there can be confusion when interpreting images; after all, these are 2D images of 3D samples (Williams and Carter, 2009). Like SEM, some samples can be sensitive to the ionizing radiation of the electron beam; as a result, some materials (particularly organic materials) may suffer heat or chemical etching damage.

In this work, samples were prepared for TEM analysis using one of two methods; nanoparticles produced in water from the reactor were washed and diluted with deionised water before being loaded onto the copper-grid mounted 'holey' carbon films and allowed to air dry on filter paper. Dry powder samples were suspended in alcohol, typically ethanol or methanol, and sonicated. A few drops of the suspension were loaded onto the grids and air dried. Alcohol is used because it tends not to react with the samples, but has relatively low surface tension (compared to water, for example) thereby allowing the particles to be well distributed over the sample grid.

Images were obtained using a JEOL 2100F HRTEM equipped with a field emission electron gun (FEG) and operating at 100 kV accelerating voltage.

2.3 Energy Dispersive X-Ray Spectroscopy (EDX/EDS)

EDX analysis is an additional feature of most SEM and TEM instruments. As previously mentioned in Section 2.1, electron interaction with a sample can also produce X-rays. This signal can be specifically detected to give information on the elements present within a sample. In the case of the FEI Quanta 600 SEM equipment mentioned in Section 2.1, collected EDX data was interpreted using Genesis software by EDAX.

EDX analysis can be a very helpful confirmatory tool, but very light elements such as H, He and Li cannot be detected.

2.4 X-Ray Diffraction (XRD)

This analysis method is used to ascertain information about the crystal structure (or arrangement of atoms) in a sample. Figure 2.3 illustrates how data can be obtained; X-rays of known wavelength (λ) are fired at the sample, which then interact with the electrons of atoms on each crystal plane. As a result, the X-rays are scattered to give a signal (elastic scattering) and are identified by the detector component of the equipment.

During analysis, X-rays are directed at the sample at a range of angles (incident angle θ seen in Figure 2.3). As the rays hit the sample, they are diffracted by the lattice structure of the crystal. A detector moves around the sample and measures the intensity of these peaks at each angle. Thus, signal intensity at each angle depends on the orientation and spacing between crystal planes.

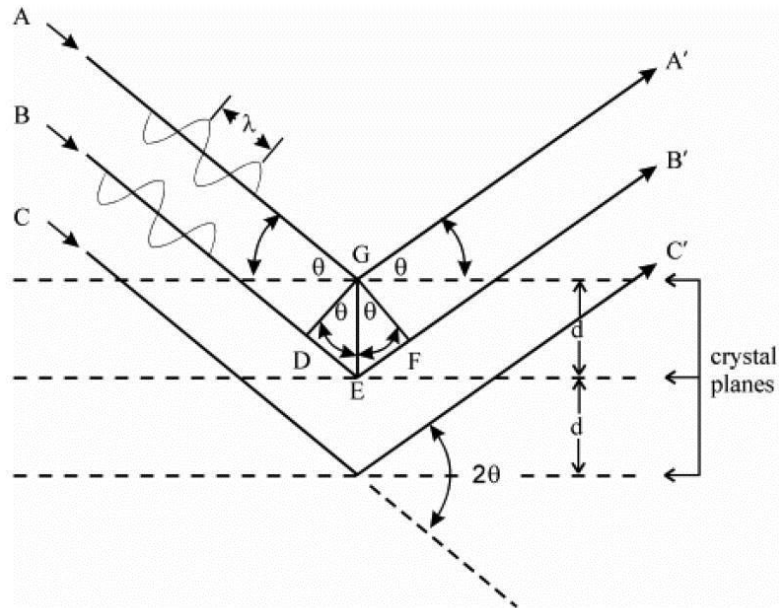


Figure 2.3. A diagram showing the basis of XRD analysis.

The relationship between the X-ray wavelength, the d-spacing, and the angle θ can be summarised by Bragg's Law:

$$n\lambda = 2d\sin\theta$$

where: n is an integer,

λ is the wavelength of the beam,

d is the spacing between diffracting planes, and

θ is the incident angle

Each crystal structure has a unique diffraction pattern, giving signal peaks of different intensity at differing angles of 2θ ; once the diffraction pattern (or corresponding d-spacings if calculated using Bragg's Law) of a sample has been measured and the constituent elements are known, it can be matched to an existing library of known structures in order to identify the crystal phase and the component compound(s) in the sample.

With specific analysis, the diffraction pattern of a sample can be used to infer much more information than just compound identification. The shape of peaks in a diffraction pattern can be an indication of the degree of crystallinity in a sample. For example, a highly crystalline sample will have consistent d-spacings and in turn, high signal intensity for a narrow range of angles. Therefore, the resulting diffraction pattern will have sharp narrow peaks. Conversely, samples with a lower degree of crystallinity will have more irregular d-spacings and the subsequent diffraction pattern will show broader, less intense peaks. Amorphous samples (those which contain atoms arranged in a random order with no distinct crystal planes) will not create a detectable signal and so, do not give any peaks or diffraction patterns.

It is important to note, however, that peak shape and size can also be ascribed to factors other than the degree of crystallinity in the sample. The instrument used can play a role in the peak profile obtained, and for small particles (principally <200 nm) - crystallite size. The Scherrer equation establishes the relationship between peak broadening and crystallite size:

$$D = \frac{K\lambda}{\beta \cos\theta}$$

Where:

- D = crystallite size
- K = the Scherrer constant, which takes into account the shape of the crystal
- λ = X-ray wavelength
- β = the full-width of the peak at half maximum (FWHM), in radians
- θ = the Bragg angle

The Scherrer equation demonstrates that crystallite size is inversely proportional to peak broadening, i.e. a wider peak indicates a smaller crystallite. Because this effect is mainly seen for small particles, size analysis by other techniques such as TEM should be used concurrently with XRD analysis, in order to infer the cause of peak broadening. It should also be noted that crystallite size is not the same as particle size, as a particle may be made up of different crystallites.

In this work, dry powder samples were analysed using a Bruker D8 Advance diffractometer, using Cu $K_{\alpha 1}$ radiation ($\lambda = 0.15406$ nm) with a step size of 0.04 and step time of 5 seconds. Typically, scans were taken for a 2θ range between 15 and 65°. Diffraction patterns were analysed using EVA processing software for phase identification, while Xfit (Cheary and Coelho, 1996) and Celref (Laugier, 1999) software were used to calculate crystallite size and cell parameters, respectively.

2.5 Time-of-Flight Secondary Ion Mass Spectrometry (ToF-SIMS)

ToF-SIMS is a method for analysing the chemical composition of the surface of a solid sample. It uses a pulsed ion beam (Bi^{3+}) to remove molecules from the very outermost surface of the sample in a chosen square area. Particles are removed from atomic monolayers on the surface (secondary ions). These particles, which could be full or fragmented molecules, are then accelerated into a "flight tube" and their mass is determined by measuring the time taken to reach the detector (i.e. time-of-flight). Three operational modes are available using ToF-SIMS: surface spectroscopy, surface imaging and depth profiling (Vickerman and Briggs, 2001).

This method has the advantages of being non-destructive, easy to use and with little sample preparation, and high sensitivity for trace elements or compounds. Nevertheless, the equipment collects a spectrum for each pixel of the chosen square area of analysis. This can provide too much data which can be very time-consuming to interpret.

Data obtained from ToF-SIMS analysis will be described in Chapter 3.

2.6 Dynamic Light Scattering (DLS)

DLS is a particle sizing technique, also referred to as photon correlation spectroscopy (PCS) or quasi-elastic light scattering (QELS), which measures the rate of particle diffusion in a suspension by Brownian motion and correlates this to particle size. In a sample of a liquid dispersion, solvent molecules move around in solution due to their thermal energy. In turn, these bombard or “kick” particles that are also present in the suspension and this is known as Brownian motion. As such, particles must be suspended in a solvent, to be analysed by DLS.

For DLS analysis, a monochromatic laser illuminates the particles in a liquid dispersion and the light is scattered. The intensity of this scattered light varies depending on the size of the particles because smaller particles are pushed further by solvent molecules and move faster. By measuring the changes in intensity of scattered light, the velocity of the Brownian motion can be found; the particle size is then calculated using the Stokes-Einstein equation:

$$d(H) = \frac{kT}{3\pi\eta D}$$

where: $d(H)$ = hydrodynamic diameter

k = Boltzmann's Constant

T = absolute temperature

η = viscosity

D = translational diffusion coefficient

The particle size calculated by DLS relates to how the particle diffuses in the surrounding dispersant and is called the 'hydrodynamic diameter' (Figure 2.4).

This value is dependent on the particle core, as well as any surface modifications to the particle, and the surrounding ions present in the solvent. The particle shape affects the reported size as well, and the measured hydrodynamic diameter for non-spherical particles is given as “the diameter of a sphere with the same translational diffusion speed as that particle” (Malvern, 2013). Consequently, the measured particle size can be larger than that seen using electron microscopy (where a particle may be out of its natural environment).

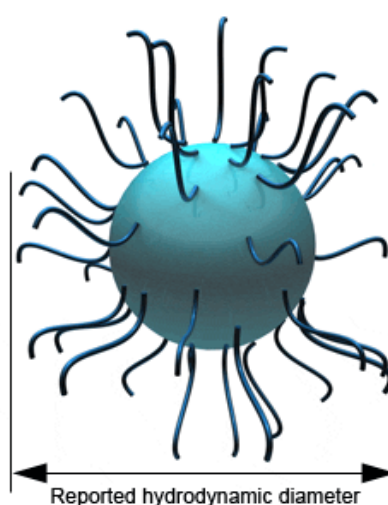


Figure 2.4. A diagram of the hydrodynamic diameter of a particle which is reported by DLS analysis (Malvern, 2013).

The application of DLS analysis will be principally discussed in Chapters 4 and 5; DLS data was obtained using a Zetasizer Nano-ZS by Malvern Instruments, which can measure particles in the range of 0.3 nm to 10 μm . This instrument uses a He-Ne laser with a wavelength of 633 nm. Where required, the Refractive Indices for sample materials were taken from the “Dispersion and Refractive Index Guide” from Malvern Instruments. Data analysis was performed using Zetasizer software Version 7.20 from Malvern Instruments. The obtained particle size data is initially given as an intensity distribution for the scattered light. In this instance, $I \propto d^6$ where I is the signal intensity and d is the particle diameter;

larger particles provide a much stronger signal than smaller particles meaning data can be skewed if larger particles, dust or agglomerates are present in the sample.

For samples which contain different sized particles, i.e. where there is more than one peak in the intensity distribution graph, it may be necessary to convert the data to a volume based distribution. To do this, the refractive index and adsorption value of the particles needs to be added to the software. Using Mie theory, the software then converts the data to a volume-basis so that the aforementioned data-skewing due to larger particles is not seen.

This technique benefits from being a non-invasive method that requires practically no sample preparation. Moreover, data acquisition takes only a few minutes – significantly shorter than most other particle sizing techniques, and a fraction of the running costs compared to electron microscopy. On the other hand, particles must be stable and well dispersed in the solvent in order to obtain a viable measurement; if particles are coagulated, the size of the clusters is measured and no information on the primary particle size can be gathered. Thus, samples with particles which have coagulated and phase separated due to gravity can be visually identified, and analysing these with DLS is redundant.

2.7 Zeta (ζ) Potential

The Zetasizer Nano ZS from Malvern Instruments can also measure the zeta potential of colloidal systems, which gives an indication of the particle stability i.e. if the particles are likely to coagulate over time.

In aqueous media, particles in dispersion carry a surface charge. This is dependent on the particle's surface groups. For example, dissociation of acidic surface groups will lead to a negative charge, while basic groups dissociate and give rise to positive charge. In addition, the presence of anionic or cationic surfactants around particles affects the surface charge. Figure 2.5 shows an example particle with a negative surface charge. Depending on the pH and ionic strength of the solution, ions of opposite charge to the surface are strongly bound to the particle, called the Stern layer. Around this layer are more loosely bound ions – part of the slipping plane. As a result, each particle has an electrical double layer which is considered a stable entity and moves in solution with the particle. Outside of this electrical double layer, the ions are considered as part of the bulk dispersant and do not move with the particle. Zeta potential is a measure of the net electrical charge for a particle and its electrical double layer.

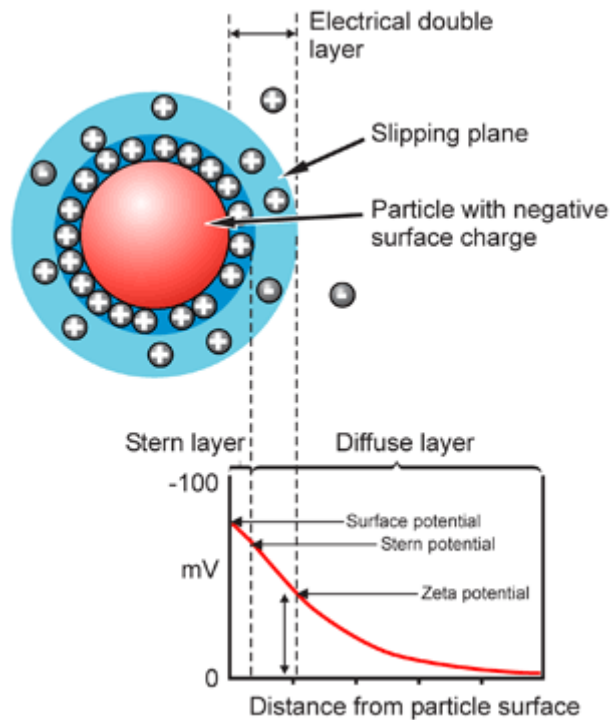


Figure 2.5. A schematic representation of what is measured by zeta potential (Malvern, 2013).

To measure zeta potential, an electric field is applied across a sample. Charged particles will move towards the electrode of opposite charge at a speed that is proportional to the size of its charge. The Zetasizer measures this velocity and, considering the viscosity of the dispersant, can calculate the zeta potential value. This data can give information on the attractive or repulsive forces present in a dispersion and in turn, how likely particles are to coagulate. A high zeta potential is considered as <-30 mV or $>+30$ mV (Malvern, 2013), and the particles in that suspension can be considered to be stable.

The zeta potential of particles varies with the pH and conductivity of the surrounding media, so measurements can be taken over a pH range in order to ascertain the conditions where particles begin to aggregate. This is known as the point of zero charge (PZC) or iso-electric point (IEP).

Zeta potential is crucial analysis for understanding colloidal systems, and in the development of stable, non-aggregating dispersions. This technique holds the advantage of rapid data acquisition as measurements generally only take a few minutes, but drawbacks include the need to prepare samples with accuracy as pH, conductivity and presence of surfactants can significantly affect zeta potential.

The application of zeta potential measurements will be discussed in Chapter 4. Measurements were taken for dilute suspensions of each sample (0.1 mg/ml) over a pH range, while the background electrolyte (sodium chloride, NaCl) was maintained at 0.01 M. Hydrochloric acid, HCl, or sodium hydroxide, NaOH, were used to alter the pH. Samples were loaded into disposable zeta cells and for each sample, three measurements were obtained using a Malvern Zetasizer Nano ZS, and standard deviations calculated. Data were analysed using Malvern Zetasizer software.

Chapter 3

Hydroxyapatite

3.1 Introduction

Prior to this project, hydroxyapatite had been established as a material of interest in the Nottingham group and some preliminary experiments have been described previously (Li, 2008). As a result, one of the objectives of this work has been to continue the synthesis of hydroxyapatite using the Nozzle reactor, to explore the experimental parameters governing formation, and to test material properties for biomedical application.

3.1.1 Hydroxyapatite (HA), $\text{Ca}_{10}(\text{PO}_4)_6(\text{OH})_2$

Apatites are a group of phosphate minerals which are widely found in nature. These are isomorphous compounds which exhibit the same hexagonal dipyramidal crystal structure. HA has unit cell dimensions of $a = 9.432 \text{ \AA}$ and $c = 6.881 \text{ \AA}$ (Posner et al., 1958) (See Chapter 2 for general details on crystal structure and how it is analysed). The OH^- ion of HA can undergo substitution with carbonate (CO_3^{2-}), fluoride (F^-) or chloride (Cl^-) ions to give carbonate-apatite, fluorapatite and chloroapatite respectively. In addition, the molar ratio of calcium to phosphorus can vary from the stoichiometric ratio of $\text{Ca/P} = 1.67$; as such, calcium-deficient HA exists. These isomorphs display different properties to HA. For example, fluorapatite is chemically more stable than HA (Montazeri et al., 2011). Such property changes can be exploited to tailor apatite

materials suitable for specific applications. Hydroxyapatite, and chemically similar forms of HA, make up the inorganic component of teeth and bones in mammals. For this reason, HA has been widely utilised in the biomedical industry for many decades. This is described in more detail in Section 3.1.2.

3.1.2 Current applications using HA

The biocompatible and bioactive nature of HA, namely that it can interact with living tissue without being rejected or causing infection, makes it a very desirable material for biomedical applications. It is already widely used in dentistry (Whitters et al., 1999), plastic surgery (Gladstone et al., 1995) and orthopaedics (Block and Thorn, 2000). In this Section, applications of HA in tissue engineering will be discussed further.

3.1.2.1 Bone Scaffolds

Ideally, bone scaffolds should be temporary structures which are implanted onto or into damaged bone, gaps caused by trauma or infection, or where fusion of joints is needed. Once implanted, the scaffold should facilitate the formation of new bone by being either osteoinductive (recruiting and stimulating immature cells to become young bone cells, or preosteoblasts) or osteoconductive (allowing the formation of new osteoblasts - cells that regulate bone tissue synthesis on the surface of or within the structure of a bone scaffold or graft). The scaffold will eventually decompose once the bone has healed. Both osteoinduction and osteoconduction are vital for the bone healing process; however, subsequent to many bone fracture incidents, much of the bone healing procedure is reliant on osteoinduction (Albrektsson et al., 2001). In craniofacial implantology, high rates of osseointegration have also been reported (Gladstone

et al., 1995), where direct bone-to-implant contact is achieved to provide the implant with a firm basis, and have led to efficient bone healing.

Through introducing or increasing porosity of HA scaffolds, an improvement in its osteoconductive properties has been demonstrated (Mastrogiacomo et al., 2006). Upon implantation, osteoblasts are able to weave into and through the HA scaffold, promoting new cell, blood vessel and bone matrix development. Nevertheless, the disadvantage of these scaffolds is the brittle nature of HA. The porosity has a further detrimental effect on the mechanical strength of the scaffold. As a result, it is not possible to use these bone grafts alone in a position where load bearing is required. In these cases, HA is applied as a coating instead.

3.1.2.2 Coating on Prosthetics

Many materials used for prosthetic implants such as titanium, titanium alloys, copper, and bone cements are exploited for their capability of load bearing duties. They are however, limited by their low biocompatibility. In turn, they demonstrate little or no osteoconduction. To solve this problem, implants are coated with HA to increase biocompatibility and in some cases, osseointegration. Implants are principally coated with HA by the plasma spray process. Here, HA powder is heated in a plasma jet until molten and then propelled towards the substrate. As it solidifies, the HA hardens onto the implant material (Zhou and Lee, 2011).

3.1.2.3 Other Applications

Hierarchical microspheres of HA have been used as drug delivery vehicles, namely in the slow release of ibuprofen (Yang et al., 2012b), while HA

has also been used for protein purification (Orlovskii et al., 2002), separation of biomolecules (Bio-Rad, 2013) and as a component of dietary supplements (Shen et al., 2007).

3.1.3 Potential Applications for HA

Researchers have recently been focussing their studies on HA with other materials incorporated into the structure, such as cations (Kalita and Bhatt, 2007, Oh et al., 2004, Webster et al., 2004), or drugs (Leprêtre et al., 2009) – these studies report on the synthesis and characterisation of such materials.

The doping of different cations into the HA structure has been found to improve upon the existing biocompatible and osteoconductive nature of HA, after all natural apatite tends to contain a range of cations other than calcium (Webster et al., 2004). For example using silver as a dopant can induce antimicrobial activity (Oh et al., 2004, Stanic et al., 2011), while magnesium-doped HA has been shown to display improved cell adhesion (Mroz et al., 2010), and HA doped with zinc was shown to be biocompatible after in vivo tests (Saraswathi Amma et al., 2008), as well as possessing antimicrobial activity (Stanić et al., 2010) and can be used for the controlled release of bone growth proteins (Azizian-Kalandaragh and Khodayari, 2010). In addition, drugs such as statins have been used to produce composite materials with HA in order to enhance osteogenic effects (Griffiths and Cartmell, 2007, Jadhav and Jain, 2006).

This research shows that although HA is a widely used material, and has been for several decades, it remains the focus for current research as there are still ways to manipulate the structure and further enhance its beneficial properties.

3.1.4 Current Methods of Producing HA

Due to its excellent properties and wide range of applications, several methods of generating HA have been reported, where products are of the nano- or micron- scale. A few of these techniques will be detailed in this Section, including some advantages and disadvantages of each.

3.1.4.1 Naturally Occurring

Many HA based ceramics and cements that are already commercially available for bone graft implants are derived from natural sources. For example, Endobon[®] and Pro-Osteon[®] are produced from bovine and coral HA respectively, and have a structure like that of human bone (Habraken et al., 2007). However, there are limitations in altering their mechanical strength and porosity, which in turn limits their applicability (e.g. as bone scaffolds). Moreover, naturally occurring HA is a limited resource.

3.1.4.2 Precipitation Method

Synthetic HA powders which are analogous to naturally occurring HA can be produced from a range of different precursors and using several different synthetic routes. A commonly used technique for manufacturing HA is the wet chemical method of precipitation. As described by Osaka's research group (Osaka et al., 1991), orthophosphoric acid solution was added to calcium hydroxide in a controlled, dropwise manner with stirring. This was conducted with various reaction temperatures between 0 and 100 °C with the pH monitored throughout. The study showed that higher reaction temperatures led to the formation of a more crystalline product, and processing at a pH lower than 9 led to the formation of calcium deficient HA.

Another study (Zhang and Lu, 2008) described the use of calcium nitrate tetrahydrate and diammonium hydrogen phosphate, $\text{Ca}(\text{NO}_3)_2 \cdot 4\text{H}_2\text{O}$ and $(\text{NH}_4)_2\text{HPO}_4$ respectively, which were mixed and kept at 85°C for 48 hours in the presence of urea, which underwent hydrolysis and then yielded calcium phosphate (CaP) crystals. The group found that the urea concentration dictated the type of CaP produced, either dicalcium phosphate or octacalcium phosphate. They went on to immerse these two CaPs in ammonium hydroxide solution (pH 12) at 60°C for 48 hours, and HA particles were obtained with nanobelt morphology. With this method, the reactants were continually stirred after the precursors were mixed, and left to age. This allowed the calcium to be slowly integrated into the apatite structure, thus aiding the material to reach the stoichiometric Ca/P ratio. This method yielded particles with a narrow size distribution; however, the lengthy time required for synthesis forms the major disadvantage of the precipitation method as both the described procedures took several days before HA powder could be obtained. In turn, this creates difficulty in producing material at commercial scale, problems with batch to batch reproducibility, and the implication of high cost.

3.1.4.3 Sol-Gel Method

This procedure essentially uses a solution ("sol"), which is left to gradually form a gel-like substance, containing a liquid and solid phase. The solvent is then removed by drying or centrifuging and decanting, to yield a powder.

Vijayalakshmi and Rajeswari (Vijayalakshmi and Rajeswari, 2006) reported the use of sol-gel method to produce microcrystalline HA. Here, they dissolved calcium acetate, $\text{Ca}(\text{C}_2\text{H}_3\text{O}_2)_2$, in water as the calcium source. To this they added

a triethyl phosphate solution, $(C_2H_5)_3PO_4$, dropwise until a calculated stoichiometric Ca/P ratio of 1.67 was achieved. After stirring at room temperature, the solution was left to age for 24 hours. This allowed gel formation which was then dried at 120 °C for 16 hours to give a powder product, which was then washed and dried again. It was found that the samples needed to be calcined at temperatures up to 700 °C before highly crystalline products could be obtained. The methodology is relatively simple but, again, this procedure is time-consuming, with limitations to scalability. Moreover, the calcination step can be energy intensive.

3.1.4.4 Microwave Synthesis Method

In recent years, various groups have used microwave radiation to produce different sizes and morphologies of hydroxyapatite powders, where the reported microwave power has ranged between 175 W and 900 W. For example, Kalita and Verma (Kalita and Verma, 2010) stirred calcium nitrate tetrahydrate with EDTA (ethylenediaminetetraacetic acid, which acts as a chelating reagent) and sodium phosphate dibasic, Na_2HPO_4 , for 240 minutes at room temperature. After the pH was adjusted to 9 using ammonium hydroxide, NH_4OH , the suspension was loaded into a 600 W domestic microwave oven with a customised reflux system, and heated on a cycle for 19 minutes. The product was reported as being highly crystalline HA with particles having a size distribution between 5-30 nm and a mixture of elliptical and rod morphologies. Unlike precipitation and sol-gel, microwave synthesis is less time-consuming, but the main disadvantages are the high equipment costs and problems associated with scaling up the technology.

3.1.4.5 Hydrothermal Synthesis of HA

Hydrothermal synthesis is a commonly used method for producing HA. A process using a Teflon-lined batch hydrothermal reactor has been described previously (Earl et al., 2006). In this study, calcium nitrate tetrahydrate and ammonium phosphate dibasic of stoichiometric ratios were dissolved into distilled water. The solution was placed in the reactor and oven heated to 200 °C for a range of time between 24 and 72 hours, then subsequently washed with distilled water by centrifuging and decanting several times. Where reaction time exceeded 24 hours, monetite (CaHPO_4), was found to be produced as well as HA.

Most reported hydrothermal methods of HA production, like the aforementioned, are batch processes, where pressure is a difficult parameter to monitor and alter. This is because most off-the-shelf batch vessels do not incorporate pressure transducers. Instead, these are typically custom-designed and manufactured; even then, the pressure inside the autoclave is autogeneous and dependent on the reaction temperature.

Conversely, the reaction temperature and pressure are arguably easier to control and monitor in continuous systems. The full benefits of continuous hydrothermal processing is outlined in Chapter 1; in brief, the ability to use this method for reliable synthesis has been dependent on a reactor geometry which allows homogeneous mixing without causing blockages in the system – the counter-current Nozzle reactor has been shown to demonstrate these qualities (Lester et al., 2006, Lester and Azzopardi, 2005)

There have been publications from a different research group using a continuous hydrothermal system to produce HA (Chaudhry et al., 2006). The reactor used in this study is described in Chapter 1, Section 1.7.1.3. In their report, the

researchers used water in one flow which was pressurised and heated to supercritical conditions. In the reactor, it was met by a cold aqueous flow of NH_4HPO_4 and $\text{Ca}(\text{NO}_3)_2$, leading to the production of HA nanorods with diameters measuring 40 nm and lengths up to 140 nm.

Following this publication by Chaudhry et al., our research group at Nottingham chose to experiment with the synthesis methodology, altering various process parameters. It was found that, rather than having water in the downflow and two metal salts in the upflow, the aqueous NH_4HPO_4 could be pumped into the heater and be used as the superheated downflow. This precursor solution remains stable at high temperatures (i.e. the precursor does not precipitate out of solution), and does not cause blockages in the heater. Moreover, HA synthesis was successful at sub-critical conditions, with the heater temperature at 200 °C, instead of supercritical conditions of 400 °C (Li, 2008). These optimisation measures meant the need for an extra pump was eliminated, and a more energy-efficient synthesis temperature could be adopted. These preliminary experiments also found that the synthesis parameters could be tuned to produce three different morphologies of HA – sheets, rods and tubes (Li, 2008).

3.1.5 Chapter Aims

Subsequent to the results obtained by other researchers in the group (Li, 2008), this current work set out to explore the effect of each experimental parameter on the morphology and crystallinity of the resulting product, in order to shed light on the formation mechanism of the different morphologies. As mentioned previously in Section 3.1.3, the incorporation of cations and drugs into HA is desirable. Because the continuous hydrothermal method employed in this project is a “bottom-up” approach, the work reported in this Chapter aimed to demonstrate the synthesis of HA composites (containing drugs or dopants),

and to assess the effect these nanomaterials have on mouse embryonic stem cells (Lester et al., 2013).

3.2 Methodology

3.2.1 Synthesis of HA

The fundamental experimental conditions for the synthesis of hydroxyapatite were taken from Section 4.7.2 of Li's Thesis (Li, 2008). The production of HA sheets or platelets was described, and so the protocol was replicated and is reported in Section 3.2.1.1.

The precursors used were ammonium phosphate dibasic, $(\text{NH}_4)_2\text{HPO}_4$ ($\geq 98\%$ purity, Sigma Aldrich, UK); calcium nitrate tetrahydrate, $\text{Ca}(\text{NO}_3)_2 \cdot 4\text{H}_2\text{O}$ ($\geq 99\%$ purity, Sigma Aldrich, UK); ammonium hydroxide, NH_4OH (35%, Fisher Scientific, UK); sodium hydroxide, NaOH ($\geq 97\%$, Sigma Aldrich, UK); zinc nitrate hexahydrate, $\text{Zn}(\text{NO}_3)_2 \cdot 6\text{H}_2\text{O}$ (98%, Sigma Aldrich, UK); simvastatin, $\text{C}_{25}\text{H}_{38}\text{O}_5$ ($\geq 97\%$, Sigma Aldrich, UK) and deionised (DI) water. All reagents were used without further purification.

3.2.1.1 Synthesis of HA Platelets

An aqueous solution containing 0.015 M $(\text{NH}_4)_2\text{HPO}_4$ was pumped at a rate of 20 ml/min through a preheater, and into the counter-current Nozzle reactor as a downflow. Simultaneously, aqueous $\text{Ca}(\text{NO}_3)_2 \cdot 4\text{H}_2\text{O}$ at a concentration of 0.05 M was used as the upflow and pumped at a rate of 10 ml/min to meet the downflow. The temperatures at different points in the system are outlined in Table 3.1, where the thermocouple positions were stated in Chapter 1, Section 1.7.2.1. The system pressure was maintained at 240 bar by the BPR. Images demonstrating the experimental setup are shown in Figure

3.1 while Table 3.1 shows the measured temperatures at different points within the system during HA synthesis.

The product appeared as a white aqueous mixture, where the white particles settled over time. This sample will be referred to as HA-1.

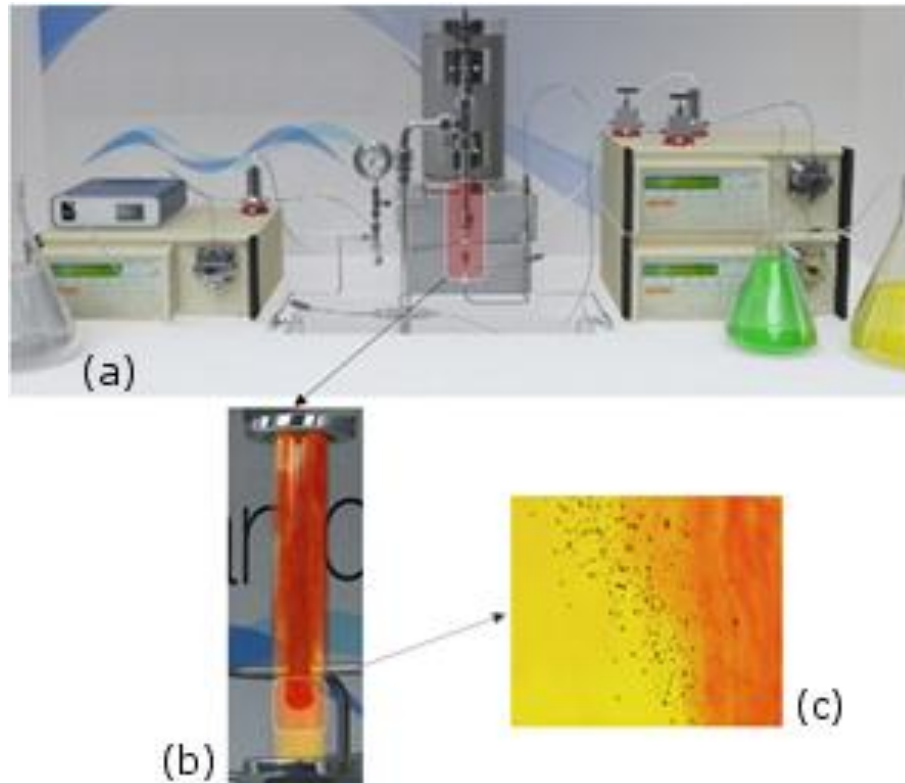


Figure 3.1 Images illustrating the continuous hydrothermal reactor system. The reactor section is highlighted in (b), showing the superheated aqueous $(\text{NH}_4)_2\text{HPO}_4$ (red) solution mixing with the ambient $\text{Ca}(\text{NO}_3)_2 \cdot 4\text{H}_2\text{O}$ (yellow) to form particles at the interface (c).

Table 3.1. Reactor system temperatures for synthesis of HA-1

| Water Heater Set Point (°C) | After Heater (°C) | Post Mixing Point (°C) | Capping Point (°C) | Post Cooler (°C) |
|-----------------------------|-------------------|------------------------|--------------------|------------------|
| 220 | 215 | 116 | 52 | 23 |

Other experiments conducted for the synthesis of HA were based on the above protocol, with slight deviations. With this reactor system and the experimental setup, several different parameters can be changed – including precursor type, precursor concentration and ratios, precursor pH, flow rates and ratios, temperature, pressure, reaction solvent, and the addition of dopants or capping agents. To investigate the effect each of these parameters has on the product (be it particle size, morphology, crystallinity, stability and/or functional properties) would lead to a massive matrix of experiments and would be too time consuming for the scope of this work. Thus, a limited set of parameters have been selected for experimental investigation, based on previous work in the group. These being precursor concentration and ratios, precursor pH, temperature, and the addition of dopants and are described in Sections 3.2.1.2 to Section 3.2.1.5.

3.2.1.2 Investigating the Effect of Precursor pH

Synthesis of HA with rod morphology was described previously by Dr Li. This involved the same reaction conditions as mentioned in Section 3.1.6.1., but with one difference – the pH of the downflow $(\text{NH}_4)_2\text{HPO}_4$ solution was increased to 10 (compared to an as-prepared pH of 8). This was achieved by the dropwise addition of NH_4OH , whilst being monitored by a pH meter (Hanna Instruments). All other reaction parameters remained unchanged. By eye, the product in this scenario looked the same as sample HA-1 – with the white particles settling over time. This sample shall be referred to as HA-2.

To determine if morphology changes are solely caused by pH alterations to the downflow solution, or if the same product is yielded from upflow precursor changes, a sample was produced using as-prepared $(\text{NH}_4)_2\text{HPO}_4$ in the downflow

(at pH 8), and $\text{Ca}(\text{NO}_3)_2 \cdot 4\text{H}_2\text{O}$ with pH increased to 10 (compared to its unaltered pH of 5), using NH_4OH . The product was labelled as HA-3.

To establish whether rod formation is base-specific (i.e. if rods are only formed when NH_4OH is used as a pH buffer), or more generally pH-specific (i.e. if any base can be used to alter the pH of the downflow and still result in this morphology being produced), experiments were conducted using NaOH as a buffer to increase downflow solution pH. To do this, a 1 M solution of NaOH was prepared using solid pellets (4g NaOH in 100 ml deionised water) and added dropwise to the $(\text{NH}_4)_2\text{HPO}_4$ solution whilst the pH was constantly being monitored.

The precursors were pumped into the system at the flow rates stated in Section 3.1.6.1, with the preheater set point ranging between 200 and 450 °C, at 50 °C increments, giving rise to samples HA-4a, 4b, 4c, 4d, 4e and 4f. Table 3.2 presents the thermocouple measured temperatures at the points in the system. A summary of experimental parameters for each sample is given in Table 3.3.

Table 3.2. System temperatures during synthesis of HA-4 sample

| Sample | Water Heater Set Point (°C) | After Heater (°C) | Post Mixing Point (°C) | Capping Point (°C) | Post Cooler (°C) |
|---------------|--|----------------------------------|---------------------------------------|-------------------------------|---------------------------------|
| HA-4a | 215 | 210 | 115 | 51 | 21 |
| HA-4b | 265 | 261 | 179 | 106 | 28 |
| HA-4c | 315 | 314 | 218 | 124 | 30 |
| HA-4d | 365 | 365 | 266 | 144 | 31 |
| HA-4e | 410 | 405 | 362 | 178 | 35 |
| HA-4f | 455 | 453 | 378 | 202 | 35 |

Following on from the work previously conducted in the group, experiments were performed using the precursors and flow rates as described for synthesis of HA-2 (i.e. downflow solution had been adjusted to pH 10 with NH_4OH), but using a higher preheater temperature of 350 °C, to give sample HA-5. This temperature was chosen because it was established that using reaction temperatures near the supercritical point of water yielded novel and interesting morphologies – specifically nanotubes (Li, 2008). Nevertheless, little work had been done to explore the factors governing the formation of this morphology, and so this work aims to test the reproducibility of those findings, and to elucidate the formation mechanism.

To investigate if these tube structures are reliant on pH alterations in a specific precursor feed, the upflow ($\text{Ca}(\text{NO}_3)_2 \cdot 4\text{H}_2\text{O}$) had NH_4OH added to it until a pH of 10 was reached. The experimental temperature was held at 350 °C, consistent

with experiment HA-5 where tube structures were produced. This yielded sample HA-6.

With the goal of identifying how morphology is affected when the pH of both precursors are as-prepared (as for HA-1) but reaction temperature is increased to 350 °C (as for tube synthesis), the sample HA-7 was produced. Table 3.3 gives a summary of experimental parameters used for the synthesis of samples.

3.2.1.3 Investigating the Effect of Precursor Concentration

There are several questions surrounding the effect of precursor concentration on the manufactured product:

1. What are the limits of reaction conversion?
2. Will HA remain the principle species produced when concentrations are increased?
3. How will particle size be affected, as the dynamic of particle nucleation versus particle growth changes?
4. In terms of reactor design, what are the limitations of the reactor system?

The latter point exists because the reactor system is composed of several constricted pipes and a BPR, all of which can become blocked if there are simply too many particles which are coagulating. To address these questions, a range of experiments were conducted where precursor concentrations were changed from those specified in Section 3.2.1.1.

In the first experiment, the stoichiometric ratio of Ca:P was retained at 1.67, but reactant concentrations were doubled from the protocol described for HA-1;

namely 0.03 M $(\text{NH}_4)_2\text{HPO}_4$ and 0.1 M $\text{Ca}(\text{NO}_3)_2 \cdot 4\text{H}_2\text{O}$ solutions were used. Here, all other parameters were unchanged – giving rise to sample HA-8.

Similarly for the second experiment, reactant concentrations were increased five-fold from the protocol for HA-1, using 0.075 M $(\text{NH}_4)_2\text{HPO}_4$ and 0.25 M $\text{Ca}(\text{NO}_3)_2 \cdot 4\text{H}_2\text{O}$ solutions. This resulted in the synthesis of sample HA-9.

Subsequent to this, a question exists: what morphological effect is observed if the pH of the downflow was increased to 10 at these increased concentrations? To solve this, the precursor concentrations described for HA-9 were used, while the downflow pH was adjusted to 10 using NH_4OH - yielding sample HA-10. This leads to another question – what happens to product morphology if, at these increased concentrations, the downflow pH is adjust using NH_4OH *and* the system temperature is increased to 350 °C? These parameters were hence employed in the synthesis of sample HA-11.

Finally, to address a change in ratios of precursor concentrations, the Ca:P ratio was changed from the stoichiometric to 2. This ratio was chosen, not only because it is a simple ratio, but with a secondary motive of producing tetracalcium phosphate (TTCP). With a formula of $\text{Ca}_4(\text{PO}_4)_2\text{O}$, TTCP has been shown to improve resorption of bone scaffolds and cements (the process whereby a scaffold is broken down by osteoclasts to release minerals for the formation of new bone), making it more beneficial to the patient in the long term (Moseke and Gbureck, 2010).

For this experiment, reactant solutions were prepared as 0.0125 M $(\text{NH}_4)_2\text{HPO}_4$ in the downflow, and 0.05 M $\text{Ca}(\text{NO}_3)_2 \cdot 4\text{H}_2\text{O}$ in the upflow. Precursor pH, flow rates, system temperatures and pressure were maintained as for HA-1. The yielded sample was called HA-12.

The HA samples described in this Section, and their corresponding reaction conditions, are summarised in Table 3.3. All samples were white in colour and the particles settled over time. SEM and XRD analysis was conducted for each sample.

3.2.1.4 Incorporation of Simvastatin into HA

As described in Section 3.1.4.5, an aim of this sub-project is to produce HA nanocomposites containing drugs or cations which will enhance its properties.

Also stated previously in Section 3.1.4.5, statins are a group of drugs which, although primarily used to tackle high blood pressure, have been shown to exhibit secondary osteogenic effects. In the literature, simvastatin is described as an example of such a statin (Griffiths and Cartmell, 2007). For this reason, and because a supply of this drug can be readily obtained commercially, simvastatin was chosen as a drug candidate for incorporation into HA. It is important to note that the chemical structure of simvastatin (depicted in Figure 3.2.) can degrade under high temperature or high pH (Park, 2009) – therefore, it will be used in the manufacture of HA platelets (HA-1), rather than other morphologies.

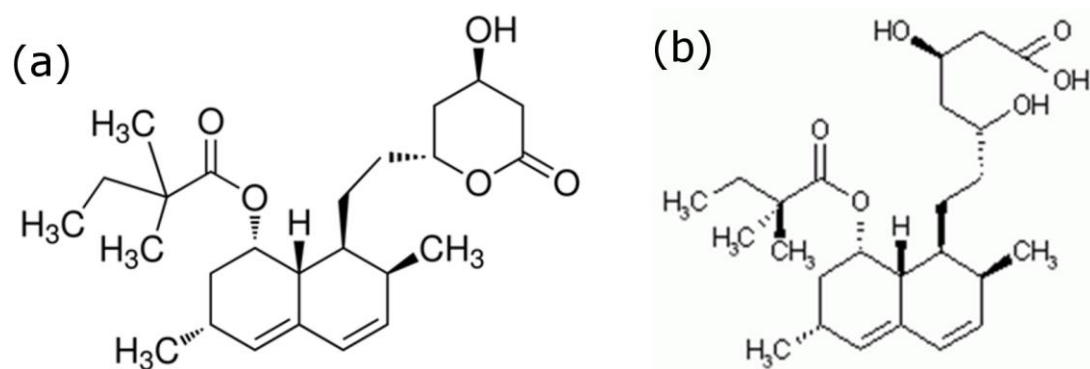


Figure 3.2. Chemical structure of (a) Simvastatin in its inactive lactone form, and (b) Simvastatin in its active hydroxyl acid form.

The simvastatin was activated using the procedure and concentrations described by Griffiths and Cartmell (2007), transforming it from its inactive lactone form (Figure 3.2. (a)) to its active hydroxyl acid form (Figure 3.2. (b)). Following this, a 5 μM solution of the statin was added to a prepared solution of $\text{Ca}(\text{NO}_3)_2 \cdot 4\text{H}_2\text{O}$ and the experiment was conducted as described for sample HA-1 in Section 3.2.1.1. The sample was called HA-SIM.

3.2.1.5 Incorporation of Zinc into HA

Of the potential cations to be used as a dopant, zinc was chosen due to its availability, its low cost and because it has previously been reported as a dopant into HA by other research groups (Webster et al., 2004, De Lima et al., 2010, Stanić et al., 2010). For this synthesis, a 0.05 M $\text{Ca}(\text{NO}_3)_2 \cdot 4\text{H}_2\text{O}$ solution containing 0.0046 mol $\text{Zn}(\text{NO}_3)_2 \cdot 6\text{H}_2\text{O}$ (equivalent to 15 %/w% Zn) was prepared and the experiment carried out as described for HA-1 in Section 3.2.1.1. The sample will be referred to as HA-Zn.

All the aforementioned samples were white products, where particles flocculated and settled to the bottom of the vessel. By eye, all the products looked the same. A summary of the reaction conditions for each sample is shown in Table 3.3.

Table 3.3. A summary of experimental details for synthesis of various HA samples.

| Sample | (NH ₄) ₂ HPO ₄ Concentration | (NH ₄) ₂ HPO ₄ pH | Ca(NO ₃) ₂ ·4H ₂ O Concentration | Ca(NO ₃) ₂ ·4H ₂ O pH | Reagent for pH alteration | Reaction Temp. (° C) | Particle Morphology | Approximate Particle Size |
|--------|---|--|---|--|------------------------------|--------------------------|--------------------------|---|
| HA-1 | 0.015 M | 8 | 0.05 M | 5 | - | 200 | Sheet | <2 μm width <80 nm thick |
| HA-2 | 0.015 M | 10 | 0.05 M | 5 | NH ₄ OH | 200 | Rod | Diameter: 30–40 nm |
| HA-3 | 0.015 M | 8 | 0.05 M | 10 | NH ₄ OH | 200 | Sheet/rod | Diameter: ~80 nm |
| HA-4a | 0.015 M | 10 | 0.05 M | 5 | NaOH | 200 | Rod | Diameter: 20 nm |
| HA-4b | 0.015 M | 10 | 0.05 M | 5 | NaOH | 250 | Rod | Diameter: 20–70 nm |
| HA-4c | 0.015 M | 10 | 0.05 M | 5 | NaOH | 300 | Rod | Diameter: 25 - 140 nm |
| HA-4d | 0.015 M | 10 | 0.05 M | 5 | NaOH | 350 | Rod | Diameter: 30 - 120 nm |
| HA-4e | 0.015 M | 10 | 0.05 M | 5 | NaOH | 400 | Low aspect Ratio Rods | Diameter: <25 nm Length: < 110 nm |
| HA-4f | 0.015 M | 10 | 0.05 M | 5 | NaOH | 450 | Low aspect Ratio Rods | Diameter: <20 nm Length: <100 nm |
| HA-5 | 0.015 M | 10 | 0.05 M | 5 | NH ₄ OH | 350 | Tubes | Outer Diameter: <0.5 μm Inner Diameter: 30–70 nm |
| HA-6 | 0.015 M | 8 | 0.05 M | 10 | NH ₄ OH | 350 | Rod/tube | Outer diameter: 100–300 nm |

| | | | | | | | | |
|---------------------|----------|----|--------|---|--------------------|-----|-----------|--------------------------------------|
| HA-7 | 0.015 M | 8 | 0.05 M | 5 | - | 350 | Sheet/Rod | Diameter: 80–300 nm |
| HA-8 | 0.03 M | 8 | 0.1 M | 5 | - | 200 | Sheet | <2 μm width <100 nm thick |
| HA-9 | 0.075 M | 8 | 0.25 M | 5 | - | 200 | Sheet/rod | Diameter: <100 nm |
| HA-10 | 0.075 M | 10 | 0.25 M | 5 | NH ₄ OH | 200 | Sheet | <2 μm width <100 nm thick |
| HA-11 | 0.075 M | 10 | 0.25 M | 5 | NH ₄ OH | 350 | Sheet/rod | Diameter: 30-40 nm |
| HA-12 | 0.0125 M | 8 | 0.05 M | 5 | - | 200 | Sheet | <2 μm width <100 nm thick |
| HA-SIM ^a | 0.015 M | 8 | 0.05 M | 5 | - | 200 | Sheet | <2 μm width <100 nm thick |
| HA-Zn ^b | 0.015 M | 8 | 0.05 M | 5 | - | 200 | Sheet | <2 μm width <100 nm thick |

^a5 μmol of activated Simvastatin was added to the Ca(NO₃)₂·4H₂O solution prior to synthesis.

^b15 w/w% Zn(NO₃)₂·6H₂O was added to the Ca(NO₃)₂·4H₂O solution prior to synthesis.

3.2.2 Characterisation Methods

All samples were washed by centrifuging, decanting the supernatant and re-suspending in deionised water. They were subsequently freeze dried for further characterisation, namely SEM and XRD. Where required, HRTEM was also utilised. Particle size analysis was performed using Digital Micrograph™ software (from Gatan Inc., USA). To assess the presence of simvastatin in HA-SIM, ToF-SIMS was used.

3.2.3 Material Application Methods

An important part of the validation work for this new approach to nano-HA manufacture has been cell proliferation assays. This is to demonstrate that HA produced in this reactor system exhibits no cytotoxic effects on mouse embryonic stem cells (mESC). This cell type is regularly used for such cytotoxicity studies. Additionally, bone nodule assays were conducted to highlight that HA synthesised in this work can promote stem cell differentiation into an osteoblast lineage.

3.2.3.1 Cell Proliferation Assay

These assays were used to ascertain if HA produced in the continuous hydrothermal reactor system exhibit a cytotoxic effect, rather than determine cell response to every sample. Therefore, only nanoparticles from sample HA-1, HA-SIM and HA-Zn were used for this study. The samples were firstly sterilised by exposure to UV light. The mESC were maintained in either standard culture media or osteogenic culture media at 37°C, 5% CO₂ at 85% relative humidity. Standard culture media contained DMEM growth media, supplemented with 10% Fetal Bovine Serum (FBS), 1% Penicillin/Streptomycin 100x solution, 1% L-

Glutamine and 100 μ M 2-Mercaptoethanol. Osteogenic media contained standard culture media and additional supplements (0.284 mM L-ascorbic acid, 50 mM β -glycerophosphate) which guide stem cells towards differentiation into an osteoblast lineage.

A 96 well plate was seeded with mESCs (7000 cells/well) and exposed to nanoparticles at one of three different concentrations (1, 10 or 100 μ g/ml). A control sample was kept with no nanoparticles added. Cell proliferation was monitored after 1, 3 and 6 days of culture using a 96® AQueous One Solution Cell Proliferation Assay (Promega, USA). The assay principle is based on the MTS tetrazolium compound being bioreduced into a coloured formazan product that is soluble in culture media. This conversion is accomplished by NADPH or NADH produced by dehydrogenase enzymes in metabolic active cells.

3.2.3.2 Bone Nodule Assay

To study osteogenic differentiation and bone mineralisation, cells were cultured in 12 well plates (100,000 cells/well) for 21 days in the presence of nanoparticles at one of three concentrations (1, 10 and 100 μ g/ml), as well as a control. After this time, cells were fixed in 10% formal saline solution for 20 minutes followed by a histological staining with 1% Alizarin red solution for 5 minutes. The cells were washed three times with deionised water to reduce the background intensity. Clusters which appeared stained with a red-brown colour were indicative of mineralised nodules.

3.3 Results and Discussion

3.3.1 HA Platelets (HA-1) and Rods (HA-2)

The synthesis of HA-1 and HA-2 were primarily to act as confirmatory work on the previously described results within the group. Indeed platelet morphology was observed in HA-1, as shown from the SEM and TEM images in Figure 3.3. The particles have widths and lengths measuring up to 2 μm while the thickness of the platelets is <80 nm.

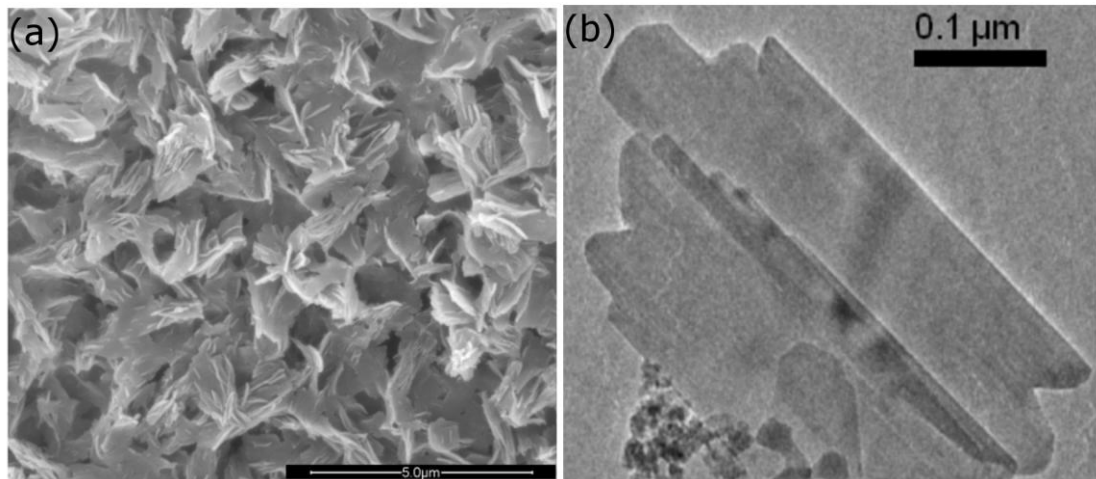


Figure 3.3. (a) SEM and (b) TEM images of particles in sample HA-1.

XRD analysis performed on this sample showed that the only crystalline phase present was hexagonal hydroxyapatite, matching to ICDD PDF 74-566 (Figure 3.10). While the peaks match to the expected pattern, they are not sharp; this may indicate that the material has low crystallinity, assuming the particle size is large (See Chapter 2, Section 2.4 for reasoning).

The SEM and TEM images in Figure 3.4 show the nanorod morphology identified in HA-2, again confirming the results previously seen in the group. These particles have diameters between 30 and 40 nm and lengths measuring up to 1 μm , and demonstrate that by merely altering the pH of one of the precursors, a different product morphology is observed. The XRD pattern for HA-2 is displayed in Figure 3.10 and also matches to the expected pattern for hexagonal HA. The peaks are sharper than those seen for HA-1, suggesting that the particles in HA-2 are more crystalline. These data show that as well as changing particle morphology, the pH (or indeed the addition of NH_4OH itself) is leading to the formation of a more crystalline product – a process which has been described before for HA synthesis. Several methods of HA synthesis use NH_4OH to increase the reaction pH above 9 in order to drive HA formation (Zhang et al., 2009a, Li et al., 2007). This is because acidic by-products are usually produced during HA synthesis; the acid can degrade the HA, and compromise the crystallinity. In this case, a by-product of the synthesis is nitric acid, HNO_3 , because of the use of $\text{Ca}(\text{NO}_3)_2$ as a precursor. Without any post-synthesis washing of HA-1, the HNO_3 is likely to decompose the HA. For HA-2 however, the addition of NH_4OH neutralises the acid formed, which may lead to higher crystallinity. It is important to note that it is apparent NH_4OH is also playing a role in the mechanism of synthesis, leading to this change in morphology.

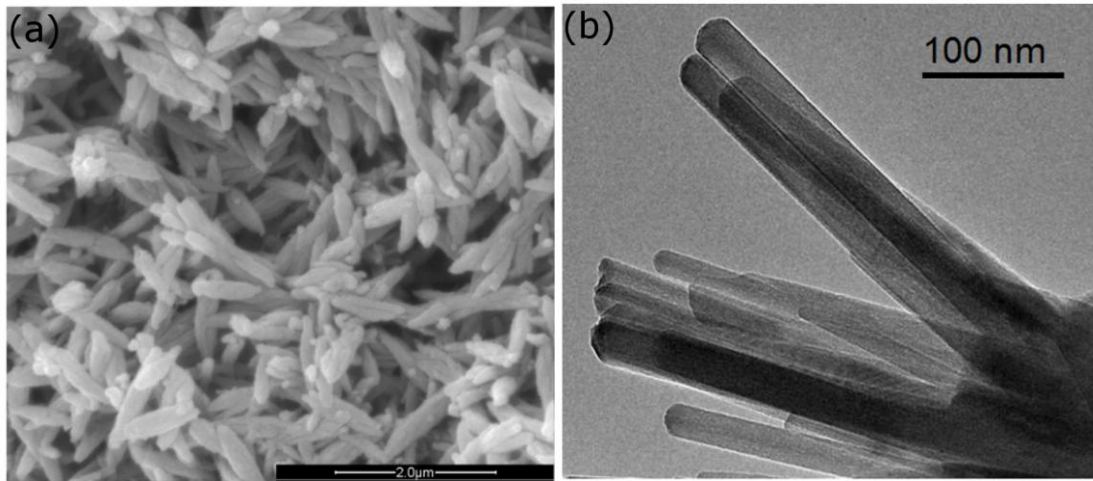


Figure 3.4. (a) SEM image and (b) TEM image of particles in HA-2.

3.3.2 The Effect of Precursor pH

It was found that the pH of either precursor solution can be increased to yield nanorods, not just the downflow $(\text{NH}_4)_2\text{HPO}_4$. Figure 3.5 shows that some rod shaped particles resulted when the $\text{Ca}(\text{NO}_3)_2$ precursor solution was adjusted to pH 10. However, there was still evidence of some platelet-type particles being produced, and the rods appear less well defined compared to those in sample HA-2. The rods in HA-3 were apparently larger than in HA-2 as well, with diameters in the region of 80 nm.

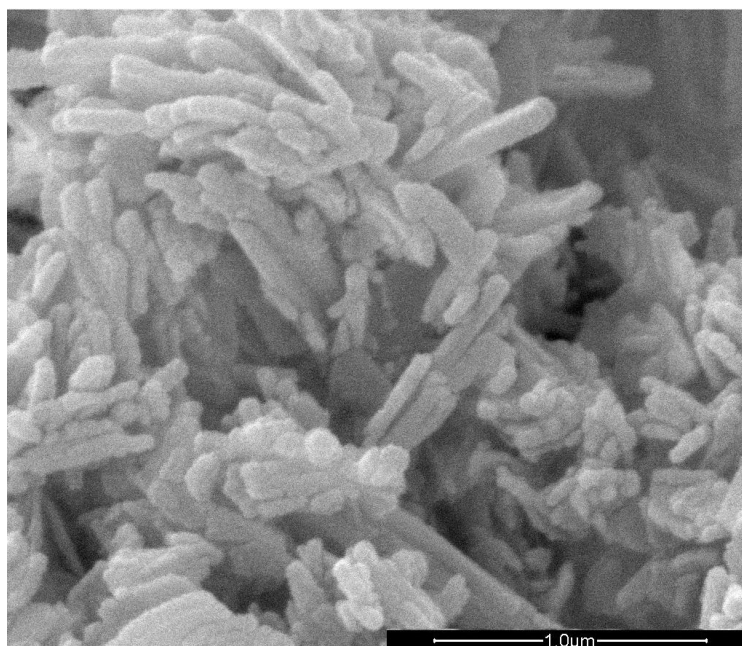


Figure 3.5. SEM image of HA-3.

Samples HA-4a to 4f were produced using NaOH as a pH buffer, as opposed to NH_4OH , over a range of reaction temperatures. This was to investigate if morphology changes were dependent on pH alone, or were base-specific. The TEM image in Figure 3.6 (a) shows the presence of rod shaped particles in HA-4a (reaction temperature ~ 200 °C); from this it can be inferred that rod morphology is a result of pH changes, but is not reliant on NH_4OH being used. Nevertheless, the size of the particles is not identical to those in HA-2. The rods in HA-4a have diameters measuring ~ 20 nm – smaller than those seen in HA-2. The XRD data for HA-4a (shown in Figure 3.10) confirms that HA is the only crystalline phase present, but the peaks are not as sharp compared to HA-2.

Samples HA-4b to 4f use the same precursors as HA-4a, but reflect increases in reaction temperature. The TEM images in Figure 3.6 indicate that reaction temperature does affect particle size and morphology. It can be observed that with increases in temperature up to 350 °C (HA-4b to 4d), the particle diameter

also increases; in HA-4b (reaction temperature ~ 250 °C) rod diameters measure between 20 and 80 nm, in HA-4c (reaction temperature ~ 300 °C) these are 25-140 nm, and in HA-4d (reaction temperature ~ 350 °C), these are 30-140 nm. In the latter two samples, some particles may even be classed as having platelet morphology rather than rod. It is possible that this trend is due to the increased thermal energy causing growth of the existing particles, rather than nucleation of new ones.

Interestingly at even higher reaction temperatures, as is the case with HA-4e (reaction temperature ~ 400 °C) and 4f (reaction temperature ~ 450 °C), the particles appear to be smaller than in the aforementioned samples, and the morphology can be described as low-aspect ratio rods. In HA-4e, the rods have diameters up to 25 nm and lengths up to 110 nm – aspect ratios between 3.69 and 6.22. In HA-4f, the diameters typically observed are no more than 20 nm, and lengths measure up to 100 nm – giving aspect ratios ca. 5.3. This is compared to the much higher aspect ratio rods seen in HA-4a (aspect ratio ca. 16.9), HA-4b (ca. 10.9), HA-4c (ca. 10.1), and HA-4d (ca. 9.1). This decrease in aspect ratio with increasing reaction temperature relates to the increase in particle diameters mentioned previously. XRD patterns were only obtained for samples HA-4a and HA-4d; these should be representative of the sample series, confirming that HA is the sole crystalline phase, rather than looking at specific changes to crystal structure between the samples. Moreover, HA-4d was chosen for XRD analysis as a comparison to sample HA-5 because a reaction temperature of 350 °C is common to both samples.

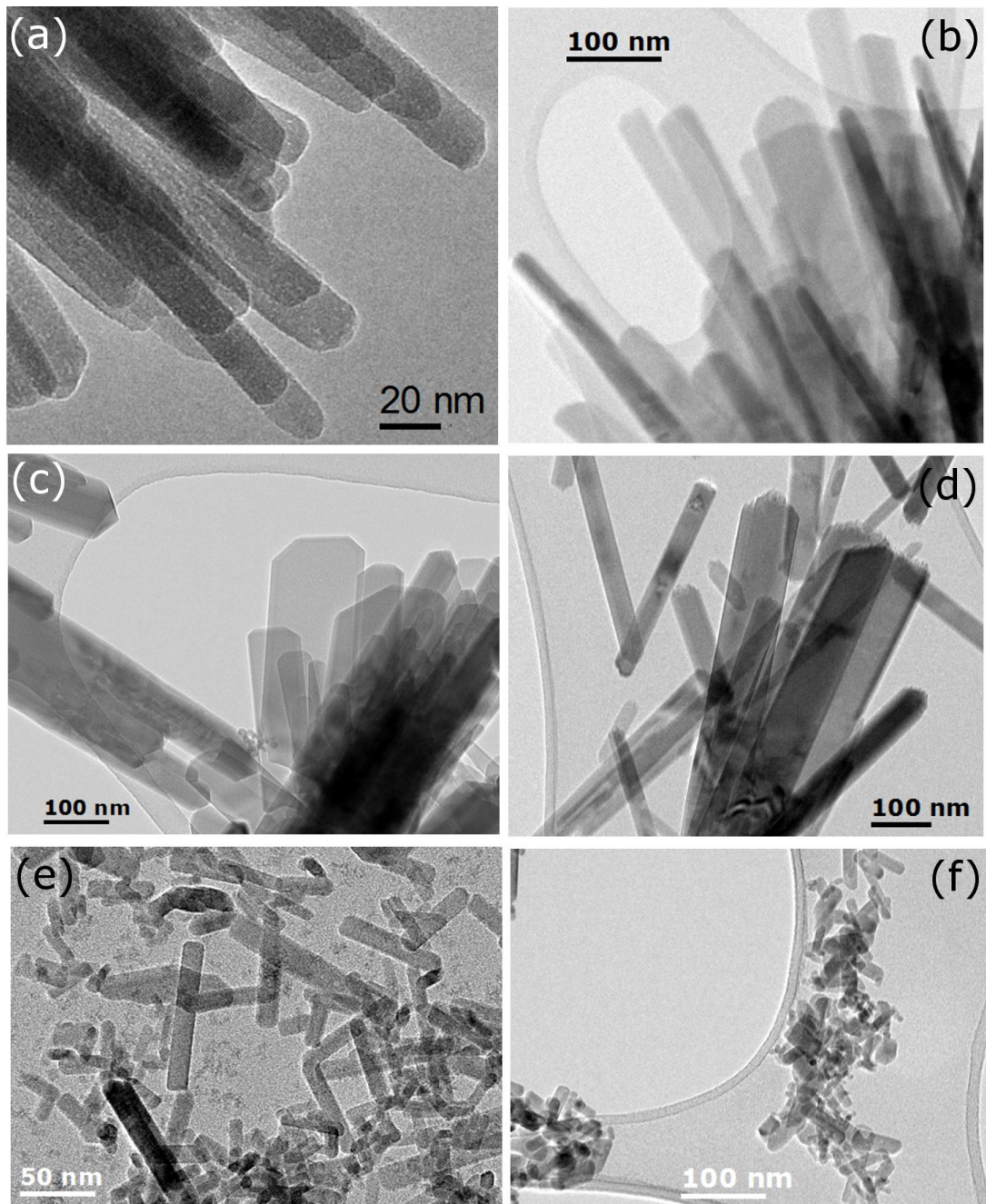


Figure 3.6. HRTEM images of (a) HA-4a; (b) HA-4b; (c) HA-4c; (d) HA-4d; (e) HA-4e; and (f) HA-4f.

HA-5 is a very interesting sample; collected SEM images (shown in Figure 3.7 (a)) firstly showed 'open-ended' rods. Using HRTEM, and darkfield imaging, these particles were shown to have a tube morphology (Figure 3.7 (b) and (c)). In these micrographs, the thicker walls are shown darker than the hollow centre

(or brighter in the case of darkfield imaging). This morphology has, to date, not been previously reported – making it a significant finding.

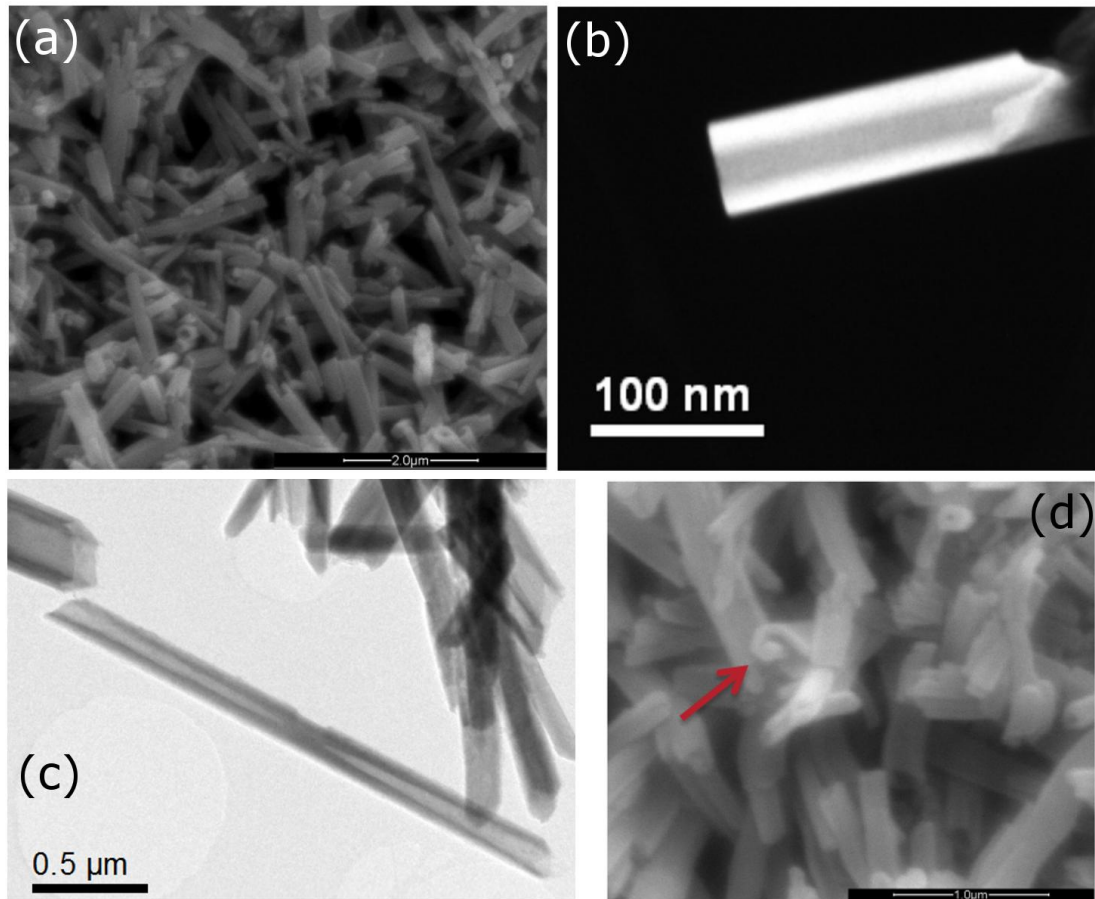


Figure 3.7. (a) SEM image of 'open-ended rods', (b) darkfield imaging in TEM and (c) TEM image show tube structures while (d) is an SEM image showing a tube in the middle of the rolling process (highlighted with a red arrow).

There are several potential applications for nanotubes of HA, which could result from the ability to fill the tubes with drugs or other nanomaterials. For example, these tubes could act as slow-release drug carriers in bone scaffolds or other drug delivery systems (Yang et al., 2012b, Netz et al., 2001). To begin this sort of research, it is important to understand the formation mechanism of these

particles. Examining the morphology; in Figure 3.7 (c), the tube looks darker in the centre, suggesting that it is not completely hollow. By considering that TEM essentially shows a projection of an image, it is entirely feasible that the tube has formed from the scrolling of a sheet (Figure 3.8), to yield the image in Figure 3.7 (c). To reinforce this notion, Figure 3.7 (d) is an SEM image apparently showing a particle in the middle of the scrolling process. The TEM images obtained for HA-5 showed these tubes to have an inner diameter or pore size between 30 and 70 nm, while the outer diameter ranged up to 0.5 μm . Therefore, by crude estimation, a sheet or platelet particle with a width of 600 nm would roll up with 3-4 layers to give a 50 nm pore. Some initial N_2 adsorption data was collected for HA-5, but proved inconclusive. This may be due to the scrolls opening up during the measurement as a result of changes to the surface charge (Lester et al., 2013).

As discussed previously, only rod structures, not tubes, are seen in HA-4d, when NaOH is used as a pH buffer, demonstrating that unlike rod formation, the synthesis of HA tubes is base-dependent.

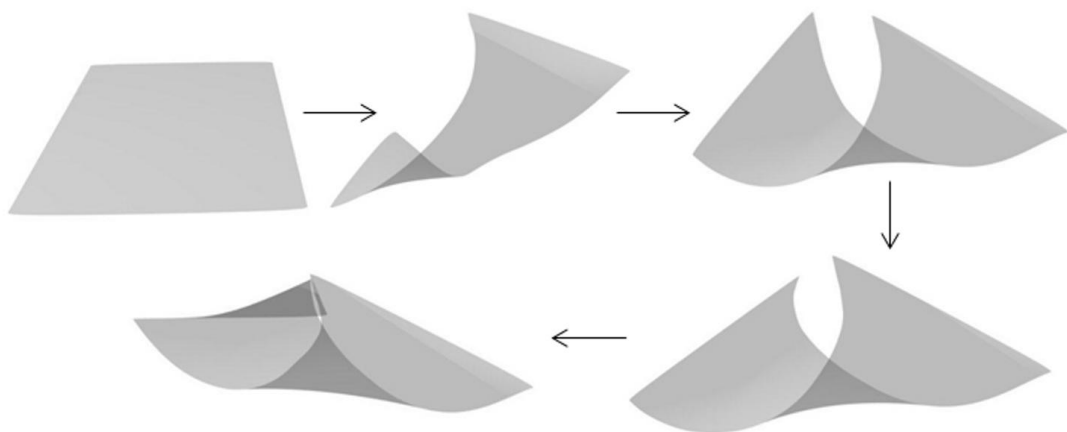


Figure 3.8. Images illustrating the scrolling of a sheet, so that the corners meet.

It was found that by adjusting the pH of the upflow precursor rather than the downflow, while keeping the reaction temperature at 350 °C (as is the case for HA-6), tube structures are again synthesised. The SEM image in Figure 3.9 (a) illustrates this. The inner and outer diameters of the particles are not significantly different from those seen in HA-5; however, the particles appear to be less well-formed with jagged edges apparent. As a result, it can be said that addition of NH_4OH to the downflow is more effective for the synthesis of tubes, than in the upflow.

Sample HA-7 was shown to contain a mixture of rods and high aspect ratio platelets, as displayed in Figure 3.9 (b). In this case, the precursors had not been treated with any pH alterations, and underwent a reaction temperature of 350 °C. The particles appear to have diameters between 80 and 300 nm, and variable lengths up to a few hundred nanometers. One possible reason for seeing these particles with higher aspect ratios is that the higher reaction temperature causes the fragmentation of sheet particles (evident from sample HA-1) into rods and smaller platelets. However, the XRD data in Figure 3.10 show that HA-7 produced more intense peaks than HA-1, indicating a higher level of crystallinity with increased reaction temperature. As such, it is more likely that the difference lies in the formation of particles, i.e. these rods and platelets are formed via a different mechanism, in which growth to larger sheets is inhibited, rather than fragmentation.

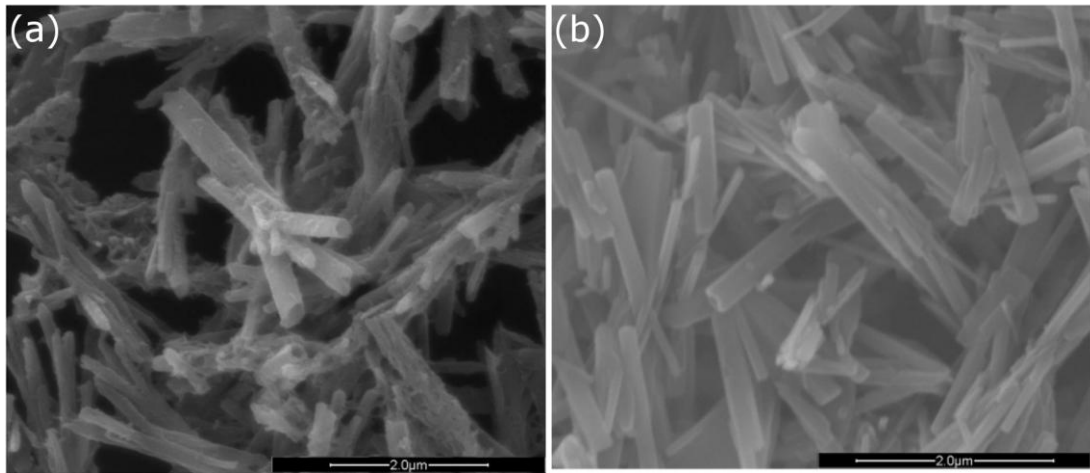


Figure 3.9. SEM images of (a) HA-6, and (b) HA-7.

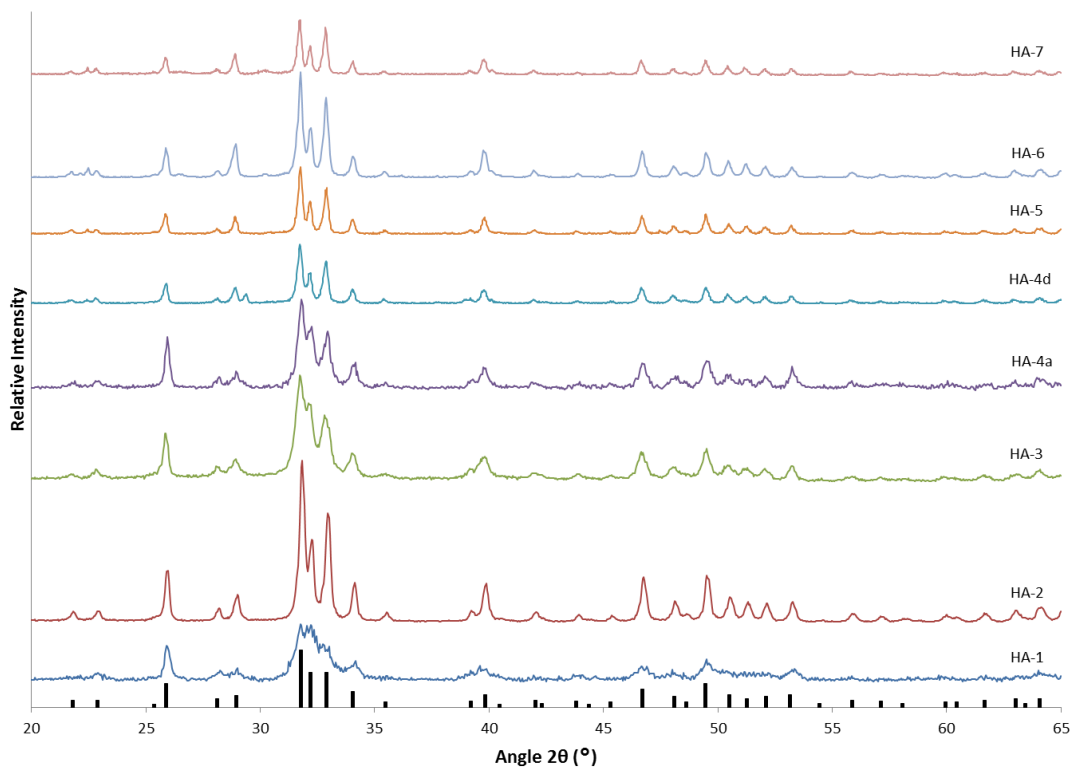


Figure 3.10. XRD patterns for samples HA-1 to HA-7. The expected peak pattern for hexagonal hydroxyapatite (ICCD PDF 74-566) is shown at the bottom.

3.3.3 The Effect of Precursor Concentration

Now focussing on the effects of modifying precursor concentration; sample HA-8 was the result of doubling precursor concentrations from those used for HA-1 (i.e. using 0.03 M $(\text{NH}_4)_2\text{HPO}_4$ and 0.1 M $\text{Ca}(\text{NO}_3)_2$). The principle test was to determine if HA remains the sole crystalline phase obtained. The XRD pattern shown in Figure 3.13 indicates that it is. Nevertheless, the pattern does not show sharp peaks, so it can be inferred that, like HA-1, the material is not very crystalline (if particle size is large). This corresponds with the reasons highlighted earlier in the discussion for HA-1. The obtained SEM images (seen in Figure 3.11 (a)) present particles with a very similar morphology and size as those in HA-1. Again, these sheets have lengths and widths up to 2 μm , and thickness of less than 100 nm.

However, it was found that when the precursor concentration is increased fivefold that of HA-1, HA is no longer the sole crystalline phase produced. The XRD pattern contains sharp peaks which correspond to monoclinic brushite, $\text{CaHPO}_4 \cdot 2\text{H}_2\text{O}$ (ICCD PDF 9-77) and some peaks which can be assigned to monetite, CaHPO_4 . These minerals are sometimes used as precursors for apatite formation (Monma and Kamiya, 1987) suggesting that these may be "intermediates" in the reaction pathway to HA formation during hydrothermal synthesis. The particles in this sample are a mixture of sheets and rods, the latter with diameters less than 100 nm. The morphology differences in this sample cannot be fairly compared to HA-1 and HA-2 because of the different phases that are present in the sample and it is difficult to distinguish between the two phases using SEM and TEM analysis.

Interestingly, it was found that by using five times the "standard" precursor concentration, increasing the downflow pH to 10 using NH_4OH , and a reaction

temperature of 200 °C (as is the case for HA-10), the sole crystalline phase is once again HA. As Figure 3.13 shows, peaks for brushite or monetite are no longer evident. Furthermore, the SEM image displayed in Figure 3.11 (c) shows the sheet like particles present in HA-10 which look very similar to the particles in HA-1. In addition, pumping these same precursors at a higher temperature of 350 °C (sample HA-11) produces rods and high aspect ratio platelets (Figure 3.11 (d)). It can be inferred from these results that NH_4OH is playing a wider role in the formation of these particles. This evidence indicates NH_4OH directs the reaction towards HA formation over other calcium phosphates; it increases the crystallinity of the product; and the particle morphology changes.

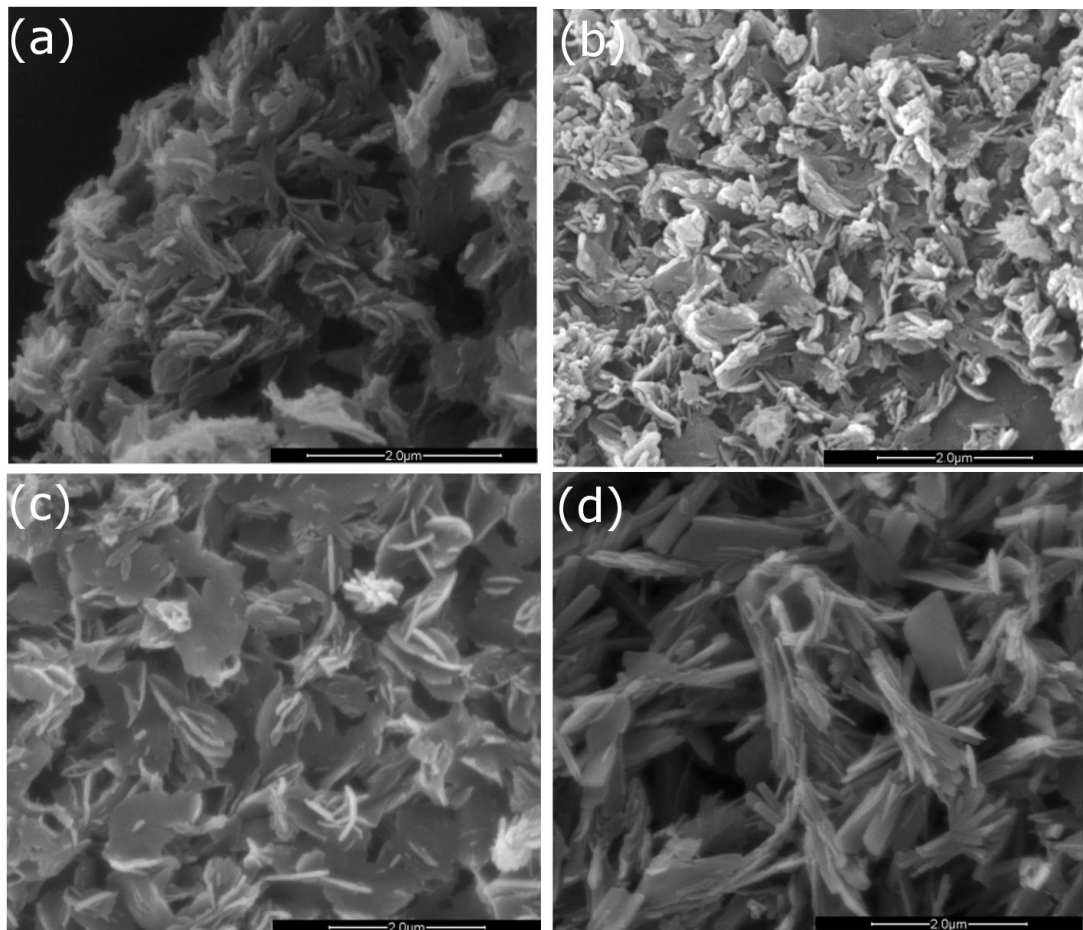


Figure 3.11. SEM images of (a) HA-8, (b) HA-9, (c) HA-10, (d) HA-11.

With the aim of synthesising TTCP, HA-12 was produced in which the precursor concentrations were altered from the stoichiometric ratio; instead, a Ca:P ratio of 2 was used. However, the XRD pattern collected for this sample (see Figure 3.13) showed that the only crystalline phase present was HA. Additionally, it was found that the particles were similar to those seen in HA-1, both in morphology and size (as seen from the SEM image in Figure 3.12). This data suggests that HA is preferentially produced in the Nozzle reactor, over other calcium phosphates, when precursor concentrations do not significantly deviate from the "standard". Furthermore, it shows that this method of HA synthesis is not sensitive to changes in the ratio of precursor concentrations, and the precise stoichiometric ratio does not need to be maintained to produce HA.

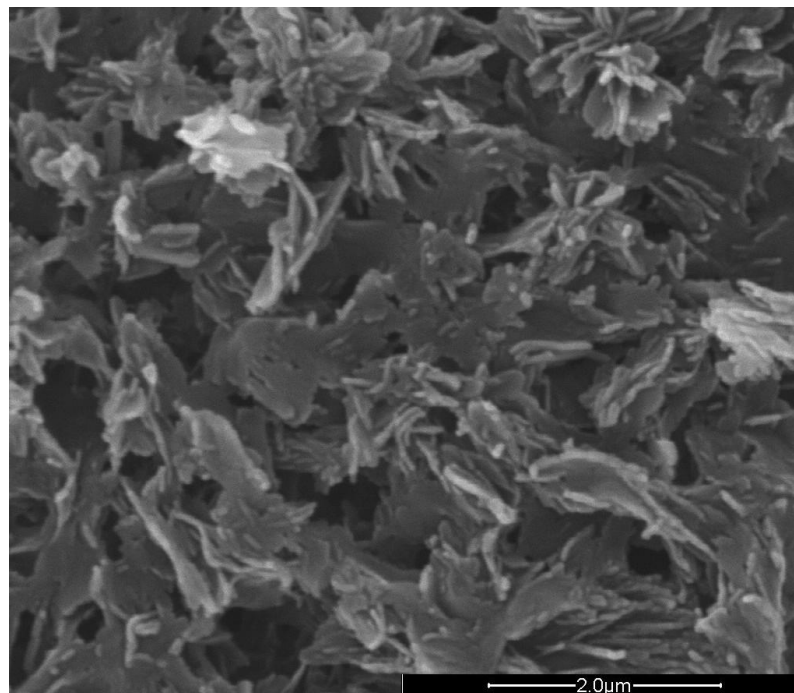


Figure 3.12. SEM image of HA-12.

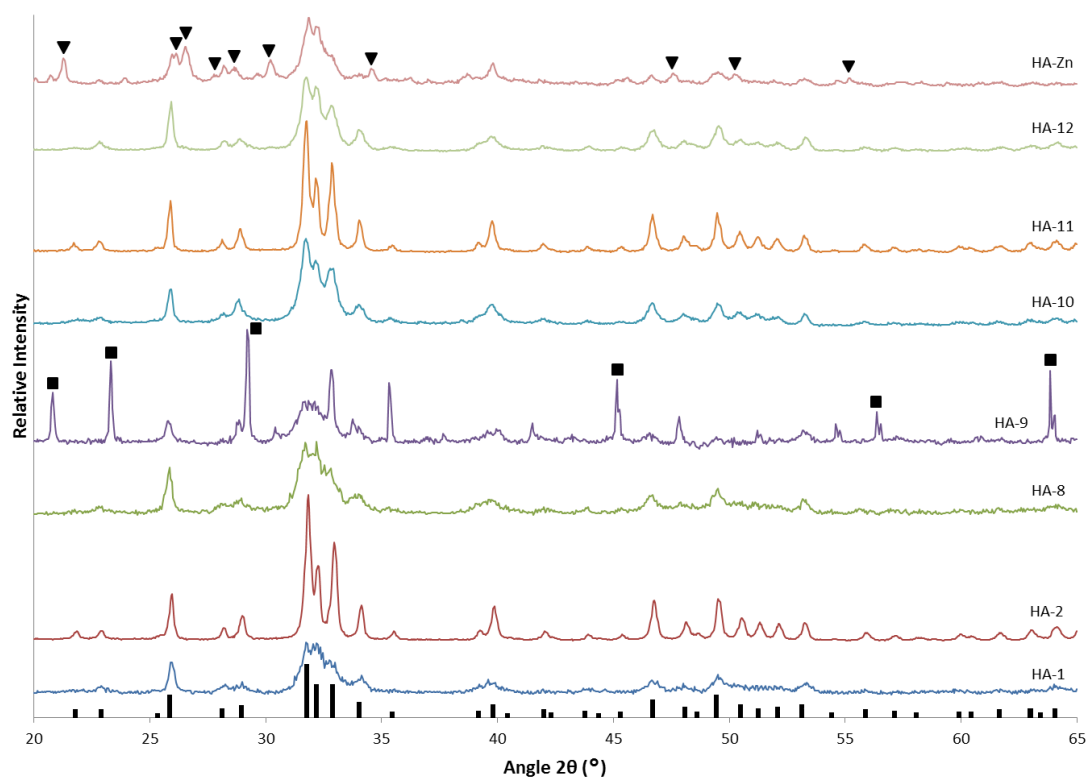


Figure 3.13. XRD patterns for HA-8 to HA-Zn. Patterns for HA-1 and HA-2 are also shown for comparison. The expected peak pattern for hexagonal hydroxyapatite (ICCD PDF 74-566) is shown at the bottom. For HA-9, peaks indicated with a black square match monoclinic brushite (ICCD PDF 9-77) while other peaks match monetite; for HA-Zn, peaks labelled with black triangles correspond to monoclinic parascholzite (ICCD PDF 35-495).

3.3.4 Addition of Simvastatin

The SEM and TEM images obtained for HA-SIM (Figure 3.14) showed particle size and morphology similar to HA-1. Given the very low concentration of simvastatin added to the sample, XRD analysis was not performed in HA-SIM to confirm the crystalline phase of the material. Instead, the aim here was to assess the presence of simvastatin in the sample. Initially, Fourier-Transform Infra-Red (FTIR) spectroscopy was performed on HA-SIM and HA-1 and the two

spectra were compared. However, there was no observed difference between the two, so it could not be concluded that the drug was present in HA-SIM. It is possible the concentration of the statin was too low in the sample, and below the sensitivity threshold of the FTIR spectrometer, meaning that if present, the drug would not be detected. As a result, the sample was also analysed using ToF-SIMS. The obtained data (Figure 3.15) showed that a fragment with a mass/charge value of 115.08 was present in HA-SIM, but not in HA-1 or HA-2. This fragment can be assigned to the molecule $C_6H_{12}O_2$, which forms part of simvastatin. However, this was the only difference observed in HA-SIM – which again, may be due to the low concentration of simvastatin used in the precursor. It should be noted that ToF-SIMS operates by bombarding the sample to create fragments which can then be detected; hence, it is difficult to ascertain from this data whether the simvastatin has been preserved during the synthesis reaction and is present as a whole molecule in the sample, or if the heat and pressure of the reaction has caused the breakdown of the drug and what is seen is actually a degraded portion of the statin. Ultimately, it is inconclusive whether simvastatin is wholly present in HA-SIM. An *in vitro* cell proliferation was also carried out using HA-SIM. The results will be discussed in Section 3.3.6.

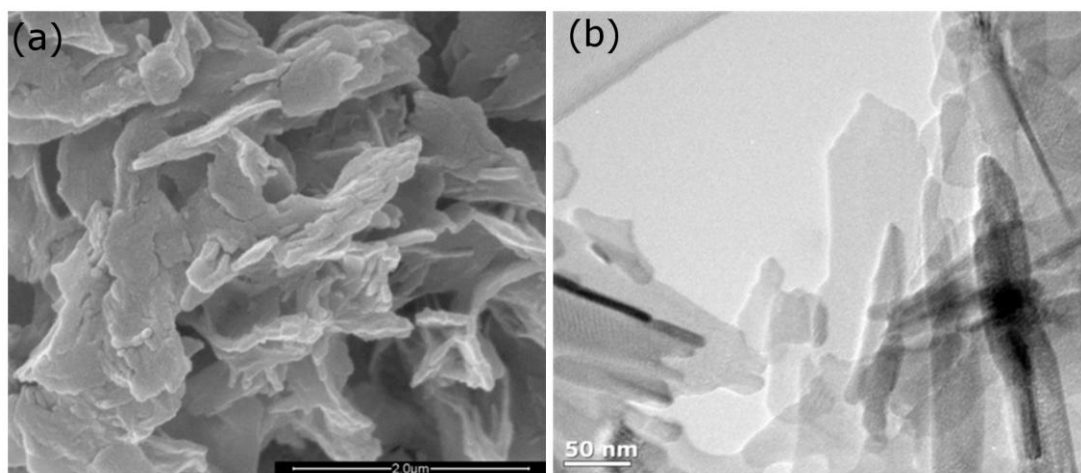


Figure 3.14. (a) SEM Image and (b) TEM image of HA-SIM.

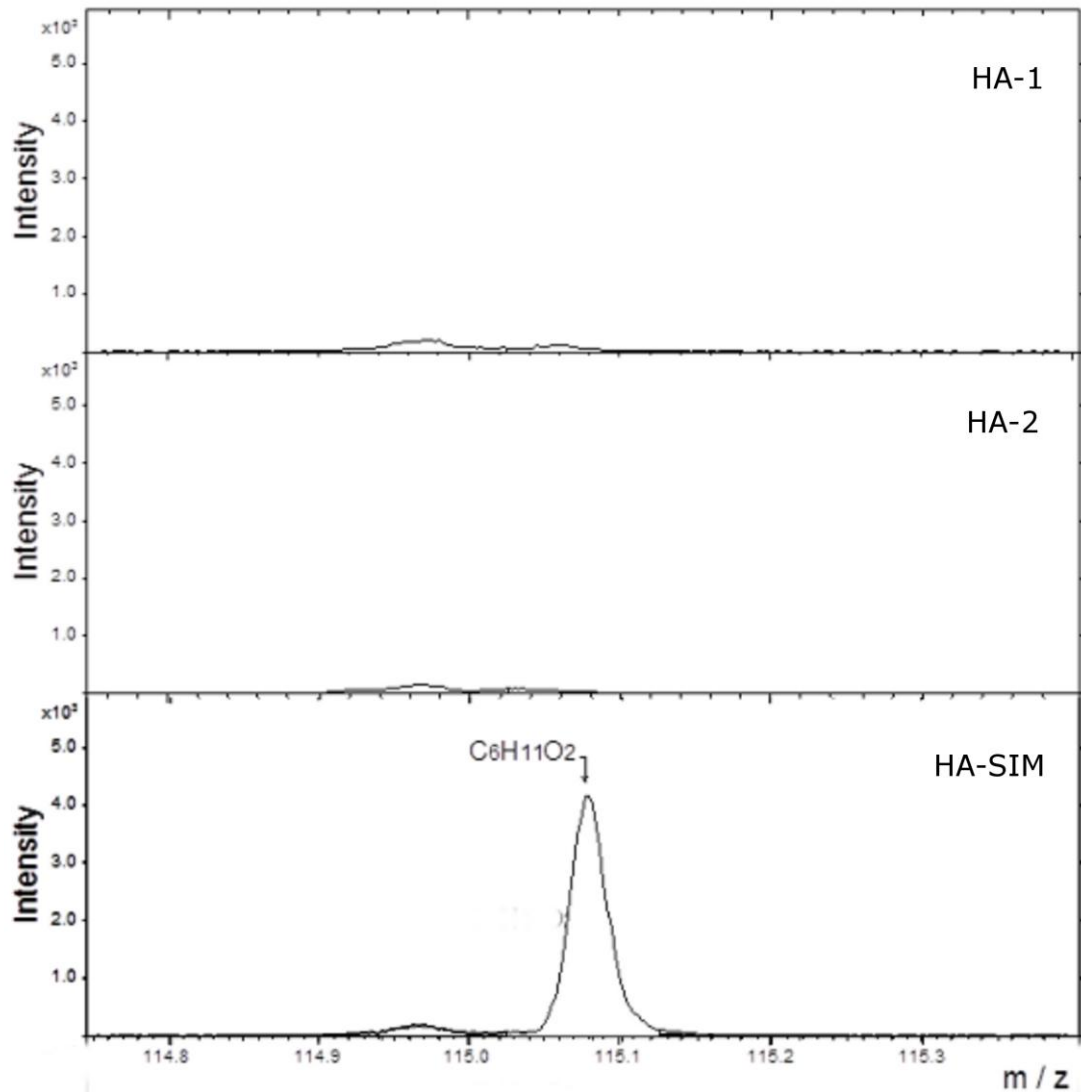


Figure 3.15. ToF-SIMS Data for HA-1, HA-2 and HA-SIM.

3.3.5 Addition of Zinc

HA-Zn was created with the aim of introducing zinc as a dopant into HA. The obtained TEM images indicated the particles had a sheet morphology, which was expected for the experimental parameters used. An elemental distribution map was also collected for the sample, during TEM analysis. The data (Figure 3.16) confirmed that zinc was indeed present in the particles, as well as the expected elemental components of HA. Nevertheless, the concentration of zinc present appeared to be higher than that of calcium - seen from the larger

number of white spots in Figure 3.16 (e) than (b). This is despite only 15 w/w % of Zn was used compared to Ca; this indicates that Zn may be preferentially taken up during particle formation. Moreover, the XRD pattern of HA-Zn (shown in Figure 3.13 and more clearly in Figure 3.17) showed that, while peaks corresponding to HA were present, there were also quite a few other peaks detected. The majority of these were ascribed to monoclinic parascorzite, $\text{CaZn}_2(\text{PO}_4)_2 \cdot 2\text{H}_2\text{O}$, a mineral first described by (Sturman et al., 1981). This confirms that the calcium to zinc ratio is consistent with the elemental map data. Since it was first reported, parascorzite has rarely been discussed in literature, and synthesis details of this material are hard to come by. Still, this material may have applications in the incorporation of zinc into bone-based materials (Sepulveda et al., 2000, Dasgupta et al., 2010) and the biocompatibility of HA-Zn is an important factor. Consequently, the *in vitro* cell proliferation assay using HA-Zn is reported in Section 3.3.6.

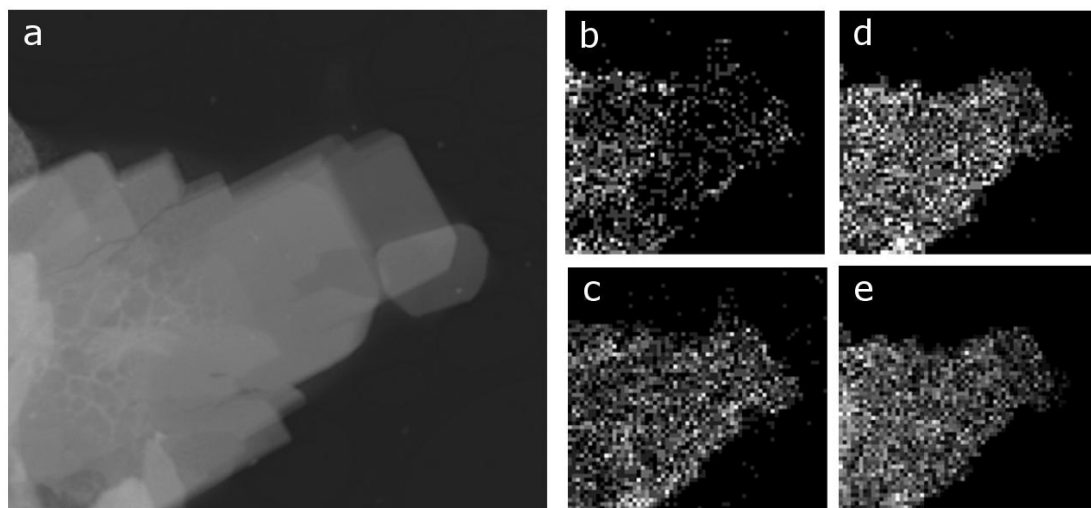


Figure 3.16. (a) TEM image of sample HA-Zn, and an elemental distribution map for (b) Ca, (c) O, (d) P, and (e) Zn.

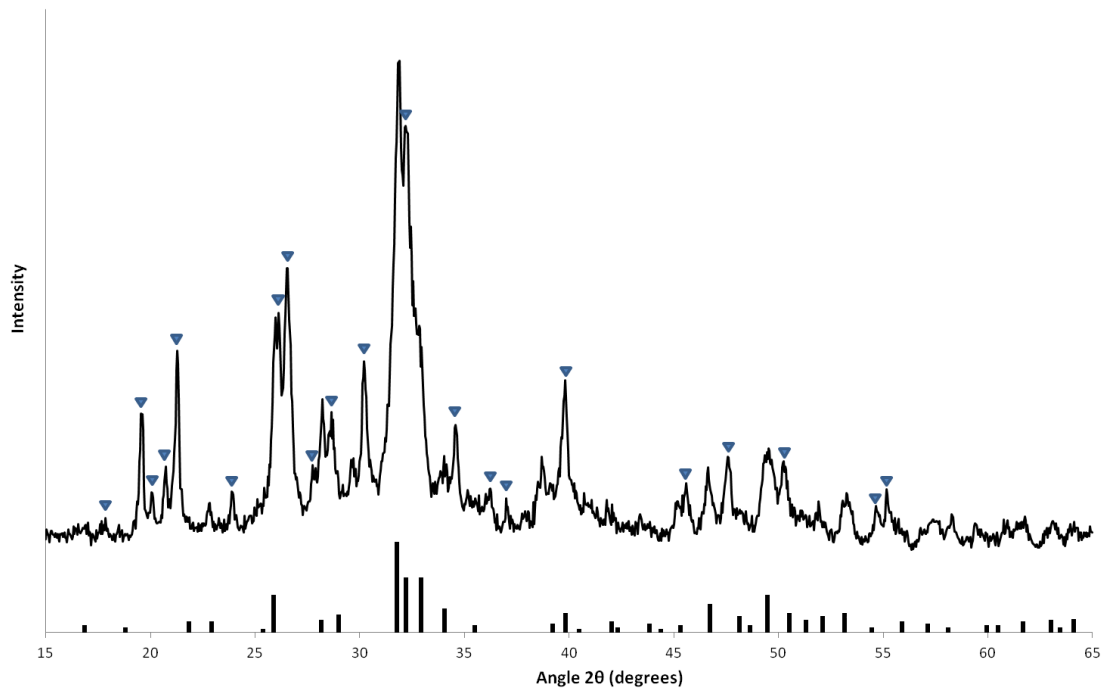


Figure 3.17. XRD pattern of HA-Zn; the predominant phases are hexagonal hydroxyapatite (ICCD PDF 74-566, shown at the bottom) and monoclinic parascholzite (ICCD PDF 35-495, peaks shown with blue triangles). Additional smaller peaks match calcium hydrogen phosphate (ICCD PDF 77-128).

3.3.6 *In Vitro* Cell Assays

The results from the cell proliferation assay (Figure 3.18) show that for the duration of the experiment, cell activity (absorbance correlates to cell activity) continued to increase for all three HA samples, irrespective of nanoparticle concentration. After 6 days, the cells cultured in control media are seen to have lower cellular metabolic activity when exposed to higher concentrations of nanoparticles, relative to the control. It is important to note that these effects are likely to be due to HA exhibiting an osteogenic effect on the cells, directing them towards an osteogenic phenotype - typically associated

with a decrease in proliferation. This is because once mESCs have differentiated into a cell line, they stop multiplying. In addition, these effects may be influenced by confluency initiated cell death (i.e. too many cells competing for resources) rather than the cytotoxic properties of the nanoparticles, the latter of which would be evident much earlier in the experiment.

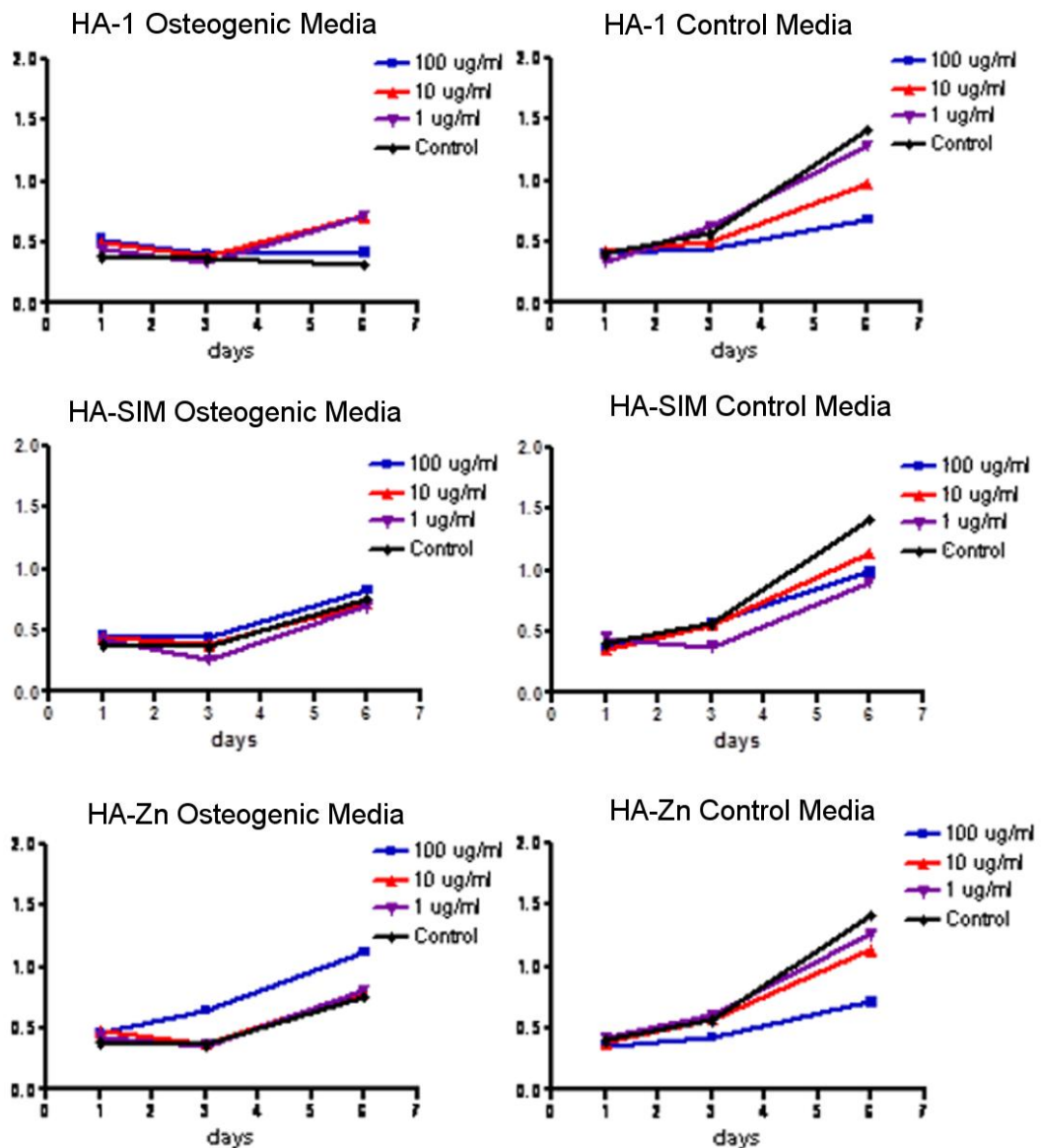


Figure 3.18. Results from the cell proliferation assay performed using three different concentrations of nanoparticles from sample HA-1 and sample HA-Zn, after 1, 3 and 6 days of incubation.

The bone nodule assay gives an indication of bone mineralisation - a distinctive marker of osteogenesis. The data (Figure 3.19) shows that the concentration of nanoparticles added to the media plays an important role in bone nodule formation. At higher nanoparticle concentrations, more intensive staining results and bone nodules can be seen. The frequency of intensely stained clusters also increases with higher concentrations of nanoparticles, indicating the formation of the extracellular matrix as cells undergo differentiation into the osteoblast lineage. The risk of calcium from HA being stained was minimised by excessive washing steps to remove residual nanoparticles prior to staining.

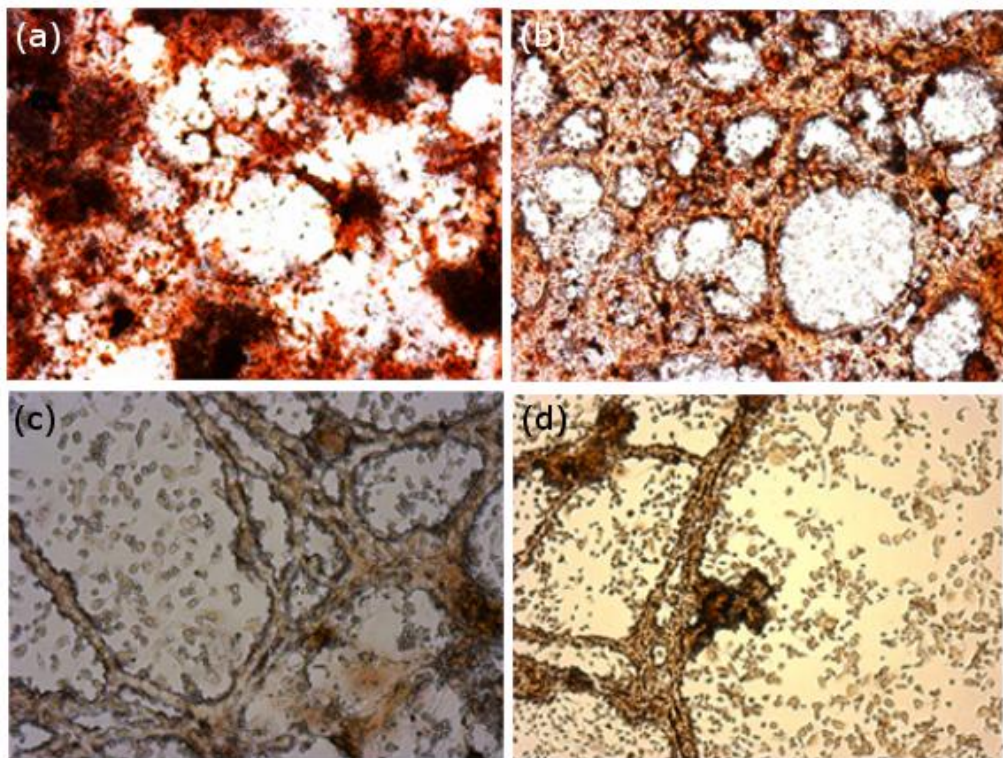


Figure 3.19. Images from the bone nodule assay - Cells cultured in osteogenic media with hydroxyapatite from Sample HA-1 at various concentrations, (a) 100 µg/ml; (b) 10 µg/ml; (c) 1 µg/ml; (d) control

3.4 Conclusions

Firstly, the work in this Chapter has shown that the counter-current Nozzle reactor can be used to reproducibly synthesise HA with three different morphologies: platelets, rods and tubes. The synthesis method is also significantly faster than other techniques previously reported in literature. Results of this study suggest that in this hydrothermal system, NH_4OH plays several roles in HA synthesis – it directs precursors towards the formation of HA over other CaP minerals, promotes the formation of rods instead of sheets at 200°C , and tubes instead of rods at 350°C . This process is more effective when NH_4OH is added to the heated downflow, compared to the cooler upflow.

In a continuous system, the process variables are linked thus making it very difficult to alter one parameter without affecting the others (Lester et al., 2012). This creates difficulty in isolating a single cause and effect, thereby making it a challenge to hypothesise a mechanism of formation for the different HA morphologies. Still, it is likely that HA sheets are the fundamental morphology of choice under 'standard' conditions. By increasing either the reaction temperature or pH, the synthesised particles are not only more crystalline, but given the observed dimensions of the particles, the sheets become fragmented into nanorods. However, the combination of a higher reaction temperature and the presence of NH_4OH specifically, appear to prevent the fragmentation of sheets, but cause the sheets to roll up - giving nanotubes. Further work is undoubtedly required to understand the formation mechanism of the different morphologies but it is apparent that the mechanisms are linked, rather than three independent schemes existing.

Experiments were conducted to introduce zinc as a dopant and simvastatin as a drug, into the structure of HA. The morphology of particles synthesised with simvastatin did not significantly differ from normal HA particles – again producing sheets. ToF-SIMS data for this sample showed the presence of a fragment which could be assigned to simvastatin, but it is inconclusive. This is likely to be due to the low concentration of statin used during synthesis. For future work, the concentration should be increased, although this does implicate higher costs. In addition, thermal analysis such as TGA (thermal gravimetric analysis) could provide additional data to ascertain the presence of simvastatin in the HA sample.

The addition of a zinc salt into the synthesis protocol yielded parascholzite, $\text{CaZn}_2(\text{PO}_4)_2 \cdot 2\text{H}_2\text{O}$, a material rarely described in literature but may have applications in bone based materials. In the scope of this work, experiments with only one concentration of Zn were attempted. For future work, the ratio of Ca:Zn can be investigated further, to determine if other calcium-zinc phosphates can be produced using the Nozzle reactor.

Finally, cell proliferation and bone nodule assays were conducted using HA produced using the Nozzle reactor. Results indicate that the HA particles have no cytotoxic effect on mESCs and promote bone nodule formation.

Chapter 4

Fluorescent Nanomaterials

4.1 Introduction

Following a previously reported hydrothermal method for the synthesis of cadmium sulphide, CdS, (Liu et al., 2001) the Nottingham research group established a synthesis procedure for the manufacture of CdS particles using the hydrothermal Nozzle reactor. Other publications using the Nozzle reactor included a method for synthesising nanoparticles of zirconium dioxide, ZrO₂, doped with europium, Eu (Hobbs et al., 2009). These particles displayed fluorescent properties while exhibiting no cytotoxic effects on Chinese hamster ovary cells; thus showing potential for use in biological cell imaging. Consequently, the motivation in this Chapter is to explore what other fluorescent materials are possible.

4.1.1 Fundamentals of Fluorescence

Fluorescence describes the emission of light by particles, upon stimulation from a form of electromagnetic radiation. There are different categories of fluorescence depending on the source of radiation.

When a molecule absorbs light photons from the UV light range (10 to 400 nm), it reaches an excited state with a higher energy level. Hence, this is known as excitation. Still, the molecule is unstable at this higher energy level and swiftly

emits light photons in order to return to its previous, more stable ground state. The emitted energy tends to be less than is absorbed by the molecule; as this energy is released in the form of light, the emitted light has a longer wavelength than the light that is absorbed (Geszke-Moritz and Moritz, 2013). Molecules which exhibit this behaviour are defined as photoluminescent (PL). Typically, PL particles emit light within the visible light range (400 to 700 nm); these are useful as they can be seen by the human eye without the need for additional detection apparatus. Nevertheless, there are particles which have been tuned to emit light in the infra-red (>700 nm) range (Hu et al., 2011, Xue et al., 2012, Poole et al., 2009).

Rather than reaching an excited state through light energy, particles stimulated by an electrical current are electroluminescent (EL), by a chemical reaction are chemiluminescent (CL), by sound are sonoluminescent and by a mechanical action are mechanoluminescent (ML) (Ronda, 2008). While electroluminescence will be briefly mentioned in subsequent Sections of this Chapter, photoluminescent properties of particles will remain the primary focus.

4.1.2 Quantum Dots

Quantum dots (QD) are a subset of fluorescent materials which are typically 1 to 20 nm in size (Geszke-Moritz and Moritz, 2013). They can be defined as crystalline semiconductor nanoparticles made up of elements from transition metals and group VI of the periodic table, such as CdSe or ZnS, or groups III and V, such as InP (Byers and Hitchman, 2011). QDs have gained much interest because of the potential to tune the PL properties through size manipulation. It has been reported that the relative brightness of QDs is dependent on the diameter of the particles and, in turn, the emission wavelength (Dickerson, 2005). For example, the intensity or brightness of QDs emitting at

525 nm (green) was 17 times lower than QDs emitting at 655 nm (red) (Xing et al., 2007).

Commonly reported QDs are comprised of a heavy metal core, usually cadmium sulphide (CdS) or cadmium selenide (CdSe), with a zinc sulphide (ZnS) shell to increase quantum yield (brightness) and avoid oxidation, as well as prevent Cd from leaching out (Byers and Hitchman, 2011). Polymer coatings and biomolecules can be attached to the surface to improve particle stability or solubility, increase biocompatibility, or target specific sites in a biological system (Jamieson et al., 2007). Section 4.1.3.4 will discuss biological applications of QDs in further detail. Figure 4.1 illustrates the structure of one example of a QD.

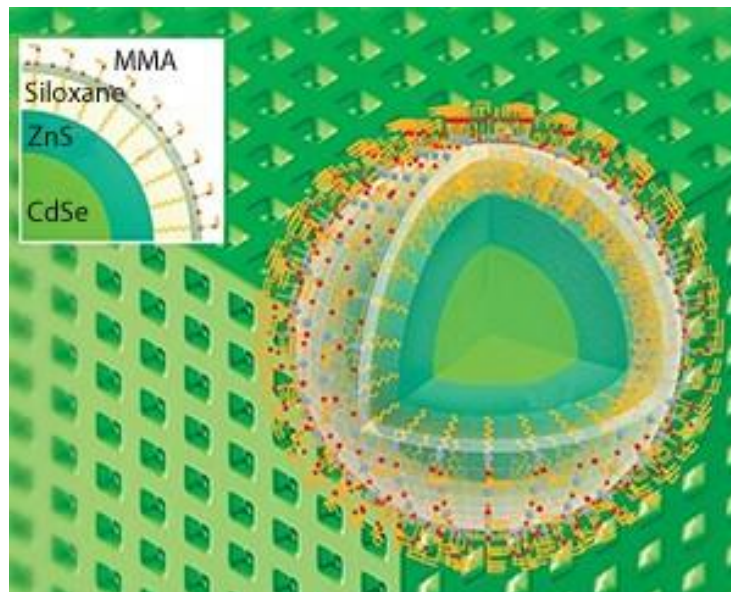


Figure 4.1. Illustration of a typical QD structure; a CdSe core is surrounded by a ZnS shell and functionalised with siloxane and methylmethacrylate (MMA) (Park et al., 2010).

4.1.3 Applications using Quantum Dots

Nanoparticles with fluorescent properties, particularly QDs, are of great interest because they can be applied in a wide range of fields - from electronics to medicine. Some of these applications will be briefly explained in this Section.

4.1.3.1 Electronic Devices

As QDs are semi-conductors, they are often reported for use as components in electronic devices. For example, SiO₂ QDs have been applied for memory storage devices (Corso et al., 2003), while PbS QDs have been used in fibre-optics amplifiers (Heo and Liu, 2007). Meanwhile, particles with EL properties have also found uses in this field. For example, ZnS-based QDs have been described in the field of printed electronics (Wood et al., 2009); in this study, an inkjet printer was used to deposit nanoparticles in a structured pattern onto substrates for use in display panels. Furthermore, InP/ZnS composite QDs have reportedly been used in light emitting diodes (LEDs) (Kim et al., 2012), while Poole et al. described the use of InAs/InP QDs in lasers (Poole et al., 2009).

4.1.3.2 Solar Panels

Increasing population and technological advances have resulted in a rise in the global demand of energy. Conversely, a limited supply of fossil fuels (coal, oil, natural gas) has meant sharp increases in energy prices. Twinned with the emission of greenhouse gases from burning fossil fuels, there has been a growing need to focus efforts in developing other more sustainable and renewable energy sources - including wind, bio-fuels, geothermal and solar cells.

The latter has generated a lot of interest as the Earth receives over 120 PW (petawatts) of energy from the Sun each day (Tsakalakos, 2008). As such, many researchers have developed various materials, including QDs, to capture solar energy. Much of the initial work in this area was conducted on silicon, but the need for more efficient materials lead to advances with other elements, namely Gallium based QDs (Tsakalakos, 2008) and CdS QDs (Santra and Kamat, 2012) being used.

4.1.3.3 Anti-Counterfeiting

QDs and other fluorescent materials have been considered for anti-counterfeiting purposes (Zhang and Ge, 2011), where genuine articles are marked with the fluorescent particles and are invisible to the naked eye. Only upon excitation with light of a particular wavelength can the distinctive mark be seen, thereby distinguishing fraudulent copies from the real article.

4.1.3.4 Biological Applications

In 1998, researchers first began to explore using QDs in the field of bio-imaging (Bruchez Jr et al., 1998, Chan and Nie, 1998). In this ground-breaking study, proteins in mice were attached to, or labelled with, water-dispersible fluorescent QDs which enabled them to be detected for the purpose of medical diagnostics. The semiconductor QDs proved to be significantly more effective than traditional organic dyes. Since then QDs have been widely used for a whole host of biological applications. In cell biology, QDs have been used for labelling and tracking cells (Jamieson et al., 2007, Byers and Hitchman, 2011). The nanoparticles can be conjugated to antibodies which target specific proteins in a cell. Once attached to the protein, its path can be tracked and imaged. This

process is particularly pertinent in the labelling of proteins specific to cancerous cells, potentially allowing the prediction of cancer onset.

Furthermore, ZnO QDs have been described as antimicrobial agents (Jin et al., 2009), while CdTe QDs were functionalised to bind to specific strands of DNA for the detection of leukaemia (Sharma et al., 2012), and QDs have been conjugated to antibodies for the detection of microorganisms in water sources (Zhu et al., 2004). Other studies using functionalised QDs in the detection of pathogens and toxins have also been conducted (Jamieson et al., 2007). In terms of live *in vivo* imaging, studied subjects tend to be mice where cells have been labelled to study embryogenesis, stem cell therapy and cancer metastasis (Byers and Hitchman, 2011). Each of these applications depends on the right biomarker or probe being chosen and attached to the QD, which can then bind to the relevant site. As such, the QD itself is very versatile.

4.1.4 Synthesis of Quantum Dots

As described in Section 4.1.2, the fluorescent properties of QDs are affected by their particle size. Furthermore, fluorescent properties can be optimised if samples contain monodisperse particles with little or no agglomeration. Hence, the route of synthesis can play a crucial role in determining the structure and function of QDs.

Given that the umbrella term 'quantum dot' covers a plethora of materials, various synthesis methods have been reported which are dependent on the chemistry of reactions. Commonly reported methods of QD preparation include aerosol-gel (Firmansyah et al., 2012), precipitation (Lang et al., 2011), photochemical (Liu et al., 2012), electrochemical (Li et al., 2013), ultrasound-

assisted (Ren and Yan, 2012), microwave (Yang et al., 2012a), solvothermal (Yang et al., 2011) and batch hydrothermal (Yu et al., 2012).

While these and many other described methods of QD synthesis in the literature yield high-quality nanoparticles, they are only capable of producing milligrams of material; consequently, there is little potential for scalability. Nevertheless, there are processes capable of producing larger quantities of QDs and companies have been founded on these technologies. One such example will be described in more detail in Section 4.1.4.1.

4.1.4.1 Commercial Synthesis of Quantum Dots

Nanoco Group Plc is a UK based company established in 2001, which produces QDs on a commercial scale (approx. 25 kg/annum). They produce both QDs which contain heavy metals, and those which are free of heavy metals. Their technology is based on the use of a “molecular seed” which acts as a nucleation point on which nanoparticle growth can occur. This patented technology produces batches of QDs, up to 1 kg each batch (Nanoco, 2013). Because QDs can be so effective, only very small volumes of material are required for application – as such, 1 kg of material is considered as commercial-scale.

Nanoco produce QDs with an array of different compounds, and for a range of applications. Their range of Cadmium Free Quantum Dots (CFQD™) have been advertised for use as electroluminescent LEDs in lighting, in electronic displays, and for biological applications such as drug-delivery, cell tracking and clinical whole-body imaging. Their more recently developed range of CIS, CGS and CIGS

QDs are composed of varying elemental ratios of copper, indium, gallium and selenium. These particles have been developed in a range of solvents which can then be printed onto substrates then cured as components for solar cells to capture light energy.

The successes of commercial manufacturers of QDs such as Nanoco highlight the existing high demand for nanomaterials with PL and EL properties.

4.1.5 Disadvantages of Cadmium-Based Materials

The majority of QDs which are described in the literature contain Cd-based particles, or other heavy metals such as lead, in the core. However, these can have highly toxic effects; in humans, Cd can accumulate in the lungs, liver and kidneys. As a result, essential proteins are excreted from the body while the metal itself is not so easily removed. The consequences are very serious, and even fatal.

Meanwhile, there has been much debate over the safety of using QDs containing heavy metals in biological applications, as the toxic cores tend to be coated with a several layers which prevent the heavy metal leaching out. Although much research has gone into the use of QDs for in vitro and in vivo cell imaging, toxicity studies of these materials are still lacking. Nevertheless, a publication has shown Cd-based QDs to cause apoptosis (programmed cell death) (Chen et al., 2012). Consequently, a Cd-free route would have more potential, especially if the PL properties are equalled. Typically, CdS particles produced with a ZnS shell exhibit peak PL emission at 438 nm, when excited at 370 nm (Saraswathi Amma et al., 2008).

In addition, the European Commission has been striving to reduce and prohibit the use of heavy metals (these being cadmium, mercury and lead) in consumer products in order to reduce human exposure to these toxic elements. Hence, legislations have been imposed to restrict the use of heavy metals in electrical and electronic items (RoHS 2002/95/EC) and in batteries (Directive 2006/66/EC). Manufacturers of household appliances (namely electronics) must limit the concentration of heavy metals to 0.1% (1000 ppm) (Nanoco, 2013). Furthermore, official analysis techniques have been imposed to test levels of heavy metals in foodstuffs (Commission Regulation (EC) No 333/2007) to ensure they do not enter the food chain. These controls indicate the severity of heavy metal poisoning and if their use can be avoided, these risks will be bypassed.

4.1.6 Zinc Sulphide, ZnS

Several literature reports state the use of ZnS as a shell around CdS or CdSe for the reasons outlined in Section 4.1.2. Unlike the latter two materials, ZnS does not carry implications of toxicity. Furthermore, due to the availability of low-cost zinc precursors, and an established method of CdS synthesis in place, ZnS was opted for as a material of interest in this PhD. The materials properties will be primarily assessed with the aim of application in biological fields.

4.1.7 Capping Agents and Stabilisers

Due to the very small size of QDs (<20 nm), the attractive forces on the surface of the particles are significant and cause the particles to coagulate and cluster, if there is nothing to prevent them from doing so (Geszke-Moritz and Moritz, 2013). This can lead to problems if the application calls for non-agglomerated particles, as most do. Particularly for biomedical applications,

particle agglomeration can mean clusters of particles no longer exhibit the properties seen in the nano-form, and can lead to undesired cell uptake or excretion (Jamieson et al., 2007). Moreover, it has already been described in Section 4.1.2 that the fluorescent properties of QDs depend on the size of the particles, and so the aggregation of these small particles results in the exhibition of bulk-like behaviour and the loss (or reduction) of fluorescent properties (Dickerson, 2005).

In this Chapter, three different capping agents have been chosen to stabilise ZnS particles. They have all been reported in the literature in stabilising ZnS; additional reasons are also described below.

Polyvinylpyrrolidone (PVP) is a low-cost, non-toxic polymer widely used for biological applications due to its high biocompatibility (Sharma et al., 2010); 3-Mercaptopropionic acid (3-MPA) has been described several times as a capping agent for QDs, especially ZnS (Luan et al., 2012, Rosli et al., 2012, Azizian-Kalandaragh and Khodayari, 2010, Geszke-Moritz and Moritz, 2013); and sodium hydroxide (NaOH) has been reported in the synthesis of ZnS (Shen et al., 2007) to improve the photo luminescent properties of particles. Moreover, all the above reagents are water-soluble, meaning experiments can be conducted in a completely hydrothermal environment without the need for organic solvents, which are potentially detrimental to biological systems.

4.1.8 Chapter Aims

The aim of this Chapter is to use the counter-current Nozzle reactor for the continuous synthesis of ZnS nanoparticles, and to assess their properties in terms of crystallinity, particle size and photoluminescence. This will be achieved by using XRD, SEM and TEM techniques, and fluorometry analysis.

4.2 Methodology

The reagents used for synthesis were cadmium nitrate tetrahydrate, $\text{Cd}(\text{NO}_3)_2 \cdot 4\text{H}_2\text{O}$ (98% purity); thiocarbohydrazide, $(\text{NH}_2\text{NH})_2\text{CS}$ (98% purity); zinc nitrate tetrahydrate, $\text{Zn}(\text{NO}_3)_2 \cdot 6\text{H}_2\text{O}$ (98% purity); thiourea, $(\text{NH}_2)_2\text{CS}$ ($\geq 99\%$ purity); 3-Mercaptopropionic acid (3-MPA), $\text{HSCH}_2\text{CH}_2\text{CO}_2\text{H}$ ($\geq 99\%$ purity); sodium hydroxide, NaOH ($\geq 98\%$ purity); polyvinylpyrrolidone, $(\text{C}_6\text{H}_9\text{NO})_n$ (average molecular weight of 10,000). All reagents were purchased from Sigma Aldrich, UK and used without further purification. DI grade water was used throughout this work.

4.2.1 Synthesis of CdS using the Nozzle Reactor

As mentioned in Section 4.1, a method was previously established for the continuous hydrothermal synthesis of CdS. This protocol will be elaborated on in this Section.

The method described a 0.01 M $\text{Cd}(\text{NO}_3)_2 \cdot 4\text{H}_2\text{O}$ solution being pumped in one metal salt pump at 5 ml/min. Simultaneously, a 0.01 M $(\text{NH}_2\text{NH})_2\text{CS}$ solution was pumped at 5 ml/min through a second metal salt pump. These met at a T-piece before the reactor and subsequently flowed into the reactor section of the system together. Here, the feed met a stream of water pumped at 10 ml/min. The method described the water downflow being pre-heated to 400 °C, and the system pressure maintained at 240 bar.

In the work described in this Chapter, a few samples of CdS were generated following this protocol, but employing a range of temperatures – either 240, 300 or 400 °C and the samples were labelled CdS 240, CdS 300 and CdS 400,

respectively. Sample CdS 400 was analysed by DLS and TEM. Fluorometry analysis was also performed.

4.2.2 Initial Synthesis of ZnS using the Nozzle Reactor

For the preliminary synthesis of ZnS, the methodology for CdS synthesis (Section 4.2.1) was adapted: quite simply $\text{Zn}(\text{NO}_3)_2 \cdot 6\text{H}_2\text{O}$ was chosen as the metal salt precursor, instead of $\text{Cd}(\text{NO}_3)_2 \cdot 4\text{H}_2\text{O}$. The precursor concentrations, flow orientation and rates were maintained, and the system pressure was again kept at 240 bar. A range of samples were produced using five different reaction temperatures; these are detailed in Table 4.1. The positions in the system from which these temperatures were taken, are outlined in Chapter 1.

Table 4.1. Reaction temperatures for each ZnS Sample.

| Sample Name | Water Heater Temp (°C) | After Heater Temp (°C) | Post Mixing Point Temp (°C) | Capping Point Temp (°C) | Post Cooler Temp (°C) |
|--------------------|-------------------------------|-------------------------------|------------------------------------|--------------------------------|------------------------------|
| ZnS 200 | 215 | 213 | 102 | 54 | 19 |
| ZnS 250 | 265 | 260 | 120 | 60 | 19 |
| ZnS 300 | 315 | 313 | 156 | 70 | 19 |
| ZnS 350 | 365 | 363 | 262 | 80 | 19 |
| ZnS 400 | 420 | 416 | 304 | 101 | 20 |

Sample ZnS 400 was analysed using TEM, EDX and XRD techniques.

4.2.3 Refined Method for ZnS Synthesis

The synthesis method was later simplified to combine both metal salt precursors in one flask, thereby eliminating the need for a third pump. The aforementioned temperatures for sample ZnS 400 in Table 4.1 were used with the experimental setup shown in Figure 4.2 to produce the sample "Uncapped ZnS" – this is the "basic" sample of ZnS without any surfactants or capping agents introduced.

SEM, XRD, ζ -potential and Fluorometry analysis was conducted on the sample Uncapped ZnS.

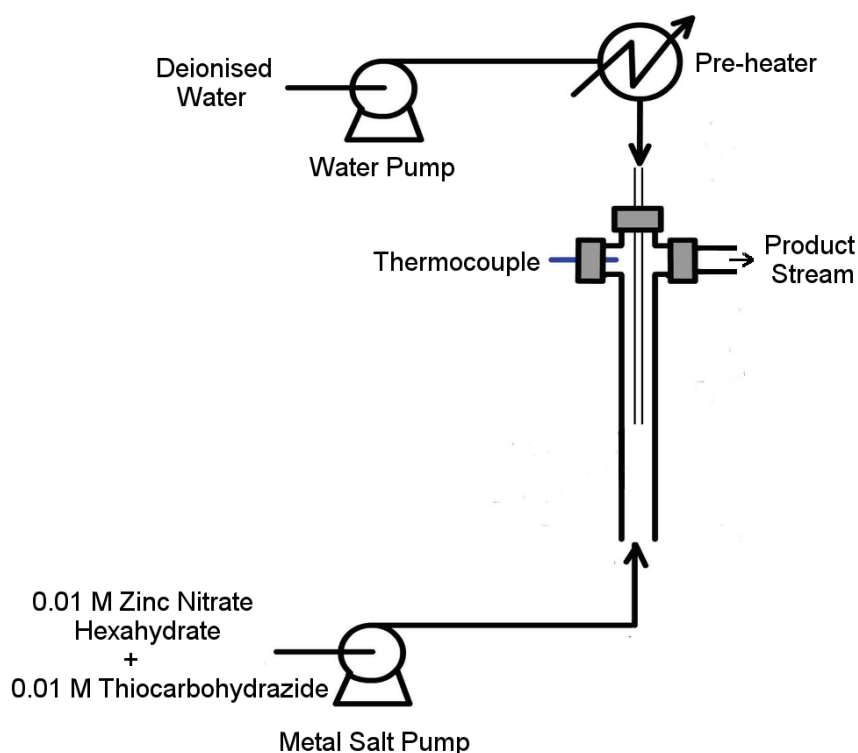


Figure 4.2. A schematic diagram showing the reactor setup for the refined synthesis method of ZnS.

4.2.4 Synthesis of ZnS using Thiourea

Due to the toxicity of $(\text{NH}_2\text{NH})_2\text{CS}$, it is desirable to use a safer sulphur source in the synthesis of ZnS. Thiourea, $(\text{NH}_2)_2\text{CS}$, was chosen as a potential substitute due to its lower toxicity, because literature describes it as working well (Wageh et al., 2003, Apte et al., 2011), it is water soluble, and was readily available. The same reaction conditions as described in Section 4.2.3 were used but using the range of reaction temperatures shown in Table 4.2. The system positions from which the thermocouple readings were taken, were outlined in Chapter 1.

Table 4.2. Reactor System temperatures for samples synthesised using thiourea.

| Sample Name | Water Heater Temp (°C) | After Heater Temp (°C) | Post Mixing Point Temp (°C) | Capping Point Temp (°C) | Post Cooler Temp (°C) |
|--------------------|-------------------------------|-------------------------------|------------------------------------|--------------------------------|------------------------------|
| ZnS- TU-150 | 190 | 162 | 79 | 49 | 19 |
| ZnS- TU-250 | 300 | 260 | 130 | 66 | 20 |
| ZnS- TU-350 | 390 | 352 | 180 | 83 | 22 |
| ZnS- TU-400 | 450 | 409 | 279 | 105 | 23 |

4.2.5 Synthesis of ZnS with Surfactants/Stabilisers

An issue affecting the synthesis of ZnS nanoparticles is agglomeration, as is the case for most QDs and indeed most nanoparticles. The problems arising from particle aggregation were described in Section 4.1.7.

Consequently, three different stabilising agents were chosen as candidates for capping ZnS in the Nozzle reactor during synthesis: 3-MPA, NaOH and PVP. The reasoning behind these choices was described in Section 4.1.7. The methodology described in Section 4.2.3 was used as a basic protocol for ZnS synthesis in this experiment set. The sample "Uncapped ZnS" described in Section 4.2.3 was used as a control for comparison.

For the experiments outlined in Sections 4.2.5.1, 4.2.5.2, and 4.2.5.3, Figure 4.3 depicts the schematic setup of the reactor section of the system and the feed orientations can be seen. The system pressure was maintained at 240 bar by the BPR, and the recorded temperatures are shown in Table 4.3.

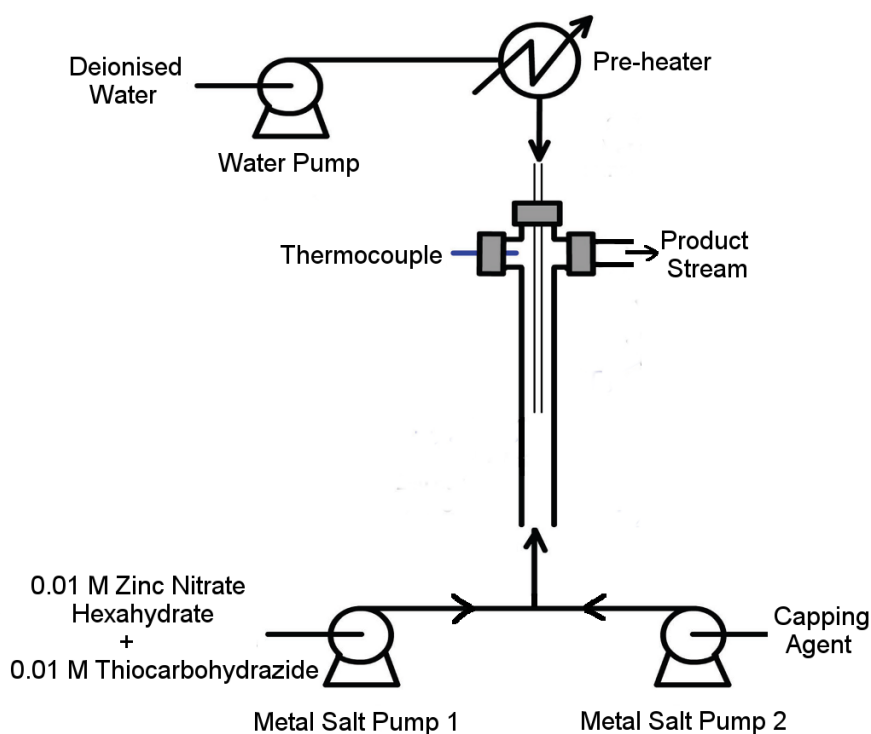


Figure 4.3. A schematic diagram displaying the reactor setup for the synthesis reaction of ZnS with capping agents.

Table 4.3. System temperatures for synthesis of ZnS with surfactants.

| Water Heater Temp (°C) | After Heater Temp (°C) | Post Mixing Point Temp (°C) | Capping Point Temp (°C) | Post Cooler Temp (°C) |
|-------------------------------|-------------------------------|------------------------------------|--------------------------------|------------------------------|
| 415 | 405 | 265 | 102 | 23 |

4.2.5.1 ZnS and 3-Mercaptopropionic Acid (3-MPA)

In this experiment set, an aqueous solution of 0.25 M 3-MPA was introduced at the second metal salt pump (MS2) while the precursors for ZnS were pumped through the first metal salt pump (MS1). The flow rate of the H₂O downflow was maintained, but the flow rates of MS1 and MS2 were altered for each sample. A summary of flow rates for each of the 5 samples produced is displayed in Table 4.4.

Table 4.4. Flow ratios for the different ZnS:3-MPA Samples.

| Sample Name | H ₂ O Feed | H ₂ O Flow Rate (ml/min) | MS 1 Feed | MS 1 Flow Rate (ml/min) | MS 2 Feed | MS 2 Flow Rate (ml/min) |
|---------------|-----------------------|-------------------------------------|---|-------------------------|--------------|-------------------------|
| ZnS:3-MPA 9/1 | | | | 9 | | 1 |
| ZnS:3-MPA 8/2 | | | | 8 | | 2 |
| ZnS:3-MPA 7/3 | H ₂ O | 10 | 0.02 M Zn(NO ₃) ₂ + 0.02 M TCH | 7 | 0.25 M 3-MPA | 3 |
| ZnS:3-MPA 6/4 | | | | 6 | | 4 |
| ZnS:3-MPA 5/5 | | | | 5 | | 5 |

MS – Metal Salt; TCH – Thiocarbohydrazide; 3-MPA – 3-Mercaptopropionic Acid

4.2.5.2 ZnS and Polyvinylpyrrolidone (PVP)

For this set of experiments, an aqueous solution of 0.005 M PVP was introduced at MS2. As with the samples produced with 3-MPA described in Section 4.2.5.1, the flow rates of MS1 and MS2 were altered for each sample. A summary of flow rates for each of the 5 samples produced is displayed in Table 4.5.

Table 4.5. Flow ratios for the different ZnS:PVP Samples.

| Sample Name | H ₂ O Feed | H ₂ O Flow Rate (ml/min) | MS 1 Feed | MS 1 Flow Rate (ml/min) | MS 2 Feed | MS 2 Flow Rate (ml/min) |
|----------------|-----------------------|-------------------------------------|--|-------------------------|----------------|-------------------------|
| ZnS:PVP 9/1 | | | | 9 | | 1 |
| ZnS:PVP 8/2 | | | | 8 | | 2 |
| ZnS:PVP 7/3 | H ₂ O | 10 | 0.02 M Zn(NO ₃) ₂ + 0.02 M TCH | 7 | 0.005 M PVP | 3 |
| ZnS:PVP 6/4 | | | | 6 | | 4 |
| ZnS:PVP 5/5 | | | | 5 | | 5 |

MS – Metal Salt; TCH – Thiocarbonylhydrazide; PVP – Polyvinylpyrrolidone

4.2.5.3 ZnS and Sodium Hydroxide (NaOH)

NaOH has been described in literature as a surfactant for ZnS (Shen et al., 2007). It was reported that the alkaline environment results in the formation of core/shell particles of ZnS/Zn(OH)₂ where the surface hydroxyl groups provide charge stabilisation as well as improving PL properties. In these reactions, an aqueous solution of 0.25 M NaOH was pumped through MS2, with the flow rates of MS1 and MS2 altered for each sample, as summarised in Table 4.6.

Table 4.6. Flow ratios for the different ZnS:NaOH Samples.

| Sample Name | H ₂ O Feed | H ₂ O Flow Rate (ml/min) | MS 1 Feed | MS 1 Flow Rate (ml/min) | MS 2 Feed | MS 2 Flow Rate (ml/min) |
|-----------------|-----------------------|-------------------------------------|--|-------------------------|----------------|-------------------------|
| ZnS:NaOH 9/1 | | | | 9 | | 1 |
| ZnS:NaOH 8/2 | | | | 8 | | 2 |
| ZnS:NaOH 7/3 | H ₂ O | 10 | 0.02 M Zn(NO ₃) ₂ + 0.02 M TCH | 7 | 0.25 M NaOH | 3 |
| ZnS:NaOH 6/4 | | | | 6 | | 4 |
| ZnS:NaOH 5/5 | | | | 5 | | 5 |

MS – Metal Salt; TCH – Thiocarbohydrazide

4.2.6 Structural Characterisation

For each of the ZnS samples described in Section 4.2.5 and produced with different ratios of precursors and surfactants, a small volume was collected for SEM analysis and fluorometry measurements (the latter is outlined in Section 4.2.6.1). In addition, XRD and ζ -potential analysis were conducted on each of the three 5/5 ratio samples. These four analysis techniques were also performed on the Uncapped ZnS sample, for comparison. The principles of these structural characterisation techniques were discussed in Chapter 2.

Samples were washed by vacuum filtration using deionised water, and then either re-suspended in deionised water for SEM and fluorescence analysis, or oven dried at 70°C for 24 hours to yield a powder for XRD analysis.

4.2.7 Fluorometry Analysis

Excitation and emission spectra were collected for each of the aqueous CdS and ZnS samples using a Flexstation II fluorometer from Molecular Devices. For each sample, 200 μ L of material was loaded into a UV-transparent 96-well plate, which was then scanned by the fluorometer.

Broad emission sweeps were firstly collected by scanning between 450 and 650 nm using a step size of 10 nm, with excitation kept at 350 nm. Likewise, broad excitation sweeps were conducted by measuring emission at 540 nm while excitation was varied between 260 and 450 nm using 10 nm increments. For both excitation and emission spectra, each sample was read 6 times.

Subsequently, more specific emission sweeps were performed by measuring emission between 430 and 650 nm with 2 nm steps. Excitation was held at 360 nm. To confirm the emission data, a detailed excitation sweep was conducted by varying excitation between 290 and 410 nm with 2 nm increments; the emission was measured at a constant 530 nm. For both excitation and emission spectra, each sample well was read 12 times.

4.3 Results and Discussion

4.3.1 Cadmium Sulphide, CdS

This Section describes the samples of CdS produced from the synthesis experiments detailed in Section 4.2.1. At the lower two temperatures, 240 and 300 °C, the collected samples were transparent and colourless – photos are provided in Figure 4.4 (a) and (b). On testing with a laser pointer, these samples did not show a beam through the dispersion. If particles were present and therefore scattering light, a beam path would be visible. Consequently, it was determined that no particles were apparent in these samples and no further tests were conducted on them. Sample CdS 400 produced a bright yellow colour (see Figure 4.4), and the particles remained in suspension for a few days.

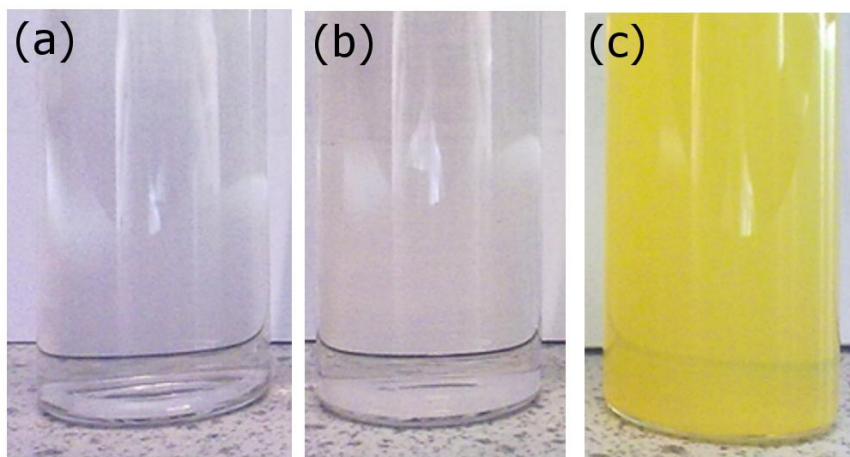


Figure 4.4. Photos of (a) CdS 240, (b) CdS 300, and (c) CdS 400.

DLS measurements performed on CdS 400 reported a particle size of 67 nm. Meanwhile, TEM analysis of sample CdS 400 revealed it to be composed of particles with diameters between 20 and 50 nm, as seen in Figure 4.5 (a). It is

likely that DLS was measuring the hydrodynamic radii of these particles, thus gave a bigger particle size than observed under TEM. Images obtained with TEM at a higher magnification (Figure 4.5 (b)) showed that these particles may in fact be clusters of individual smaller particles because crystal planes can be seen in different alignments. Nevertheless, the images do not distinctly show particle boundaries, and another possibility is that the particles are composed of different crystallites, which explains the presence of differently aligned planes.

Fluorometry analysis was performed on sample CdS 400, but the data was inconclusive as there was no discernible difference between the excitation and emission spectra for the sample, compared to that of the control water blank. In the latter, no excitation or emission activity is expected; instead, the sample peaks were seen for both the CdS 400 sample and the water blank. It is most likely that the signal for the water blank is caused by the fluorescence of the CdS, as the sample well was adjacent to the well holding the water blank during analysis – a process known as “bleedthrough”. Because CdS was not the main material of interest in this study, a full data set (XRD analysis etc.) was not acquired. Instead, most effort was directed towards ZnS analysis.

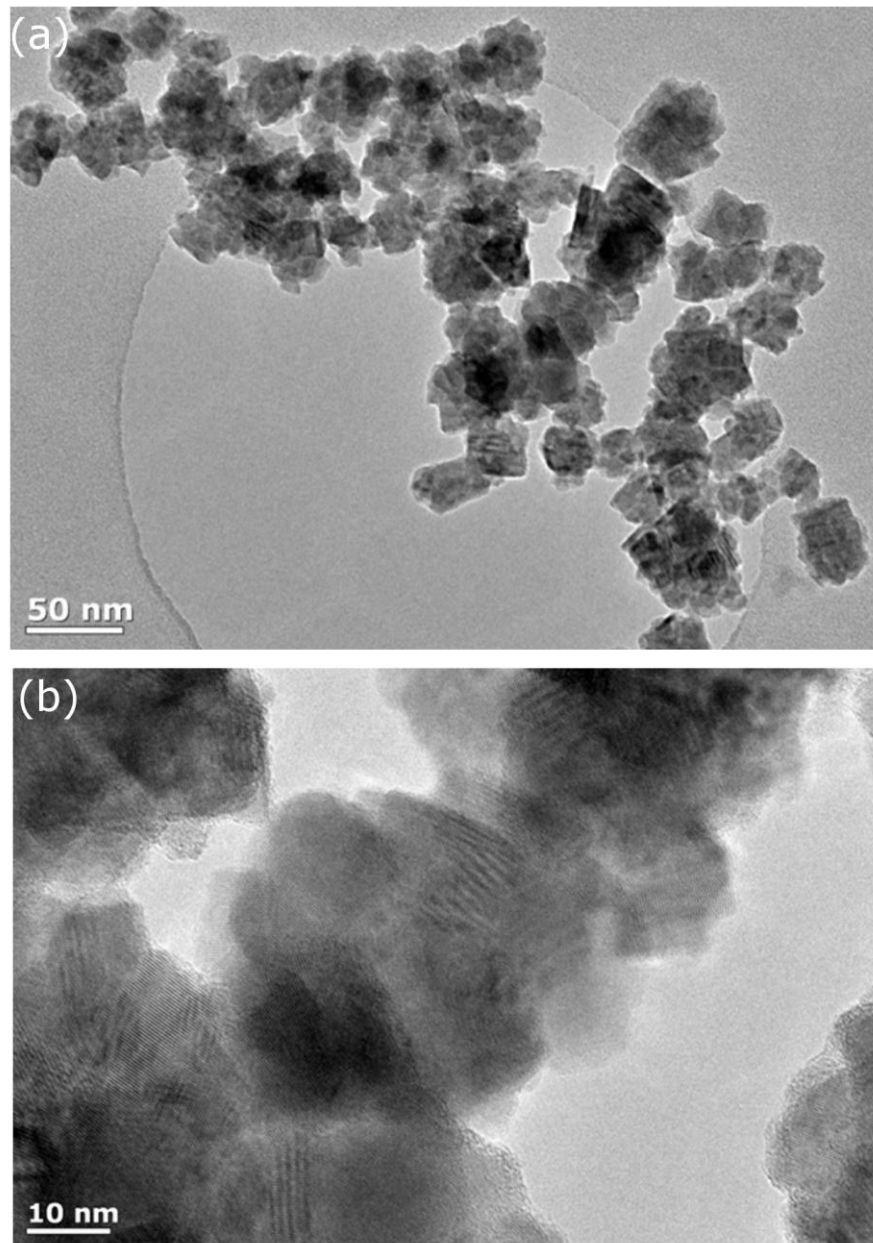


Figure 4.5. (a) and (b) show TEM images of sample CdS 400.

4.3.2 Initial synthesis of ZnS

The samples produced under the methodology described in Section 4.2.2 will be discussed in this Section. With the exception of sample ZnS 400, all samples were transparent and colourless when collected from the BPR outlet. When tested with a laser, there was no indication of the presence of particles –

therefore these samples were not analysed further. Still, sample ZnS 400 was a white/grey suspension when collected from the BPR outlet, with the coloured particles sedimenting at the bottom of the vessel within a few hours. The XRD pattern collected for this sample is shown in Figure 4.6; the peaks can be ascribed to ICCD PDF 80-20, cubic phase ZnS, and 80-7, hexagonal phase ZnS.

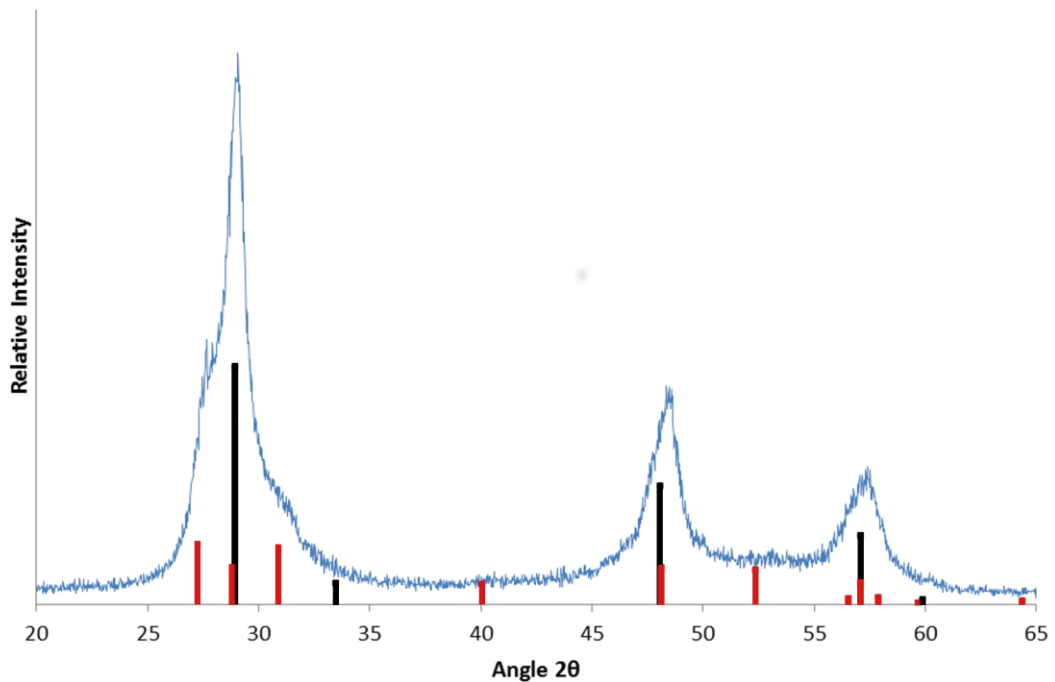


Figure 4.6. XRD pattern for sample ZnS 400, with expected peak positions of cubic ZnS (ICCD PDF 80-20) shown in black, and hexagonal ZnS (ICCD PDF 80-7) shown in red.

The TEM images which were captured of sample ZnS 400 showed clustered particles where each cluster measured between 50 and 100 nm (see Figure 4.7 (a) and (b)). At higher magnifications, the clusters appeared to be composed of primary particles with diameters <15 nm (Figure 4.7 (c)). Furthermore, at high resolution, the crystal lattice of the particles can be observed (Figure 4.7 (d)).

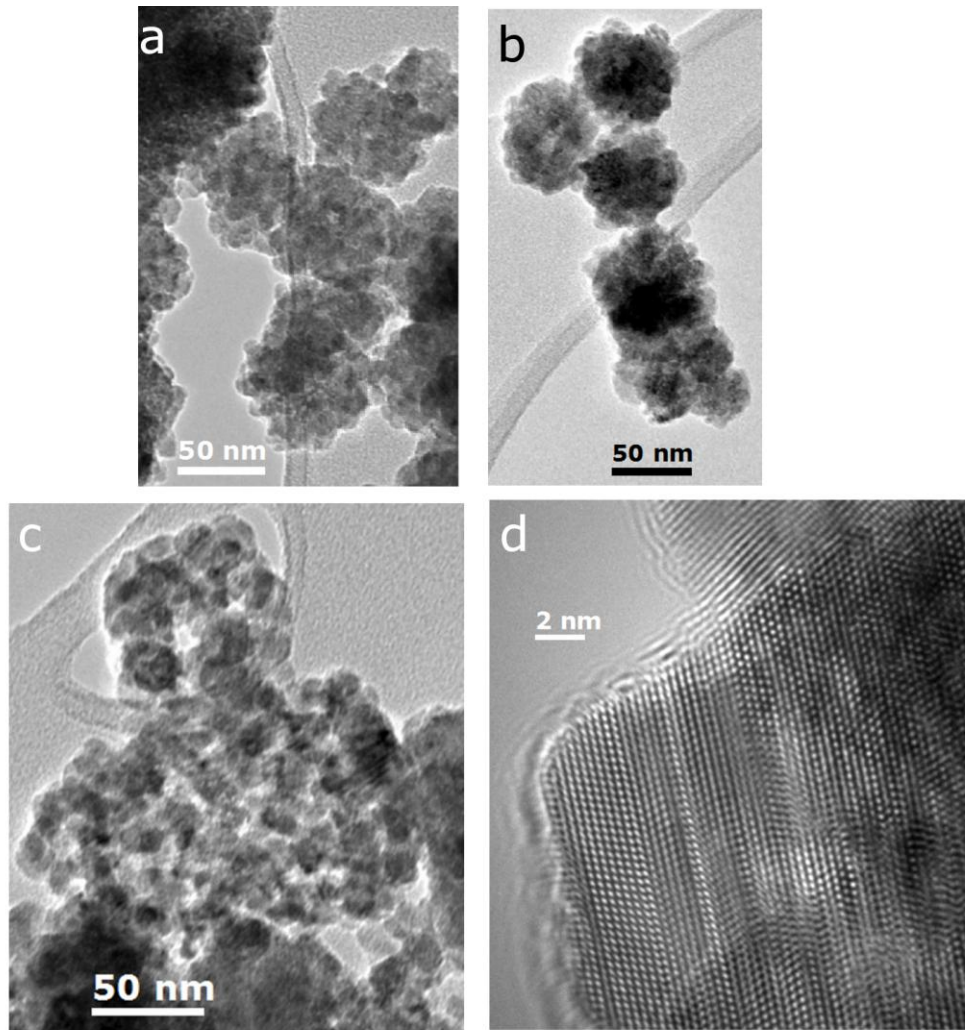


Figure 4.7. a) and b) TEM images and c) HRTEM images of sample ZnS 400.

The elements expected from sample ZnS 400 are indeed present, seen from the EDX spectrum in Figure 4.8. The Cu and C peaks can be assigned to the copper and carbon of the TEM sample grid. A small peak for oxygen is present which is likely to have been introduced during sample preparation as the XRD pattern (Figure 4.6) shows a match to the expected peaks for cubic ZnS, rather than a crystal structure containing an oxide group.

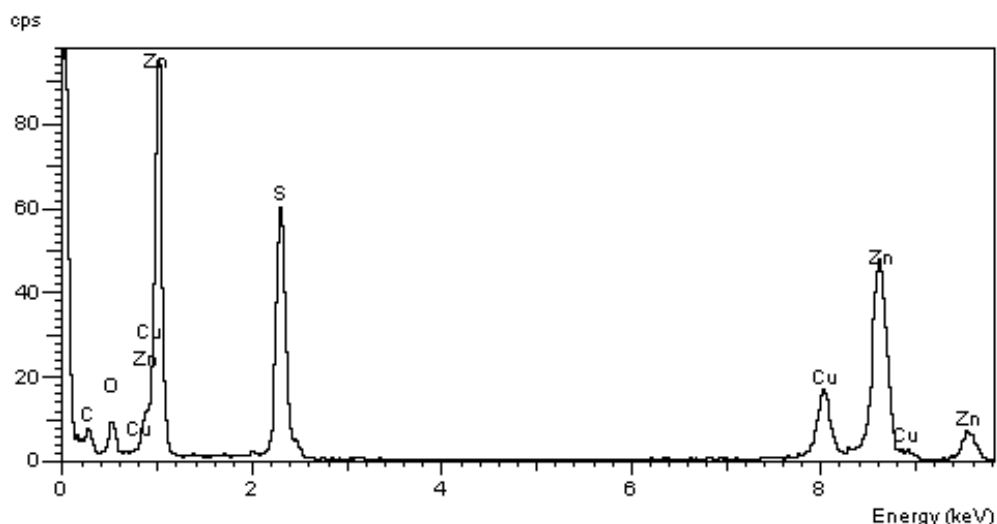


Figure 4.8. EDX Spectrum collected for sample ZnS 400

4.3.3 Synthesis with Thiourea as the Sulphur Source

The experiments described in Section 4.2.4 (using thiourea as a sulphur source) resulted in clear, colourless products at reaction temperatures up to and including 350 °C. The samples were also shown to be negative when tested with a laser. From this, it can be inferred that a minimum reaction temperature of 400 °C is required for particle formation as a cloudy white suspension was obtained for sample ZnS- TU-400. This sample was dried and the powder analysed with XRD. The resulting pattern, shown in Figure 4.9, displayed no obvious peaks matching ZnS but the peaks were matched to zinc sulphate hydrate and zinc hydrogen sulphate (ICCD PDF 74-1331 and 78-2208 respectively).

This result shows that thiourea cannot be used interchangeably with thiocarbonylhydrazide to produce ZnS. To maintain the focus of this project, all further reactions were conducted using thiocarbonylhydrazide as the sulphur

source. Nevertheless, the method of using thiourea as a sulphur source for ZnS synthesis could be optimised in future work.

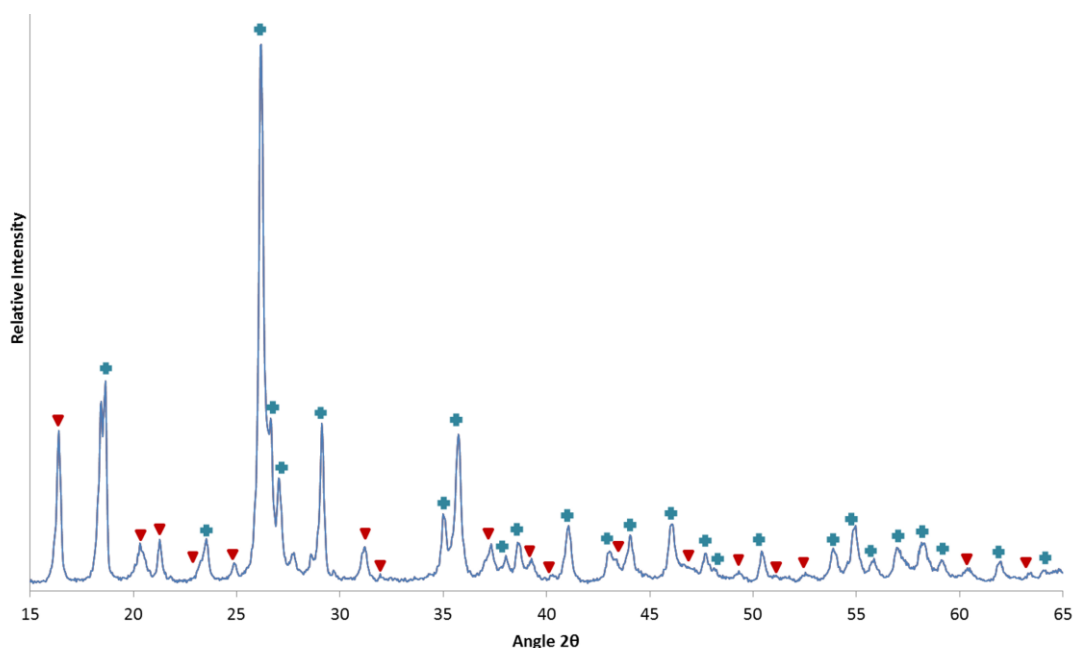


Figure 4.9. XRD pattern for Sample ZnS-TU-400. Peaks labelled with red triangles match zinc hydrogen phosphate and peaks labelled with blue crosses match zinc sulphate hydrate.

4.3.4 Synthesis of ZnS with Surfactants

In this Section the results from the experiments described previously in Section 4.2.5 will be presented and discussed. For each type of analysis performed, the ZnS products synthesised with the three different surfactants will be discussed together and compared to each other, and to ZnS particles produced in the absence of any surfactants – Uncapped ZnS.

For all the samples produced, at each flow ratio of the 3 different surfactants, samples were collected as cloudy suspensions - white/grey in colour - where the particles settled to the bottom of the vessel within a few hours.

4.3.4.1 XRD Data

XRD analysis performed on ZnS:NaOH 5/5, ZnS:PVP 5/5, ZnS:3-MPA 5/5 and Uncapped ZnS produced only peaks which could be assigned to ZnS. Therefore, it can be concluded that ZnS is the only crystalline phase present in the samples. However, each sample is composed of different crystal phases of ZnS – as such, there are discrepancies between the XRD patterns of the four samples. Of the four samples, the patterns for Uncapped ZnS and ZnS:PVP 5/5 are the most similar to each other. Both have peak positions matching ICCD PDFs 80-20 and 80-7 - corresponding to cubic and hexagonal ZnS respectively. Nevertheless, the peaks consistent with hexagonal ZnS are more distinct in ZnS:PVP, compared to Uncapped ZnS, which suggests either that the hexagonal phase is more abundant, or more crystalline. Moreover, the pattern for ZnS:PVP contains peaks matching ICCD PDF 12-688, the pattern for another phase of hexagonal ZnS. From this, it can be inferred that the presence of PVP in the reaction promotes the formation of hexagonal crystal phase over cubic phase.

The XRD pattern for ZnS:NaOH contains peaks which can also be ascribed to cubic and hexagonal phases of ZnS (ICCD PDFs 80-20, 5-566 and 12-688), as does the pattern for ZnS:3-MPA. The peaks in the latter sample match the database pattern file 75-1534. It is difficult to conclude from this data if the pattern also matches PDF 12-688, which is hexagonal phase, or PDF 5-566, which is cubic phase, as the peaks lie in similar positions. However, as the pattern for ZnS:3-MPA is very similar to that of the other ZnS samples, it is likely to also be a mixture of cubic and hexagonal phases.

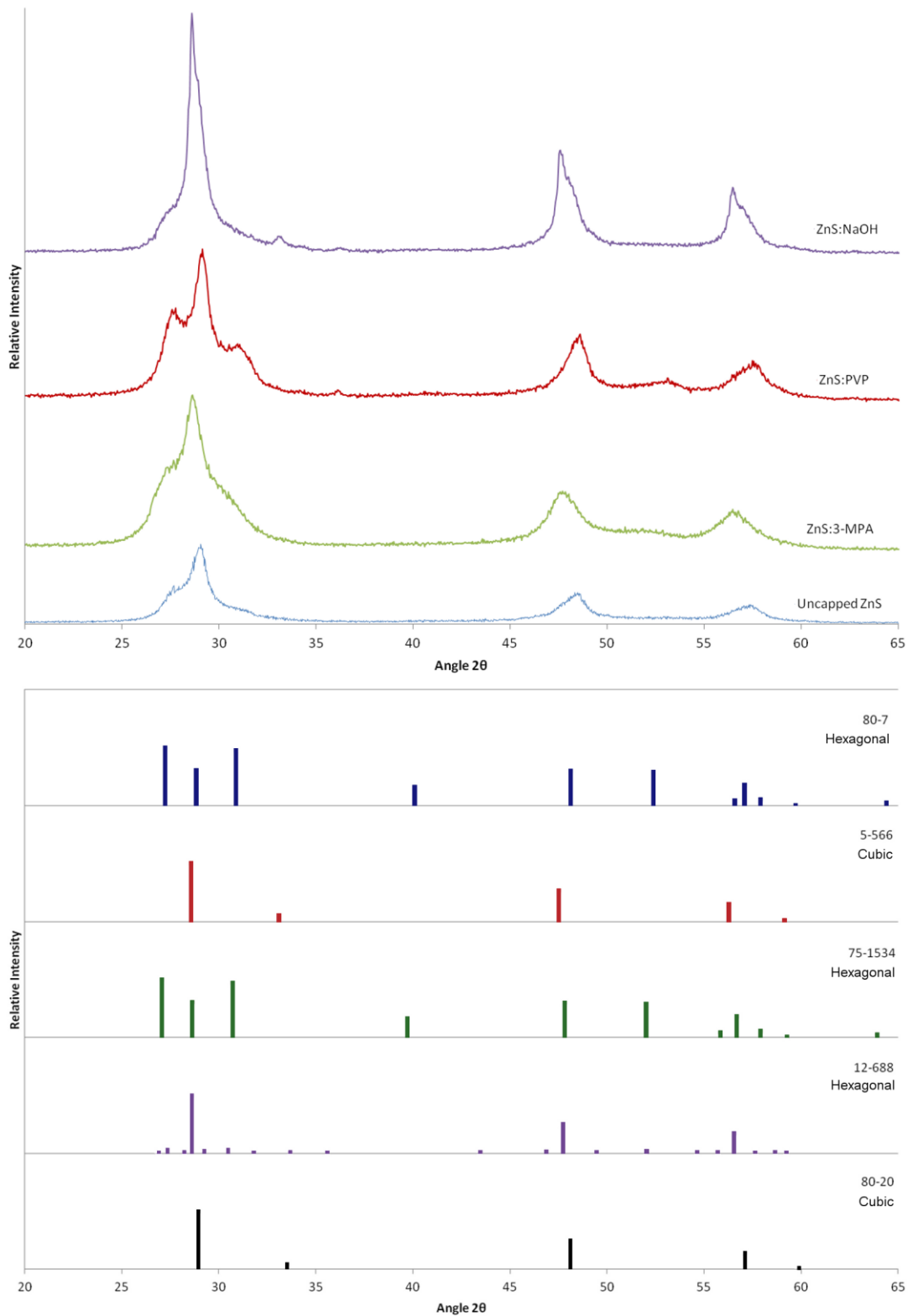


Figure 4.10. XRD Patterns of the four ZnS samples with the matched peak positions of different ZnS phases shown below. Numbered labels indicate the ICDD PDF file number and the corresponding crystal phase is given.

4.3.4.2 Crystallite Size

In terms of peak shape, the XRD pattern obtained for ZnS:NaOH contains peaks which are slightly narrower and sharper than those seen for the other three samples. As discussed in Chapter 2, sharper, narrower peaks can either mean a higher degree of crystallinity in the sample, or, in the case of nanoparticles, a larger average crystallite size compared to samples which exhibit broader XRD peaks.

To determine if the crystallite size phenomena is valid in the case of these samples, particle size analysis was required. As such, SEM images were collected for the four samples. These are presented in Figure 4.11. The micrographs indicate the presence of clustered particles where the level of clustering, and the size of the clusters varies between samples. In all four samples, the clusters are <300 nm and the compositional particles much smaller than this (<50 nm as seen under SEM at higher magnification, and based on TEM images collected for sample ZnS 400). Hence, the XRD peak broadening can be ascribed to the presence of small crystallites. The crystallite size calculations will be discussed in this Section, while more in depth analysis of the SEM data will be detailed in Section 4.3.4.3.

To calculate the average crystallite size for each sample, Xfit software was used. The results, along with the crystal phase data inferred from XRD patterns, are presented in Table 4.7. For Uncapped ZnS, the calculated crystallite size is 4.1 nm while for ZnS:PVP it is slightly bigger at 4.6 nm. For ZnS:NaOH, it appears that addition of NaOH to the ZnS synthesis reaction leads to a significant increase in the crystallite size, as the calculated value here is 5.8 nm (this corresponds to the earlier point of sharper narrower peaks seen in the XRD pattern of this sample). This significant increase in crystallite size may be due to

NaOH having a neutralising effect on the synthesis reaction; the nitrate precursor creates acidic conditions through the generation of HNO₃, which leads to surface oxidation of the particles and termination of growth. However the presence of NaOH counteracts this, the surfaces do not become oxidised, and crystal growth prevails.

Finally, the average crystallite size for sample ZnS:3-MPA was calculated as 3.1 nm – significantly smaller than the other three samples. A possible explanation for this is the efficient binding of 3-MPA to the surface of the ZnS nanoparticles, which prevents further crystallite or particle growth.

Table 4.7. Summary of crystal phase and crystalline size for each sample, as derived from XRD analysis.

| Sample | ICCD PDF Match | Crystal Phase [^] | Crystallite Size* |
|--------------|--------------------------|----------------------------|-------------------|
| Uncapped ZnS | 80-20 80-7 | Cubic/Hexagonal | 4.1 nm |
| ZnS:PVP | 80-20 80-7 12-688 | Cubic/Hexagonal | 4.6 nm |
| ZnS:NaOH | 80-20 5-566 12-688 | Cubic/Hexagonal | 5.8 nm |
| ZnS:3-MPA | 5-566 75-1534 | Cubic/Hexagonal | 3.1 nm |

[^] Crystal phase identified using EVA software

*Crystallite size calculated using Xfit software

4.3.4.3 SEM Analysis

The SEM images shown in Figure 4.11 will be discussed in this Section. As mentioned previously in Section 4.3.4.2, the images show clusters of particles. To some extent, the clustering effect is due to the sample preparation step prior to SEM analysis – where liquid samples are dried on the sample stub, surface tension may cause particles to stick together. Nevertheless, the effect that each surfactant has on particle aggregation can be assessed from this data.

SEM images were also collected for the samples synthesised using different flow ratios of each of the surfactants; these are shown in the Appendix but in the interest of comparison, only SEM images of the samples produced at 5/5 flow ratios are presented and discussed here.

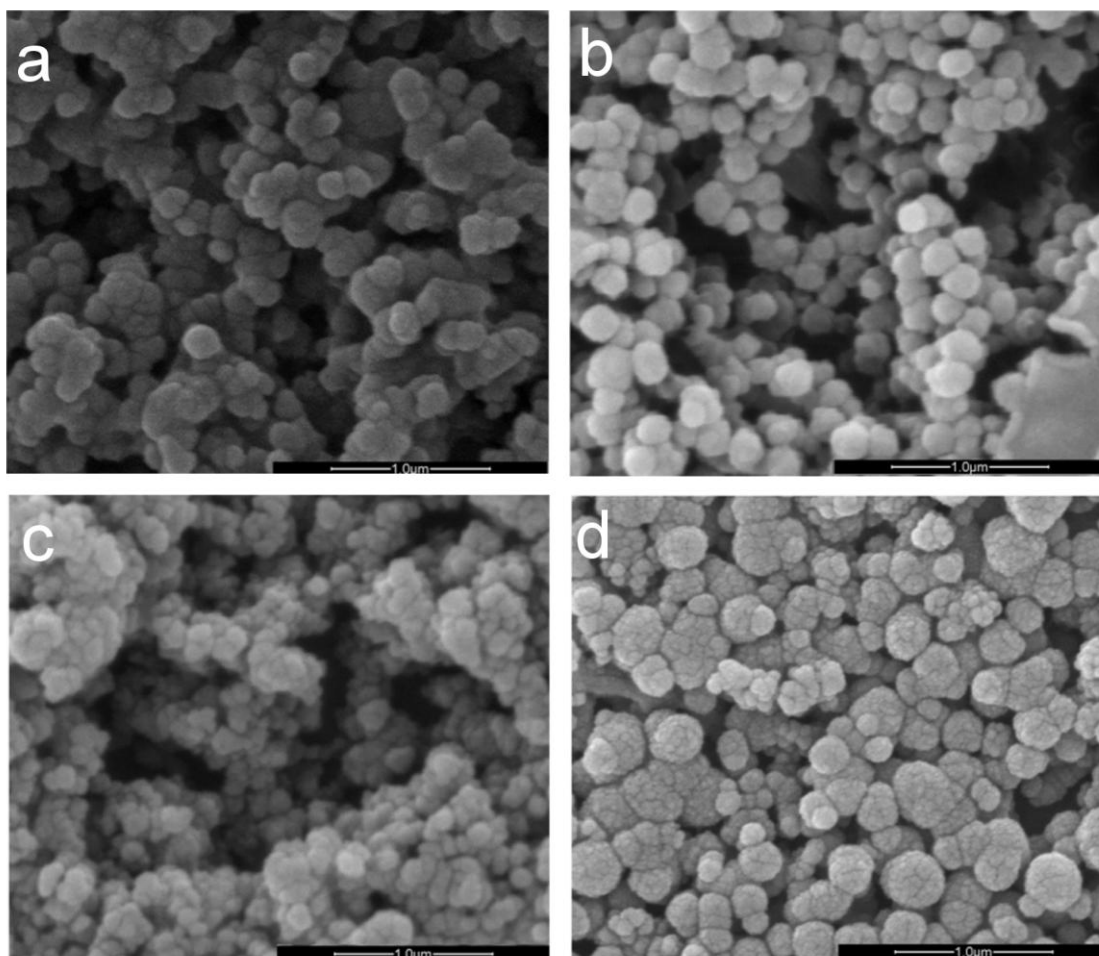


Figure 4.11. SEM images of (a) Uncapped ZnS; (b) ZnS:PVP 5/5; (c) ZnS:NaOH 5/5; and (d) ZnS:3-MPA 5/5.

The sizes of 20 clusters in each sample were measured from the SEM images, and an average calculated along with the standard deviation from the mean. This data is shown in Table 4.8. The 20 clusters were chosen at random for analysis from the top of the sample as seen in the micrograph. This was to ensure any differences in scale, due to the sample depth of view, were minimised.

Table 4.8. A table showing the average cluster size for each sample, as measured from SEM images.

| Sample | Average Cluster Size (nm) |
|---------------|---------------------------|
| Uncapped ZnS | 201.7 ± 46.5 |
| ZnS:PVP 5/5 | 207.4 ± 39.2 |
| ZnS:NaOH 5/5 | 165.3 ± 25.7 |
| ZnS:3-MPA 5/5 | 157.2 ± 65.7 |

The clusters seen in ZnS:PVP are slightly bigger than those present in Uncapped ZnS, while in ZnS:NaOH and ZnS:3-MPA, they are smaller. This difference may be due to the effectiveness of each of the surfactants in preventing the aggregation of primary particles. It can be deduced, following the data presented in Section 4.3.2 for sample ZnS 400, that without the addition of any capping agents or surfactants, the nanoparticles in sample Uncapped ZnS aggregate and form the clusters seen in Figure 4.11 (a). However, if the presence of NaOH and 3-MPA are indeed preventing particle aggregation (even if only to some extent), then the clusters would be smaller than in the control sample, which is what can be observed in Figure 4.11 (c) and Figure 4.11 (d). Therefore, the SEM data suggests NaOH and 3-MPA are lessening the degree of ZnS particle aggregation. On the contrary, the larger average cluster size seen for ZnS:PVP (in Figure 4.11 (b)) may be a result of the PVP polymer coating the clustered particles, as opposed to the desired effect of coating the individual primary particles.

Unlike the images for the other three samples, the clustered particles present for ZnS:3-MPA (in Figure 4.11 (d)) are apparently more “textured” and can be clearly seen, even at lower magnifications, to be formed of smaller particles. This may be further indication of 3-MPA preventing the formation of tightly aggregated particles; instead the particles are only loosely coagulated. It is likely

that the observed coagulation of particles is due to an insufficient concentration of 3-MPA present during synthesis, therefore the nanoparticles have not been completely coated with the surfactant.

To further investigate the effect of each surfactant on the stability of ZnS particles, zeta potential measurements were taken over a pH range. These data are presented and discussed in Section 4.3.4.4.

4.3.4.4 Zeta Potential Measurements

Zeta potential measurements were taken over a pH range for the four samples, to ascertain the point of zero charge (PZC) or iso-electric point (IEP). These data are shown in Figure 4.12 and with the individual data points for each sample given in the Appendix. The zeta potential profile for Uncapped ZnS confirms that in acidic conditions, the particles have a positive zeta potential and under basic conditions, the particles have a negative zeta potential. From this profile, it can be deduced that the IEP of Uncapped ZnS is approximately pH 7.8. This means that at this pH, there are little repulsive forces keeping the particles apart, and they are likely to coagulate rapidly. The IEP of ZnS particles has previously been reported at pH 5.5 (Durán et al., 1995); the IEP measured for sample Uncapped ZnS may be higher due to the surface oxidation reactions which occur as a result of the acidic conditions of synthesis (due to the nitrate precursor used).

Only in basic conditions (pH 10 or higher) is the zeta potential of Uncapped ZnS < -30 mV and the dispersion can be considered stable. These data corresponds with the problems associated with particle aggregation seen for unmodified QDs, which were outlined in Section 4.1 and reinforces the need for viable surfactants.

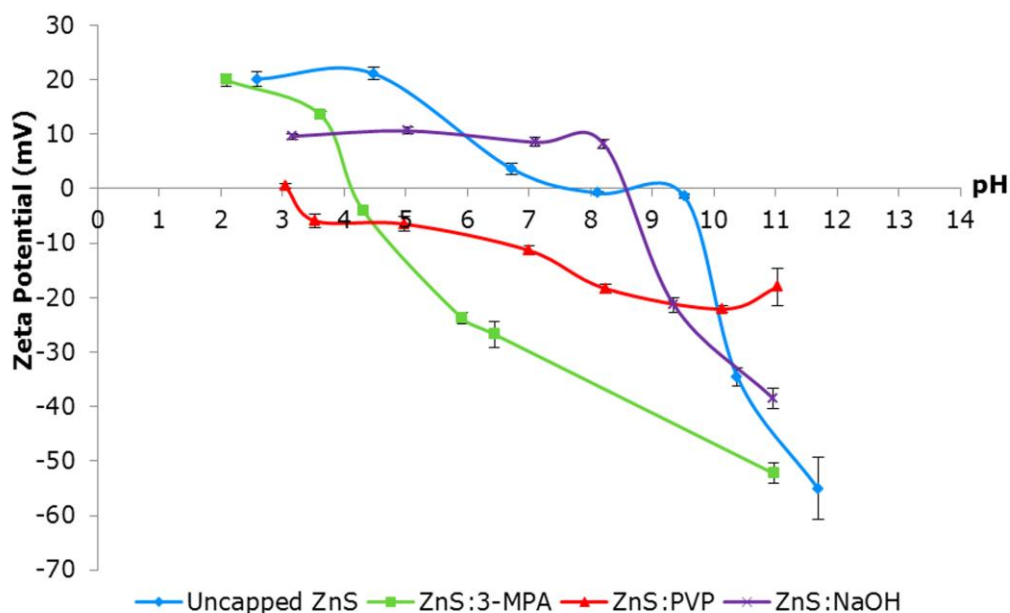


Figure 4.12. Zeta potential profiles for the four samples, as a function of pH.

It can be seen that the zeta potential profiles for the four samples are indeed different, indicating that the different capping agents are affecting the surface chemistry of the ZnS particle. In the case of ZnS:3-MPA the IEP is reached ca. pH 4.1 – a shift compared to Uncapped ZnS – and at neutral pH, the zeta potential is <-30 mV suggesting the particles are stable. In this sample, the particles are capped by an acidic species; Figure 4.13 shows the predicted surface modification of ZnS particles with 3-MPA. In water, the acid group dissociates to leave COO^- at the surface. As a result, the electrical double layer of the particle (and in turn the zeta potential) is negative at neutral pH. In addition, more H^+ ions must be added (i.e. the pH reduced further) in order to give a positive zeta potential, compared to the Uncapped ZnS sample.

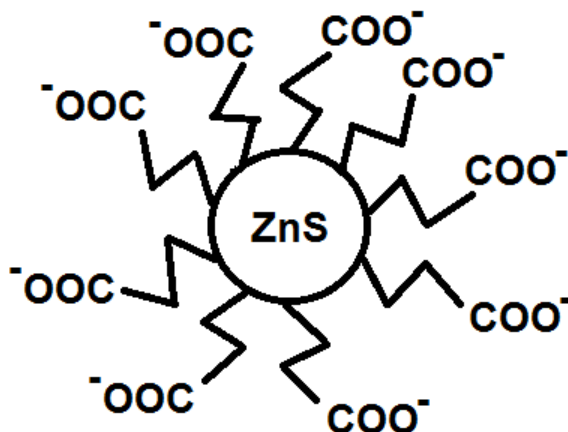


Figure 4.13. A schematic diagram depicting ZnS particles surface modified with 3-MPA.

On the contrary, sample ZnS:NaOH - which has been capped with an alkaline species - has a slightly positive zeta potential value at pH 7 and an IEP ca. pH 8.5, marginally more basic compared to Uncapped ZnS. Like the sample Uncapped ZnS, particles in ZnS:NaOH exhibited a zeta potential < -30 mV, and are deemed stable, at pH 10 or more.

Unlike NaOH and 3-MPA, PVP is a non-ionic surfactant - where it provides stabilisation through steric hindrance as opposed to surface charge modifications. Therefore, the zeta potential profile for ZnS:PVP is largely unaffected by changes to pH, and over the pH range tested, the sample did not have a zeta potential which could be concluded as stable. Although the resulting profile yields an IEP ca. pH 3, it was not possible to measure the zeta potential at a lower pH.

At pH values less than 2-3 or more than 11-12, the conductivity of the samples were too high to be measured by the same means and equipment; thus accurate data could not be obtained at these pH environments.

This zeta potential data demonstrates that PVP is not a suitable surfactant for the charge stabilisation of ZnS particles. The addition of NaOH to the reaction scheme does appear to affect the surface chemistry of the ZnS particles, but the zeta potential profile is still similar to that of the Uncapped ZnS particles. The most effective surfactant of the three tested is 3-MPA, as the IEP is significantly shifted away from neutral pH. Instead, the particles have a zeta potential of < -30 mV at pH 7. This means that the ZnS particles are less likely to aggregate at neutral pH when surface modified with 3-MPA. This is particularly pertinent for biological applications, where cellular environments tend to be ca. pH 7.

4.3.4.5 Fluorometry Analysis

The specific excitation and emission sweeps for the four samples, Uncapped ZnS and ZnS synthesised with each of the three surfactants at a 5/5 flow ratio, are shown in Figure 4.14. The intensity of fluorescence is measured in relative fluorescence units, RFU. It is important to note that the measured RFU is dependent on the concentration of ZnS present in the sample; however, the ZnS concentration varies between the samples so the fluorometry data obtained can only be assessed qualitatively, and not quantitatively, i.e. the peak positions for each sample are of importance, but the signal intensity cannot be compared in a meaningful way. For all samples and blanks, the excitation spectra were collected with the emission held at 540 nm. The emission spectra were collected with excitation maintained at 360 nm.

The excitation spectrum for Uncapped ZnS shows that the unmodified particles fluoresce with the highest intensity at 540 nm, when excited with light at 360 nm. Parallel to this data, the emission spectrum shows that when excited with light at 360 nm, the emission by particles actually covers a broad wavelength

range, with the peak intensity at 558 nm – a wavelength corresponding to green colour in the visible light range.

Samples ZnS:PVP and ZnS:NaOH display very comparable excitation and emission spectra to Uncapped ZnS, with peaks in similar positions. Nevertheless, there are subtle differences. For both these modified samples of ZnS, the excitation peak at 360 nm is less intense than at lower wavelengths. Instead, the peak falls at 282 nm. However, there is still a fluorescence signal when excited at 360 nm; as such, emission data was taken at this excitation wavelength for ease of analysis. Figure 4.14 (b) shows that the emission peak for ZnS:NaOH is broad, but the most intense emission is at a wavelength of 556 nm – very similar to Uncapped ZnS and again, corresponds to green light. This is somewhat different to PL data previously reported, where ZnS particles synthesised with NaOH showed emission at 440 nm when excited at 323 nm (Shen et al., 2007). This is likely to be because the particles prepared in the literature by ultrasonication resulted in the formation of ZnS/ZnS(OH)₂ core/shell nanoparticles where Zn(OH)₂ alters the PL properties.

The emission peak for ZnS:PVP also covers a broad range of wavelengths, but the highest RFU was detected at 572 nm – slightly red shifted compared to Uncapped ZnS, and correlates to yellow light. Many existing reports using PVP as a capping agent discuss QDs with a cadmium-based core and a ZnS shell; as such, the PL data cannot be directly compared (Saraswathi Amma et al., 2008).

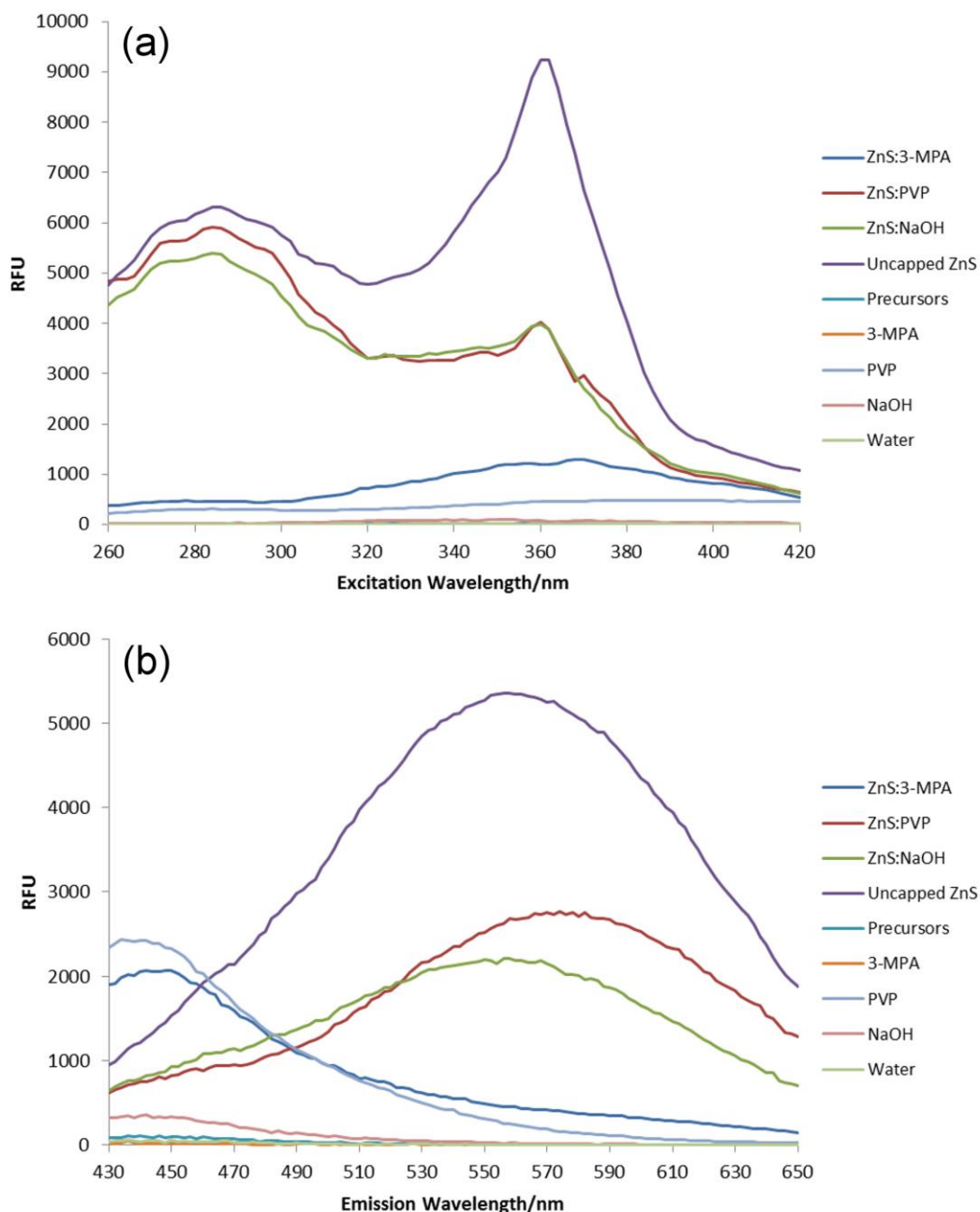


Figure 4.14. (a) The excitation spectra ($\lambda_{em} = 540$ nm) and (b) emission spectra ($\lambda_{ex} = 360$ nm) for Uncapped ZnS and ZnS produced with three different surfactants using 5:5 flow ratios. The spectra of the precursors and water blank were obtained as a control.

The excitation and emission spectra for ZnS:3-MPA is unlike that of the other samples. The excitation spectrum exhibits only one peak, as opposed to the two

seen in the other three samples. While the excitation peak does reach a maximum at 366 nm, similar to that of Uncapped ZnS, the emission spectrum was significantly different to that of the other three samples. Although the emission signal was detected over a wide range of wavelengths, the most intense signal was detected at 450 nm – violet or blue colour in the visible light range. This emission data is comparable to previous reports of ZnS capped with MPA; particles synthesised by a chemical precipitation method yielded a broad emission spectrum with a peak at 425 nm (blue light) when excited at 310 nm (Rosli et al., 2012). Conversely, introducing a dopant appears to have a vast effect on PL; ZnS particles doped with Mn and capped with MPA gave broad PL emission peaks around 598 nm – orange light – when excited at 320 nm (Kong et al., 2012).

As a control, the excitation and emission spectra were also collected for a water blank, and for each of the precursors. With the exception of PVP, no fluorescence signal was detected in these controls. This shows that the fluorescence signal detected in the samples can indeed be attributed to the ZnS, rather than their starting materials. In the case of PVP, the excitation and emission spectra are remarkably similar to that of ZnS:3-MPA, with the emission peak ca. 450 nm. As PVP is not expected to fluoresce, the signal is most likely due to bleedthrough fluorescence from the ZnS:3-MPA sample which was in the adjacent well during analysis. Moreover, the emission peak at 450 nm was not detected in the sample ZnS:PVP, reinforcing that bleedthrough is the most likely cause.

To further investigate the effect of 3-MPA on the PL properties of ZnS, the excitation and emission spectra for the ZnS:3-MPA samples produced using different precursor flow ratios, are displayed in Figure 4.15. The excitation spectra, seen in Figure 4.15 (a), shows that ZnS:3-MPA 9/1 has a very similar spectra to that of Uncapped ZnS, with peaks at the same wavelength. Increasing

the concentration of 3-MPA only slightly, as is the case for the 8/2 sample, saw a discernible change in the excitation spectrum from Uncapped ZnS; the secondary peak seen ca. 280 nm has flattened out in ZnS:3-MPA 8/2, while the most intense fluorescence signal is still produced when excited at 360 nm. When the ratio of 3-MPA to ZnS is increased beyond this, the excitation spectra collected for the samples are significantly different and show only one peak, around 365 nm.

Correspondingly, the emission spectra in Figure 4.15 (b) shows that ZnS:3-MPA 9/1 yields a similar profile to Uncapped ZnS, and there is only a slight red-shift in the peak to 548 nm. Sample 8/2, however, shows a more obvious shift in the peak, to 526 nm – although still in the range of green light. With a higher ratio of 3-MPA in the samples (ratios 7/3, 6/4 and 5/5), the peak shifts to the blue light range below 495 nm.

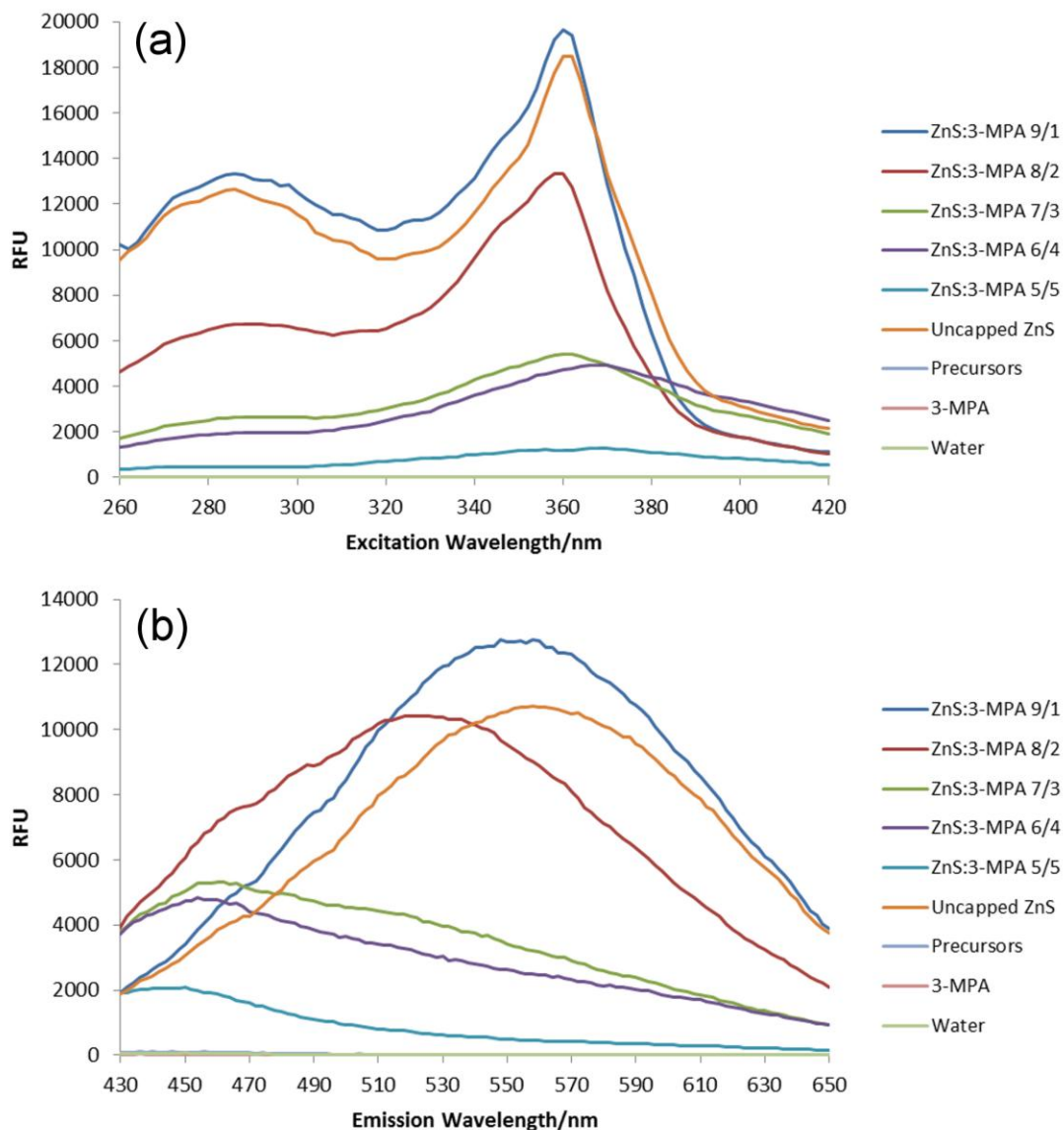


Figure 4.15. (a) The excitation spectra ($\lambda_{em} = 540$ nm) and (b) emission spectra ($\lambda_{ex} = 360$ nm) for ZnS:3-MPA samples produced using different precursor flow ratios. The spectra of the precursors and water blank were obtained as a control.

This PL data suggests that there is a critical concentration ratio of 3-MPA to ZnS which changes fluorescent properties. This work can be further investigated in future work, to optimise surfactant concentration. The PL data for ZnS samples produced with different ratios of PVP and NaOH did not show significant

differences from the PL data of Uncapped ZnS, so are presented in the Appendix, but will not be discussed in detail in this Chapter.

The difference in wavelengths at which the particles in each sample fluoresce is of interest, because there is a correlation to the average cluster size which was discussed in Section 4.3.4.3. The crystallite size, cluster size and emission data for the four samples is reviewed in Table 4.9. It can be seen that there is a trend: the larger the average cluster size, the longer the wavelength at which particles peak in emission.

Table 4.9. A summary of the average crystallite size, average cluster size, and wavelength of peak emission for each ZnS sample.

| Sample | Average Crystallite Size (nm) | Average Cluster Size (nm) | Wavelength of emission peak (nm) |
|---------------|--------------------------------------|----------------------------------|---|
| Uncapped ZnS | 4.1 | 201.7 | 558 |
| ZnS:PVP | 4.6 | 207.4 | 572 |
| ZnS:NaOH | 5.8 | 165.3 | 556 |
| ZnS:3-MPA | 3.1 | 157.2 | 450 |

The differences in wavelength of peak emission between the different ZnS samples indicates that the band gap energies of the particles are varied; another factor which is affected by the choice of surfactant.

This correlation also suggests that the particles are behaving (namely fluorescing) as clusters, rather than as primary particles or crystallites. Consequently, this means there is still some degree of particle aggregation in all the samples. While the addition of the surfactants has been shown to lessen the aggregation, the process has not been optimised to completely eradicate it. The

broad emission peaks seen for all four samples in Figure 4.14 (b) also suggests that there is a wide particle or cluster size distribution (Bruchez Jr et al., 1998), as QDs have size-dependent optical properties as explained by quantum confinement theory (Dickerson, 2005).

4.4 Conclusions

In this Chapter, the protocol for CdS synthesis was replicated and bright yellow particles of diameters 20 to 50 nm were produced at 240 bar and 400 °C - consistent with what was seen previously. In addition, it was found that at temperatures below 400 °C, no particles were formed. The TEM images captured for the sample were not clear enough to distinguish if the particles were composed of smaller, aggregated particles, or were just formed of different crystallites. The fluorometry data collected for the CdS sample were inconclusive within the scope of this Thesis; instead, the aim of the synthesis experiment was to demonstrate the reproducibility of the method established by previous researchers.

The methodology for CdS synthesis was adapted to produce ZnS nanoparticles. Using $\text{Zn}(\text{NO}_3)_2 \cdot 6\text{H}_2\text{O}$ instead of the $\text{Cd}(\text{NO}_3)_2 \cdot 4\text{H}_2\text{O}$ precursor, white/grey particles were synthesised at 240 bar and 400 °C. As with CdS, no particles were produced at temperatures below this. The XRD pattern collected for the sample proved it to contain a mixture of hexagonal and cubic phases of ZnS, but no other crystalline phases were detected. The sample was also analysed under TEM which showed primary particle sizes <15nm but had aggregated into clusters – 50 to 100 nm in diameter. Furthermore, EDX data confirmed the presence of only the expected elements.

Attempts were made to produce ZnS nanoparticles using thiourea as a sulphur source, rather than the more toxic reagent thiocarbohydrazide. Consistent with previous experiments, no particles were generated at temperatures up to and including 350 °C (with the system pressure at 240 bar). However, at 400 °C, white/grey particles were synthesised. XRD analysis on these particles revealed

them to be a mixture of zinc sulphate hydrate and zinc hydrogen sulphate rather than ZnS. This demonstrates that, in the established protocol for ZnS synthesis, thiocarbonylhydrazide and thiourea cannot be used interchangeably to produce ZnS.

The final set of experiments described in this Chapter yielded unmodified ZnS particles which were compared to ZnS produced with three different capping agents – an acid, a base and a polymer. The samples were analysed using SEM, XRD, zeta potential and fluorometry techniques. The results showed that without any capping agents, and consistent with previous data, a mixture of hexagonal and cubic phases of ZnS was produced. The average crystallite size is 4.1 nm, but the particles aggregate into clusters with an average diameter of 202 nm. The particles were shown to reach their IEP at a pH ~7.8 and upon excitation with UV light at 360 nm, they fluoresced in the visible light range; while the emission range was broad, the strongest signal was detected at 558 nm – green light.

Introducing NaOH into the reactor during synthesis of ZnS does not appear to affect the crystal phase of the product, but the average crystallite size was increased to 5.8 nm. This is likely to be due to neutralisation of the reaction environment, meaning crystal surfaces are not oxidised and growth continues to a degree. The base did have an effect on aggregation as the average cluster size was decreased to 165 nm, and the zeta potential data showed that the pH at which the IEP of particle was reached had shifted from 7.8 to 8.5. However, the obtained fluorescence data was very similar to that of Uncapped ZnS, with a broad emission peak and the optimum fluorescence detected at 556 nm – again, green light.

The addition of PVP to the synthesis method did not appear to prevent primary particles from aggregating; instead the polymer seemed to coat the clustered particles. PVP also did not affect the crystal phase of ZnS produced, but the calculated average crystallite size was marginally bigger at 4.6 nm. As PVP is a non-ionic surfactant, the zeta potential data collected could not conclusively show the IEP of ZnS:PVP. The fluorometry analysis did show this sample had a red shifted emission peak compared to Uncapped ZnS, with the highest emission at 572 nm – yellow light.

The work described in this Chapter shows that, of the three surfactants tested, 3-MPA has the most potential in the stabilisation of ZnS nanoparticles. The XRD data indicated that hexagonal and cubic phase crystals were produced with a smaller calculated crystallite size than Uncapped ZnS – 3.1 nm - which may be due to the prevention of further crystallite growth after 3-MPA had successfully bound to the particle surface. While some degree of particle aggregation was still evident from the SEM data, the average cluster size had decreased to 157 nm. Moreover, the zeta potential data showed a shift in the profile and the IEP was reached at pH 4.1. The excitation and emission data was radically different to the other samples, with emission blue shifted and reaching a peak at 450 nm – corresponding to violet or blue light. The difference in emission peak position between the four samples is likely due to differences in particle band gap energies. In addition, the PL emission data from ZnS:3-MPA is in a comparable wavelength range to that previously reported for cadmium-based QDs (Saraswathi Amma et al., 2008), thus there is the potential to develop ZnS as a heavy-metal free QD alternative.

Prior to this work, continuous hydrothermal synthesis had not been used to produce fluorescent nanoparticles of ZnS. Although the samples described in this work have not been fully stabilised to isolate the primary particles and prevent

them from aggregating, their fluorescent potential has been demonstrated, and 3-MPA was shown to be the most effective at stabilising these ZnS particles. The ratio between surfactant and particle concentration must be carefully balanced in order to achieve stabilisation, and is dependent on several factors, including particle size. It is therefore likely that the surfactant concentrations used in this work were insufficient to effectively cap the particles completely. Consequently, there is scope for additional studies which investigate the optimum surfactant concentration to coat and stabilise ZnS nanoparticles, while supplementary analysis could also quantify the quantum yield of these particles. While fluorometry analysis has been conducted in this Thesis to assess the PL properties of the ZnS particles, other tests can also be carried out to measure their electroluminescent properties. This would allow the material to be applied in several different potential applications, such as in electronic devices.

Chapter 5

Magnetic Resonance Imaging (MRI) Contrast Agents

5.1 Introduction

5.1.1 Principles of MRI

While X-rays have been used since their discovery in 1895 to gather information about the internal structure of human and animal bodies - from diagnostic to research purposes - they are not without their drawbacks. X-rays can only image hard tissue, such as bone, clearly; this means soft tissues such as tendons, ligaments, organs and even blood cannot be detected or imaged well. Furthermore, X-rays are a form of ionising radiation which can, above certain thresholds, cause defects in the DNA of individuals exposed to it, and lead to knock-on effects - including cancer formation (Chang and Hou, 2011). As such, X-ray exposure in patients must be carefully monitored and only used if absolutely necessary. From this, there was no doubt that a more effective alternative was required. In the 1970's, a technique called Magnetic Resonance Imaging (MRI) was developed and applied to the field of medicine, which could image the soft tissues and blood in the body, without the use of any form of ionising radiation (Mansfield and Maudsley, 1977, Mansfield and Pykett, 1978).

An MRI scanner is composed of several parts. The predominant part is a large, powerful magnet (a clinical scanner usually has a 1.5 T magnet) which forms a cylinder around the area holding the sample or the patient (see Figure 5.1). MRI operates by manipulating and measuring the hydrogen atoms present in a sample or a patient. Because humans are predominantly composed of water, there are plenty of hydrogen atoms to measure.

The positive charge of the hydrogen nuclei (a single proton), coupled with the spin it possesses, gives rise to a magnetic field or magnetic moment. Under the influence of a large external magnetic field (such as a body or sample being placed into an MRI scanner), the magnetic moments of the hydrogen nuclei become aligned. Within an MRI scanner, there are Radio Frequency (RF) coils to produce extra gradients of magnetic field; these can be rapidly switched on and off to create a non-uniform magnetic field in the body or sample being scanned. The RF coils emit an RF pulse which is specific to H atoms only, and the energy is absorbed by the atoms. This causes them to 'flip', so that the magnetic dipole now faces 180° from its previous direction. When the RF pulse is switched off, the H atoms flip back to their previous alignment in the magnetic field and release a signal or "spin echo", as well as the energy that it had absorbed. The spin echo is made up of several frequencies, which correspond to the different positions along the magnetic field gradient; it is detected by the RF coil and is converted to its component frequencies. At each frequency, the signal magnitude is related to the density of hydrogen nuclei at that respective position. As a result, the spin echo signal also contains spatial information and can be used to generate a greyscale image (Conn, 2009).

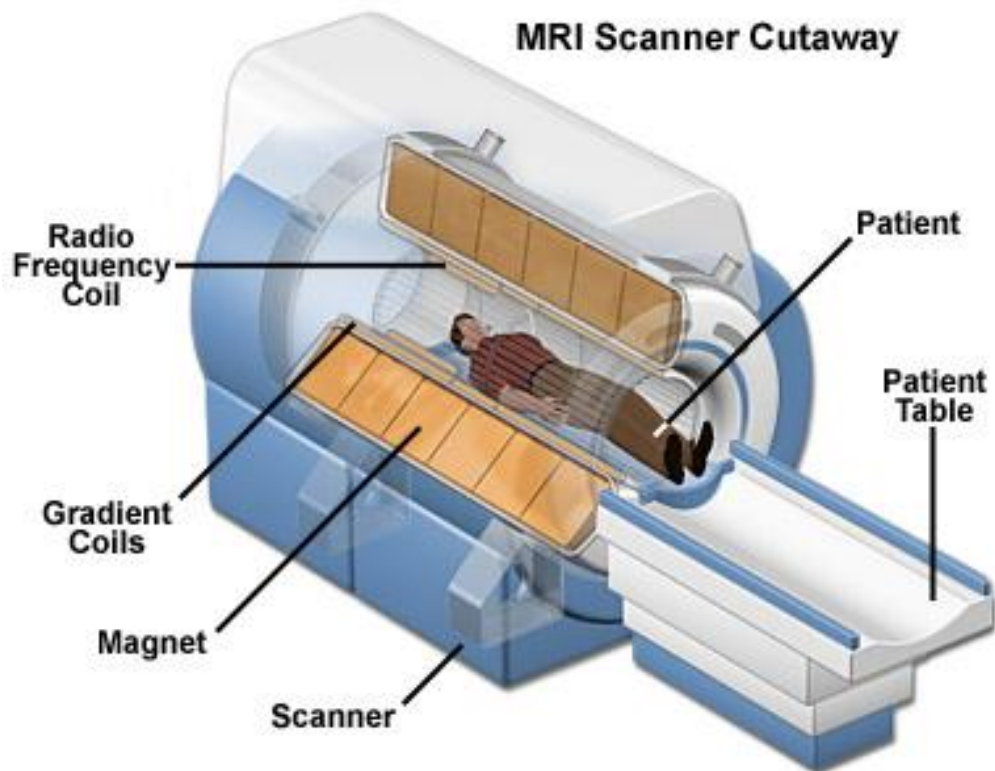


Figure 5.1. An image of an MRI scanner depicting the different components (Action, 2013).

Where there is a high concentration of hydrogen atoms present (due to the large quantity of water), there will be a large signal, and will show up as bright white patches in the image. Conversely, where there is a low concentration of H atoms (such as lipid or fatty tissues), the signal will be small, and therefore manifest as dark patches in the image (Oldendorf, 1988).

Also present in MRI scanners are gradient coils. These can fine tune the magnetic field so that only a specific region of the patient or sample is analysed. For example, if the liver is of interest then only a cross-section, down to a few millimetres, of the liver can be imaged. This cross-section is known as a 'slice'. The presence of these gradient coils also means that different regions can be

imaged and analysed without having to move the patient or sample (Conn, 2009).

5.1.2 MRI Scans

As the RF pulse is switched off, the H nuclei recover to their natural alignment; the magnetisation of the nuclei exists along the direction of the applied field (termed the longitudinal component or z plane) and perpendicular to the direction (termed the transverse component or xy plane). These planes are shown in Figure 5.2. Relaxation times T_1 and T_2 , which are typically measured during MRI scans, indicate the time required for the recovery of the H nuclei to equilibrium, in the longitudinal and transverse components, respectively. This forms the basis of the two main types of MRI scan – T_1 -weighted and T_2 -weighted.

T_1 relaxation is also called spin-lattice relaxation and denotes the rate at which the longitudinal component of the magnetization vector recovers to equilibrium maximum from zero. It measures the degree to which the spins are being disrupted by the surrounding tissue, hence it is known as spin-lattice relaxation. The image produced distinguishes between water, which appears darker, and fat, which is shown as lighter areas (Oldendorf, 1988).

Conversely, T_2 -weighted scans measure the time (usually in milliseconds, ms) taken for the transverse component of the magnetisation vector to recover and decay the signal. In the transverse direction, magnetisation recovery is dependent on how spins interact with each other and put each other out of phase, so it is also called spin-spin relaxation. T_2 -weighted images are almost an inverse of T_1 -weighted images – water and fluids appears lighter while fat, darker. The T_2 relaxation time is actually the time taken for the signal to decay

to 37% of its original value (Brown and Semelka, 2010). Figure 5.2 summarises the relationship between T_2 relaxation time and spin recovery.

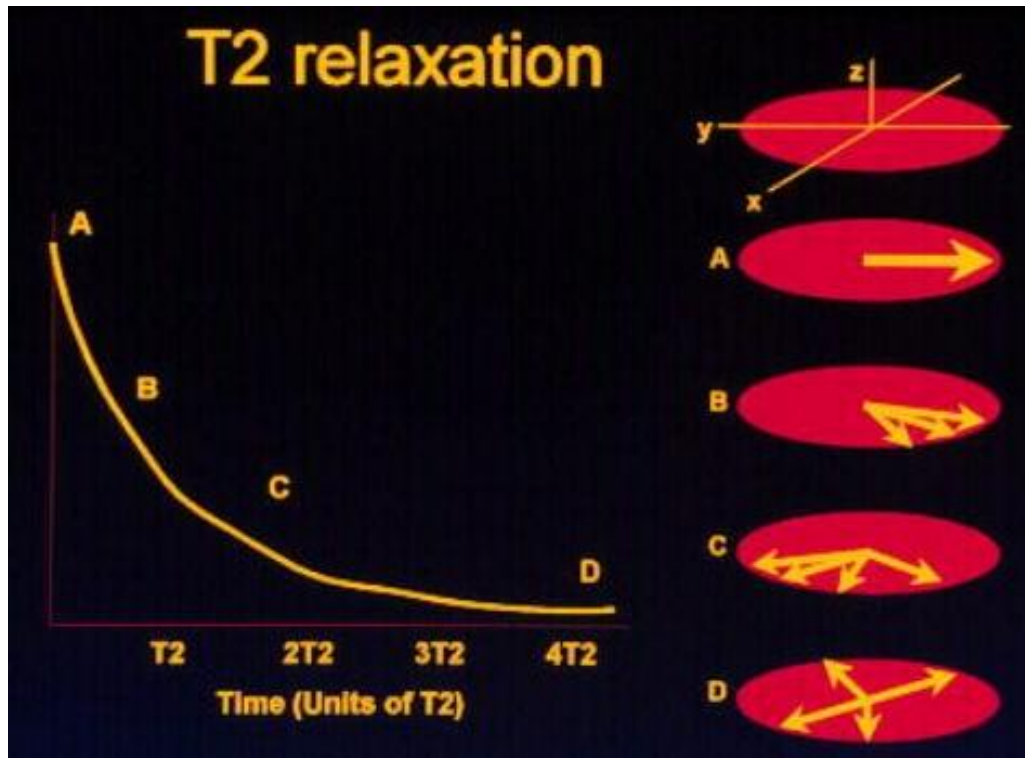


Figure 5.2. A diagram showing the z (longitudinal) and xy (transverse) planes of magnetisation. The relationship between T_2 relaxation time and spin recovery is also summarised (Oldendorf, 1988).

5.1.3 Relaxation Time, Rate and Relaxivity

It is important to note that the relaxation time of a tissue or a contrast agent is not to be confused with its relaxation rate. The latter, represented as R_2 , is an inverse of the T_2 relaxation time, or $1/T_2$. Moreover, contrast agents can be compared by their relaxivity, or their ability to increase the relaxation rates of the surrounding water proton spins. The relationship between relaxivity, r_2 , and R_2 is shown by the following equation (Brown and Semelka, 2010):

Equation 1
$$R_2 = \frac{1}{T_{2,H_2O}} + r_2 [\text{Fe}]$$

Where: R_2 is $1/T_2$ in s^{-1} ;
 T_2, H_2O is the relaxation time of protons in water (s);
 r_2 is the relaxivity of the contrast agent ($mM^{-1} s^{-1}$), and
 $[\text{Fe}]$ is the concentration of iron (mM)

Rearranging the equation allows for the relaxivity (r_2) to be calculated:

Equation 2
$$r_2 = \left(\frac{1}{T_2} - \frac{1}{T_{2,H_2O}} \right) / [\text{Fe}]$$

As T_2 relaxation times are concentration-dependent, comparing contrast agents by relaxivity rather than T_2 times gives a better indication of how effective each material is as a contrast agent.

5.1.4 Role of Contrast Agents

In most cases of clinical MRI scans, the region of interest contains tissues with sufficient contrast to allow the operator or consultant to distinguish between two different tissues (e.g. normal healthy tissue and a tumour). However, this is not always true and the different tissues can manifest as two very similar shades of grey in the image. To overcome this problem, contrast agents can be used. These are materials which can be introduced to a subject or patient, and improve visibility of the organ by reducing the T_1 or T_2 relaxation time of water protons in the tissue of interest, thereby enhancing the contrast. Organs which are commonly imaged by MRI include the gastrointestinal tract, the brain, liver, and spleen (Conn, 2009).

Contrast agents are usually inorganic compounds which can be conjugated to a chosen biomarker - which will target and bind to a specific tissue, such as a tumour, to ensure the contrast agent highlights only a designated region of interest (McCann et al., 2011). Contrast agents which are currently used are administered either orally or intravenously, depending on the target organ.

Reports indicate particles to be used as contrast agents for MRI must be smaller than 5 μm in order to avoid being trapped in the lungs (Bammer et al., 2005). Furthermore, particles with superparamagnetic properties (this is where the magnetisation is at an average of zero, but particles can become magnetised by an external magnetic field) give the best effects for T_2 -weighted imaging; thus, nanoparticles of iron oxide are typically used for transverse scans. These fall into two main categories: superparamagnetic iron oxide nanoparticles (SPIOs) and ultrasmall superparamagnetic iron oxide nanoparticles (USPIOs); ultrasmall nanoparticles are classed as having a diameter 30 nm or smaller (Thomsen and Webb, 2009). A few SPIO-based contrast agents are commercially available, including Feridex IV[®], and Combidex[®] (Stephen et al., 2011). These and a few other commercially available contrast agents will be described in Section 5.1.5. Meanwhile, T_1 -weighted scans typically use paramagnetic gadolinium (Gd) or manganese (Mn)-based agents (Conn, 2009); these are materials which become slightly magnetised when placed in a magnetic field, but lose this magnetism when the field is removed.

Coatings may be applied to the surfaces of contrast agents to improve stability and dispersion of the particles, thereby preventing coagulation (Tsai et al., 2010) (See Chapter 1, Section 1.9.2); to lengthen the shelf life of the suspension; and in some cases, to improve the biocompatibility or to provide an anchor on which other materials can be attached (Chekina et al., 2011). Other researchers have

reported the use of silica (Casula et al., 2011), oleic acid (Zhang et al., 2006), and sodium bis(2-ethylhexyl)sulfosuccinate (AOT) (Zheng et al., 2006) as coating materials.

Figure 5.3 (a) shows an MR image of the liver of a patient with cancerous lesions, without any contrast agents being administered. By contrast, Figure 5.3 (b) is an MR image of the same patient's liver 10 minutes after a T_2 weighted contrast agent had been injected. The targeted cancerous region can be visibly seen as the darker area, making it easier for radiologists locate lesions for treatment.

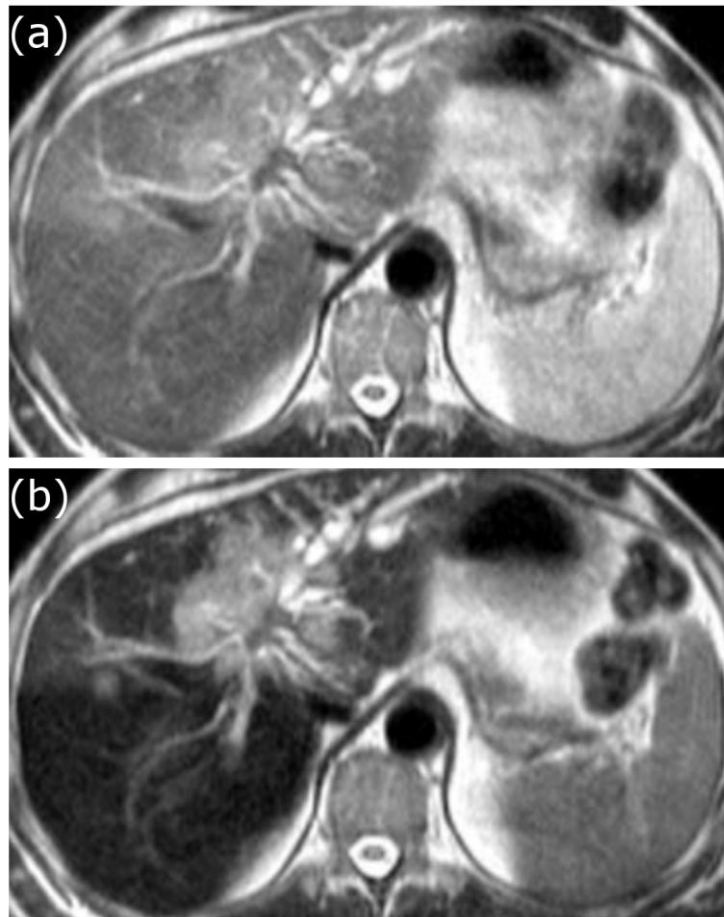


Figure 5.3. (a) Native MR Image (no contrast agent present) of liver in a patient with cholangiocellular carcinoma (cancer), and (b) MR image after T₂ weighted contrast agent has been administered. Differentiation of the lesion is vastly improved after contrast agent is introduced (AG, 2013).

After a SPION contrast agent is administered (typically by intravenous injection), it enters the bloodstream of an animal model or patient and is subsequently taken up into the liver, spleen, lymph nodes and bone marrow, through phagocytosis (internalisation and ingestion of foreign materials by phagocyte cells as a means of cell defence). Once in these organs, the contrast agents can begin localised decay of MR signal to create contrasted images (Wang, 2011). USPIOs, on the other hand, are small enough to remain in the blood pool,

rather than being taken up into organs (Bammer et al., 2005). Once the contrast agent takes effect, the window for optimum imaging lasts only a few hours (this varies depending on the contrast agent used) as the particles begin to be metabolised by lysosomes. These are cell components which secrete enzymes to 'digest' waste materials and remove them; the contrast agent is consequently broken down and excreted. In the case of SPIONs and USPIOs, these are metabolised to a non-superparamagnetic form of iron which can then be 'recycled' in cells, such as in haemoglobin.

In the current market, the most commonly used contrast agents are gadolinium (Gd) based molecules. However, as a heavy metal, Gd is extremely toxic and accumulation in the body can be fatal. Consequently, the contrast agents are synthesised so that the Gd^{3+} ion is trapped in a molecular cage or strongly bound to ligands, so that it does not bind to cell components (Carbonaro et al., 2011). Other species, including iron oxide-based agents, are arguably better for use in MRI as the particles can be digested by natural cell processes without posing toxicity risks. In conclusion, good contrast agents feasible for commercial application should strike a balance between having high relaxivity and low toxicity, whilst being economically feasible.

5.1.5 Commercial Contrast Agents

A variety of nanoscale contrast agents are currently used, or have been used in the past, for clinical MRI scans; the majority of these are based on iron oxide nanoparticles. A few will be briefly described in this Section.

5.1.5.1 Feridex IV[®]

Developed by AMAG Pharmaceuticals, Feridex IV[®] are SPIONs coated with low molecular weight Dextran. Particle size ranges between 120 and 180 nm, and its r_2 relaxivity is $98.3 \text{ mM}^{-1} \text{ s}^{-1}$ (Wang, 2011). Feridex I.V[®] is used specifically for MR imaging in the liver to detect lesions and is administered as a drip infusion which takes roughly 30 minutes. Around 6-8% of the SPIONs are taken up by the liver starting within 8 minutes of injection, though optimum imaging (maximum signal decay) occurs after one hour. The length of time for contrast agent activity varies between patients but is typically between 30 minutes and 6 hours from administration (Wang, 2011). Although Feridex IV[®] was, and possibly still is, used in a clinical background; its manufacture has since been discontinued by AMAG Pharmaceuticals (AMAG Pharmaceuticals, 2013).

5.1.5.2 Resovist[®]

Produced by Schering AG, the active ingredient in Resovist[®] are carboxydextrane-coated SPIO particles. These have a reported hydrodynamic diameter of 45-60 nm, where larger particles are taken up faster, and a r_2 relaxivity of $151 \text{ mM}^{-1} \text{ s}^{-1}$ (Wang, 2011). Resovist[®] is also used for T_1 -weighted MRI, but with mixed results – therefore it is principally used for T_2 -weighted imaging in the liver. Quick uptake by the reticuloendothelial system (part of the body's defence mechanism) means Resovist[®] is effective in as little as 10 minutes after injection, with approximately 85% of the administered dose taken up by cells in the liver. Furthermore, Resovist[®] has shown a very good safety profile and is widely used by radiologists (AG, 2013).

5.1.5.3 Ferumoxtran-10

Known as Combidex in the USA and Sinerem in Europe, this contrast agent was developed by AMAG Pharmaceuticals and is based on USPIOs (35 nm in diameter) coated in dextran (Hudgins et al., 2002). Sinerem was used in Europe on a clinical basis, but Combidex did not advance past trial stages in the USA. Both products have since been discontinued.

The r_2 relaxivity of Sinerem was $60 \text{ mM}^{-1} \text{ s}^{-1}$ and due to the small size of particles, they tended to build up in lymph nodes. However nodes containing cancerous tissue, and lacking certain cell components, could not uptake Sinerem and hence did not show a decayed MR signal and could be easily spotted (Harisinghani et al., 2003). Nevertheless, it took over 24 hours before particles were properly uptaken and MR images could be obtained.

In 2009, a study on 296 patients with prostate cancer assessed the use of ferumoxtran-10 and MRI to detect cancerous lymph nodes (Heesakkers et al., 2009). Findings of a 24.1% false positive rate lead to the clinical development of ferumoxtran-10 being halted, and AMAG Pharmaceuticals subsequently discontinued production. While Combidex/Sinerem had some flaws, the underlying research approach into its development is still considered to be promising (Wang, 2011).

5.1.5.4 Clariscan™

Composed of SPIONs with a carbohydrate polyethylene glycol (PEG) coating, Clariscan™ was developed by GE Healthcare (formerly Nycomed Imaging). Total particle diameters lie in the region of 20 nm, with r_2 relaxivity measuring $35.3 \text{ mM}^{-1} \text{ s}^{-1}$ (Bjørnerud et al., 2001). Clariscan™ is principally

uptaken to the liver and spleen, and has been used to characterise tumour development by providing contrast in the MRI of blood vessels (Wang, 2011). However, production of Clariscan™ was discontinued amid safety concerns.

5.1.5.5 Omniscan®

The active ingredient in Omniscan® is the Gd(DTPA-bismethylamide)(H₂O) complex, which yields an r₂ relaxivity of 3.4 mM⁻¹ s⁻¹. However, it is principally used as a T₁-weighted contrast agent due to its good r₁ relaxivity of 4.9 mM⁻¹ s⁻¹ (Dutta et al., 2008). Manufactured by GE Healthcare, Omniscan® has been used in clinical applications, mainly in the USA, for over 20 years. It is administered intravenously, and can be used to image the brain, spine, kidney, intrathoracic, intra-abdominal and pelvic regions (Healthcare, 2013).

5.1.6 Current Methods of Synthesising Contrast Agents

While there is little information publically available detailing the synthesis methods for commercial contrast agents, there is a vast array of journal publications describing the synthesis and testing of nanomaterials for MRI use.

As is the case with many nanomaterials, co-precipitation is one of the most widely used synthesis methods. One example described this synthetic route for the production of Fe₃O₄, NiFe₂O₄ and CuFe₂O₄ nanoparticles (Covaliu et al., 2011). In this study, chitosan and sodium alginate were used to coat the particles but while magnetic measurements confirmed the superparamagnetic nature of the coated particles, neither their relaxation times nor relaxivities were analysed.

Other commonly described methods to manufacture magnetic nanoparticles include thermal decomposition (Bateer et al., 2013, Khodadadi-Moghaddam et al., 2013), microemulsion (Darbandi et al., 2012, Bao et al., 2006), hydrothermal synthesis (Haw et al., 2010, Bae et al., 2012) and sonochemical routes (Zhang et al., 2012).

Regardless of the synthesis route chosen, a common observation which researchers have identified is the need for particles to be coated in order to improve biocompatibility and dispersibility in water (Jadhav and Bongiovanni, 2012, Karimi et al., 2013).

5.1.7 Chapter Aims

To avoid these issues of toxicity, this Chapter focuses on non-Gd based contrast agents, namely iron oxide nanoparticles hematite (Fe_2O_3) and magnetite (Fe_3O_4). Hence the aim of this Chapter is to use the counter-current Nozzle reactor to synthesise materials of interest as MRI contrast agents, and to characterise their respective particle sizes, crystallinity, and applicability as a contrast agent, where the latter will be measured as the T_2 time. These values will then be used to calculate the material's relaxivity.

Although the principle focus will be on iron oxides synthesised by the continuous hydrothermal reactor, and their suitability as T_2 -weighted contrast agents, cobalt oxide (Co_3O_4) and gadolinium hydroxide ($\text{Gd}(\text{OH})_3$) will also be synthesised and analysed. These materials were chosen because they have previously been manufactured successfully on the counter-current Nozzle reactor (Lester et al., 2012). Furthermore, cobalt-based nanoparticles have reportedly exhibited positive results for MRI (Parkes et al., 2008). Although Gd-based contrast agents after typically used for T_1 -weighted MR imaging, it is possible these particles also

exhibit positive results for T₂-weighted scans (Dutta et al., 2008); hence, Gd(OH)₃ will also be tested along with the iron oxide samples.

Products will be produced pure (no coatings or surfactants added), or with one of three different polymers added as a coating; these being polyvinylpyrrolidone (PVP), dextran or sodium alginate. PVP was chosen due to its known biocompatibility, low cost and its widespread availability (Sharma et al., 2010); Dextran has been widely reported as a surfactant for Fe₃O₄ particles in MRI applications (Ding et al., 2010, Mornet et al., 2004); and sodium alginate has been reported in coating magnetic nanoparticles for biomedical applications (Mu et al., 2012, Covaliu et al., 2011).

5.2 Methodology

5.2.1 Hydrothermal Synthesis of Nanoparticles

The reagents used for synthesis were hydrogen peroxide, H_2O_2 ; iron (III) nitrate nonahydrate, $\text{Fe}(\text{NO}_3)_3 \cdot 9\text{H}_2\text{O}$ ($\geq 98\%$ purity); ammonium iron (III) citrate, $\text{NH}_3 \text{Fe}(\text{C}_6\text{H}_5\text{O}_7)$ (reagent grade); cobalt acetate tetrahydrate, $\text{Co}(\text{CH}_3\text{COO})_2 \cdot 4\text{H}_2\text{O}$ (reagent grade); gadolinium (III) acetate hydrate, $\text{Gd}(\text{CH}_3\text{CO}_2)_3 \cdot x\text{H}_2\text{O}$ (99.9% purity); polyvinylpyrrolidone (PVP), $(\text{C}_6\text{H}_9\text{NO})_n$ (average molecular weight of 10,000); dextran low fraction, $(\text{C}_6\text{H}_{10}\text{O}_5)_n$, from Acros Organics; and sodium alginate, $\text{NaC}_6\text{H}_7\text{O}_6$.

Unless otherwise stated, all chemical reagents were purchased from Sigma Aldrich (UK) and used without further purification. DI grade water was used for the work in this Chapter.

5.2.1.1 Hematite, Fe_2O_3

To produce Fe_2O_3 , a 0.05 M $\text{Fe}(\text{NO}_3)_3 \cdot 9\text{H}_2\text{O}$ aqueous solution was used as a precursor. A brief reaction schematic with flows and flow rates can be seen in Figure 5.4. Three different reaction temperatures were employed to produce samples, ~ 150 , ~ 200 and ~ 300 °C, as this has previously been shown to affect particle size (Li, 2008). For each of these temperatures, a control sample was produced without any surfactants, and then each of the three capping agents, PVP 10, dextran or sodium alginate, was introduced. Therefore, twelve samples of Fe_2O_3 were synthesised. The temperatures at different points in the reactor system are summarised in Table 5.1, Table 5.2 and Table 5.3. The positions of the thermocouples where these temperatures were logged can be found in

Chapter 1, Section 1.7.2.1. For all samples, the system pressure was maintained at 240 bar by the BPR. Previous unpublished work by other researchers using the Nozzle reactor found that adding surfactants or capping agents at the second metal salt pump was more effective at coating particles than introducing them at the capping point. It is for this reason that the capping agents were introduced in this manner.

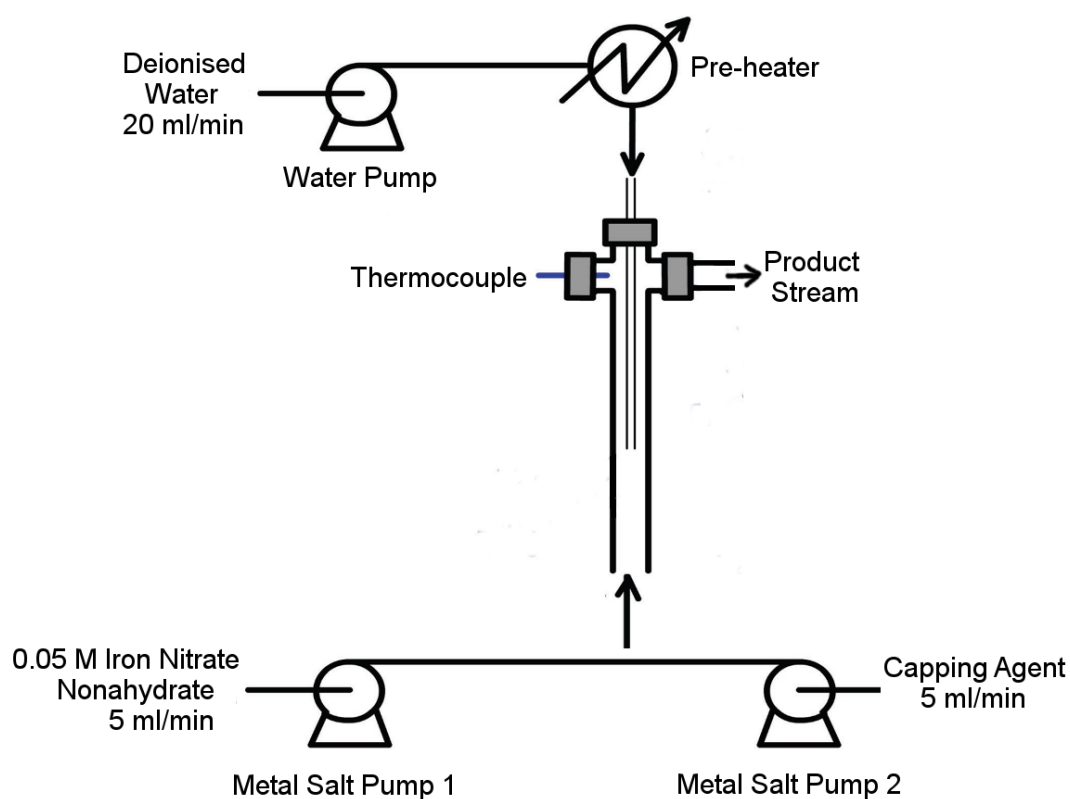


Figure 5.4. A schematic diagram showing the reaction setup for synthesis of Fe_2O_3 .

Table 5.1. Summary of Temperatures and Flows for first set of Fe₂O₃ Samples.

| Sample Name | Capping Agent Flow | Temperatures (°C) | | | | |
|-------------|--------------------------------|------------------------|--------------|-------------------|---------------|-------------|
| | | Water Heater Set Point | After Heater | Post Mixing Point | Capping Point | Post Cooler |
| HEM A1 | Water | | | | | |
| HEM A2 | 1 wt% PVP 10 | | | | | |
| HEM A3 | 1 wt% Dextran | 185 | 154 | 107 | 71 | 29 |
| HEM A4 | 0.25 wt% Sodium Alginate | | | | | |

Table 5.2. Summary of Temperatures and Flows for second set of Fe₂O₃ Samples.

| Sample Name | Capping Agent Flow | Temperatures (°C) | | | | |
|-------------|--------------------------------|------------------------|--------------|-------------------|---------------|-------------|
| | | Water Heater Set Point | After Heater | Post Mixing Point | Capping Point | Post Cooler |
| HEM B1 | Water | | | | | |
| HEM B2 | 1 wt% PVP 10 | | | | | |
| HEM B3 | 1 wt% Dextran | 240 | 203 | 135 | 86 | 31 |
| HEM B4 | 0.25 wt% Sodium Alginate | | | | | |

Table 5.3. Summary of Temperatures and Flows for third set of Fe₂O₃ Samples.

| Sample Name | Capping Agent Flow | Temperatures (°C) | | | | |
|-------------|--------------------------------|------------------------|--------------|-------------------|---------------|-------------|
| | | Water Heater Set Point | After Heater | Post Mixing Point | Capping Point | Post Cooler |
| HEM C1 | Water | | | | | |
| HEM C2 | 1 wt% PVP 10 | | | | | |
| HEM C3 | 1 wt% Dextran | 345 | 307 | 206 | 117 | 38 |
| HEM C4 | 0.25 wt% Sodium Alginate | | | | | |

The twelve synthesised samples were characterised using a 0.5 T MRI scanner to measure their T₂ times (see Section 5.2.2), and using DLS to determine the particle size of each sample. Samples HEM A1, B1 and C1 were oven dried in air at 70 °C overnight to obtain powders; these were then analysed using XRD. Details of the DLS and XRD equipment used were given in Chapter 2.

5.2.1.2 Magnetite, Fe₃O₄

For the synthesis of Fe₃O₄, a 0.05 M NH₃ Fe(C₆H₅O₇) aqueous solution was used as a precursor. Figure 5.5 shows a simple reaction schematic of the flow orientations and flow rates. Samples were produced with the water heater set at two different temperatures: ~350 and ~400 °C. For each of these temperatures, a control sample was produced without any surfactants, and then each of the three capping agents, PVP 10, dextran or sodium alginate, were introduced. In total, eight samples of Fe₃O₄ were obtained. The temperatures at different points

in the reactor system are summarised in Table 5.4 and Table 5.5. The positions of the thermocouples where these temperatures were logged can be found in Chapter 1, Section 1.7.2.1. For all samples, the system pressure was maintained at 240 bar by the BPR.

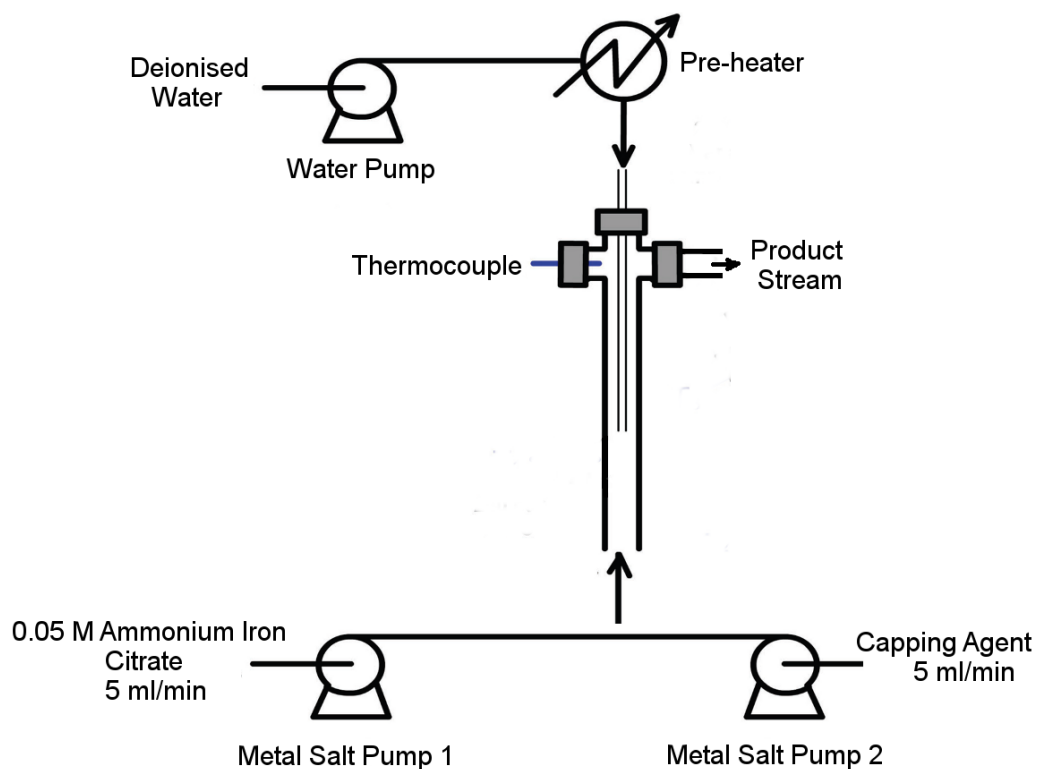


Figure 5.5. A schematic diagram showing the reaction setup for Fe₃O₄ synthesis.

Table 5.4. Summary of Temperatures and Flows for First Set of Fe₃O₄ Samples.

| Sample Name | Capping Agent Flow | Temperatures (°C) | | | | |
|-------------|--------------------------|------------------------|--------------|-------------------|---------------|-------------|
| | | Water Heater Set Point | After Heater | Post Mixing Point | Capping Point | Post Cooler |
| MAG F1 | Water | | | | | |
| MAG F2 | 1 wt% PVP 10 | | | | | |
| MAG F3 | 1 wt% Dextran | 385 | 353 | 239 | 127 | 40 |
| MAG F4 | 0.25 wt% Sodium Alginate | | | | | |

Table 5.5. Summary of Temperatures and Flows for Second Set of Fe₃O₄ Samples.

| Sample Name | Capping Agent Flow | Temperatures (°C) | | | | |
|-------------|--------------------------|------------------------|--------------|-------------------|---------------|-------------|
| | | Water Heater Set Point | After Heater | Post Mixing Point | Capping Point | Post Cooler |
| MAG G1 | Water | | | | | |
| MAG G2 | 1 wt% PVP 10 | | | | | |
| MAG G3 | 1 wt% Dextran | 450 | 402 | 340 | 211 | 50 |
| MAG G4 | 0.25 wt% Sodium Alginate | | | | | |

Samples MAG G1-G4 were characterised using a 0.5 T MRI scanner and a 2.35 T MRI scanner to measure their T_2 times (see Section 5.2.2). Samples MAG G1 and G3 were oven dried in air at 70 °C overnight to obtain powders, and analysed using XRD. These two samples were also analysed using TEM, for particle size and morphology data. Details of the XRD and TEM equipment used were given in Chapter 2.

5.2.1.3 Cobalt Oxide, Co_3O_4

The synthesis of Co_3O_4 was performed for a separate study (Moro et al., 2013), however a sample was also taken for MRI analysis. Here, a 0.05 M $\text{Co}(\text{CH}_3\text{COO})_3$ aqueous solution was used as a precursor. Figure 5.6 shows a simple reaction schematic of the flow orientations and flow rates. Hydrogen peroxide, H_2O_2 , was added to the water feed during synthesis, to provide a more oxidising environment for the breakdown of the CH_3COO^- ion from the precursor, and to drive oxidation of the Co^{3+} cation. Samples were produced with the water heater set at a temperature of ~ 400 °C. Unlike the samples of Fe_2O_3 and Fe_3O_4 , no surfactants were added to the synthesis of Co_3O_4 as it was not required for the separate study, and so one sample was obtained. The temperatures at different points in the system during synthesis are summarised in Table 5.6. The positions of the thermocouples where these temperatures were logged can be found in Chapter 1, Section 1.7.2.1. For all samples, the system pressure was maintained at 240 bar by the BPR.

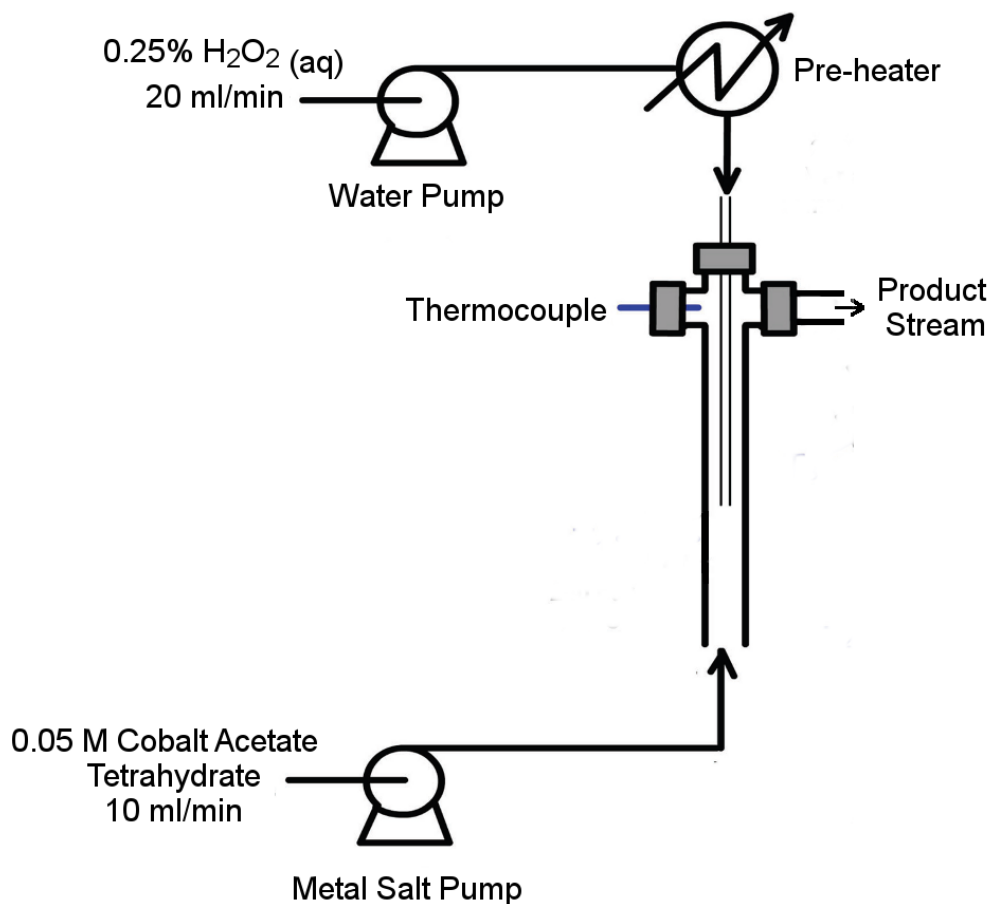


Figure 5.6. A schematic diagram showing the reaction setup for Co_3O_4 synthesis.

Table 5.6. A Summary of Temperatures for the Synthesis of Co_3O_4 Sample.

| Sample Name | Temperatures ($^{\circ}\text{C}$) | | | | |
|-------------------------|-------------------------------------|--------------|-------------------|---------------|-------------|
| | Water Heater Set Point | After Heater | Post Mixing Point | Capping Point | Post Cooler |
| Co_3O_4 | 430 | 427 | 376 | 173 | 32 |

The sample of Co_3O_4 was analysed using a 0.5 T MRI scanner (see Section 5.2.2). Because this material was produced as part of a separate study, XRD and TEM was also conducted on the sample and the acquired data will be presented in this Chapter.

5.2.1.4 Gadolinium Hydroxide, $\text{Gd}(\text{OH})_3$

To synthesise $\text{Gd}(\text{OH})_3$, a 0.05 M $\text{Gd}(\text{CH}_3\text{COO})_3$ aqueous solution was used as a precursor. Figure 5.7 shows a simple reaction schematic of the flow orientations and flow rates. Hydrogen peroxide, H_2O_2 , was added to the water feed during synthesis to provide a more oxidising environment for the breakdown of the CH_3COO^- ion from the precursor, and to drive oxidation of the Gd^{3+} cation. Samples were produced with the water heater set at one of two temperatures. At each temperature, a control sample was produced without any surfactants, and then each of the three capping agents, PVP 10, dextran or sodium alginate, was introduced. In total, eight samples were obtained. The temperatures at different points in the reactor system are summarised in Table 5.7 and Table 5.8. The positions of the thermocouples where these temperatures were logged can be found in Chapter 1, Section 1.7.2.1. For all samples, the system pressure was maintained at 240 bar by the BPR.

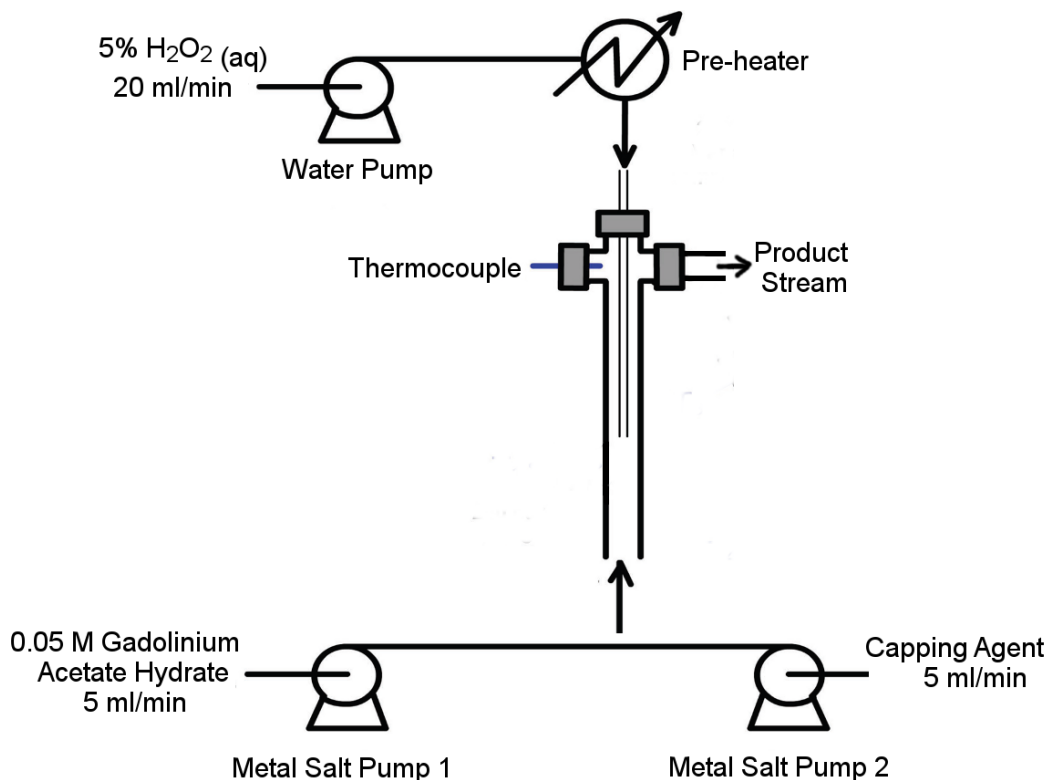


Figure 5.7. A schematic diagram showing the reaction setup for $\text{Gd}(\text{OH})_3$ synthesis.

Table 5.7. A Summary of Temperatures and Flows for the Synthesis of the First Set of $\text{Gd}(\text{OH})_3$ Samples.

| Sample Name | Capping Agent Flow | Temperatures ($^{\circ}\text{C}$) | | | | |
|-------------|--------------------------|-------------------------------------|--------------|-------------------|---------------|-------------|
| | | Water Heater Set Point | After Heater | Post Mixing Point | Capping Point | Post Cooler |
| GAD D1 | Water | | | | | |
| GAD D2 | 1 wt% PVP 10 | | | | | |
| GAD D3 | 1 wt% Dextran | 385 | 352 | 191 | 124 | 46 |
| GAD D4 | 0.25 wt% Sodium Alginate | | | | | |

Table 5.8 . A Summary of Temperatures and Flows for the Synthesis of the Second Set of Gd(OH)₃ Samples.

| Sample Name | Capping Agent Flow | Temperatures (°C) | | | | |
|-------------|--------------------------|------------------------|--------------|-------------------|---------------|-------------|
| | | Water Heater Set Point | After Heater | Post Mixing Point | Capping Point | Post Cooler |
| GAD E1 | Water | | | | | |
| GAD E2 | 1 wt% PVP 10 | | | | | |
| GAD E3 | 1 wt% Dextran | 450 | 406 | 303 | 185 | 60 |
| GAD E4 | 0.25 wt% Sodium Alginate | | | | | |

The four Gd(OH)₃ samples produced in the second experimental set were characterised using a 0.5T MRI scanner (see Section 5.2.2). Sample GAD E1 was also oven dried at 70 °C overnight to yield a white powder, which was then analysed using XRD to confirm the crystal phase produced.

5.2.2 MRI Characterisation of Samples

5.2.2.1 Halbach 0.5T Table-Top Scanner

Due to the high sample turnover from the continuous hydrothermal reactor, a large number of samples were synthesised. A preliminary MRI screening process was employed to ascertain an average T₂ relaxation time for each sample. This was conducted using a 0.5 T Halbach MRI system, based at Nottingham Trent University, using a repetition time of 2000 ms and 4 averages; thus each scan took 8 seconds. For the majority of samples, 128 echoes were

used; however, with the sample of Co_3O_4 and its precursor, 512 echoes were chosen to provide a more reliable result. Data analysis was performed with Prospa v2.1 software. This scanner, a photo of which is given in Figure 5.8, provided a rapid method for measuring T_2 values for each sample. Those which were most promising were then characterised further using DLS or TEM, and where appropriate, XRD. Details of these techniques were given in Chapter 2. Samples with low T_2 relaxation times from the 0.5 T Halbach system were also tested on a more powerful MRI scanner – a 2.35 T Bruker kit (described in Section 5.2.2.2.).

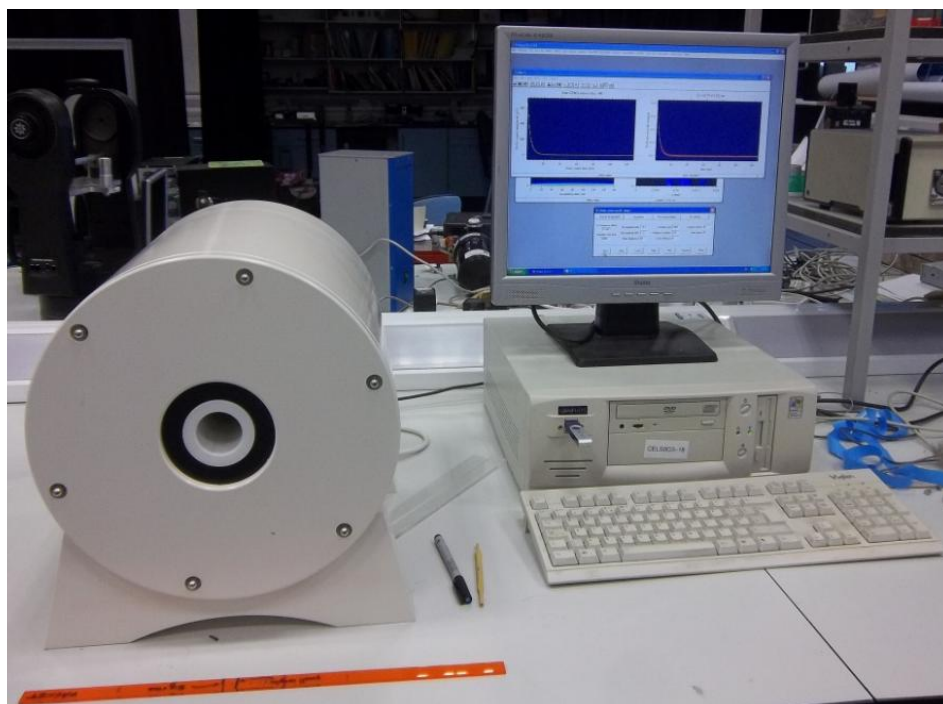


Figure 5.8. Photo of the Halbach 0.5 T Table-Top MRI Scanner at Nottingham Trent University.

5.2.2.2 Bruker 2.35 T Scanner

A select number of samples were taken forward to be scanned on the Bruker Biospin 2.3 T MRI system, based at Nottingham Trent University, and T_2

images were acquired. A photo of the equipment is shown in Figure 5.9. For each scan, a multi slice multi echo (MSME) sequence and the following parameters were used:

Field of View = 7 cm x 7 cm

Repetition Time = 2000 ms

Slice Thickness = 3 mm

Number of Slices = 5

Echo Time = 10.25 ms

Number of echoes = 24

It should be noted that 1 pixel in the obtained images corresponds to approximately 0.3 mm of real space.

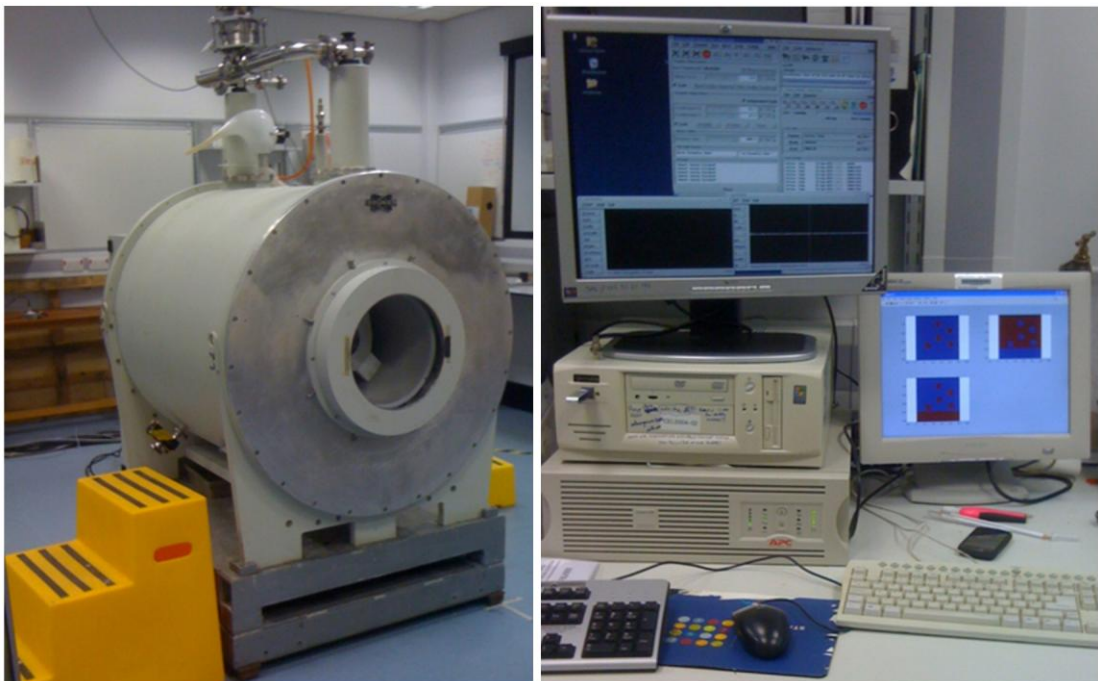


Figure 5.9. Photos of the Bruker 2.35 T MRI scanner at Nottingham Trent University.

5.3 Results and Discussion

5.3.1 Hematite, Fe_2O_3

The four samples of Fe_2O_3 synthesised at ~ 150 °C are shown in the photograph in Figure 5.10. Likewise, the four samples produced at ~ 250 °C are displayed in Figure 5.11, and the four samples obtained at ~ 350 °C are shown in Figure 5.12. When a laser light was passed through each sample vial, a beam path could be seen – indicative of particles being present in all samples. As the synthesis temperature increased, the colour of the samples became darker – this could be an indication of a change to particle size, or a difference in particle concentration.



Figure 5.10. Photograph of Fe_2O_3 Samples in First Temperature Set.



Figure 5.11. Photograph of Fe_2O_3 Samples in Second Temperature Set.



Figure 5.12. Photograph of Fe_2O_3 Samples in Third Temperature Set.

The T_2 relaxation times of the 12 HEM samples are given in Table 5.9; these were measured using the Halbach 0.5 T table-top scanner. Also shown in Table 5.9 are the r_2 relaxivities of each of the samples, calculated using Equation 2 which was stated in Section 5.1.3. For a more straightforward comparison of the different T_2 times, the data is summarised as a bar chart in Figure 5.13.

Table 5.9. Summary of the measured T_2 relaxation times for the Fe_2O_3 samples, precursor and water blank. The r_2 values, calculated using Equation 2, are also given.

| Sample Code | T_2 Time (ms) | Error (\pm) | r_2 ($mM^{-1} s^{-1}$) |
|------------------------------------|-----------------|-----------------|----------------------------|
| HEM A1 | 7.44 | 0.01 | 8.03 |
| HEM A2 | 6.89 | 0.01 | 8.68 |
| HEM A3 | 6.66 | 0.01 | 8.98 |
| HEM A4 | 8.56 | 0.01 | 6.98 |
| HEM B1 | 8.13 | 0.01 | 7.35 |
| HEM B2 | 7.43 | 0.01 | 8.04 |
| HEM B3 | 7.25 | 0.009 | 8.24 |
| HEM B4 | 8.31 | 0.01 | 7.19 |
| HEM C1 | 8.08 | 0.008 | 7.40 |
| HEM C2 | 9.18 | 0.009 | 6.51 |
| HEM C3 | 8.99 | 0.01 | 6.64 |
| HEM C4 | 9.25 | 0.01 | 6.46 |
| 0.05 M Iron Nitrate Nonahydrate | 15.6 | 0.002 | 1.27 |
| Water | 2122 | 0.01 | - |

Given the T_2 and r_2 data presented in Table 5.9, the set of samples with the highest and most promising relaxivities are HEM A – samples synthesised at the lowest reaction temperature. These samples were therefore taken for additional analysis using the Bruker 2.35 T scanner. The images obtained from these scans are presented in Figure 5.14.

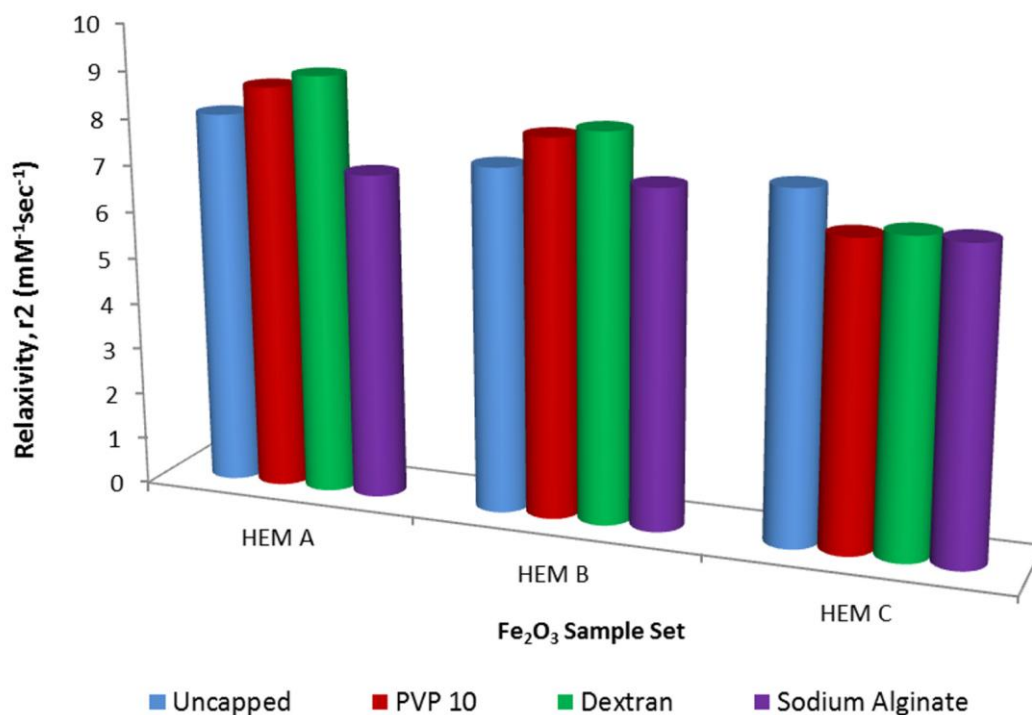


Figure 5.13. A bar chart summarising the r_2 relaxivities of the 12 samples of synthesised Fe_2O_3 , calculated using the T_2 times acquired using the 0.5 T Halbach scanner, and Equation 2.

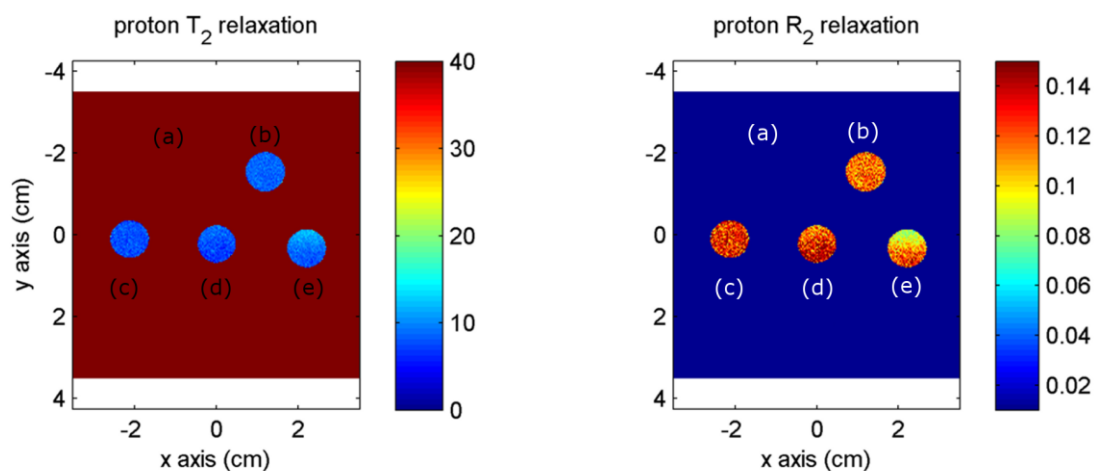


Figure 5.14. Images collected from the 2.35 T MRI scanner showing T₂ relaxation times (in ms) and R₂ relaxation for a) Fe(NO₃)₃·9H₂O, b) HEM A1, c) HEM A2, d) HEM A3, e) HEM A4.

The data acquired from the T₂ scans indicate that samples HEM A1-4 have the highest relaxivity, compared to the samples synthesised at different temperatures. The particle size data obtained using DLS is given in Figure 5.15 and shows that, with the exception of sample HEM A2 (PVP 10 coating), samples produced at this temperature contain the smallest particles. From this, it can be gathered that smaller particles result in increased proton relaxation and MR signal decay, a trend consistent with what has previously been described in literature. It can be seen from Figure 5.13 that for each of the capping agents used, r₂ decreases as synthesis temperature increases.

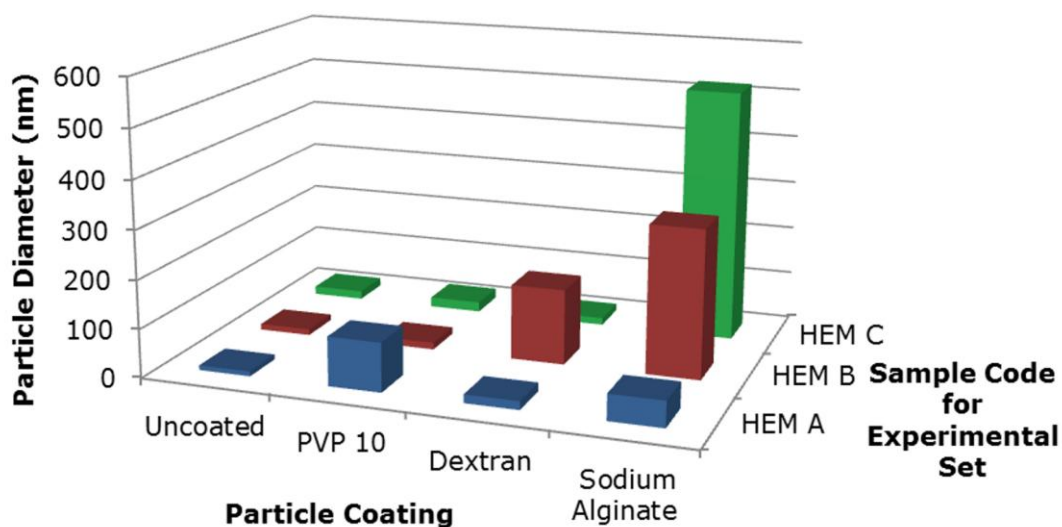


Figure 5.15. A chart summarising the particle size data obtained from DLS analysis, for the 12 synthesised Fe_2O_3 samples.

The DLS data presented in Figure 5.15 shows that, in general, particle size increases with an increase in temperature. This is a pattern seen previously for Fe_2O_3 synthesised in the counter-current Nozzle reactor (Li, 2008). Nevertheless, sample HEM A2 serves as an exception. One possible explanation for the large particles measured in HEM A2 is that these large particles are globules of PVP 10, as opposed to Fe_2O_3 . At a low reaction temperature of 150 °C, it is possible (or altogether probable) that conversion rate of precursor to particles is low. As such, the concentration ratio of PVP 10 to Fe_2O_3 in the product is skewed in favour of the former. This excess of polymer could result in it binding to itself rather than to the nanoparticles.

The DLS data for samples containing sodium alginate as a capping agent (HEM A4, HEM B4 and HEM C4) suggest the particles have a significantly larger diameter than the uncoated particles. Parallel to this data, these samples have the r_2 relaxivities across their sample sets. Moreover, the MR image obtained for HEM A4 using the Bruker 2.35 T scanner and displayed in Figure 5.14 e), shows

a colour gradient across the circle. This is because the particles, which are causing signal decay, are sedimenting at the bottom of the sample cell. Conversely, the particles are more dispersed in the uncoated sample HEM A1. This data suggests that the addition of sodium alginate creates a “matrix” or network around the particles, forming a large aggregate rather than coating individual particles. This amorphous matrix surrounding the particles hinders the superparamagnetic effect of the Fe_2O_3 nanoparticles, as well as enveloping particles into a larger entity – which leads to sedimentation. Moreover, the photos of samples HEM A4, HEM B4 and HEM C4 in Figure 5.10, Figure 5.11 and Figure 5.12 respectively, show that the dispersions are more opaque than their uncoated counterparts; this suggests particle flocculation is occurring which could be due to a sodium alginate matrix.

In sample sets HEM A and HEM B, the samples containing dextran as a capping agent (HEM A3 and HEM B3) yield the highest r_2 relaxivities – this is unsurprising as dextran is commonly used to coat superparamagnetic particles for MRI. Interestingly, this is not the case for sample HEM C3, which has a lower r_2 relaxivity than the equivalent uncoated particles in HEM C1. This could be attributed to thermal decomposition of dextran in the reactor during synthesis, which has been reported to occur at temperatures ca. 300 °C (Carp et al., 2010) – the temperature used to synthesise samples in the HEM C set. The DLS data for sample HEM C3 also shows smaller particles than in HEM B3, and does not follow the trend of increasing particle size with increasing temperature. This result reinforces the notion of thermal breakdown; the resulting fragments of dextran would not scatter light in the same way as if there were coated particles, and the latter would have a larger hydrodynamic radius.

The XRD data for Samples HEM A1, HEM B1 and HEM C1 are given in Figure 5.16, along with the expected peak positions for Fe_2O_3 . The three patterns do

not exhibit strong peaks, suggesting that the samples are quite amorphous. In addition, the XRD data may be influenced by small crystallite sizes in the samples, which would give rise to peaks with a broad width. Still, HEM A1 and HEM C1 do contain peaks ca. $2\theta = 33.1$ and 35.7° , which correspond to Fe_2O_3 . For sample HEM B1, these peaks are not obvious but signal intensity does increase a little around these 2θ regions, suggesting that this phase may also be present in this sample. In HEM C1, the extra peak at $2\theta = 20.4^\circ$ corresponds to a peak for iron nitrate hydroxide hydrate, $\text{Fe}_4\text{NO}_3(\text{OH})_{11}\cdot 2\text{H}_2\text{O}$ (ICCD PDF 44-519). This composition is similar to the starting precursor, which suggests that there may be incomplete conversion during the reaction.

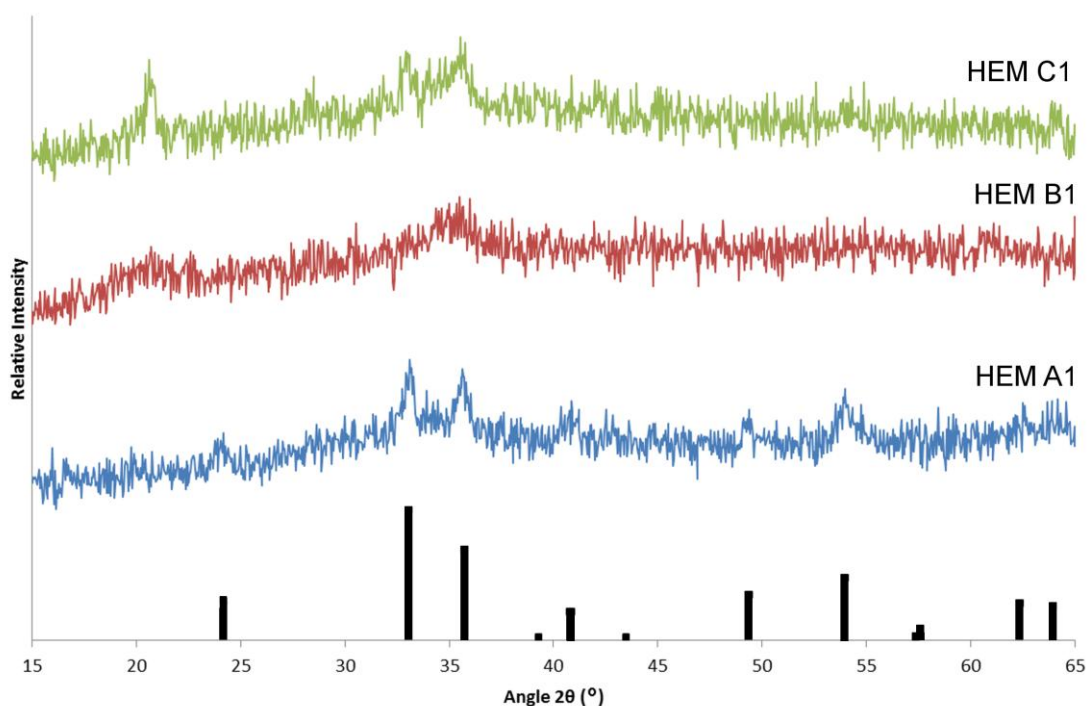


Figure 5.16. XRD patterns obtained for samples HEM A1, HEM B1, and HEM C1. At the bottom are the expected peak positions for Fe_2O_3 (ICCD PDF 86-550).

5.3.2 Magnetite, Fe_3O_4

The samples produced at a temperature ~ 350 °C (MAG F1-4) were a similar colour to the precursor. When a laser light was passed through each sample vial, no beam path could be seen, suggesting that no particles were produced at this temperature. It is likely that this temperature is insufficient to drive synthesis of Fe_3O_4 . Therefore, samples MAG F1-4 were not characterised or analysed further.

The samples synthesised at a temperature of ~ 400 °C (MAG G1-4) are shown in Figure 5.17. All four samples were dark brown in colour and the particles sedimented to the bottom of the vial over time. Due to this sedimentation, the samples could not be analysed using DLS (the reasons for this were discussed in Chapter 2 Section 2.6).



Figure 5.17. Photo of Fe_3O_4 Samples in Second Temperature Set.

The four samples, along with the precursor, were tested on the 0.5 T Halbach MRI Scanner and their T_2 times obtained. These values, as well as the T_2 time of water for comparison, are presented in Table 5.10. It can be seen that the T_2 times for all four samples are significantly shorter than that of water, and much shorter than that of the precursor – confirming that the synthesised particles are having a positive effect on proton relaxation. The data shows that, while the addition of PVP has little effect on the particle's T_2 time (MAG G1 compared to MAG G2), the incorporation of dextran shortens the T_2 time significantly (as seen from MAG G3). This, in turn, increases the r_2 value from 22.68 to 33.47 $\text{mm}^{-1} \text{s}^{-1}$. On the contrary, the addition of sodium alginate appears to have a detrimental effect on the relaxation effect, as the T_2 time for MAG G4 is much higher than that of MAG G1.

Table 5.10. Summary of the T_2 relaxation times for the Fe_3O_4 samples, precursor and water blank, measured using the Halbach 0.5 T MRI Scanner. The r_2 values, calculated using Equation 2, are also given.

| Sample Code | T_2 Time (ms) | Error (\pm) | r_2 ($\text{mM}^{-1} \text{s}^{-1}$) |
|------------------------------|-----------------|-----------------|--|
| MAG G1 | 2.642 | 0.01 | 22.68 |
| MAG G2 | 2.634 | 0.009 | 22.75 |
| MAG G3 | 1.791 | 0.007 | 33.47 |
| MAG G4 | 4.84 | 0.02 | 12.37 |
| 0.05 M Ammonium Iron Citrate | 44.28 | 0.02 | 0.44 |
| Water | 2122 | 0.01 | - |

The Fe_3O_4 samples were tested using a 2.35 T Bruker MRI scanner; the obtained images depicting proton T_2 relaxation time (ms) and the corresponding R_2

relaxation are given in Figure 5.18. In Figure 5.18 (a), the T_2 relaxation time for water is so high, that the image appears as if there is no sample present. Likewise the R_2 relaxation value is so low that there is no discernible difference between the water sample and background.

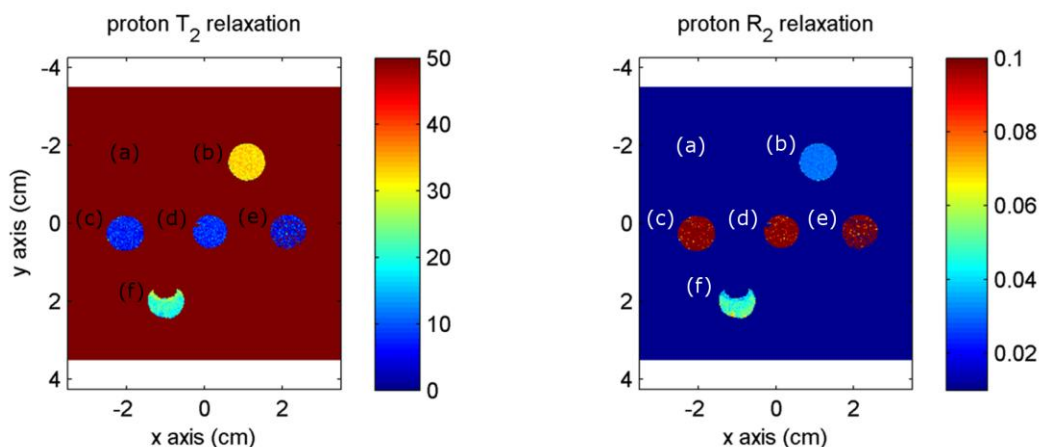


Figure 5.18. Images collected from the 2.35 T MRI scanner showing T_2 relaxation times (in ms) and R_2 relaxation for (a) water blank, (b) 0.025 M Ammonium Iron Citrate (precursor), (c) MAG G1, (d) MAG G2, (e) MAG G3, and (f) MAG G4.

On the contrary, The T_2 relaxation times for samples MAG G1-4 are much shorter, and correspond to the values shown in Table 5.10. The non-circular image seen in Figure 5.18 (f) generated by sample MAG G4 is caused by an air bubble present in the sample vial during analysis, rather than the MR properties of the sample itself. The colour of the obtained images for MAG G4 are significantly different to those of MAG G1-3 - ascribed to its longer T_2 relaxation time, and smaller R_2 , compared to the other three samples. This is consistent with the data obtained using the Halbach 0.5 T system.

The r_2 relaxivity values can be calculated using the T_2 times and the theoretical concentration of Fe in the samples, and are summarised in Table 5.10. The

relaxivity of all the synthesised samples of Fe_3O_4 are lower than the commercial contrast agents Feridex IV[®], which has a relaxivity of $98.3 \text{ mM}^{-1} \text{ s}^{-1}$ (Wang, 2011), and Resovist[®], which has an r_2 value of $151 \text{ mM}^{-1} \text{ s}^{-1}$ (Wang, 2011). This is most likely to be due to effects of particle coagulation, thereby eliminating the benefits seen at the nanoscale. This is a common problem when synthesising nanoparticles, especially Fe_3O_4 , and so surfactants or capping agents need to be introduced.

The addition of PVP to the synthesis reaction has little effect on relaxivity, and a similar value to the uncapped sample is derived, $22.75 \text{ mM}^{-1} \text{ s}^{-1}$. This may be because PVP is not having a very effective stabilising influence on the Fe_3O_4 particles; or that the PVP is indeed preventing particle aggregation to some degree, but also reducing the surface interactions of the particles.

Sample MAG G4, with sodium alginate as a capping agent, has a much longer T_2 time than the other samples, and consequently a lower relaxivity of $12.37 \text{ mM}^{-1} \text{ s}^{-1}$. This could be a result of the capping agent interacting with the surfaces of the Fe_3O_4 particles and hindering the superparamagnetic properties.

Lastly, sample MAG G3 shows the most promise as a contrast agent, with a T_2 time of 1.79 ms and corresponding r_2 of $33.47 \text{ mM}^{-1} \text{ s}^{-1}$ – a relaxivity comparable to some of the commercial contrast agents highlighted in Section 5.1.5. In sample HEM C3, which was discussed in Section 5.3.1, a detrimental effect on r_2 relaxivity was observed with the incorporation of dextran as a capping agent – this was attributed to possible thermal decomposition of the surfactant. Interestingly, this effect is not seen in the case of MAG G3 in comparison to MAG G1, the uncoated sample, despite reaction temperatures ca. $400 \text{ }^\circ\text{C}$. Instead, dextran improves the r_2 . This difference in results could be due to the phase change of water into the supercritical region during magnetite

synthesis compared to water being subcritical during synthesis of HEM C3. At the supercritical state, water is less dense and in turn, the residence time of particles/dextran in the reactor is shorter. This means dextran is exposed to the high temperatures in the reactor for less time during synthesis of MAG G3 and may not be enough time for thermal decomposition to occur.

While the r_2 value for MAG G3 is promising, but lower than some commercial contrast agents, it is derived from a theoretical concentration of Fe which assumes 100% conversion during the synthesis reaction. Therefore, it is possible that the actual concentration of Fe in the sample is lower, thus yielding a higher relaxivity still. If the ratio of Fe_3O_4 and dextran were optimised to ensure there is no particle aggregation at all, it is likely that the relaxivity could be enhanced further.

As MAG G3 gave this promising T_2 result, it was characterised further. The sample was dried to a powder and analysed using XRD to ascertain its crystal structure. XRD was also performed on sample MAG G1, for comparison. The XRD patterns of both samples are given in Figure 5.19, with the reference peak positions of cubic phase Fe_3O_4 also shown. All the peaks corresponding to the reference phase are present in both samples, confirming that cubic phase Fe_3O_4 is the predominant crystal structure for both MAG G1 and G3. Nevertheless, there are differences between the two samples; the pattern for MAG G3 contains a lot more noise than that of MAG G1. This may be due to the amorphous dextran content in MAG G3, which is not present in MAG G1.

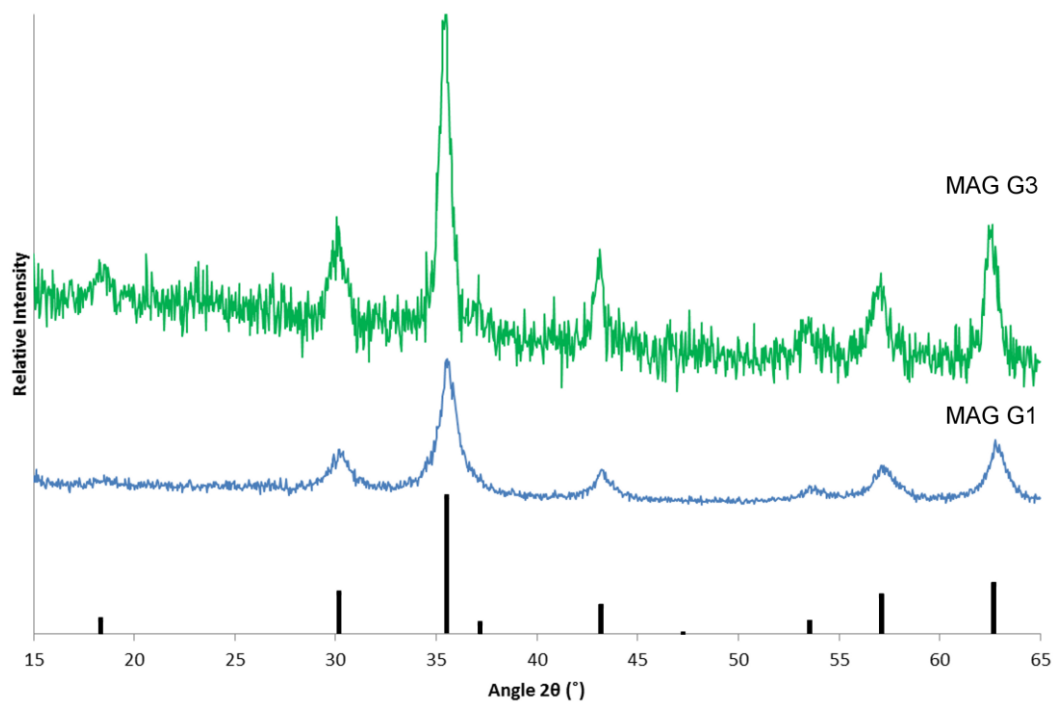


Figure 5.19. XRD patterns obtained for samples MAG G1 and MAG G3. At the bottom are the expected peak positions for cubic Fe₃O₄ (ICCD PDF 88-315).

The images of MAG G1 collected using TEM analysis are shown in Figure 5.20. It can be seen that the particles are spherical in morphology with their diameters measuring between 9 and 30 nm. TEM images collected at a higher magnification (Figure 5.20 (b)) highlight the crystalline nature of the particles.

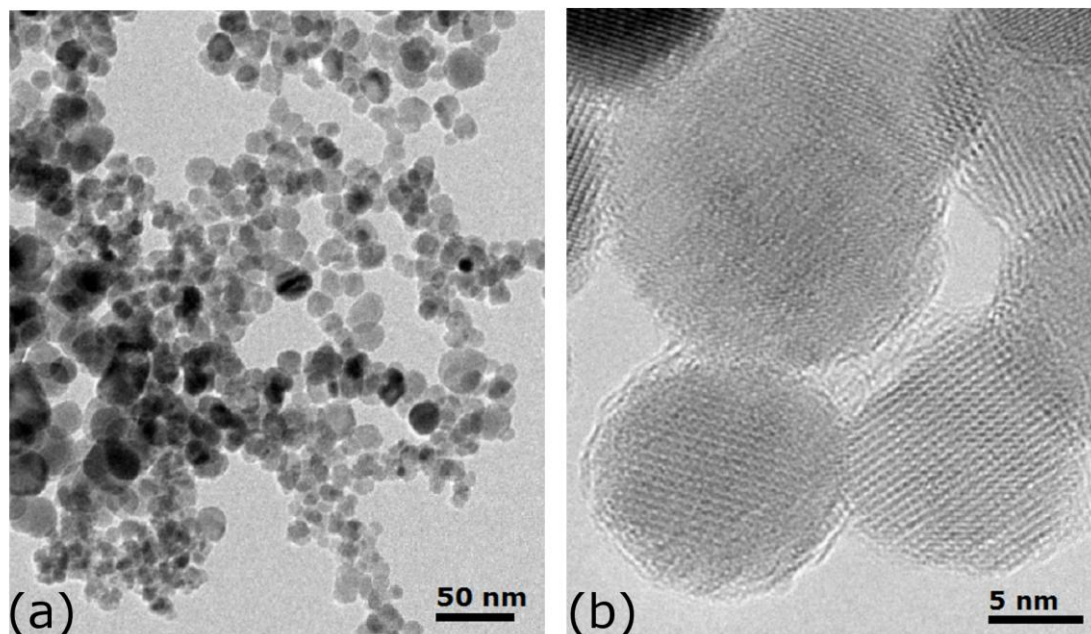


Figure 5.20. (a) and (b) are TEM images of MAG G1, uncoated Fe₃O₄.

A TEM image collected for sample MAG G3 is given in Figure 5.21. It was seen that particle morphology and size did not deviate significantly from those seen in MAG G1. Yet the principle difference observed between the two samples was the apparent presence of an amorphous coating around the Fe₃O₄ particles in MAG G3 – ascribed to dextran. It can be seen that while the dextran sufficiently covers the entirety of the nanoparticles, it does appear that there is still some degree of particle aggregation which the dextran has not completely prevented. Here, the capping agent is enveloping the small clusters of particles, rather than coating the individual particles as desired. This is an issue which can be addressed by either changing (increasing) the concentration ratio of dextran to iron precursor used, or altering the method of how the dextran is introduced to coat the particles. This provides scope for future work.

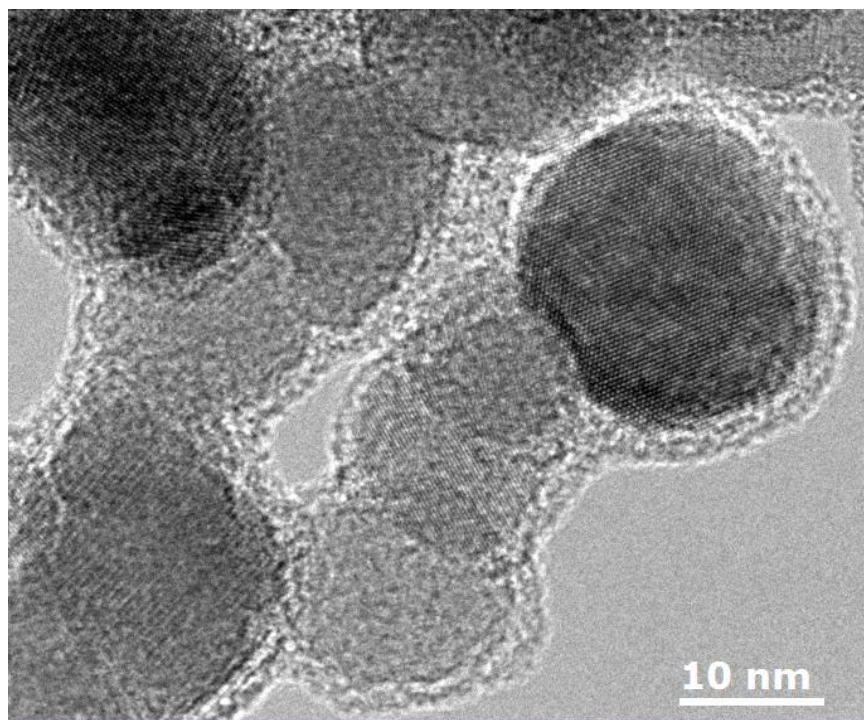


Figure 5.21. TEM image of MAG G3, Fe_3O_4 nanoparticles coated in dextran.

5.3.3 Gadolinium Hydroxide, $\text{Gd}(\text{OH})_3$

The first set of $\text{Gd}(\text{OH})_3$ samples synthesised with the water heater set point at 385 °C all gave rise to transparent, colourless samples. When tested with a laser pointer, no beam path could be seen – indicating no particles were present. As such, it was concluded that the reaction temperature was not high enough to produce particles and the samples were not characterised further.

The second set of samples manufactured with the water heater set point at 450 °C yielded the samples shown in Figure 5.22. Sample GAD E1 was translucent with a white haze, and when tested with a laser pointer, showed a positive beam path. GAD E3 and E4 were a more opaque white, while GAD E2 appeared to contain a slight yellow tinge. The particles in all four samples

sedimented over time, meaning particle sizing by DLS technique was not possible. A day or so after synthesis, the particles in GAD E1 dissolved; this may be due to the HNO_3 which is produced as a by-product. Still, before this occurred, a sample of the particles were dried and analysed by XRD.



Figure 5.22. Photo of the Second Set of $\text{Gd}(\text{OH})_3$ Samples.

The four samples of $\text{Gd}(\text{OH})_3$ produced in the second experimental set were analysed using the Halbach 0.5 T scanner, along with the precursor, and the obtained T_2 times are shown in Table 5.11. Their r_2 relaxivities were calculated using the measured T_2 times and Equation 2 which was listed in Section 5.1.3. These are also displayed in Table 5.11. It can be seen the T_2 time for the precursor, gadolinium acetate hydrate, is the lowest value obtained for this sample set, at 1.69 ms. Hence the calculated r_2 relaxivity of $11.82 \text{ mM}^{-1} \text{ s}^{-1}$ is the highest for all in this sample set. This is unsurprising, as the Gd^{3+} ion has been reported as having the highest degree of paramagnetism of all metal ions (Dutta et al., 2008). Nevertheless, the cytotoxicity issues associated with Gd^{3+} ions

which were previously described in Section 5.1.4 mean it cannot be used as a free ion for clinical MRI applications.

Table 5.11 also shows that a relatively low T_2 time and high r_2 value is produced from GAD E1, uncapped $Gd(OH)_3$ – 7.32 ms and $8.17 \text{ mM}^{-1} \text{ s}^{-1}$ respectively. However, it was observed that the white particles which were produced in this sample began to ‘disappear’ after a day or so. This is likely to be due to chemical decomposition caused by HNO_3 which is produced as a by-product. Consequently, it is probable that particle breakdown occurred before and during analysis. This means the $Gd(OH)_3$ particles were being dissolved to yield Gd^{3+} ions and give rise to the efficient signal decay in MRI scans. While a good T_2 and r_2 result, this sample presents the same problem of cytotoxicity as the precursor and cannot be considered as a potentially viable contrast agent.

Table 5.11. Summary of the measured T_2 relaxation times for the $Gd(OH)_3$ samples, precursor and water blank. The r_2 values, calculated using Equation 2, are also given.

| Sample Code | T_2 Time (ms) | Error (\pm) | r_2 ($\text{mM}^{-1} \text{ s}^{-1}$) |
|------------------------------------|-----------------|-----------------|---|
| GAD E1 | 7.32 | 0.01 | 8.17 |
| GAD E2 | 17.2 | 0.02 | 3.46 |
| GAD E3 | 9.952 | 0.01 | 6.00 |
| GAD E4 | 16.26 | 0.02 | 3.66 |
| 0.025 M Gadolinium Acetate Hydrate | 1.69 | 0.001 | 11.82 |
| Water | 2122 | 0.01 | - |

Unlike sample GAD E1, samples GAD E2-4 did not exhibit visible signs of particle decomposition after synthesis. The T_2 and r_2 values for GAD E2 and GAD E4 are very similar, with GAD E2 possessing a relaxivity of $3.46 \text{ mM}^{-1} \text{ s}^{-1}$ and GAD E4 of $3.66 \text{ mM}^{-1} \text{ s}^{-1}$. These values, a fair degree lower than GAD E1 and the precursor, suggests that PVP and sodium alginate are having an effect in coating particles and preventing particle decomposition. Still, the extent of this positive effect cannot be concluded from this data, as the T_2 and r_2 data may also be affected by the capping agents themselves either enhancing or pacifying the paramagnetic behaviour of the $\text{Gd}(\text{OH})_3$ particles.

Sample GAD E3, with dextran as the capping agent, shows a promising T_2 time of 9.952 ms, which translates to an r_2 of $6.00 \text{ mM}^{-1} \text{ s}^{-1}$. Like the other GAD samples though, it cannot be determined from this data if the signal decay can be entirely attributed to the synthesised particles, or if it due (even in part) to the presence of Gd^{3+} ions present in the samples. To eliminate this possibility during analysis in future work, samples should be washed prior to analysis.

The relaxivity of GAD E3, and those of GAD E2 and GAD E4, are quite comparable to that of the commercial contrast agent Omniscan[®], which has an r_2 of $3.4 \text{ mM}^{-1} \text{ s}^{-1}$. As well as the possible presence of Gd^{3+} ions in the samples which has been discussed, it should also be noted that the Gd-based complexes in Omniscan[®] contain tightly bound ligands to prevent leaching of toxic ions. These could be partially diminishing the paramagnetic properties of Gd^{3+} ions and decreasing the r_2 value. Nevertheless, the r_2 values of the $\text{Gd}(\text{OH})_3$ samples described in the Chapter show promising r_2 data which provides scope for further future investigation.

To confirm the nanomaterial species being produced in this set of experiments, XRD analysis was performed on sample GAD E1. The acquired pattern is shown

in Figure 5.23, with the peak positions for hexagonal $\text{Gd}(\text{OH})_3$ also given. It can be seen that all the expected peaks are indeed exhibited by the samples, denoting that this is principle and sole crystalline phase in GAD E1. In addition, the peaks are sharp and narrow, which suggests a high level of crystallinity and probably large crystallites (See Chapter 2 for reasoning). With the exception of different organic capping agents being introduced, the experimental parameters for synthesis of GAD E2-4 did not change, so it is gathered that $\text{Gd}(\text{OH})_3$ is synthesised in the other three samples.

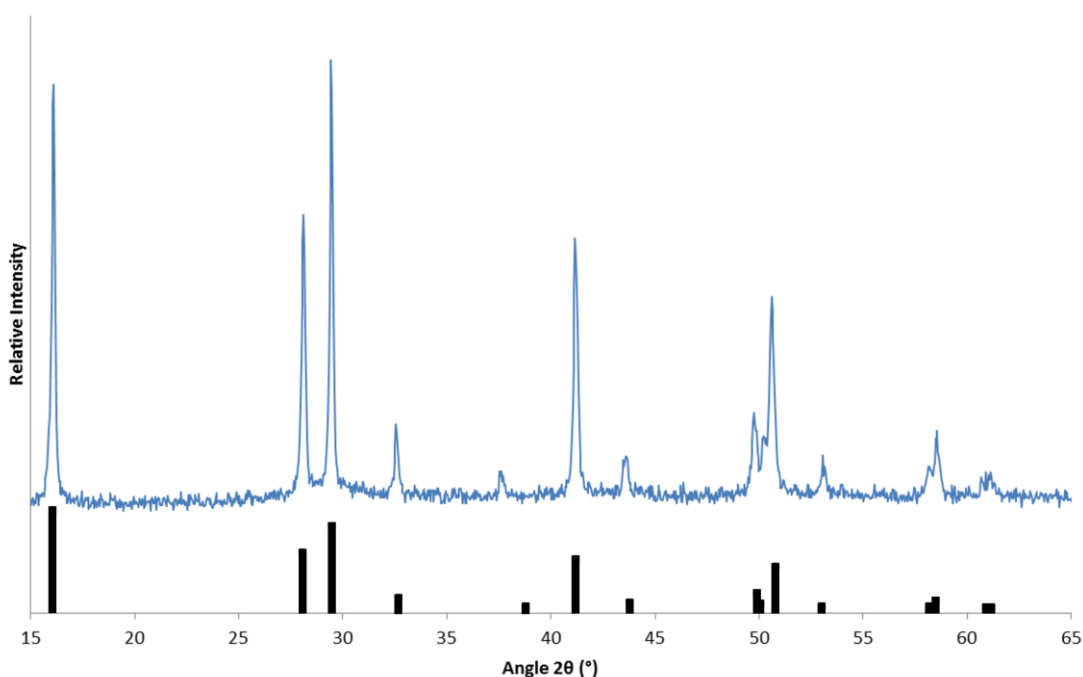


Figure 5.23. XRD Pattern obtained for GAD E1, with the expected peak positions of hexagonal $\text{Gd}(\text{OH})_3$ (ICCD PDF 83-2037) shown below.

5.3.4 Cobalt Oxide, Co_3O_4

The synthesised sample of Co_3O_4 was opaque and black in colour, where the particles remained in dispersion over time, i.e. the particles did not sediment. The MRI properties of the sample, and its precursor, were tested using

the Halbach 0.5 T kit. The T_2 times and respective r_2 values are given in Table 5.12. The measured T_2 time of Co_3O_4 was 578.1 ms and significantly longer than those of Fe_2O_3 and Fe_3O_4 described in Sections 5.3.1 and 5.3.2 respectively. This gave rise to a low r_2 value of $0.30 \text{ mM}^{-1} \text{ s}^{-1}$; consequently, the sample of Co_3O_4 was not tested on the 2.35 T MRI scanner.

Table 5.12. Summary of the measured T_2 relaxation times for the sample of Co_3O_4 , its precursor, and water blank. The r_2 values, calculated using Equation 2, are also given.

| Sample Code | T_2 Time (ms) | Error (\pm) | r_2 ($\text{mM}^{-1} \text{ s}^{-1}$) |
|------------------------------------|-----------------|-----------------|---|
| Co_3O_4 | 578.1 | 0.2 | 0.30 |
| 0.05 M Cobalt Acetate Tetrahydrate | 101.95 | 0.02 | 0.19 |
| Water | 2122 | 0.01 | - |

This sample of Co_3O_4 was found to possess antiferromagnetic properties (Moro et al., 2013); though T_2 -weighted contrast agents are usually superparamagnetic, and T_1 -weighted agents have paramagnetic properties (Conn, 2009). This explains the low r_2 values. This sample of Co_3O_4 was produced for analysis of its other properties which are described elsewhere (Moro et al., 2013) and so, despite the poor MR properties, TEM and XRD analysis was conducted on the sample. A darkfield TEM image of the particles is given in Figure 5.24, which shows the cubic morphology of the particles. Using Digital Micrograph software from Gatan, the edge lengths of 300 particles were measured and a mean length of 7.03 nm was calculated. Using this data, the particle size distribution graph displayed in Figure 5.25 was generated, showing the majority of nanoparticles have an edge length between 2 and 10 nm.

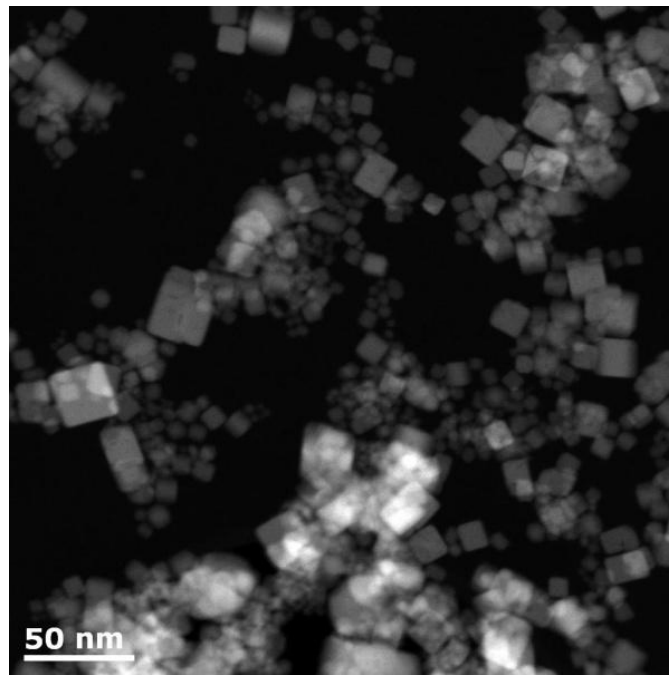


Figure 5.24. Darkfield TEM image of sample Co_3O_4 showing particles with cubic morphology.

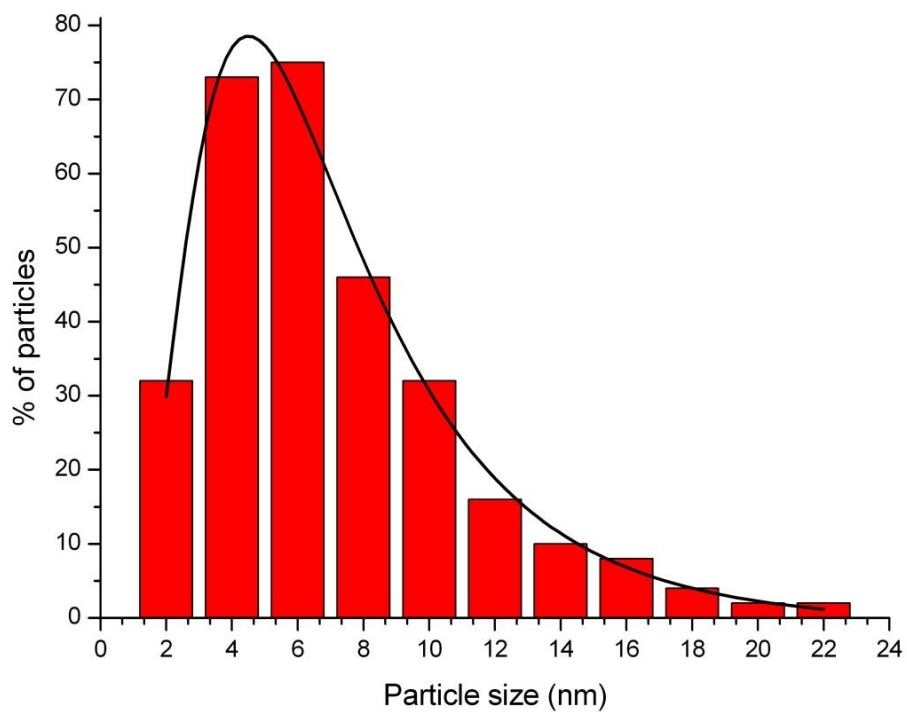


Figure 5.25. Graph showing the particle size distribution of Co_3O_4 particles.

Figure 5.26 shows the XRD pattern of the sample, which matches the expected pattern for cubic phase spinel cobalt oxide (ICCD PDF 9-418). No other peaks were detected, indicating the purity of the sample. Xfit software was used to calculate an average crystallite size of 12.3 nm, a value slightly larger than that calculated from TEM analysis; this may be due to the amorphous nature of smaller particles which are observed by TEM but not detected by XRD. Bragg's equation was used to calculate the d-spacing of each plane then checked and verified with Celref software. Table 5.13 shows the calculated d-spacing and the hkl plane for each peak. Considering the highest intensity peak at $2\theta = 36.8031$, corresponding to the plane (311), the calculated d-spacing is 2.44\AA (0.244 nm). This value is confirmed by the high magnification TEM image shown in Figure 5.27. Furthermore, Celref software was used to refine the unit cell parameters of the sample and yielded a lattice constant $a = 8.0937 \pm 0.004\text{\AA}$. This figure is close to, but slightly larger than the theoretical cell unit size of 8.084\AA . The expansion of lattice parameters in nanoparticles has been previously reported and ascribed to the high surface to volume ratio which leads to a "stretched" unit cell because of surface tension attraction between nanoparticles (Wei et al., 2007).

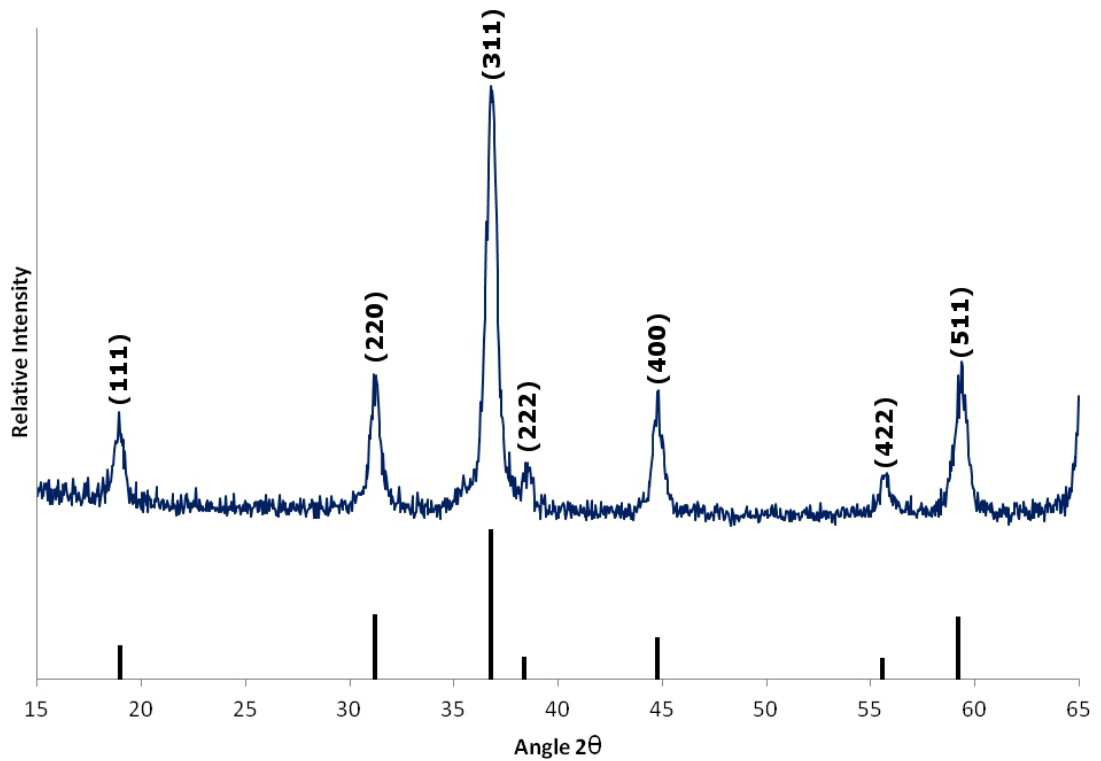


Figure 5.26. The XRD pattern obtained for sample Co_3O_4 . Peaks correspond with the expected pattern of cubic Co_3O_4 (ICCD PDF 009-0418), which are shown below.

Table 5.13. The d -spacing for each plane in the Co_3O_4 crystal, and the respective peak position, as calculated from the XRD pattern.

| Peak Position, 2θ ($^\circ$) | (hkl) Plane | d -spacing, d_{hkl} (\AA) |
|---------------------------------------|-------------|--|
| 18.904 | (111) | 4.69 |
| 31.223 | (220) | 2.87 |
| 36.803 | (311) | 2.44 |
| 38.535 | (222) | 2.34 |
| 44.785 | (400) | 2.02 |
| 55.698 | (422) | 1.65 |
| 59.343 | (511) | 1.56 |

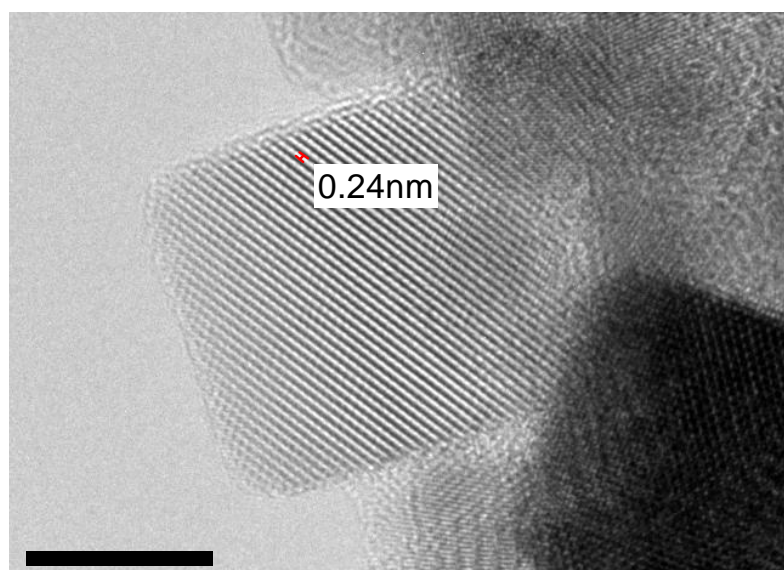


Figure 5.27. High magnification HRTEM image of Co₃O₄ nanoparticles illustrating the interplanar spacing.

5.4 Conclusions

In this Chapter, the synthesis of Fe_2O_3 , Fe_3O_4 , $\text{Gd}(\text{OH})_3$ and Co_3O_4 were described. With the exception of Co_3O_4 , synthesis was attempted using different reactor temperatures. For Fe_3O_4 and $\text{Gd}(\text{OH})_3$, it was found that particles were not produced at 350 °C but were at 400 °C; this indicates supercritical conditions are required for particle formation. In addition, three different capping agents (PVP 10, dextran and sodium alginate) were added to coat particles during synthesis, as well as uncoated particles being made for comparison.

In the case of Fe_2O_3 , the samples were manufactured at three different reaction temperatures; DLS data showed a general trend of increasing particle size with increasing synthesis temperature. Another general trend showed that smaller particles exhibited higher r_2 relaxivities. At the lower two reaction temperatures, the highest relaxivities were produced by particles coated with dextran (HEM A3 had an r_2 of $8.98 \text{ mM}^{-1}\text{s}^{-1}$, which HEM B3 was calculated as $8.24 \text{ mM}^{-1}\text{s}^{-1}$) – consistent with previous reports in the literature that dextran improves relaxivity. At the highest reaction temperature, the largest r_2 value was attributed to the sample of uncoated particles (HEM C1) rather than those coated with dextran (HEM C3); this may be a result of thermal decomposition of dextran caused by the reactor temperature. These r_2 values for Fe_2O_3 particles are higher than some commercial contrast agents, such as Omniscan at $3.4 \text{ mM}^{-1}\text{s}^{-1}$, but lower than most.

The synthesised samples of Fe_3O_4 which contained particles were analysed using a 0.5 T MRI scanner to acquire T_2 relaxation times. A 2.35 T scanner was then used to acquire MR images showing relaxation. The obtained data showed that MAG G3, Fe_3O_4 with dextran as a capping agent, had the lowest T_2 time and

consequently, the highest r_2 relaxivity of $33.47 \text{ mM}^{-1} \text{ s}^{-1}$. This complies with results from the literature. The r_2 value is also comparable to some commercial contrast agents, such as Clariscan which has a relaxivity of $35.3 \text{ mM}^{-1} \text{ s}^{-1}$. Unlike the sample of hematite, use of dextran at a high reaction temperature was not detrimental to the r_2 value; it is plausible that thermal decomposition is not a problem in this case due to the supercritical nature of water meaning lower solvent density and lower residence times. Obtained TEM images and XRD patterns showed that dextran did not affect crystal phase or primary particle size, but did form a partial coating around particles. The ratio between particles and capping agent can be optimised in future work to ensure ideal particle coating, which will then prevent particle coagulation and may enhance relaxivity. PVP 10 did not appear to affect relaxivity, as the r_2 value was similar to that of uncoated particles, while sodium alginate had a detrimental effect on particle relaxivity. This may be due to sodium alginate enveloping particles and diminishing their superparamagnetic properties.

The relaxivity values calculated in this Chapter were based on theoretical Fe concentrations and assumed 100% reaction conversion; the actual concentrations of Fe could be experimentally measured to give more accurate r_2 values. These may actually be higher than those presented here.

Of the four samples of $\text{Gd}(\text{OH})_3$ synthesised, the uncoated particles were not chemically stable and became digested by the acidic by-product after a few days. However, the obtained XRD data of the isolated particles confirmed the principle crystal phase to be hexagonal $\text{Gd}(\text{OH})_3$. Gd^{3+} ions are known to be highly paramagnetic and so the precursor and uncoated particles displayed high r_2 relaxivities. However, the cytotoxic nature of the cation means it cannot be used as a contrast agent. Sample GAD E3, $\text{Gd}(\text{OH})_3$ coated with dextran exhibited a promising T_2 relaxation time; further studies should focus on analysis of washed

samples to eliminate the possibility of Gd^{3+} ions (which could be present in the unwashed sample) contributing to relaxation. Meanwhile, samples containing PVP 10 and sodium alginate gave the lowest r_2 , but these were still values comparable to those previously reported for Gd-based materials. So, these maintain potential as contrast agent materials for further investigation. These materials could be characterised using T_1 -weighted scans as well, in order to gather information about their effects on spin-lattice relaxation.

Lastly, the Nozzle reactor was used to synthesise Co_3O_4 for a separate study, but was also analysed for possible application in MRI. From the acquired TEM and XRD data, particles are crystalline with cubic morphology. TEM analysis yielded a mean edge length of 7.03 nm while XRD analysis presented an average crystallite size of 12.3 nm; this discrepancy could be due to smaller amorphous particles which are not detected by XRD. Analysis of Co_3O_4 on the 0.5 T MRI scanner showed poor T_2 relaxation times; the particles were then found to be antiferromagnetic which explained this data.

To summarise, dextran was generally shown to be the most effective capping agent in terms of improving r_2 relaxivity of samples. Conversely, sodium alginate had a detrimental effect on relaxivity. Hematite, Fe_2O_3 ; magnetite, Fe_3O_4 ; and gadolinium hydroxide, $Gd(OH)_3$ produced using the Nozzle reactor have been shown to exhibit properties for MRI which are comparable to commercial contrast agents. As such, these materials have the potential for further research and development which can serve to enhance their r_2 relaxivities further.

Chapter 6

Conclusions and Future Work

6.1 Conclusions

The work described in this Thesis follows on from that of previous researchers using the Nozzle reactor, including Li (Li, 2008), Hobbs (Hobbs et al., 2009) and Aksomaityte (Aksomaityte et al., 2013, Lester et al., 2012). Since the reactor geometry was invented in 2005 (Lester and Azzopardi, 2005), the wide range of materials which could potentially be synthesised using it, has only been touched upon. Furthermore, the industries and applications which could (or already do) benefit from the implementation of nanomaterials is vast. In this Thesis, the objective was to investigate the synthesis of, and subsequently characterise, nanomaterials which could be applied into biological or biomedical fields.

Firstly, Chapter 1 showed that the Nozzle reactor could be used to reproducibly synthesise HA with either platelet, rod or tube morphology. Data obtained from this investigation suggested that NH_4OH plays several roles during HA synthesis, from directing precursors towards the formation of HA over other CaP minerals, to promoting the formation particular morphologies. In particular, it was found that in the presence of NH_4OH , rods were produced instead of sheets at 200°C , and tubes instead of rods at 350°C . While more data needs to be gathered before a formation mechanism can be concluded, it appears that the mechanisms for the three morphologies are linked. Cell proliferation and bone

nodule assays performed using HA from the Nozzle reactor indicated that the nanoparticles did not have cytotoxic effects and appeared to promote bone nodule formation.

Chapter 1 also detailed experiments to introduce zinc and simvastatin into the structure of HA. It was found that the morphology of synthesised particles did not change by adding other compounds into the reaction. However, it was unclear from the obtained data whether simvastatin was successfully incorporated into the structure. By adding a zinc salt into the synthesis method, parascholzite ($\text{CaZn}_2(\text{PO}_4)_2 \cdot 2\text{H}_2\text{O}$) was formed. This could have potential applications in bone based materials where zinc may provide antimicrobial properties (Stanić et al., 2010).

In Chapter 4, synthesis of CdS yielded bright yellow particles of diameters 20 to 50 nm - consistent with what others had observed previously. The fluorometry data collected for the CdS sample were inconclusive within the scope of this Thesis. The methodology for CdS synthesis was adapted to produce ZnS nanoparticles - a material which had not been previously produced by a continuous hydrothermal route. For both CdS and ZnS, a minimum reaction temperature of 400 °C was required to yield particles. The ZnS sample was shown to contain a mixture of hexagonal and cubic phases of ZnS, with primary particle sizes <15nm; these had aggregated into clusters with diameters of 50 to 100 nm. Under the same experimental conditions, but using thiourea as a sulphur source, ZnS was not produced - showing that thiocarbohydrazide and thiourea cannot be used interchangeably.

Also in Chapter 4, the synthesis of ZnS with 3 different capping agents was reported. Structural and photoluminescent properties of these products were compared to unmodified ZnS. It was found that the addition of 3-MPA to the

synthesis method yielded particles with an average crystallite size of 3.1 nm, with a PL emission peak in the violet or blue light range (450 nm). This was compared to a peak at 558 nm, in the green light range, for Uncapped ZnS nanoparticles. This emission data for ZnS:3-MPA is in a wavelength range comparable to previous reports for cadmium-based QDs (Saraswathi Amma et al., 2008), thus there is the potential to develop ZnS as a heavy-metal free QD alternative. Furthermore, the zeta potential data highlighted a change in the IEP of particles in response to capping with 3-MPA; uncapped particles had an IEP at pH 7.8 while ZnS:3MPA 5/5 had an IEP at pH 4.1 and a stable zeta potential at pH 7.

Coating particles with PVP had little observed effect on structural properties of particles. In addition, the zeta potential data was inconclusive. However, the PL data showed a shift in the optimum emission wavelength compared to uncoated particles, with the peak reached at 572 nm, corresponding to yellow light.

Meanwhile, the obtained data showed that the addition of NaOH to synthesis did not have any discernible effect on the structural or PL characteristics. It is inferred that differences in emission peak wavelength between the four samples are linked to differences in particle band gap energies.

In Chapter 5, the synthesis of Fe_2O_3 , Fe_3O_4 , $\text{Gd}(\text{OH})_3$ and Co_3O_4 were described. With the exception of Co_3O_4 , synthesis was attempted using different reactor temperatures. For Fe_3O_4 and $\text{Gd}(\text{OH})_3$, it was found that particles were not produced at temperatures below 400 °C, indicating supercritical conditions are required for particle formation. Three different capping agents (PVP 10, dextran and sodium alginate) were added to coat Fe_2O_3 , Fe_3O_4 and $\text{Gd}(\text{OH})_3$ particles during synthesis, as well as uncoated particles being made for comparison.

Samples of Fe_2O_3 were synthesised at three different reaction temperatures; a general trend of increasing particle size with increasing temperature was observed. Moreover, smaller particles typically exhibited higher r_2 relaxivities. The highest relaxivity seen for the Fe_2O_3 sample set was ascribed to particles coated in dextran and synthesised at the lowest reaction temperature of ~ 150 °C. Still, all of the uncoated particles produced at the three different temperatures appeared to be quite amorphous when analysed using XRD.

Likewise for Fe_3O_4 , particles coated with dextran displayed the highest relaxivity. It was shown that the dextran coating did not affect primary particle size or crystallinity, but did partially coat individual particles.

Without the use of capping agents, $\text{Gd}(\text{OH})_3$ produced in the scope of this Thesis was chemically unstable and dissolved. As Gd^{3+} ions are known to be highly paramagnetic, the uncapped sample exhibited high relaxivity. Particles coated with dextran also showed high relaxivity. However, samples were not washed prior to analysis, so the effect of Gd^{3+} ions - which may be present in the sample - on relaxivity is unknown.

For all samples, sodium alginate had a detrimental effect on r_2 relaxivity. It is thought that the alginate may have a dampening effect on the superparamagnetic properties of the iron oxide particles. Hematite, Fe_2O_3 ; magnetite, Fe_3O_4 ; and gadolinium hydroxide, $\text{Gd}(\text{OH})_3$ produced using the Nozzle reactor have been shown to exhibit properties for MRI which are comparable to commercial contrast agents. As such, these materials have the potential for further research and development which can serve to enhance their r_2 relaxivities even more.

Synthesis of Co_3O_4 was also reported in Chapter 5, but the particles were found to be antiferromagnetic so did not display good relaxivity data. Still, this material may find use in other applications (Moro et al., 2013).

6.2 Future Work

Following on from the work on HA reported in Chapter 1, further attempts to incorporate drugs into the structure of HA can be made. Here, it is important to use compounds with high thermal stability. The work in this Thesis developed issues due to the low concentration of statin used, so this should be increased in future work. As well as FTIR or ToF-SIMS, thermal analysis such as TGA could provide additional data to ascertain the presence of organic compounds in samples.

Subsequent to the addition of $\text{Zn}(\text{NO}_3)_2 \cdot 6\text{H}_2\text{O}$ to HA synthesis which resulted in the novel synthesis of parascholzite, the ratio of Ca:Zn can be investigated further, to determine if other calcium-zinc phosphates can be produced using the Nozzle reactor.

The work described in Chapters 4 and 5 began to look at the use of stabilisers or capping agents to coat nanoparticles and prevent their aggregation. Meanwhile, the difficulty in choosing suitable surfactants for each particle, which are also compatible with the synthesis reaction system, was highlighted in Chapter 1. Nevertheless, the work in this Thesis described the positive effects of using 3-MPA as a surfactant for ZnS, and dextran for iron oxide nanoparticles (Fe_2O_3 and Fe_3O_4). There is scope for determining the optimum concentration ratios between these particles and surfactants. By improving the coating of these nanoparticles, their properties could be enhanced even further.

Also in Chapter 5, the relaxivities of samples was calculated based upon theoretical concentrations of Fe or Gd. Elemental analysis, such as atomic adsorption (AA) or inductively coupled plasma (ICP) could provide experimental concentrations for more accurate relaxivity values.

The functional properties of HA, ZnS, Fe₂O₃, Fe₃O₄ and Gd(OH)₃ were tested in this Thesis. However, other such tests could be performed to acquire more information on how these nanomaterials would perform if applied to commercial products. For example, more in depth cell assays or using other cell lines would yield additional cytotoxicity data for HA; tests could be carried out to determine the electroluminescent properties of ZnS; and T₁-weighted scans could be used on Fe₂O₃, Fe₃O₄ and Gd(OH)₃, in order to gather information about their effects on spin-lattice relaxation.

Bibliography

- ACTION, P. C. 2013. *Pancreatic Cancer Action - MRI Scans* [Online]. Available: www.pancreaticcanceraction.org.
- ADSCHIRI, T., HAKUTA, Y. & ARAI, K. 2000. Hydrothermal synthesis of metal oxide fine particles at supercritical conditions. *Industrial & Engineering Chemistry Research*, 39, 4901-4907.
- ADSCHIRI, T., HAKUTA, Y., SUE, K. & ARAI, K. 2001. Hydrothermal synthesis of metal oxide nanoparticles at supercritical conditions. *Journal of Nanoparticle Research*, 3, 227-235.
- ADSCHIRI, T., KANAZAWA, K. & ARAI, K. 1992. Rapid and continuous hydrothermal crystallization of metal-oxide particles in supercritical water. *Journal of the American Ceramic Society*, 75, 1019-1022.
- ADSCHIRI, T., LEE, Y. W., GOTO, M. & TAKAMI, S. 2011. Green materials synthesis with supercritical water. *Green Chemistry*, 13, 1380-1390.
- AG, S. 2013. Resovist: Information for Radiologists. Available: http://radiologie-uni-frankfurt.de/sites/radiologie-uni-frankfurt.de/content/e43/e2321/e2331/resofinal_eng.pdf.
- AIMABLE, A., AYMES, D., BERNARD, F. & LE CRAS, F. 2009a. Characteristics of LiFePO₄ obtained through a one step continuous hydrothermal synthesis process working in supercritical water. *Solid State Ionics*, 180, 861-866.
- AIMABLE, A., MUHR, H., GENTRIC, C., BERNARD, F., LE CRAS, F. & AYMES, D. 2009b. Continuous hydrothermal synthesis of inorganic nanopowders in supercritical water: Towards a better control of the process. *Powder Technology*, 190, 99-106.
- AIMABLE, A., XIN, B., MILLOT, N. & AYMES, D. 2008. Continuous hydrothermal synthesis of nanometric BaZrO₃ in supercritical water. *Journal of Solid State Chemistry*, 181, 183-189.
- AKSOMAITYTE, G., POLIAKOFF, M. & LESTER, E. 2013. The production and formulation of silver nanoparticles using continuous hydrothermal synthesis. *Chemical Engineering Science*, 85, 2-10.
- AL-DURI, B., PINTO, L., ASHRAF-BALL, N. H. & SANTOS, R. C. D. 2008. Thermal abatement of nitrogen-containing hydrocarbons by non-catalytic supercritical water oxidation (SCWO). *Journal of Materials Science*, 43, 1421-1428.
- ALBERTS, B., JOHNSON, A., LEWIS, J., RAFF, M., ROBERTS, K. & WALTER, P. 2002. The Shape and Structure of Proteins. *Molecular Biology of the Cell*. 4th ed. New York: Garland Science.
- ALBREKTSSON, ALBREKTSSON, T., JOHANSSON & JOHANSSON, C. 2001. Osteoinduction, osteoconduction and osseointegration. *European Spine Journal*, 10, S96-S101.
- AMAG PHARMACEUTICALS, I. 2013. *AMAG Pharmaceuticals* [Online]. Available: <http://www.amagpharma.com/about/partners.php> 2013].
- AMENDOLA, V., MENEGHETTI, M., GRANOZZI, G., AGNOLI, S., POLIZZI, S., RIELLO, P., BOSCAINI, A., ANSELMINI, C., FRACASSO, G., COLOMBATTI, M., INNOCENTI, C., GATTESCHI, D. & SANGREGORIO, C. 2011. Top-down synthesis of multifunctional iron oxide nanoparticles for macrophage labelling and manipulation. *Journal of Materials Chemistry*, 21, 3803-3813.
- AMIRI, S. & SHOKROLLAHI, H. 2013. The role of cobalt ferrite magnetic nanoparticles in medical science. *Materials Science and Engineering C*, 33, 1-8.
- APTE, S. K., GARAJE, S. N., ARBUJ, S. S., KALE, B. B., BAEG, J. O., MULIK, U. P., NAIK, S. D., AMALNERKAR, D. P. & GOSAVI, S. W. 2011. A novel

- template free, one pot large scale synthesis of cubic zinc sulfide nanotriangles and its functionality as an efficient photocatalyst for hydrogen production and dye degradation. *Journal of Materials Chemistry*, 21, 19241-19248.
- AYMES, D., ARIANE, M., BERNARD, F., MUHR, H. & DEMOISSON, F. 2011. *Particle synthesis by means of the thermal hydrolysis of mineral precursors*. PCT/FR2010/051520.
- AZIZIAN-KALANDARAGH, Y. & KHODAYARI, A. 2010. Aqueous synthesis and characterization of nearly monodispersed ZnS nanocrystals. *Physica Status Solidi (A) Applications and Materials Science*, 207, 2144-2148.
- BAE, H., AHMAD, T., RHEE, I., CHANG, Y., JIN, S.-U. & HONG, S. 2012. Carbon-coated iron oxide nanoparticles as contrast agents in magnetic resonance imaging. *Nanoscale Research Letters*, 7, 44.
- BALLMAN, A. A. & LAUDISE, R. A. 1963. Hydrothermal growth. *The Art and Science of Growing Crystals*, 231-251.
- BAMMER, R., SKARE, S., NEWBOULD, R., LIU, C., THIJS, V., ROPELE, S., CLAYTON, D. B., KRUEGER, G., MOSELEY, M. E. & GLOVER, G. H. 2005. Foundations of advanced magnetic resonance imaging. *NeuroRx*, 2, 167-196.
- BAO, X., LIN, M., KOH, H. Z. & ZHANG, Q. 2006. Preparation of Iron Oxide and Iron Oxide/Silicon Oxide Nanoparticles Via Water-in-Oil Microemulsion. *Ceramic Nanomaterials and Nanotechnology II*. John Wiley & Sons, Inc.
- BASA, S., MUNIYAPPAN, T., KARATGI, P., PRABHU, R. & PILLAI, R. 2008. Production and in vitro characterization of solid dosage form incorporating drug nanoparticles. *Drug Development and Industrial Pharmacy*, 34, 1209-1218.
- BASF. 2013. *Further research on effects of nanomaterials* [Online]. <http://www.basf.com/group/pressrelease/P-13-323>. Available: <http://www.basf.com/group/pressrelease/P-13-323>.
- BATEER, B., TIAN, C., QU, Y., DU, S., TAN, T., WANG, R., TIAN, G. & FU, H. 2013. Facile synthesis and shape control of Fe₃O₄ nanocrystals with good dispersion and stabilization. *CrystEngComm*, 15, 3366-3371.
- BAVYKIN, D. V., PARMON, V. N., LAPKIN, A. A. & WALSH, F. C. 2004. The effect of hydrothermal conditions on the mesoporous structure of TiO₂ nanotubes. *Journal of Materials Chemistry*, 14, 3370-3377.
- BEZZI, G., CELOTTI, G., LANDI, E., LA TORRETTA, T. M. G., SOPYAN, I. & TAMPIERI, A. 2003. A novel sol-gel technique for hydroxyapatite preparation. *Materials Chemistry and Physics*, 78, 816-824.
- BHUSHAN, B. 2010. *Springer Handbook of Nanotechnology*, Springer.
- BIO-RAD 2013. CHT™ Ceramic Hydroxyapatite. In: BIO-RAD (ed.). http://www.bio-rad.com/webroot/web/pdf/psd/literature/Bulletin_5667.pdf.
- BJØRNERUD, A., JOHANSSON, L. O. & AHLSTRÖM, H. K. 2001. Pre-clinical results with clariscan™ (NC100150 Injection); experience from different disease models. *Magnetic Resonance Materials in Physics, Biology and Medicine*, 12, 99-103.
- BLOCK, J. E. & THORN, M. R. 2000. Clinical indications of calcium-phosphate biomaterials and related composites for orthopedic procedures. *Calcified Tissue International*, 66, 234-238.
- BLOOD, P. J., DENYER, J. P., AZZOPARDI, B. J., POLIAKOFF, M. & LESTER, E. 2004. A versatile flow visualisation technique for quantifying mixing in a binary system: Application to continuous supercritical water hydrothermal synthesis (SWHS). *Chemical Engineering Science*, 59, 2853-2861.
- BOLDRIN, P., HEBB, A. K., CHAUDHRY, A. A., OTLEY, L., THIEBAUT, B., BISHOP, P. & DARR, J. A. 2007. Direct synthesis of nanosized NiCo₂O₄ spinel and related compounds via continuous hydrothermal synthesis methods. *Industrial and Engineering Chemistry Research*, 46, 4830-4838.

- BROWN, M. A. & SEMELKA, R. C. 2010. *MRI: Basic Principles and Applications*, Wiley-Blackwell.
- BRUCHEZ JR, M., MORONNE, M., GIN, P., WEISS, S. & ALIVISATOS, A. P. 1998. Semiconductor nanocrystals as fluorescent biological labels. *Science*, 281, 2013-2016.
- BUFFAT, P. & BOREL, J.-P. 1976. Size effect on the melting temperature of gold particles. *Physical Review A*, 13, 2287-2298.
- BYERS, R. J. & HITCHMAN, E. R. 2011. Quantum Dots Brighten Biological Imaging. *Progress in Histochemistry and Cytochemistry*, 45, 201-237.
- CABANAS, A., DARR, J. A., LESTER, E. & POLIAKOFF, M. 2000. A continuous and clean one-step synthesis of nano-particulate Ce(1-x)Zr(x)O₂ solid solutions in near-critical water. *Chemical Communications*, 901-902.
- CABAÑAS, A., LI, J., BLOOD, P., CHUDOBA, T., LOJKOWSKI, W., POLIAKOFF, M. & LESTER, E. 2007. Synthesis of nanoparticulate yttrium aluminum garnet in supercritical water-ethanol mixtures. *Journal of Supercritical Fluids*, 40, 284-292.
- CABAÑAS, A. & POLIAKOFF, M. 2001. The continuous hydrothermal synthesis of nano-particulate ferrites in near critical and supercritical water. *Journal of Materials Chemistry*, 11, 1408-1416.
- CARBONARO, L. A., PEDICONI, F., VERARDI, N., TRIMBOLI, R. M., CALABRESE, M. & SARDANELLI, F. 2011. Breast MRI using a high-relaxivity contrast agent: An overview. *American Journal of Roentgenology*, 196, 942-955.
- CARP, O., PATRON, L., CULITA, D. C., BUDRUGEAC, P., FEDER, M. & DIAMANDESCU, L. 2010. Thermal analysis of two types of dextran-coated magnetite. *Journal of Thermal Analysis and Calorimetry*, 101, 181-187.
- CASULA, M. F., CORRIAS, A., AROSIO, P., LASCIALFARI, A., SEN, T., FLORIS, P. & BRUCE, I. J. 2011. Design of water-based ferrofluids as contrast agents for magnetic resonance imaging. *Journal of Colloid and Interface Science*, 357, 50-55.
- CHAN, W. C. W. & NIE, S. 1998. Quantum dot bioconjugates for ultrasensitive nonisotopic detection. *Science*, 281, 2016-2018.
- CHANG, M. L. & HOU, J. K. 2011. Cancer risk related to gastrointestinal diagnostic radiation exposure. *Current Gastroenterology Reports*, 13, 449-457.
- CHAUDHRY, A. A., HAQUE, S., KELLICI, S., BOLDRIN, P., REHMAN, I., KHALID, F. A. & DARR, J. A. 2006. Instant nano-hydroxyapatite: A continuous and rapid hydrothermal synthesis. *Chemical Communications*, 2286-2288.
- CHEARY, R. W. & COELHO, A. A. 1996. XFIT. CCP14 Powder Diffraction Library: Engineering and Physical Sciences Research Council, Daresbury Laboratory, Warrington, England.
- CHEKINA, N., HORAK, D., JENDELOVA, P., TRCHOVA, M., BENES, M. J., HRUBY, M., HERYNEK, V., TURNOVCOVA, K. & SYKOVA, E. 2011. Fluorescent magnetic nanoparticles for biomedical applications. *Journal of Materials Chemistry*, 21, 7630-7639.
- CHEN, N., HE, Y., SU, Y., LI, X., HUANG, Q., WANG, H., ZHANG, X., TAI, R. & FAN, C. 2012. The cytotoxicity of cadmium-based quantum dots. *Biomaterials*, 33, 1238-1244.
- CHEN, Z., CAO, Y., QIAN, J., AI, X. & YANG, H. 2010. Facile synthesis and stable lithium storage performances of Sn-sandwiched nanoparticles as a high capacity anode material for rechargeable Li batteries. *Journal of Materials Chemistry*, 20, 7266-7271.
- CHOI, H., VERIANSYAH, B., KIM, J., KIM, J. D. & KANG, J. W. 2010. Continuous synthesis of metal nanoparticles in supercritical methanol. *Journal of Supercritical Fluids*, 52, 285-291.
- CHON CHEN, C., CHENG, C. H. & LIN, C. K. 2013. Template assisted fabrication of TiO₂ and WO₃ nanotubes. *Ceramics International*, 39, 6631-6636.
- CONN, P. M. 2009. *Essential Bioimaging Methods*, Elsevier Science.

- CORSO, D., CRUPI, I., AMMENDOLA, G., LOMBARDO, S. & GERARDI, C. 2003. Programming options for nanocrystal MOS memories. *Materials Science and Engineering C*, 23, 687-689.
- COVALIU, C. I., BERGER, D., MATEI, C., DIAMANDESCU, L., VASILE, E., CRISTEA, C., IONITA, V. & IOVU, H. 2011. Magnetic nanoparticles coated with polysaccharide polymers for potential biomedical applications. *Journal of Nanoparticle Research*, 13, 6169-6180.
- DARBANDI, M., STROMBERG, F., LANDERS, J., RECKERS, N., SANYAL, B., KEUNE, W. & WENDE, H. 2012. Nanoscale size effect on surface spin canting in iron oxide nanoparticles synthesized by the microemulsion method. *Journal of Physics D: Applied Physics*, 45.
- DASGUPTA, S., BANERJEE, S. S., BANDYOPADHYAY, A. & BOSE, S. 2010. Zn- and Mg-doped hydroxyapatite nanoparticles for controlled release of protein. *Langmuir*, 26, 4958-4964.
- DASOG, M. & VEINOT, J. G. C. 2012. Solid-state synthesis of luminescent silicon nitride nanocrystals. *Chemical Communications*, 48, 3760-3762.
- DAWSON, W. J. 1988. Hydrothermal synthesis of advanced ceramic powders. *American Ceramic Society Bulletin*, 67, 1673-1678.
- DE LIMA, I. R., ALVES, G. G., DE OLIVEIRA FERNANDES, G. V., DIAS, E. P., DE ALMEIDA SOARES, G. & GRANJEIRO, J. M. 2010. Evaluation of the in vivo biocompatibility of hydroxyapatite granules incorporated with zinc ions. *Materials Research*, 13, 563-568.
- DEMAZEAU, G. Solvothermal and Hydrothermal Processes: Main Physico-Chemical Factors Involved and New Trends. International Solvothermal and Hydrothermal Association Conference, 2010 Beijing, China.
- DEMOISSON, F., ARIANE, M., LEYBROS, A., MUHR, H. & BERNARD, F. 2011. Design of a reactor operating in supercritical water conditions using CFD simulations. Examples of synthesized nanomaterials. *Journal of Supercritical Fluids*, 58, 371-377.
- DICKERSON, B. D. 2005. *Organometallic synthesis kinetics of CdSe quantum dots*. Virginia Polytechnic Institute and State University.
- DING, J., TAO, K., LI, J., SONG, S. & SUN, K. 2010. Cell-specific cytotoxicity of dextran-stabilized magnetite nanoparticles. *Colloids and Surfaces B: Biointerfaces*, 79, 184-190.
- DURÁN, J. D. G., GUINDO, M. C., DELGADO, A. V. & GONZÁLEZ-CABALLERO, F. 1995. Stability of monodisperse zinc sulfide colloidal dispersions. *Langmuir*, 11, 3648-3655.
- DUTTA, S., PARK, J. A., JUNG, J. C., CHANG, Y. & KIM, T. J. 2008. Gd-complexes of DTPA-bis(amide) conjugates of tranexamic acid and its esters with high relaxivity and stability for magnetic resonance imaging. *Dalton Transactions*, 2199-2206.
- EARL, J. S., WOOD, D. J. & MILNE, S. J. 2006. Hydrothermal synthesis of hydroxyapatite. *Journal of Physics: Conference Series*, 26, 268-271.
- ELOUALI, S., BLOOR, L. G., BINIONS, R., PARKIN, I. P., CARMALT, C. J. & DARR, J. A. 2012. Gas sensing with nano-indium oxides (In₂O₃) prepared via continuous hydrothermal flow synthesis. *Langmuir*, 28, 1879-1885.
- FANG, Z. 2010. *Rapid Production of Micro- and Nano-particles Using Supercritical Water*, Springer Berlin Heidelberg.
- FANUN, M. 2010. *Microemulsions: Properties and Applications*, Taylor & Francis.
- FIGGEMEIER, E., KYLBERG, W., CONSTABLE, E., SCARISOREANU, M., ALEXANDRESCU, R., MORJAN, I., SOARE, I., BIRJEGA, R., POPOVICI, E., FLEACA, C., GAVRILA-FLORESCU, L. & PRODAN, G. 2007. Titanium dioxide nanoparticles prepared by laser pyrolysis: Synthesis and photocatalytic properties. *Applied Surface Science*, 254, 1037-1041.
- FIRMANSYAH, D. A., KIM, S. G., LEE, K. S., ZAHAF, R., KIM, Y. H. & LEE, D. 2012. Microstructure-controlled aerosol-gel synthesis of ZnO quantum dots dispersed in SiO₂ nanospheres. *Langmuir*, 28, 2890-2896.

- FLEGLER, S., HECKMAN JR, J. & KLOMPARENS, K. 1995. *Scanning and transmission electron microscopy: an introduction*, Oxford University Press.
- FRENKEL, J. & DORFMAN, J. 1930. Spontaneous and induced magnetisation in ferromagnetic bodies [1]. *Nature*, 126, 274-275.
- GANGULI, A. K., AHMAD, T., VAIDYA, S. & AHMED, J. 2008. Microemulsion route to the synthesis of nanoparticles. *Pure and Applied Chemistry*, 80, 2451-2477.
- GEINGUENAUD, F., SOUISSI, I., FAGARD, R., MOTTE, L. & LALATONNE, Y. 2012. Electrostatic assembly of a DNA superparamagnetic nano-tool for simultaneous intracellular delivery and in situ monitoring. *Nanomedicine: Nanotechnology, Biology, and Medicine*, 8, 1106-1115.
- GERMAN, R. M. 2010. Coarsening in sintering: Grain shape distribution, grain size distribution, and grain growth kinetics in solid-pore systems. *Critical Reviews in Solid State and Materials Sciences*, 35, 263-305.
- GESZKE-MORITZ, M. & MORITZ, M. 2013. Quantum dots as versatile probes in medical sciences: Synthesis, modification and properties. *Materials Science and Engineering: C*, 33, 1008-1021.
- GIMENO-FABRA, M., MUNN, A. S., STEVENS, L. A., DRAGE, T. C., GRANT, D. M., KASHTIBAN, R. J., SLOAN, J., LESTER, E. & WALTON, R. I. 2012. Instant MOFs: Continuous synthesis of metal-organic frameworks by rapid solvent mixing. *Chemical Communications*, 48, 10642-10644.
- GLADSTONE, H. B., MCDERMOTT, M. W. & COOKE, D. D. 1995. Implants for cranioplasty. *Otolaryngologic Clinics of North America*, 28, 381-400.
- GRIFFITH, E. M. & DANILATOS, G. D. 1993. *Environmental scanning electron microscopy*, Wiley-Liss.
- GRIFFITHS, S. L. & CARTMELL, S. H. 2007. Use of statins for enhancing bone-tissue-engineered grafts. *European Journal of Plastic Surgery*, 1-7.
- GRUAR, R. I., TIGHE, C. J. & DARR, J. A. 2013. Scaling-up a confined jet reactor for the continuous hydrothermal manufacture of nanomaterials. *Industrial and Engineering Chemistry Research*, 52, 5270-5281.
- GRUAR, R. I., TIGHE, C. J., MUIR, J., KITTLER, J. T., WODJAK, M., KENYON, A. J. & DARR, J. A. 2012. Continuous hydrothermal synthesis of surface-functionalised nanophosphors for biological imaging. *RSC Advances*, 2, 10037-10047.
- HABRAKEN, W. J. E. M., WOLKE, J. G. C. & JANSEN, J. A. 2007. Ceramic composites as matrices and scaffolds for drug delivery in tissue engineering. *Advanced Drug Delivery Reviews*, 59, 234-248.
- HAKUTA, Y., ONAI, S., TERAYAMA, H., ADSCHIRI, T. & ARAI, K. 1998. Production of ultra-fine ceria particles by hydrothermal synthesis under supercritical conditions. *Journal of Materials Science Letters*, 17, 1211-1213.
- HAKUTA, Y., URA, H., HAYASHI, H. & ARAI, K. 2005. Effects of hydrothermal synthetic conditions on the particle size of γ -AlO(OH) in sub and supercritical water using a flow reaction system. *Materials Chemistry and Physics*, 93, 466-472.
- HALLMANN, S., FINK, M. J. & MITCHELL, B. S. 2011. The mechanochemical formation of functionalized semiconductor nanoparticles for biological, electronic and superhydrophobic surface applications. Houston, TX.
- HANWHA. 2013. *Hanwha Chemical Co. Ltd* [Online]. Available: http://hcc.hanwha.co.kr/eng/index_eng.jsp 2013].
- HARISINGHANI, M. G., BARENTSZ, J., HAHN, P. F., DESERNO, W. M., TABATABAEI, S., VAN DE KAA, C. H., DE LA ROSETTE, J. & WEISSLEDER, R. 2003. Noninvasive Detection of Clinically Occult Lymph-Node Metastases in Prostate Cancer. *New England Journal of Medicine*, 348, 2491-2499.

- HAW, C. Y., MOHAMED, F., CHIA, C. H., RADIMAN, S., ZAKARIA, S., HUANG, N. M. & LIM, H. N. 2010. Hydrothermal synthesis of magnetite nanoparticles as MRI contrast agents. *Ceramics International*, 36, 1417-1422.
- HEALTHCARE, G. 2013. *Omniscan* [Online]. Available: http://www3.gehealthcare.com/en/Products/Categories/Contrast_Media/Omniscan#tabs/tab488621DABE7848C7837C18A88CFE9FFF 2013].
- HEESAKKERS, R. A. M., JAGER, G. J., HÖVELS, A. M., DE HOOP, B., VAN DEN BOSCH, H. C. M., RAAT, F., WITJES, J. A., MULDER, P. F. A., VAN DER KAA, C. H. & BARENTS, J. O. 2009. Prostate cancer: Detection of lymph node metastases outside the routine surgical area with ferumoxtran-10-enhanced MR imaging. *Radiology*, 251, 408-414.
- HEO, J. & LIU, C. 2007. Pbs quantum-dots in glass matrix for universal fiber-optic amplifier. *Journal of Materials Science: Materials in Electronics*, 18, 135-139.
- HOBBS, H., BRIDDON, S. & LESTER, E. 2009. The synthesis and fluorescent properties of nanoparticulate ZrO₂ doped with Eu using continuous hydrothermal synthesis. *Green Chemistry*, 11, 484-491.
- HONG, S.-A., KIM, S. J., CHUNG, K. Y., CHUN, M.-S., LEE, B. G. & KIM, J. 2013. Continuous synthesis of lithium iron phosphate (LiFePO₄) nanoparticles in supercritical water: Effect of mixing tee. *The Journal of Supercritical Fluids*, 73, 70-79.
- HU, D., ZHANG, P., GONG, P., LIAN, S., LU, Y., GAO, D. & CAI, L. 2011. A fast synthesis of near-infrared emitting CdTe/CdSe quantum dots with small hydrodynamic diameter for in vivo imaging probes. *Nanoscale*, 3, 4724-4732.
- HUDGINS, P. A., ANZAI, Y., MORRIS, M. R. & LUCAS, M. A. 2002. Ferumoxtran-10, A Superparamagnetic Iron Oxide as a Magnetic Resonance Enhancement Agent for Imaging Lymph Nodes: A Phase 2 Dose Study. *American Journal of Neuroradiology*, 23, 649-656.
- IOKU, K., YOSHIMURA, M. & SOMIYA, S. 1988. Post-sintering of apatite ceramics from fine powders synthesized under hydrothermal conditions. *Journal of the Ceramic Society of Japan. International ed.*, 96, 111-112.
- ISASI-MARÍN, J., PÉREZ-ESTÉBANEZ, M., DÍAZ-GUERRA, C., CASTILLO, J. F., CORRECHER, V. & CUERVO-RODRÍGUEZ, M. R. 2009. Structural, magnetic and luminescent characteristics of Pr³⁺-doped ZrO₂ powders synthesized by a sol-gel method. *Journal of Physics D: Applied Physics*, 42.
- JADHAV, S. A. & BONGIOVANNI, R. 2012. Synthesis and organic functionalization approaches for magnetite (Fe₃O₄) nanoparticles. *Advanced Materials Letters*, 3, 356-361.
- JADHAV, S. B. & JAIN, G. K. 2006. Statins and osteoporosis: New role for old drugs. *Journal of Pharmacy and Pharmacology*, 58, 3-18.
- JAMIESON, T., BAKHSHI, R., PETROVA, D., POCOCK, R., IMANI, M. & SEIFALIAN, A. M. 2007. Biological applications of quantum dots. *Biomaterials*, 28, 4717-4732.
- JIN, T., SUN, D., SU, J. Y., ZHANG, H. & SUE, H. J. 2009. Antimicrobial efficacy of zinc oxide quantum dots against *Listeria monocytogenes*, *Salmonella Enteritidis*, and *Escherichia coli* O157:H7. *Journal of Food Science*, 74, M46-M52.
- KALITA, S. J. & BHATT, H. A. 2007. Nanocrystalline hydroxyapatite doped with magnesium and zinc: Synthesis and characterization. *Materials Science and Engineering: C*, 27, 837-848.
- KALITA, S. J. & VERMA, S. 2010. Nanocrystalline hydroxyapatite bioceramic using microwave radiation: Synthesis and characterization. *Materials Science and Engineering C*, 30, 295-303.

- KARIMI, Z., KARIMI, L. & SHOKROLLAHI, H. 2013. Nano-magnetic particles used in biomedicine: Core and coating materials. *Materials Science and Engineering C*, 33, 2465-2475.
- KASUGA, T., HIRAMATSU, K., HOSON, A., SEKINO, T. & NIIHARA, K. 1998. Formation of Titanium Oxide Nanotube. *Langmuir*, 1998, 3160-3163.
- KAWASAKI, S. I., SUE, K., OOKAWARA, R., WAKASHIMA, Y., SUZUKI, A., HAKUTA, Y. & ARAI, K. 2010. Engineering study of continuous supercritical hydrothermal method using a T-shaped mixer: Experimental synthesis of NiO nanoparticles and CFD simulation. *Journal of Supercritical Fluids*, 54, 96-102.
- KHODADADI-MOGHADDAM, M., SALIMI, F., SAHEBALZAMANI, H. & JAFARI, N. 2013. Synthesis of Fe₂O₃ nanoparticles via various methods and coating with silica for drug immobilization. *Synthesis and Reactivity in Inorganic, Metal-Organic and Nano-Metal Chemistry*, 43, 1224-1227.
- KIM, J., PARK, Y. S., VERIANSYAH, B., KIM, J. D. & LEE, Y. W. 2008. Continuous synthesis of surface-modified metal oxide nanoparticles using supercritical methanol for highly stabilized nanofluids. *Chemistry of Materials*, 20, 6301-6303.
- KIM, K., JEONG, S., WOO, J. Y. & HAN, C. S. 2012. Successive and large-scale synthesis of InP/ZnS quantum dots in a hybrid reactor and their application to white LEDs. *Nanotechnology*, 23.
- KONG, H. Y., HWANG, C. S. & BYUN, J. 2012. Biological toxicity changes of mercaptoacetic acid and mercaptopropionic acid upon coordination onto ZnS:Mn nanocrystal. *Bulletin of the Korean Chemical Society*, 33, 657-662.
- KRITZER, P., BOUKIS, N. & DINJUS, E. 1999. Factors controlling corrosion in high-temperature aqueous solutions: A contribution to the dissociation and solubility data influencing corrosion processes. *Journal of Supercritical Fluids*, 15, 205-227.
- KROL, S., MACREZ, R., DOCAGNE, F., DEFER, G., LAURENT, S., RAHMAN, M., HAJIPOUR, M. J., KEHOE, P. G. & MAHMOUDI, M. 2013. Therapeutic benefits from nanoparticles: The potential significance of nanoscience in diseases with compromise to the blood brain barrier. *Chemical Reviews*, 113, 1877-1903.
- LAAKSONEN, T., LIU, P., RAHIKKALA, A., PELTONEN, L., KAUPPINEN, E. I., HIRVONEN, J., JÄRVINEN, K. & RAULA, J. 2011. Intact nanoparticulate indomethacin in fast-dissolving carrier particles by combined wet milling and aerosol flow reactor methods. *Pharmaceutical Research*, 28, 2403-2411.
- LANG, J., LI, X., YANG, J., YANG, L., ZHANG, Y., YAN, Y., HAN, Q., WEI, M., GAO, M., LIU, X. & WANG, R. 2011. Rapid synthesis and luminescence of the Eu³⁺, Er³⁺ codoped ZnO quantum-dot chain via chemical precipitation method. *Applied Surface Science*, 257, 9574-9577.
- LAUGIER, J. 1999. Celref v3. Laboratoire des Matériaux et du Génie Physique de l'Ecole Supérieure de Physique de Grenoble, France.
- LEPRÊTRE, S., CHAI, F., HORNEZ, J. C., VERMET, G., NEUT, C., DESCAMPS, M., HILDEBRAND, H. F. & MARTEL, B. 2009. Prolonged local antibiotics delivery from hydroxyapatite functionalised with cyclodextrin polymers. *Biomaterials*, 30, 6086-6093.
- LESTER, E., AKSOMAITYTE, G., LI, J., GOMEZ, S., GONZALEZ-GONZALEZ, J. & POLIAKOFF, M. 2012. Controlled continuous hydrothermal synthesis of cobalt oxide (Co₃O₄) nanoparticles. *Progress in Crystal Growth and Characterization of Materials*, 58, 3-13.
- LESTER, E., BLOOD, P., DENYER, J., GIDDINGS, D., AZZOPARDI, B. & POLIAKOFF, M. 2006. Reaction engineering: The supercritical water hydrothermal synthesis of nano-particles. *Journal of Supercritical Fluids*, 37, 209-214.

- LESTER, E., TANG, S. V. Y., KHLOBYSTOV, A., ROSE, V. L., BUTTERY, L. & ROBERTS, C. J. 2013. Producing nanotubes of biocompatible hydroxyapatite by continuous hydrothermal synthesis. *CrystEngComm*, 15, 3256-3260.
- LESTER, E. H. & AZZOPARDI, B. J. 2005. *Counter Current Mixing Reactor*. WO2005/077505.
- LEYBROS, A., PIOLET, R., ARIANE, M., MUHR, H., BERNARD, F. & DEMOISSON, F. 2012. CFD simulation of ZnO nanoparticle precipitation in a supercritical water synthesis reactor. *Journal of Supercritical Fluids*, 70, 17-26.
- LI, B., WANG, X. L., GUO, B., XIAO, Y. M., FAN, H. S. & ZHANG, X. D. 2007. Preparation and characterization of nano hydroxyapatite. *Key Engineering Materials*, 330-332, 235-238.
- LI, J. 2008. *Engineering Nanoparticles in Near-critical and Supercritical Water*. Ph.D Chemical Engineering The University of Nottingham.
- LI, S., ZHAO, H. & TIAN, D. 2013. Aqueous synthesis of highly monodispersed thiol-capped CdSe quantum dots based on the electrochemical method. *Materials Science in Semiconductor Processing*, 16, 149-153.
- LIN, T., KELLICI, S., GONG, K., THOMPSON, K., EVANS, J. R. G., WANG, X. & DARR, J. A. 2010. Rapid automated materials synthesis instrument: Exploring the composition and heat-treatment of nanoprecursors toward low temperature red phosphors. *Journal of Combinatorial Chemistry*, 12, 383-392.
- LIU, H. & WEBSTER, T. J. 2007. Nanomedicine for implants: A review of studies and necessary experimental tools. *Biomaterials*, 28, 354-369.
- LIU, M., ZHAO, H., CHEN, S., WANG, H. & QUAN, X. 2012. Photochemical synthesis of highly fluorescent CdTe quantum dots for "on-off-on" detection of Cu(II) ions. *Inorganica Chimica Acta*, 392, 236-240.
- LIU, Y., ZHAN, J., REN, M., TANG, K., YU, W. & QIAN, Y. 2001. Hydrothermal synthesis of square thin flake CdS by using surfactants and thiocarbohydrate. *Materials Research Bulletin*, 36, 1231-1236.
- LÓPEZ-QUINTELA, M. A., RIVAS, J., BLANCO, M. C. & TOJO, C. 2004. Synthesis of Nanoparticles in Microemulsions. In: LIZ-MARZÁN, L. & KAMAT, P. (eds.) *Nanoscale Materials*. Springer US.
- LORYUENYONG, V., BUASRI, A., POCHANA, J., HOSAWANGWONG, S., THAISANG, S. & SOOKSAEN, P. 2013. Synthesis of anatase TiO₂ nanoparticles by template sol-gel method and its application in photocatalytic degradation of organic pollutants. *Advanced Science Letters*, 19, 2919-2922.
- LU, A. H., SALABAS, E. L. & SCHÜTH, F. 2007. Magnetic nanoparticles: Synthesis, protection, functionalization, and application. *Angewandte Chemie - International Edition*, 46, 1222-1244.
- LU, J., HAKUTA, Y., HAYASHI, H., OHASHI, T., NAGASE, T., HOSHI, Y., SATO, K., NISHIOKA, M., INOUE, T. & HAMAKAWA, S. 2008. Preparation of Ca_{0.8}Sr_{0.2}Ti_{1-x}FexO_{3-δ} (x = 0.1-0.3) nanoparticles using a flow supercritical reaction system. *Journal of Supercritical Fluids*, 46, 77-82.
- LU, J., MINAMI, K., TAKAMI, S. & ADSCHIRI, T. 2013. Rapid and continuous synthesis of cobalt aluminate nanoparticles under subcritical hydrothermal conditions with in-situ surface modification. *Chemical Engineering Science*, 85, 50-54.
- LUAN, W., YANG, H., WAN, Z., YUAN, B., YU, X. & TU, S. T. 2012. Mercaptopropionic acid capped CdSe/ZnS quantum dots as fluorescence probe for lead(II). *Journal of Nanoparticle Research*, 14, 1-8.
- LUBRIZOL. 2013. Hyperdispersants - Technology and Benefits.
- MALVERN. 2013. *Dynamic Light Scattering* [Online]. Available: <http://www.malvern.com>.

- MANH, D. H., THUAN, N. C., PHONG, P. T., HONG, L. V. & PHUC, N. X. 2009. Magnetic properties of La_{0.7}Ca_{0.3}MnO₃ nanoparticles prepared by reactive milling. *Journal of Alloys and Compounds*, 479, 828-831.
- MANSFIELD, P. & MAUDSLEY, A. A. 1977. Medical imaging by NMR. *British Journal of Radiology*, 50, 188-194.
- MANSFIELD, P. & PYKETT, I. L. 1978. Biological and medical imaging by NMR. *Journal of Magnetic Resonance (1969)*, 29, 355-373.
- MASTROGIACOMO, M., SCAGLIONE, S., MARTINETTI, R., DOLCINI, L., BELTRAME, F., CANCEDDA, R. & QUARTO, R. 2006. Role of scaffold internal structure on in vivo bone formation in macroporous calcium phosphate bioceramics. *Biomaterials*, 27, 3230-3237.
- MATSUI, K., NOGUCHI, T., ISLAM, N. M., HAKUTA, Y. & HAYASHI, H. 2008. Rapid synthesis of BaTiO₃ nanoparticles in supercritical water by continuous hydrothermal flow reaction system. *Journal of Crystal Growth*, 310, 2584-2589.
- MCCANN, T. E., KOSAKA, N., TURKBEY, B., MITSUNAGA, M., CHOYKE, P. L. & KOBAYASHI, H. 2011. Molecular imaging of tumor invasion and metastases: The role of MRI. *NMR in Biomedicine*, 24, 561-568.
- MONMA, H. & KAMIYA, T. 1987. Preparation of hydroxyapatite by the hydrolysis of brushite. *Journal of Materials Science*, 22, 4247-4250.
- MONTAZERI, N., JAHANDIDEH, R. & BIAZAR, E. 2011. Synthesis of fluorapatite-hydroxyapatite nanoparticles and toxicity investigations. *International journal of nanomedicine*, 6, 197-201.
- MORNET, S., VASSEUR, S., GRASSET, F. & DUGUET, E. 2004. Magnetic nanoparticle design for medical diagnosis and therapy. *Journal of Materials Chemistry*, 14, 2161-2175.
- MORO, F., TANG, S. V. Y., TUNA, F. & LESTER, E. 2013. Magnetic properties of cobalt oxide nanoparticles synthesised by a continuous hydrothermal method. *Journal of Magnetism and Magnetic Materials*, 348, 1-7.
- MOSEKE, C. & GBURECK, U. 2010. Tetracalcium phosphate: Synthesis, properties and biomedical applications. *Acta Biomaterialia*, 6, 3815-3823.
- MOUSAVAND, T., OHARA, S., UMETSU, M., ZHANG, J., TAKAMI, S., NAKA, T. & ADSCHIRI, T. 2007. Hydrothermal synthesis and in situ surface modification of boehmite nanoparticles in supercritical water. *Journal of Supercritical Fluids*, 40, 397-401.
- MOUSAVAND, T., TAKAMI, S., UMETSU, M., OHARA, S. & ADSCHIRI, T. 2006. Supercritical hydrothermal synthesis of organic-inorganic hybrid nanoparticles. *Journal of Materials Science*, 41, 1445-1448.
- MROZ, W., BOMBALSKA, A., BURDYNKA, S., JEDYNSKI, M., PROKOPIUK, A., BUDNER, B., SLOSARCZYK, A., ZIMA, A., MENASZEK, E., SCISLOWSKA-CZARNECKA, A. & NIEDZIELSKI, K. 2010. Structural studies of magnesium doped hydroxyapatite coatings after osteoblast culture. *Journal of Molecular Structure*, 977, 145-152.
- MU, B., ZHONG, W., DONG, Y., DU, P. & LIU, P. 2012. Encapsulation of drug microparticles with self-assembled Fe₃O₄/alginate hybrid multilayers for targeted controlled release. *Journal of Biomedical Materials Research - Part B Applied Biomaterials*, 100 B, 825-831.
- NANDA, K. K., MAISELS, A., KRUIS, F. E., FISSAN, H. & STAPPERT, S. 2003. Higher Surface Energy of Free Nanoparticles. *Physical Review Letters*, 91, 1061021-1061024.
- NANO.GOV. 2013. *What's So Special about the Nanoscale?* [Online]. Available: <http://www.nano.gov/nanotech-101/special>.
- NANOCO. 2013. *Nanoco Group Plc* [Online]. Available: <http://www.nanocotechnologies.com/>.
- NASSAR, M. Y. 2013. Size-controlled synthesis of CoCO₃ and Co₃O₄ nanoparticles by free-surfactant hydrothermal method. *Materials Letters*, 94, 112-115.

- NETZ, D. J. A., SEPULVEDA, P., PANDOLFELLI, V. C., SPADARO, A. C. C., ALENCASTRE, J. B., BENTLEY, M. & MARCHETTI, J. M. 2001. Potential use of gelcasting hydroxyapatite porous ceramic as an implantable drug delivery system. *International Journal of Pharmaceutics*, 213, 117-125.
- NI, S., YANG, X. & LI, T. 2011. Hydrothermal synthesis and photoluminescence properties of SrCO₃. *Materials Letters*, 65, 766-768.
- NOGUCHI, T., MATSUI, K., ISLAM, N. M., HAKUTA, Y. & HAYASHI, H. 2008. Rapid synthesis of γ -Al₂O₃ nanoparticles in supercritical water by continuous hydrothermal flow reaction system. *Journal of Supercritical Fluids*, 46, 129-136.
- OGI, T., KAIHATSU, Y., ISKANDAR, F., TANABE, E. & OKUYAMA, K. 2009. Synthesis of nanocrystalline GaN from Ga₂O₃ nanoparticles derived from salt-assisted spray pyrolysis. *Advanced Powder Technology*, 20, 29-34.
- OH, K. S., KIM, K. J., JEONG, Y. K., PARK, E. K., KIM, S. Y., KWON, J. H., RYOO, H. M. & SHIN, H. I. 2004. Cytotoxicity and antimicrobial effect of Ag doped hydroxyapatite. In: MANDAL, H. & OVECOGLU, L. (eds.) *Key Engineering Materials*. Istanbul.
- OHARA, S., MOUSAVAND, T., SASAKI, T., UMETSU, M., NAKA, T. & ADSCHIRI, T. 2008. Continuous production of fine zinc oxide nanorods by hydrothermal synthesis in supercritical water. *Journal of Materials Science*, 43, 2393-2396.
- OLDENDORF, W. 1988. *Basics of Magnetic Resonance Imaging*, Springer.
- ORLOVSKII, V. P., KOMLEV, V. S. & BARINOV, S. M. 2002. Hydroxyapatite and hydroxyapatite-based ceramics. *Inorganic Materials*, 38, 973-984.
- OSAKA, A., MIURA, Y., TAKEUCHI, K., ASADA, M. & TAKAHASHI, K. 1991. Calcium apatite prepared from calcium hydroxide and orthophosphoric acid. *Journal of Materials Science: Materials in Medicine*, 2, 51-55.
- PARK, J. B. 2009. The use of simvastatin in bone regeneration. *Medicina Oral, Patologia Oral y Cirugia Bucal*, 14, e485-e488.
- PARK, J. J., PRABHAKARAN, P., JANG, K. K., LEE, Y., LEE, J., LEE, K., HUR, J., KIM, J. M., CHO, N., SON, Y., YANG, D. Y. & LEE, K. S. 2010. Photopatternable quantum dots forming quasi-ordered arrays. *Nano Letters*, 10, 2310-2317.
- PARKER, J. E., THOMPSON, S. P., COBB, T. M., YUAN, F., POTTER, J., LENNIE, A. R., ALEXANDER, S., TIGHE, C. J., DARR, J. A., COCKCROFT, J. C. & TANG, C. C. 2011. High-throughput powder diffraction on beamline I11 at Diamond. *Journal of Applied Crystallography*, 44, 102-110.
- PARKES, L. M., HODGSON, R., LU, L. T., TUNG, L. D., ROBINSON, I., FERNIG, D. G. & THANH, N. T. K. 2008. Cobalt nanoparticles as a novel magnetic resonance contrast agent - Relaxivities at 1.5 and 3 Tesla. *Contrast Media and Molecular Imaging*, 3, 150-156.
- PIÑERO-HERNANZ, R., DODDS, C., HYDE, J., GARCÍA-SERNA, J., POLIAKOFF, M., LESTER, E., COCERO, M. J., KINGMAN, S., PICKERING, S. & WONG, K. H. 2008. Chemical recycling of carbon fibre reinforced composites in nearcritical and supercritical water. *Composites Part A: Applied Science and Manufacturing*, 39, 454-461.
- POOLE, P. J., KAMINSKA, K., BARRIOS, P., LU, Z. & LIU, J. 2009. Growth of InAs/InP-based quantum dots for 1.55 μ m laser applications. *Journal of Crystal Growth*, 311, 1482-1486.
- POSNER, A. S., PERLOFF, A. & DIORIO, A. F. 1958. Refinement of the hydroxyapatite structure. *Acta. Cryst.*, 11, 308.
- RAHMAN, S., NADEEM, K., ANIS-UR-REHMAN, M., MUMTAZ, M., NAEEM, S. & LETOFSKY-PAPST, I. 2013. Structural and magnetic properties of ZnMg-ferrite nanoparticles prepared using the co-precipitation method. *Ceramics International*, 39, 5235-5239.
- REN, H. B. & YAN, X. P. 2012. Ultrasonic assisted synthesis of adenosine triphosphate capped manganese-doped ZnS quantum dots for selective

- room temperature phosphorescence detection of arginine and methylated arginine in urine based on supramolecular Mg²⁺-adenosine triphosphate-arginine ternary system. *Talanta*, 97, 16-22.
- RONDA, C. R. 2008. *Luminescence*, Wiley.
- ROSLI, S. A., ZUBIR, Z. A. & AZIZ, N. M. A. 2012. Characterization of zns nanoparticles using Mpa as capping agents. Selangor.
- ROTELLO, V. M. 2004. *Nanoparticles: Building Blocks for Nanotechnology*, Kluwer Academic/Plenum Publishers.
- SAHRANESHIN, A., ASAHINA, S., TOGASHI, T., SINGH, V., TAKAMI, S., HOJO, D., ARITA, T., MINAMI, K. & ADSCHIRI, T. 2012a. Surfactant-assisted hydrothermal synthesis of water-dispersible hafnium oxide nanoparticles in highly alkaline media. *Crystal Growth and Design*, 12, 5219-5226.
- SAHRANESHIN, A., TAKAMI, S., HOJO, D., ARITA, T., MINAMI, K. & ADSCHIRI, T. 2012b. Mechanistic study on the synthesis of one-dimensional yttrium aluminum garnet nanostructures under supercritical hydrothermal conditions in the presence of organic amines. *CrystEngComm*, 14, 6085-6092.
- SAMPATHKUMARAN, E. V., MUKHERJEE, K., IYER, K. K., MOHAPATRA, N. & DAS, S. D. 2011. Magnetism of fine particles of kondo lattices, obtained by high-energy ball-milling. *Journal of Physics Condensed Matter*, 23.
- SANTRA, P. K. & KAMAT, P. V. 2012. Mn-doped quantum dot sensitized solar cells: A strategy to boost efficiency over 5%. *Journal of the American Chemical Society*, 134, 2508-2511.
- SARASWATHI AMMA, B., MANZOOR, K., RAMAKRISHNA, K. & PATTABI, M. 2008. Synthesis and optical properties of CdS/ZnS core-shell nanoparticles. *Materials Chemistry and Physics*, 112, 789-792.
- SATO, T., IJIMA, T., SEKI, M. & INAGAKI, N. 1987. Magnetic properties of ultrafine ferrite particles. *Journal of Magnetism and Magnetic Materials*, 65, 252-256.
- SATO, T., SUE, K., SUZUKI, W., SUZUKI, M., MATSUI, K., HAKUTA, Y., HAYASHI, H., ARAI, K., KAWASAKI, S. I., KAWAI-NAKAMURA, A. & HIAKI, T. 2008. Rapid and continuous production of ferrite nanoparticles by hydrothermal synthesis at 673 K and 30 MPa. *Industrial and Engineering Chemistry Research*, 47, 1855-1860.
- SEKINO, T., OKAMOTO, T., KASUGA, T., KUSUNOSE, T., NAKAYAMA, T. & NIIHARA, K. 2006. Synthesis and properties of titania nanotube doped with small amount of cations. *Key Engineering Materials*, 317-318, 251-254.
- SENTHILKUMAAR, S. & SELVI, R. T. 2008. Synthesis and Characterization of One Dimensional ZnS Nanorods. *Synthesis and Reactivity in Inorganic Metal-Organic and Nano-Metal Chemistry*, 38, 710-715.
- SEPULVEDA, P., BINNER, J. G. P., ROGERO, S. O., HIGA, O. Z. & BRESSIANI, J. C. 2000. Production of porous hydroxyapatite by the gel-casting of foams and cytotoxic evaluation. *Journal of Biomedical Materials Research*, 50, 27-34.
- SHARMA, A., PANDEY, C. M., SUMANA, G., SONI, U., SAPRA, S., SRIVASTAVA, A. K., CHATTERJEE, T. & MALHOTRA, B. D. 2012. Chitosan encapsulated quantum dots platform for leukemia detection. *Biosensors and Bioelectronics*, 38, 107-113.
- SHARMA, M., KUMAR, S. & PANDEY, O. P. 2010. Study of energy transfer from capping agents to intrinsic vacancies/defects in passivated ZnS nanoparticles. *Journal of Nanoparticle Research*, 12, 2655-2666.
- SHEN, L., CUI, X., QI, H. & ZHANG, C. 2007. Electrogenerated chemiluminescence of ZnS nanoparticles in alkaline aqueous solution. *Journal of Physical Chemistry C*, 111, 8172-8175.

- SHIN, N. C., LEE, Y. H., SHIN, Y. H., KIM, J. & LEE, Y. W. 2010. Synthesis of cobalt nanoparticles in supercritical methanol. *Materials Chemistry and Physics*, 124, 140-144.
- SHYMAN. 2013. *Sustainable Hydrothermal Manufacturing of Nanomaterials* [Online]. <http://www.shyman.eu/>. Available: <http://www.shyman.eu/2013>].
- SOHRABNEZHAD, S. & VALIPOUR, A. 2013. Synthesis of Cu/CuO nanoparticles in mesoporous material by solid state reaction. *Spectrochimica Acta - Part A: Molecular and Biomolecular Spectroscopy*, 114, 298-302.
- SOMIYA, S. & ROY, R. 2000. Hydrothermal synthesis of fine oxide powders. *Bulletin of Materials Science*, 23, 453-460.
- STANIĆ, V., DIMITRIJEVIĆ, S., ANTIĆ-STANKOVIĆ, J., MITRIĆ, M., JOKIĆ, B., PLEČAŠ, I. B. & RAIČEVIĆ, S. 2010. Synthesis, characterization and antimicrobial activity of copper and zinc-doped hydroxyapatite nanopowders. *Applied Surface Science*, 256, 6083-6089.
- STANIC, V., JANACKOVIC, D., DIMITRIJEVIC, S., TANASKOVIC, S. B., MITRIC, M., PAVLOVIC, M. S., KRSTIC, A., JOVANOVIC, D. & RAICEVIC, S. 2011. Synthesis of antimicrobial monophasic silver-doped hydroxyapatite nanopowders for bone tissue engineering. *Applied Surface Science*, 257, 4510-4518.
- STEPHEN, Z. R., KIEVIT, F. M. & ZHANG, M. 2011. Magnetite nanoparticles for medical MR imaging. *Materials Today*, 14, 330-338.
- STURMAN, B. D., ROUSE, R. C. & DUNN, P. J. 1981. Parascholzite, a new mineral from Hagendorf, Bavaria, and its relationship to scholzite. *American Mineralogist*, 66, 843-851.
- SUE, K., AOKI, M., SATO, T., NISHIO-HAMANE, D., KAWASAKI, S. I., HAKUTA, Y., TAKEBAYASHI, Y., YODA, S., FURUYA, T. & HIAKI, T. 2011. Continuous hydrothermal synthesis of nickel ferrite nanoparticles using a central collision-type micromixer: Effects of temperature, residence time, metal salt molality, and naoh addition on conversion, particle size, and crystal phase. *Industrial and Engineering Chemistry Research*, 50, 9625-9631.
- SUE, K., SUZUKI, A., HAKUTA, Y., HAYASHI, H., ARAI, K., TAKEBAYASHI, Y., YODA, S. & FURUYA, T. 2009. Hydrothermal-reduction synthesis of Ni nanoparticles by superrapid heating using a micromixer. *Chemistry Letters*, 38, 1018-1019.
- SUE, K., SUZUKI, M., ARAI, K., OHASHI, T., URA, H., MATSUI, K., HAKUTA, Y., HAYASHI, H., WATANABE, M. & HIAKI, T. 2006. Size-controlled synthesis of metal oxide nanoparticles with a flow-through supercritical water method. *Green Chemistry*, 8, 634-638.
- TAGUCHI, M., TAKAMI, S., ADSCHIRI, T., NAKANE, T., SATO, K. & NAKA, T. 2012. Synthesis of surface-modified monoclinic ZrO₂ nanoparticles using supercritical water. *CrystEngComm*, 14, 2132-2138.
- TAKAMI, S., SUGIOKA, K. I., TSUKADA, T., ADSCHIRI, T., SUGIMOTO, K., TAKENAKA, N. & SAITO, Y. 2012. Neutron radiography on tubular flow reactor for hydrothermal synthesis: In situ monitoring of mixing behavior of supercritical water and room-temperature water. *Journal of Supercritical Fluids*, 63, 46-51.
- TANG, G., LIU, S., TANG, H., ZHANG, D., LI, C. & YANG, X. 2013. Template-assisted hydrothermal synthesis and photocatalytic activity of novel TiO₂ hollow nanostructures. *Ceramics International*, 39, 4969-4974.
- TANG, S. Y., BOURNE, R. A., SMITH, R. L. & POLIAKOFF, M. 2008. The 24 Principles of Green Engineering and Green Chemistry: "IMPROVEMENTS PRODUCTIVELY". *Green Chemistry*, 10, 268-269.
- THOMSEN, H. S. & WEBB, J. A. W. 2009. MR Contrast Media: Organ specific. In: BAERT, A. L., BRADY, L. W., HEILMANN, H. P., KNAUTH, M., MOLLS, M. &

- NEIDER, C. (eds.) *Contrast Media: Safety Issues and ESUR Guidelines*. 2 ed.: Springer.
- TIGHE, C. J., CABRERA, R. Q., GRUAR, R. I. & DARR, J. A. 2013. Scale up production of nanoparticles: Continuous supercritical water synthesis of Ce-Zn oxides. *Industrial and Engineering Chemistry Research*, 52, 5522-5528.
- TIGHE, C. J., GRUAR, R. I., MA, C. Y., MAHMUD, T., WANG, X. Z. & DARR, J. A. 2012. Investigation of counter-current mixing in a continuous hydrothermal flow reactor. *Journal of Supercritical Fluids*, 62, 165-172.
- TSAI, Z.-T., WANG, J.-F., KUO, H.-Y., SHEN, C.-R., WANG, J.-J. & YEN, T.-C. 2010. In situ preparation of high relaxivity iron oxide nanoparticles by coating with chitosan: A potential MRI contrast agent useful for cell tracking. *Journal of Magnetism and Magnetic Materials*, 322, 208-213.
- TSAKALAKOS, L. 2008. Nanostructures for photovoltaics. *Materials Science and Engineering R: Reports*, 62, 175-189.
- TSUZUKI, T. 2009. Commercial scale production of inorganic nanoparticles. *International Journal of Nanotechnology*, 6, 567-578.
- VERIANSYAH, B., KIM, J. D., MIN, B. K. & KIM, J. 2010a. Continuous synthesis of magnetite nanoparticles in supercritical methanol. *Materials Letters*, 64, 2197-2200.
- VERIANSYAH, B., KIM, J. D., MIN, B. K., SHIN, Y. H., LEE, Y. W. & KIM, J. 2010b. Continuous synthesis of surface-modified zinc oxide nanoparticles in supercritical methanol. *Journal of Supercritical Fluids*, 52, 76-83.
- VERIANSYAH, B., PARK, H., KIM, J. D., MIN, B. K., SHIN, Y. H., LEE, Y. W. & KIM, J. 2009. Characterization of surface-modified ceria oxide nanoparticles synthesized continuously in supercritical methanol. *Journal of Supercritical Fluids*, 50, 283-291.
- VICKERMAN, J. C. & BRIGGS, D. 2001. *ToF-SIMS: Surface Analysis by Mass Spectrometry*, IM.
- VIJAYALAKSHMI, U. & RAJESWARI, S. 2006. Preparation and characterization of microcrystalline hydroxyapatite using sol gel method. *Trends in Biomaterials and Artificial Organs*, 19, 57-62.
- WAGEH, S., SHU-MAN, L., YOU, F. T. & XU-RONG, X. 2003. Optical properties of strongly luminescing mercaptoacetic-acid-capped ZnS nanoparticles. *Journal of Luminescence*, 102-103, 768-773.
- WAKASHIMA, Y., SUZUKI, A., KAWASAKI, S. I., MATSUI, K. & HAKUTA, Y. 2007. Development of a new swirling micro mixer for continuous hydrothermal synthesis of nano-size particles. *Journal of Chemical Engineering of Japan*, 40, 622-629.
- WANDELER, R. & BAIKER, A. 2000. Supercritical fluids: Opportunities in heterogeneous catalysis. *CATTECH*, 4, 34-50.
- WANG, Q., TANG, S. V. Y., LESTER, E. & O'HARE, D. 2013. Synthesis of ultrafine layered double hydroxide (LDHs) nanoplates using a continuous-flow hydrothermal reactor. *Nanoscale*, 5, 114-117.
- WANG, Y.-X. J. 2011. Superparamagnetic iron oxide based MRI contrast agents: Current status of clinical application. *Quantitative Imaging in Medicine and Surgery*, 1, 35-40.
- WEBSTER, T. J., MASSA-SCHLUETER, E. A., SMITH, J. L. & SLAMOVICH, E. B. 2004. Osteoblast response to hydroxyapatite doped with divalent and trivalent cations. *Biomaterials*, 25, 2111-2121.
- WEI, Z., XIA, T., MA, J., FENG, W., DAI, J., WANG, Q. & YAN, P. 2007. Investigation of the lattice expansion for Ni nanoparticles. *Materials Characterization*, 58, 1019-1024.
- WENG, X., COCKCROFT, J. K., HYETT, G., VICKERS, M., BOLDRIN, P., TANG, C. C., THOMPSON, S. P., PARKER, J. E., KNOWLES, J. C., REHMAN, I., PARKIN, I., EVANS, J. R. G. & DARR, J. A. 2009. High-throughput

- continuous hydrothermal synthesis of an entire nanoceramic phase diagram. *Journal of Combinatorial Chemistry*, 11, 829-834.
- WHITTERS, C. J., STRANG, R., BROWN, D., CLARKE, R. L., CURTIS, R. V., HATTON, P. V., IRELAND, A. J., LLOYD, C. H., MCCABE, J. F., NICHOLSON, J. W., SCRIMGEOUR, S. N., SETCOS, J. C., SHERRIFF, M., VAN NOORT, R., WATTS, B. C. & WOOD, D. 1999. Dental materials: 1997 literature review. *Journal of Dentistry*, 27, 401-435.
- WILLARD, M. A., KURIHARA, L. K., CARPENTER, E. E., CALVIN, S. & HARRIS, V. G. 2004. Chemically prepared magnetic nanoparticles. *International Materials Reviews*, 49, 125-170.
- WILLIAMS, D. B. & CARTER, C. B. 2009. *Transmission electron microscopy: a textbook for materials science.*, Springer.
- WOOD, V., PANZER, M. J., CHEN, J., BRADLEY, M. S., HALPERT, J. E., BAWENDI, M. C. & BULOVIĆ, V. 2009. Inkjet-printed quantum dot-polymer composites for full-color AC-driven displays. *Advanced Materials*, 21, 2151-2155.
- XING, Y., CHAUDRY, Q., SHEN, C., KONG, K. Y., ZHAU, H. E., CHUNG, L. W., PETROS, J. A., O'REGAN, R. M., YEZHELYEV, M. V., SIMONS, J. W., WANG, M. D. & NIE, S. 2007. Bioconjugated quantum dots for multiplexed and quantitative immunohistochemistry. *Nature Protocols*, 2, 1152-1165.
- XU, B. & WANG, X. 2012. Solvothermal synthesis of monodisperse nanocrystals. *Dalton Transactions*, 41, 4719-4725.
- XUE, B., DENG, D. W., CAO, J., LIU, F., LI, X., AKERS, W., ACHILEFU, S. & GU, Y. Q. 2012. Synthesis of NAC capped near infrared-emitting CdTeS alloyed quantum dots and application for in vivo early tumor imaging. *Dalton Transactions*, 41, 4935-4947.
- YANG, F., XU, Z., WANG, J., ZAN, F., DONG, C. & REN, J. 2012a. Microwave-assisted aqueous synthesis of new quaternary-alloyed CdSeTeS quantum dots; and their bioapplications in targeted imaging of cancer cells. *Luminescence*.
- YANG, H., LUAN, W., CHENG, R., CHU, H. & TU, S. T. 2011. Synthesis of quantum dots via microreaction: Structure optimization for microreactor system. *Journal of Nanoparticle Research*, 13, 3335-3344.
- YANG, L.-X., YIN, J.-J., WANG, L.-L., XING, G.-X., YIN, P. & LIU, Q.-W. 2012b. Hydrothermal synthesis of hierarchical hydroxyapatite: Preparation, growth mechanism and drug release property. *Ceramics International*, 38, 495-502.
- YU, Y., XU, L., CHEN, J., GAO, H., WANG, S., FANG, J. & XU, S. 2012. Hydrothermal synthesis of GSH-TGA co-capped CdTe quantum dots and their application in labeling colorectal cancer cells. *Colloids and Surfaces B: Biointerfaces*, 95, 247-253.
- ZAGHIB, K., CHAREST, P., DONTIGNY, M., LABRECQUE, J. F., MAUGER, A. & JULIEN, C. A new synthetic route of LiFePO₄ nanoparticles from molten ingot. 2011 Las Vegas, NV. 23-31.
- ZHANG, C., YANG, J., QUAN, Z., YANG, P., LI, C., HOU, Z. & LIN, J. 2009a. Hydroxyapatite nano- and microcrystals with multiform morphologies: Controllable synthesis and luminescence properties. *Crystal Growth and Design*, 9, 2725-2733.
- ZHANG, J. & GE, M. 2011. Effecting factors of the emission spectral characteristics of rare-earth strontium aluminate for anti-counterfeiting application. *Journal of Luminescence*, 131, 1765-1769.
- ZHANG, L., HE, R. & GU, H.-C. 2006. Oleic acid coating on the monodisperse magnetite nanoparticles. *Applied Surface Science*, 253, 2611-2617.
- ZHANG, S., ZHANG, Y., WANG, Y., LIU, S. & DENG, Y. 2012. Sonochemical formation of iron oxide nanoparticles in ionic liquids for magnetic liquid marble. *Physical Chemistry Chemical Physics*, 14, 5132-5138.

- ZHANG, Y. & LU, J. 2008. The transformation of single-crystal calcium phosphate ribbon-like fibres to hydroxyapatite spheres assembled from nanorods. *Nanotechnology*, 19.
- ZHANG, Z., BROWN, S., GOODALL, J. B. M., WENG, X., THOMPSON, K., GONG, K., KELLICI, S., CLARK, R. J. H., EVANS, J. R. G. & DARR, J. A. 2009b. Direct continuous hydrothermal synthesis of high surface area nanosized titania. *Journal of Alloys and Compounds*, 476, 451-456.
- ZHANG, Z., GOODALL, J. B. M., BROWN, S., KARLSSON, L., CLARK, R. J. H., HUTCHISON, J. L., REHMAN, I. U. & DARR, J. A. 2010. Continuous hydrothermal synthesis of extensive 2D sodium titanate (Na₂Ti₃O₇) nano-sheets. *Dalton Transactions*, 39, 711-714.
- ZHENG, Y.-H., CHENG, Y., BAO, F. & WANG, Y.-S. 2006. Synthesis and magnetic properties of Fe₃O₄ nanoparticles. *Materials Research Bulletin*, 41, 525-529.
- ZHOU, H. & LEE, J. 2011. Nanoscale hydroxyapatite particles for bone tissue engineering. *Acta Biomaterialia*, 7, 2769-2781.
- ZHU, L., ANG, S. & LIU, W. T. 2004. Quantum Dots as a Novel Immunofluorescent Detection System for *Cryptosporidium parvum* and *Giardia lamblia*. *Applied and Environmental Microbiology*, 70, 597-598.

Appendix

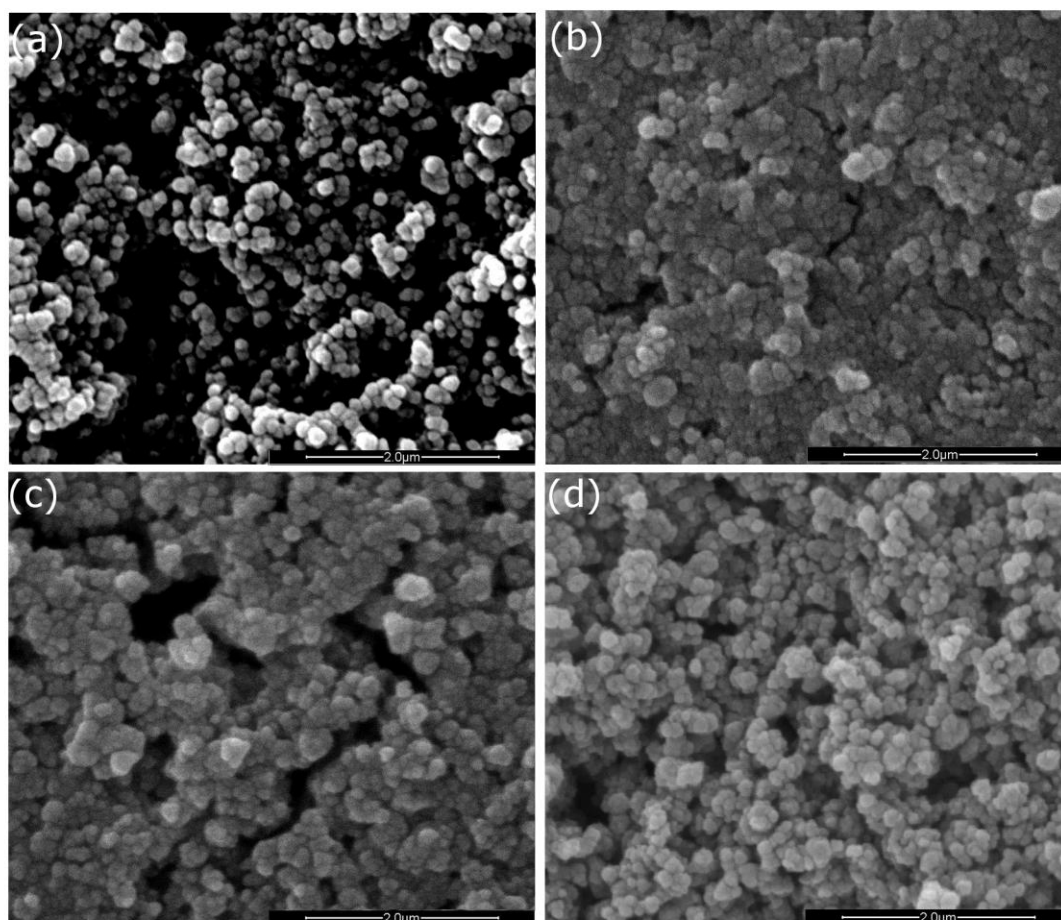


Figure A1. SEM images of (a) ZnS:NaOH 9/1, (b) ZnS:NaOH 8/2, (c) ZnS:NaOH 7/3, (d) ZnS:NaOH 6/4.

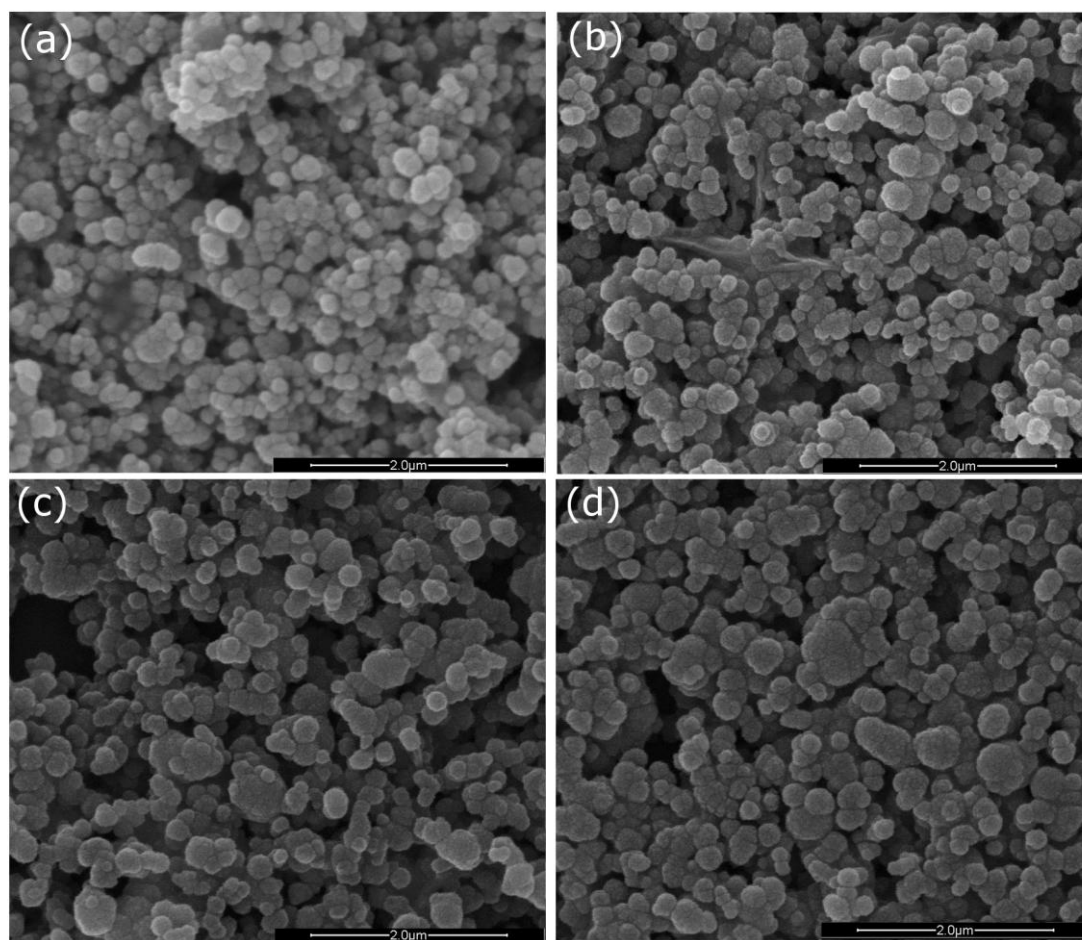


Figure A2. SEM images of (a) ZnS:3MPA 9/1, (b) ZnS:3MPA 8/2, (c) ZnS:3MPA 7/3, (d) ZnS:3MPA 6/4.

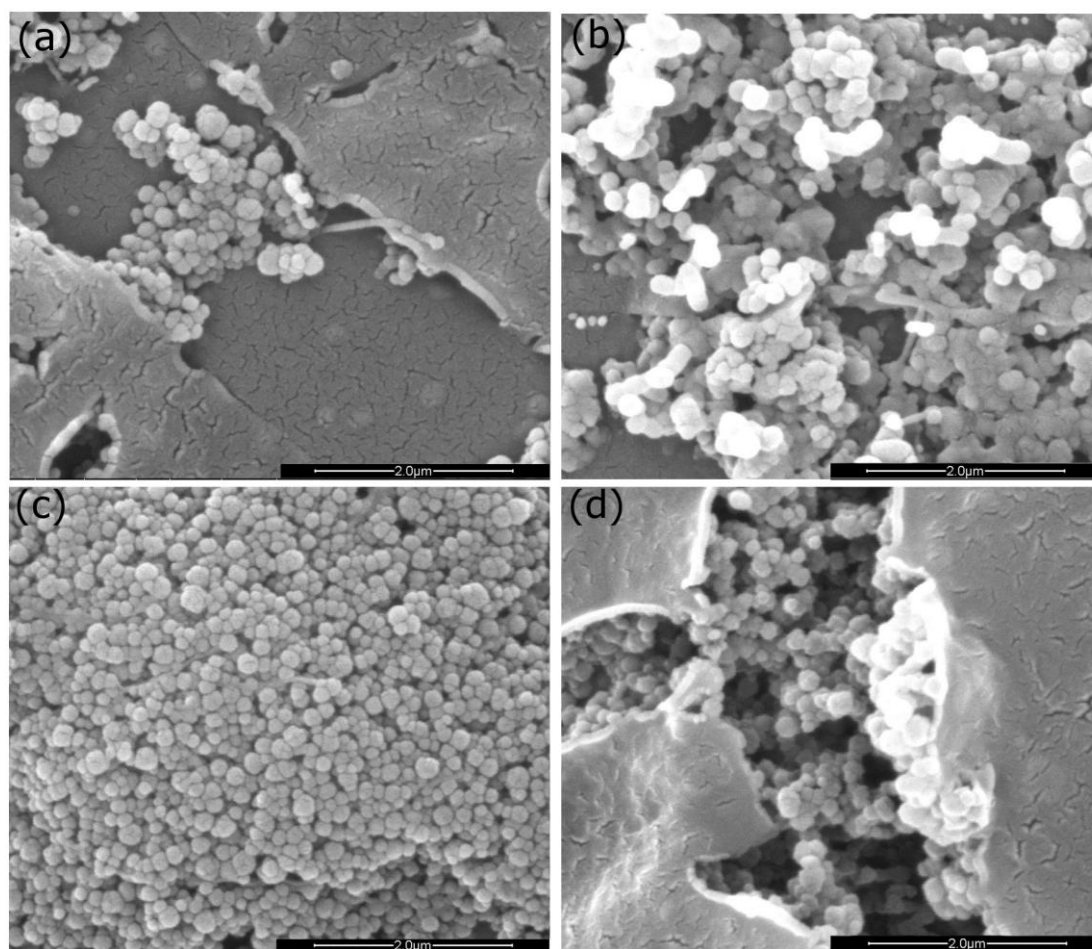


Figure A3. SEM images of (a) ZnS:PVP 9/1, (b) ZnS:PVP 8/2, (c) ZnS:PVP 7/3, (d) ZnS:PVP 6/4.

Table A1. Zeta Potential data for Uncapped ZnS.

| pH | Average ζ potential (mV) | Standard Deviation |
|-----------|--|---------------------------|
| 2.59 | 20.1 | 1.362 |
| 4.48 | 21.12 | 1.126 |
| 6.72 | 3.668 | 0.991 |
| 8.12 | -0.843 | 0.274 |
| 9.52 | -1.407 | 0.46 |
| 10.38 | -34.6 | 1.589 |
| 11.69 | -55.1 | 5.704 |

Table A2. Zeta Potential data for ZnS:3MPA 5/5.

| pH | Average ζ potential (mV) | Standard Deviation |
|-----------|--|---------------------------|
| 2.09 | 19.92 | 1.184 |
| 3.62 | 13.5 | 0.731 |
| 4.31 | -3.992 | 0.767 |
| 5.92 | -23.86 | 1.036 |
| 6.44 | -26.74 | 2.348 |
| 9.33 | -22.34 | 1.074 |
| 10.97 | -52.28 | 1.875 |

Table A3. Zeta Potential data for ZnS:PVP 5/5.

| pH | Average ζ potential (mV) | Standard Deviation |
|-----------|--|---------------------------|
| 3.05 | 0.443 | 0.423 |
| 3.53 | -5.926 | 1.318 |
| 4.98 | -6.492 | 1.37 |
| 7 | -11.34 | 0.811 |
| 8.24 | -18.34 | 0.879 |
| 10.14 | -22.1 | 0.675 |
| 11.03 | -18.06 | 3.469 |

Table A4. Zeta Potential data for ZnS:NaOH 5/5.

| pH | Average ζ potential (mV) | Standard Deviation |
|-----------|--|---------------------------|
| 3.16 | 9.622 | 0.518 |
| 5.04 | 10.598 | 0.635 |
| 7.1 | 8.52 | 0.835 |
| 8.21 | 8.244 | 0.859 |
| 9.35 | -21.34 | 1.378 |
| 10.96 | -38.48 | 1.813 |

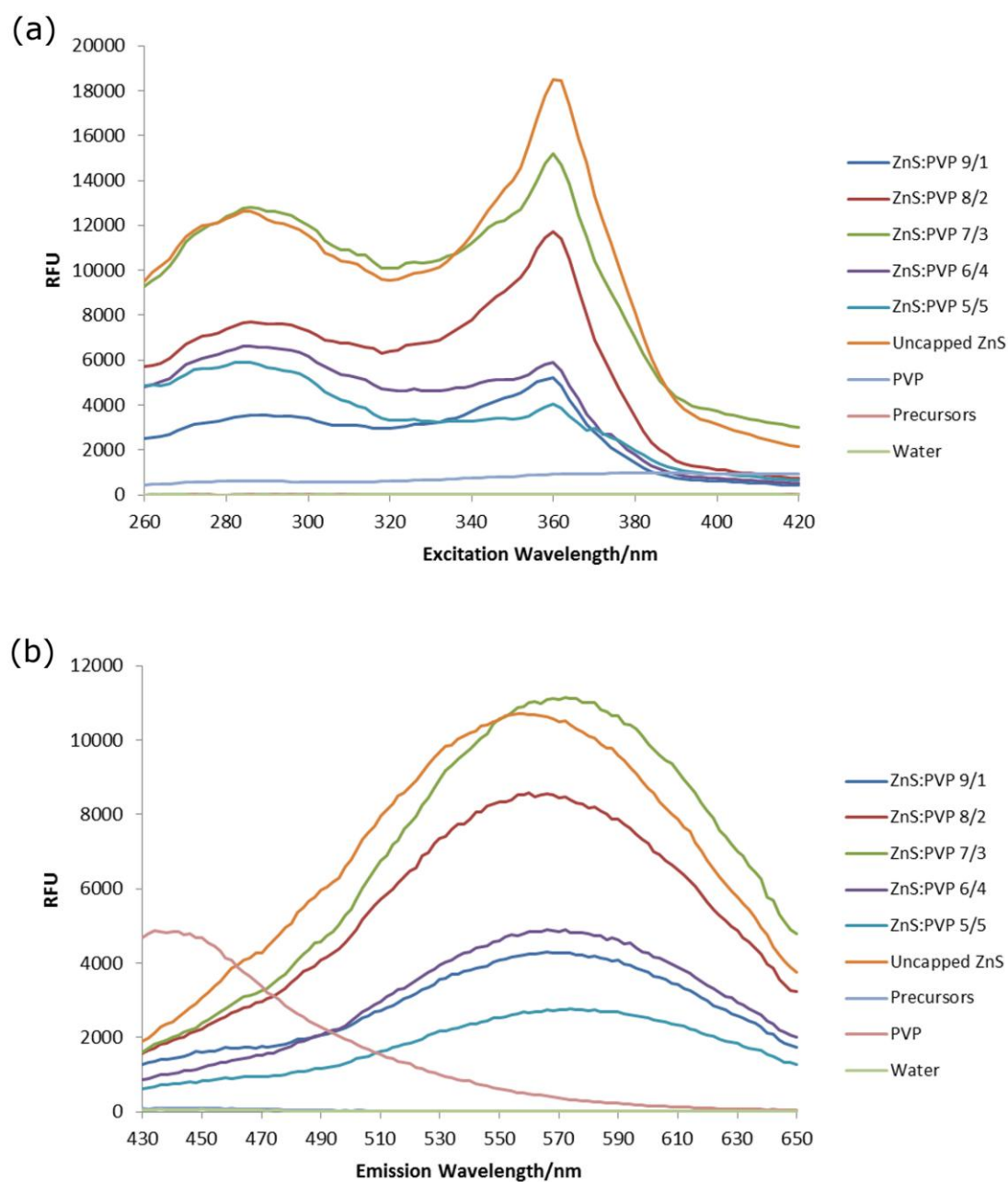


Figure A4. (a) The excitation spectra ($\lambda_{em} = 540$ nm) and (b) emission spectra ($\lambda_{ex} = 360$ nm) for ZnS:PVP samples produced using different precursor flow ratios. The spectra of the precursors and water blank were obtained as a control.

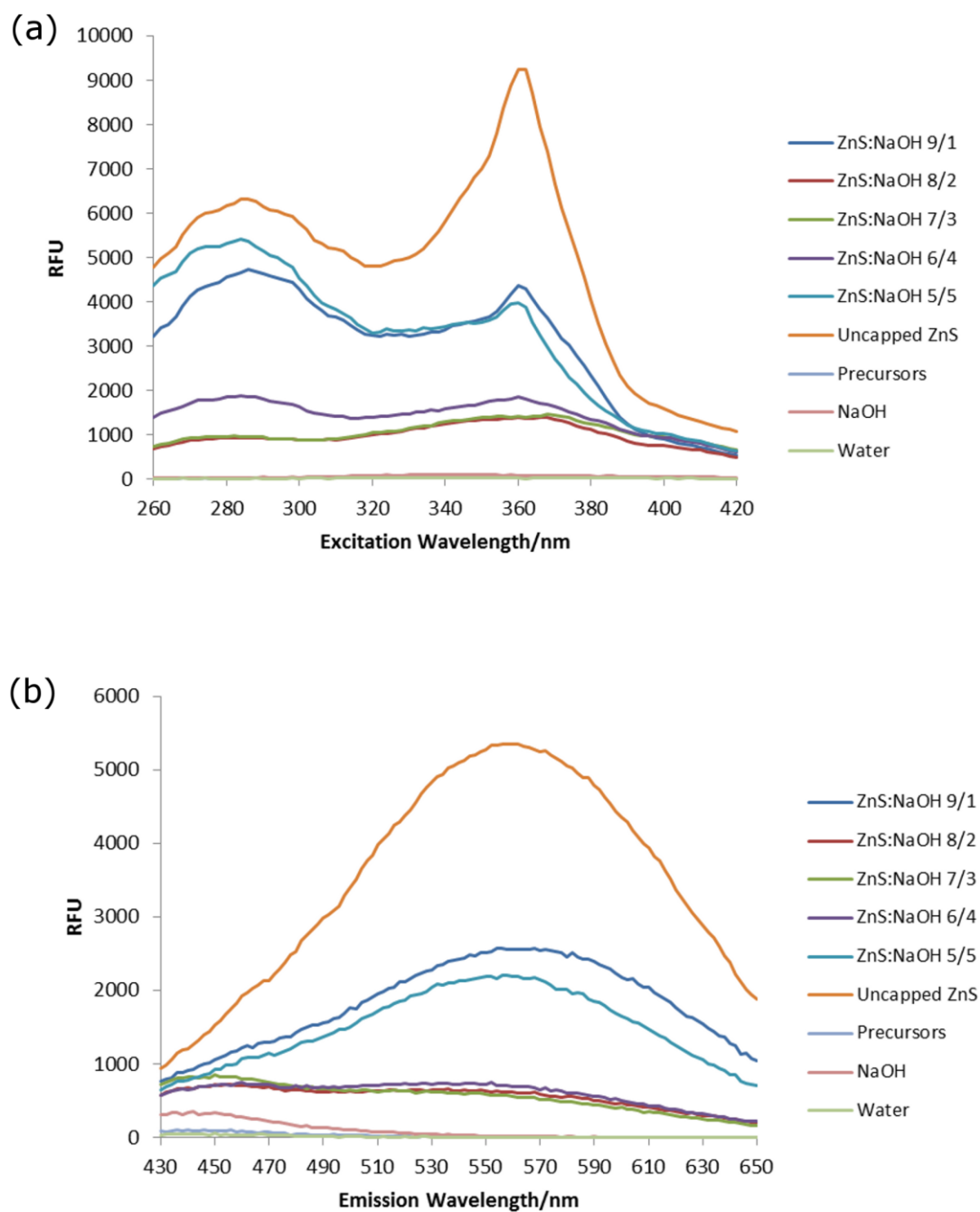


Figure A5. (a) The excitation spectra ($\lambda_{em} = 540$ nm) and (b) emission spectra ($\lambda_{ex} = 360$ nm) for ZnS:NaOH samples produced using different precursor flow ratios. The spectra of the precursors and water blank were obtained as a control.